Manipulation and control of ultra-cold rubidium atoms

Thesis

A thesis submitted for the degree of Doctor of Philosophy

Anna Urszula Kowalczyk

Manipulation and control of ultra-cold rubidium atoms

The Open University

Department of Physical Sciences

February 18, 2013

Date of Submission: 30 September 2012

Date of Award: 13 February 2013

AN EXPERT IS A MAN

WHO HAS MADE ALL THE MISTAKES

WHICH CAN BE MADE

IN A VERY NARROW FIELD.

Niels Bohr

ABSTRACT

During the course of this PhD an experimental set-up has been designed and implemented to confine neutral atoms in microscopic dipole traps and to manipulate their internal states by laser excitation to Rydberg states.

A lot of effort was devoted to the stabilization of the laser sources for two-photon excitation to the Rydberg states, using techniques based on modulation transfer spectroscopy and electromagnetically induced transparency (EIT). Taking advantage of the EIT spectroscopy scheme, we have measured for the first time the electric dipole moments for the transitions between the first excited $5P_{3/2}$ and Rydberg $nD_{5/2}$ level of rubidium. These measurements provided benchmarking of existing theoretical models to calculate the reduced matrix elements and have helped us to identify the D'yachkov-Pankratov method as a particularly reliable one. Therefore we made use of the existing code to calculate the relative radial matrix elements for bound-bound, bound-free and free-free transitions between arbitrary states of alkali atoms. Our results allowed us to identify many features of interest and several Cooper minima have been revealed for the first time.

The preparation of a new apparatus required ultra-high vacuum for efficient laser cooling and trapping experiments. A unique 4-beam magneto-optical trap has been designed and implemented in our new system. The tetrahedral MOT operating at a very acute beams angle has been demonstrated for the first time. The characterisation of the basic properties of our MOT has highlighted some interesting new cooling mechanisms that do not fully match existing theoretical models and will require further investigation. It has been demonstrated that our tetrahedral MOT is suitable to prepare cold, diluted reservoirs of atoms and therefore efficiently load our microscopic dipole trap.

ACKNOWLEDGEMENTS

Now is the time to summarize the 4 years I have spent in sunny England, more precisely in a weird place called Milton Keynes at the unusual university - The Open University. Those were amazing years for me: new country, new language, variety of cultures and people... It was a brilliant and completely new adventure in my life! I would like to thank to my supervisor Silvia Bergamini, the person responsible for my coming here, for giving me the opportunity to experience all of that. Silvia, you have introduced me to the world of science and guided me through this PhD, for that I am eternally grateful! Thank you for your professional advice, patience and help during difficult moments, especially for the last couple of months. I would like to thank my other supervisors Jim Hague and Nick Braithwaite for all their support and guidance. Many thanks to Calum MacCormick and Michał Piotrowicz, guys without you I wouldn't have survived in the lab! Thank you for all your patience and help during the first few months of my fight against the lab equipment ;-) All I know I've learnt from you! I would also like to thank to Chris Mansell for our very interesting lab-conversations! I am also very grateful to our collaborator Ilya Beterov for very interesting discussions we had during his visits at the OU, his help in the lab and nice company at various conferences!

I feel very grateful to many people around the university who helped me a lot with bits of my experiment: Fraser Robertson and Brendan Aengenheister always ready to deal with whims of the electronics, Chris Hall, Martin Percy and Roger for cutting, drilling and all other "emergency" jobs. I would also like to thank Sandra Mills and

Beverley Bishop for taking care about the administration.

Now it's the time to name all the people who made my social life in this weird "city" a little bit more interesting. Lana George and Katarina Miljković, who introduced me to the secret life of MK and OU! Girls, or I should write: you party animals! thanks for all the fun we had together! I should also mention all the people who contributed to these superb events: Stefano, Ziad, Andres, Bethany and many others who I've met in the Pavilion, Plough or PP[1]. And "The Party Department": Camilla, Mauro, Paul, Ben, Kuba and Kathryn. These past two years at 5 Marshworth were a marvellous time! Camilla and Mauro, thank you for sharing all the cooking experience we have gained during "writing up time" and our lovely tasting-evenings! Many thanks to Gosia for taking care of me at RS school in Durham ;-) And to Aga for our "blue-sofa" meetings in Venables. I would also like to mention my officemates Andy, Jon, Zdeněk and Anthony. Our long hours conversations were very helpful during my writing ;-) And many other interesting people I have met, who helped me to survive here!

Special thanks I dedicate to Państwo Skolimowscy for the extremely nice and relaxing evenings at their house ;-) and to Pani Ewelinka for our very early morning tea breaks. And the last but not least: I am endlessly thankful to my dear Polish friend Ania R. for listening of all my complaints and always providing with a professional advice ;-) I would like to thank Ola for our visits to Hi-Fi. Many thanks to Aneta[2] and Maciek, who motivated me to start my PhD!

I would like to dedicate this thesis to my parents, Barbara and Zenon Kowalczyk, and thank them for unconditional support, motivating and believing in me! I realise that raising a physicist is not easy ;-) Many thanks also to my wonderful little-brothers Dumilek and Bartuś and to Kuzinki[3] for keeping me on-line company whenever I needed it! Chciałabym dedykować te tezy moim rodzicom Barbarze i Zenonowi Kowalczyk, oraz podziękować im za bezwarunkowe wsparcie, motywowanie i wiarę w moje możliwości. Zdaję sobie sprawę, że wychowywanie fizyka nie jest proste ;-) Wielkie dzięki dla moich cudownych braciszków Dumilka i Bartusia oraz Kuzinek za dotrzymywanie towarzystwa przez internet kiedy tego potrzebowałam!

[1] I have also visited many other interesting and more educational places during my stay in England, e.g. most of museums in London...

[2] I think you still owe me couple of euro for all the papers I send you!

[3] Well known as Oszustki

Summarizing[4], those were a memorable years I have spent here. Thanks to all of you who contributed! Finally, to those of you who are unable to read this thesis from cover to cover, I would like to provide you with a brief summary of my research: **I investigate ultra-cold Rydberg atoms** (see the figure) **because they are very cool**[5]! To those who manage to read it and have lots of difficult questions, I would

like to quote *Niels Bohr* again. Please, accept it as the answer to everything: *"... at this stage there is essentially the question of an influence on the very conditions which define the possible types of predictions regarding the future behaviour of the system..."*

[4] A little habit I developed after writing this thesis.

[5] And most of the funny pictures in this thesis present my "toys" I have built for this purpose

LIST OF FIGURES

2.1 Interaction between two charged particles A and B 17

2.2 Two-body interaction strengths taken from Walker and Saffman (2005) 18

2.3 Dipole-dipole interactions between two atoms and energy levels of atomic pair states coupled by dipole-dipole interactions 20

2.4 Principle of the dipole blockade and illustration of collective excitation 22

2.5 Different types of collective oscillations 23

2.6 Quantum logic gates with neutral atoms 28

3.1 Energy levels of a two-level atom in the light field 34

3.2 Excitation probability of a two-level atom for different detunings 37

3.3 Radiation pressure force 41

3.4 The principle of Doppler cooling in 1D 42

3.5 The mechanism of a magneto-optical trap 45

3.6 Details of the Sisyphus cooling 48

3.7 Fine and hyperfine structure of ^{85}Rb and ^{87}Rb 51

3.8 Saturated absorption spectrum of the rubidium D_2 line 52

3.9 Layout of the optics for laser cooling 53

4.1 Saturated absorption spectra of ^{85}Rb $F = 3 \rightarrow F'$, ^{85}Rb $F = 2 \rightarrow F'$, ^{87}Rb $F = 2 \rightarrow F'$ and ^{87}Rb $F = 1 \rightarrow F'$ 62

4.2 Error signals for transitions ^{85}Rb $F = 3 \rightarrow F'$, ^{85}Rb $F = 2 \rightarrow F'$, ^{87}Rb $F = 2 \rightarrow F'$ and ^{87}Rb $F = 1 \rightarrow F'$ recorded with FM SA spectroscopy . 63
4.3 A two-photon transition in rubidium 64
4.4 Schematic diagram of the ECDL 68
4.5 Photo of an extended cavity diode laser 69
4.6 Scheme of the TA/DL-SHG 110 laser system by Toptica 71
4.7 Illustration of the modulation transfer process via reflection 74
4.8 Experimental realisation of the laser stabilisation system for the two-photon excitation scheme 78
4.9 SA spectra and MTS error signals for ^{85}Rb $F = 3 \rightarrow F'$ and ^{87}Rb $F = 2 \rightarrow F'$ transitions 79
4.10 Block diagram of FALC 110 81
4.11 Traces recorded at different stages of the error signal generation using MTS technique 82
4.12 Electromagnetically induced transparency in a cascade system 84
4.13 Oscilloscope trace of the EIT signal 87
4.14 Traces recorded at different stages of the error signal generation using EIT technique 91

5.1 Three-level ladder scheme 95
5.2 Experimental set-up for measuring of electric dipole moments 97
5.3 AT spectra recorded for the upper state $44D_{5/2}$ and $22D_{5/2}$ 99
5.4 The dependence of the Rabi frequency on the $\sqrt{P}$ 100
5.5 Obtained reduced matrix elements versus n and comparison to theoretical models. 102
5.6 The calculated radial matrix elements for bound-bound transitions in rubidium, caesium, potassium and lithium. 105
5.7 Density plots of the relative matrix elements for (a) Rb bound-free $nS_{1/2} \rightarrow E'P_{1/2}$ transitions; (b) arbitrary Rb free-free $ES_{1/2} \rightarrow E'P_{1/2}$ transitions including discrete and continuum spectra; (c) Rb bound-bound $nS_{1/2} \rightarrow n'P_{1/2}$ transitions; (d) Rb bound-free $nP_{1/2} \rightarrow E'S_{1/2}$ transitions. 109

5.8 Density plots of the relative matrix elements in Rb atoms for (a) bound-free $nP_{3/2} \rightarrow E'D_{5/2}$ transitions; (b) all $EP_{3/2} \rightarrow E'D_{5/2}$ transitions; (c) bound-bound $nP_{3/2} \rightarrow n'D_{5/2}$ transitions; (d) bound-free $nD_{5/2} \rightarrow E'P_{3/2}$ transitions; (e) bound-free $nD_{3/2} \rightarrow E'F_{5/2}$ transitions; (f) all $ED_{3/2} \rightarrow E'F_{5/2}$ transitions; (g) bound-bound $nD_{3/2} \rightarrow n'F_{5/2}$ transitions; (h) bound-free $nF_{5/2} \rightarrow E'D_{3/2}$ transitions. 110

6.1 Scheme of the interior of the vacuum chamber with components 115

6.2 Positioning of the aspheric lenses using shearing interferometry 117

6.3 Photo of the assembled apparatus 120

6.4 Scheme of the whole apparatus 121

6.5 Cleaning of all components of the chamber 124

6.6 Baking of the chamber 126

6.7 Change of the pressure and the mean temperature during the baking . 127

7.1 Configuration of a tetrahedral MOT 133

7.2 The influence of mirror declination angle on the efficiency of laser cooling and trapping, from Vangeleyn *et al.* (2009) 134

7.3 The photo of the MOT created in the new chamber 136

7.4 Magnetic field generated by the compensation coils 138

7.5 Scheme of the experimental set-up for the absorption imaging technique 142

7.6 Comparison of images taken with fluorescence and absorption imaging techniques 143

7.7 The tetrahedral MOT in the old-vacuum system 145

7.8 The determination of the temperature of atoms in the MOT 146

7.9 The ^{85}Rb MOT loading curve from a background pressure 148

7.10 The temperature of atoms after cooling in optical molasses 150

7.11 The imaging system implemented in our lab 155

7.12 Absorption image of the dipole trap 156

LIST OF TABLES

2.1 Scaling properties of Rydberg atoms 13

2.2 Quantum defect coefficients for Rubidium 85 16

CONTENTS

List of Figures vii

List of Tables x

1 Introduction 1

2 Rydberg states of atoms 9

2.1 A bit of history 10

2.2 Properties of Rydberg atoms 11

2.3 Rydberg states of alkali atoms 14

2.4 Rydberg-Rydberg interactions in a frozen gas 16

2.4.1 Dipole - dipole interactions between two Rydberg atoms 19

2.4.2 Dipole blockade effect and "super-atoms" 21

2.4.3 Applications of Rydberg atoms 24

2.4.4 Our project: long term goal 29

3 Laser cooling and trapping of alkali atoms 31

3.1 General principles of laser cooling 32

3.1.1 Atom-light interaction 33

3.1.2 The light forces 40

3.1.3 Doppler cooling 41

3.1.4 Cooling limits 43

3.2 The magneto-optical trap 44
3.2.1 Sub-Doppler cooling 47
3.3 Implementation of laser cooling for rubidium 49
3.3.1 Apparatus for laser cooling 52

4 Laser system **57**
4.1 The cooling lasers 58
4.1.1 Laser frequency stabilisation to an atomic transition 59
4.1.2 Frequency modulation spectroscopy 60
4.2 Excitation of Rubidium atoms into Rydberg states 64
4.2.1 Extended cavity diode laser (red laser source) 66
4.2.2 SHG laser system (blue laser source) 70
4.3 Laser frequency stabilisation using MTS 72
4.3.1 Basic theory of modulation transfer 73
4.3.2 Frequency modulated signal generation and demodulation . . . 75
4.3.3 780nm laser frequency stabilisation system 77
4.4 Laser frequency stabilisation using EIT signal 83
4.4.1 Electromagnetically Induced Transparency 83
4.4.2 480nm laser frequency stabilisation system 86

5 Electric dipole moments of atomic transitions **93**
5.1 Measurements of electric dipole moments 94
5.1.1 The method and the experiment 95
5.1.2 Spectra analysis 98
5.1.3 Results 100
5.2 Cooper minima 104
5.2.1 Applications 104
5.2.2 Dyachkov and Pankratov model 106
5.2.3 Maps of the Cooper minima for rubidium 107
5.3 Summary 111

6 New vacuum system **113**
6.1 Design of the chamber 114

6.2 Cleaning and Assembling 122
6.3 Baking of the chamber 125

7 MOT in the 4-beam configuration **131**
7.1 A tetrahedral MOT 132
7.1.1 Magnetic fields 136
7.2 Characterisation of the MOT 139
7.2.1 Fluorescence imaging 139
7.2.2 Absorption imaging 140
7.2.3 Temperature 143
7.3 Results and characterisation of the trap 144
7.4 Dipole trapping 151
7.4.1 Classical model of the optical dipole force 152
7.4.2 Experimental set-up 153
7.4.3 Loading the dipole trap 155

8 Summary and future plans **159**

Bibliography **163**

CHAPTER 1

INTRODUCTION

The age of traditional silicon based computation is coming to its end. Since the 1960s information technology followed Moore's law, stating that the power of the computer is doubled every 18th months (Moore, 1965). This requires doubling the number of transistors fitted into a given size silicon chip and thus reducing the size of the computing elements. If the tremendous progress in information technology keeps the current rate, the ultimate limit of miniaturisation will be reached by the year of 2020, when the transistors reach the size of an atom. In the microscopic regime the classical laws of physics do not apply any more. Information processing devices based on atoms will obey the rules of quantum mechanics.

In classical computation information is encoded as a string of *bits*, which in the case of classical computation can assume two logical states 0 and 1. In quantum mechanics a system, e.g. an atom, can exist in many states simultaneously. As a result, quantum bits - the so-called *qubits* can be in any superposition of the logical states $|0\rangle$ and $|1\rangle$. Thus the quantum computer can perform many calculations simultaneously significantly reducing the computation time. The power of a quantum computer can be demonstrated solving the problem of factorizing large numbers. To perform this factorization classical algorithms require a computation time which grows exponentially with the number of digits. Quantum algorithms enable performing the same calculation much faster as the required time grows polynomially with the number of digits (Shor,

1994).

Quantum information and computation are revolutionary and exciting new fields of science which are currently growing very rapidly. However, building a prototype quantum computer is a very challenging and complex task. The difficulties lay not only in the development of the new quantum algorithms. The delicate nature of the quantum superposition complicates the physical realisation of quantum registers and quantum processors. Many experimental and theoretical physicist and engineers are working on the development of physical systems capable of performing quantum computation. There are several criteria identified by DiVincenzo (2000), which a quantum system should fulfil in order to be of use for quantum computation. To build a quantum computer one needs to find a scalable physical system with well defined qubits, be able to initialize qubits in a certain state and to implement a universal set of quantum gates. The system should have coherence times much longer than the gate operation time and finally one needs to be able to read-out the output of the computation.

Many physical system can be adapted to perform quantum information e.g. single photons in combination with linear optics (Kok *et al.*, 2007), trapped ions (Blatt and Wineland, 2008), semiconductors quantum dots (Li *et al.*, 2003*b*), superconducting circuits (Clarke and Wilhelm, 2008). The experiments with trapped ions have achieved so far the most advanced progress towards quantum information as high fidelity quantum gates and small algorithms have been demonstrated (Blatt and Wineland, 2008). However an interesting approach towards quantum computation, proposed by Jaksch *et al.* (2000), is to create neutral atomic qubits and to perform quantum logic gate operations using interactions between Rydberg atoms. This proposal constitutes the basis of our research. We aim to exploit interactions of highly excited Rydberg atoms to demonstrate known quantum algorithms.

In this thesis a state-of-the-art apparatus developed at the Open University for quantum information with neutral atoms is described. During the design and development of this apparatus, experiments have been carried out to prepare, characterize and manipulate cold atoms and their excited states which have given remarkable results. In my thesis I will answer 4 fundamental questions concerning our project: Why Rydberg atoms? What is our goal? What do we need? How do we progress?

Why Rydberg atoms?

Similarly to ions, neutral atoms possess long-lived states and the possibility to encode the information in the hyperfine ground state. Using lasers the internal states of qubits can be manipulated and measured. However, in order to design a quantum logic gate a strong and controllable interaction between qubits is required. Neutral atoms interact via van der Waals and dipole-dipole interactions. In the case of ground state atoms these interactions are negligible for inter-atomic distances larger than a few μm. However, the strength of these interactions can be increased rapidly over 12 orders of magnitude by laser excitation to high n states, Rydberg states.

To prepare the qubits, the atoms need to be slowed down first, so laser cooling and trapping techniques are used. These techniques have been developing since 1980s and are well suited for cooling and trapping of alkali-metal atoms, which belong to hydrogen group of periodic table. The properties of atoms with a single electron excited to the Rydberg state are presented in Section 2.2, in particular the unique features of Rydberg states of alkali atoms are described in Section 2.3. Highly excited atoms possess unique properties. Large polarizability makes Rydberg atoms very sensitive to the electric fields, even those created by neighbouring Rydberg atoms, thus Rydberg atoms interact strongly. In some cases this enhanced sensitivity to other atoms leads to the *dipole blockade* effect, where one Rydberg atom hinders the excitation of its neighbours. Moreover, all the atoms within the interaction range share the excitation exhibiting a collective behaviour. Section 2.4.1 explains these phenomena in detail. Taking advantage of single atom trapping (Schlosser *et al.*, 2001), entanglement between two atoms trapped in individual dipole traps experiencing Rydberg blockade has been demonstrated experimentally (Wilk *et al.*, 2010; Urban *et al.*, 2009).

The Rydberg-Rydberg interactions and the resulting dipole blockade effect set the basis for proposed schemes quantum information with Rydberg atoms (Jaksch *et al.*, 2000). Many theoretical proposals exist for quantum logic gates which can be implemented experimentally with Rydberg atoms (Nielsen and Chuang, 2000). As an example a CNOT gate is given in Section 2.4.1. CNOT gate between single atoms has been recently realised experimentally for the first time by Isenhower *et al.* (2010). These encouraging results suggest that using laser manipulation quantum qubits based

on single atoms trapped in dipole traps can be prepared and quantum gate operations can be performed. Such systems have long coherence times much longer than the gate operation time. Thus Rydberg atoms fulfil most of the criteria for successful quantum computation and are a great candidate for setting the basis of a prototype quantum computer.

What is our goal?

The goal of this research is to perform quantum computation with Rydberg atoms. One of the most challenging criteria for successful quantum computation is "true" scalability. For example quantum algorithms for factorisation require registers of thousand of qubits. Single atoms can be loaded into the dipole trap with efficiency of ~50 % using collisional blockade (Schlosser *et al.*, 2001) or even ~80 % (Zhang *et al.*, 2010) using light assisted collisions. However, the probability of loading N independent traps with single atoms decreases exponentially with the number of traps. A solution to this problem can be to extend the quantum protocols known for single atom qubits to many atomic ensembles qubits - *meso-qubits*, as proposed by Lukin *et al.* (2001).

We want to exploit long range dipole-dipole interactions between Rydberg atoms to generate multi-particle entanglement in interacting many atoms ensembles to create such meso-qubit, as presented in Section 2.4.4.

Quantum information with meso-qubits brings several advantages. The probability of loading a small dipole trap with few atoms is 100 % (Frese *et al.*, 2000) and the preparation of the sample in a singly excited state can be achieved deterministically (Beterov *et al.*, 2011). Thus arrays of meso-qubits can be easily prepared. Quantum gate operations can be realised on a much faster time-scale compared to a single qubit operations. And finally meso-qubits are very robust to decoherence (Dür *et al.*, 2000). The quantum gate operations have not been performed with meso-qubits so far, however a promising result is demonstrated recently single Rydberg excitation in a mesoscopic ensemble of hundreds of atoms carried out by (Dudin and Kuzmich, 2012).

The ultimate goal of our experiment is to investigate multi-particle entanglement within a single meso-qubit and between meso-qubits geometrically arranged in arrays of dipole traps. The long range goal is to extend the validity of known single-qubit

protocols to meso-qubits.

What do we need?

Each experiment involving meso-qubits requires cooling, trapping, excitation and detection. We want to exploit laser cooling techniques to load a small number of atoms into micron-sized far-detuned dipole traps. We also need a reliable laser system to excite the atoms to the Rydberg state and an efficient detection system. At this purpose a new state-of-the-art facility for the experiments with ultra-cold Rydberg atoms has been developed in our laboratory and is presented in this thesis in Chapters 4, 6 and 7.

The atoms are first prepared in a magneto-optical trap and then between 1-100 atoms are loaded into micron-sized dipole traps. The dipole trap allows to store the qubits for long times preserving their internal states. To prepare the dipole traps we use a high numerical aperture aspheric lens. This is the key feature of our apparatus as it is later used for the collection of fluorescence and imaging of atoms either on intensified CCD camera or avalanche photo-diode. Registers of meso-qubits will be prepared in arrays of dipole traps. It has been demonstrated that using a programmable spatial light modulator any spatial distribution of the dipole traps can be arranged and easily manipulated (Bergamini *et al.*, 2004).

The technical aspects of the apparatus for cooling and trapping of atoms is described in detail in Chapter 6. A crucial parameter of such experimental set-up is very low background gas pressure. The collisions of trapped atoms with the background gas particles can kick them out of the trap leading to decoherence. Thus the pressure inside the chamber should be as low as possible. For this reason obtaining of ultra-high vacuum in our system is essential. Chapter 6 describes in details the process of preparation of UHV.

The laser system also plays a fundamental role for the manipulation of the atomic states, as well as for cooling and trapping, and is presented in Chapter 4. Key parameters of each laser system are the linewidth, coherence and the phase stability. The control over the frequency drifts is done by use of a laser locking technique, where the change of the frequency of the laser is turned into an electronic signal and fed back into the diode control system. The methods we employ for frequency locking of each laser

in our lab are primarily based on frequency modulation technique. The only difference between the individual set-ups is the way of obtaining frequency dependent electronic error signal.

The basic theory of laser cooling and trapping is introduced in Chapter 3 and the apparatus for laser cooling is presented in Section 3.3.1. Efficient cooling requires the lasers linewidth to be narrower than the natural linewidth of the cooling transition and the stability at the level of at least few minutes. The error signal is obtained using Doppler-free saturated absorption spectroscopy.

The most critical part of our laser system are the lasers employed for the excitation of atoms to the Rydberg state. We use a two-photon transition scheme, which is explained in Section 4.2. The 780 nm laser is almost in resonance with the first excited state of rubidium and together with the 480 nm it is in resonance with the ns or nd Rydberg state. The error signal for both lasers are obtained using techniques pioneered recently in Durham (McCarron *et al.*, 2008; Abel *et al.*, 2009). For the 780 nm laser signals are obtained using modulation transfer spectroscopy (McCarron *et al.*, 2008) and for the 480 nm laser electromagnetically induced transparency (Harris, 1989; Fleischhauer *et al.*, 2005) spectroscopy is employed (Abel *et al.*, 2009). Chapter 4 presents in detail all the techniques employed and the results obtained.

How do we progress? Our Results

We have carried out both theoretical and experimental work. To accurately manipulate the atoms the understanding of its spectroscopic properties is essential. The calculations of polarizabilities, lifetimes, transition probabilities or excitation pulse duration in the two-photon excitation scheme require the knowledge of radial matrix elements. Although alkali metal atoms have a single valence electron, the calculation of radial integral for states of small angular momentum is not trivial, and there is no analytical solution to this problem. Therefore many theoretical approaches for the calculation of radial matrix element have been developed. However these models need an experimental verification. We have taken advantage of our experimental set-up and EIT spectroscopy scheme to experimentally measure for the first time the electric dipole moments of the transitions between the first excited and Rydberg $nD_{5/2}$ level of rubid-

ium, recently published in Piotrowicz *et al.* (2011). The measurement method together with analysis of the measured spectra is presented in Chapter 5. The results obtained were compared to the theoretical models and they have been found to be in a good agreement with the theory.

We have identified a model developed by D'yachkov and Pankratov (1994) as a particularly fast and reliable method of calculation of the radial matrix elements. This semi-classical model has been implemented for the calculation of the radial matrix elements of transitions between S, P, D and F of alkali atoms. In Chapter 5 the results of the numerical calculations for rubidium atom is presented as density plots. The plots obtained reveal the presence of minima in the transition probabilities alkali atoms, the so-called Cooper minima. This work has been submitted for review (Beterov *et al.*, 2012).

The experimental work focused on the implementation of a new system for cooling and dipole trapping of atoms. The key elements are the aspheric lenses used to create a micro-dipole trap, which have a working distance of 6 mm. The optical access for cooling and trapping laser beams is considerably restricted and building of a standard six-beam MOT is not possible. Therefore our trap operates in an unusual tetrahedral configuration. Additionally the beam intersection angle is very acute. A lot of effort has been put into the characterisation of this trap. Using absorption and fluorescence imaging techniques, the number of atoms, the density and the temperature of the trap have been measured. The results of the performance of the MOT together with the basic description of implemented methods is provided in Chapter 7. The temperature of our MOT seems to be rather high, however cooling the atoms further in the molasses stage reduces it significantly. As a result the loading of a dipole trap with small ensemble of atoms was efficient, as demonstrated at the end of this thesis.

BLANK PAGE IN ORIGINAL

CHAPTER 2

RYDBERG STATES OF ATOMS

Rydberg atoms are atoms having at least one outer electron excited to a high energy state. These atoms are named in memory of Johannes Rydberg who introduced a formula linking the wavelengths of spectral lines of atoms. This chapter begins with a brief historical summary of the development of this equation, leading to the definition of an empirical parameter known as the Rydberg constant.

In this thesis atoms with only one highly excited outer electron are considered. The large distance between the atomic core and electron leads to exaggerated properties of these atoms. The basic physical properties of Rydberg atoms are introduced in Section 2.2 and Section 2.3 focuses on highly excited alkali-metal atoms. As a result of their unique properties, closely spaced Rydberg atoms interact strongly with each other. Two main types of Rydberg-Rydberg interactions are presented in Section 2.4.1. The consequences of these strong interactions, the *blockade effect* and the collective behaviour of interacting atoms can manifest in ensembles of atoms, as described in Section 2.4.2. Rydberg blockade finds its natural application in quantum computation, as a key ingredient for realisation of quantum logic gates based on neutral atoms (Section 2.4.3). The investigation of strongly interacting atomic ensembles is the main motivation for this thesis and is presented at the end of this chapter (Section 2.4.4).

2.1 A bit of history

In the eighteen seventies Ångström identified and measured four lines in the visible part of the emission spectrum of hydrogen. A few years later, in 1885, the Swiss mathematician Balmer, showed that these lines are related to each other by a simple equation (Balmer, 1885):

$$\lambda = \frac{bn^2}{n^2 - m^2} \tag{2.1}$$

where $b = 3645.6\,\text{mm} \times 10^{-7}$, $m = 2$ and $n = 2, 3, 4, \ldots$, making hydrogen the first atom described in a quantitative way. The above formula was purely empirical and did not provide an immediate interpretation of the spectra of other atoms available at that time. The Swedish scientist Rydberg, particularly interested in explaining the nature of the periodic system, began working on those data. Following observations of Liveing and Dewar (1879), who connected Na and K spectral lines into groups with 'sharp' or 'diffuse' edges, Rydberg classified the spectra of all alkali atoms into series and was the first to establish a relation between 'principal' lines and distinct series. To simplify the mathematical expression he introduced the wavenumber ν, which is the inverse of the wavelength λ in vacuum, and he realized that the wavenumbers of the series are related and can be expressed by the formula (Rydberg, 1889):

$$\nu_l = \nu_{\infty l} - \frac{R_{Ryd}}{(n + \delta_l)} \quad \text{for} \quad l = s, p, d, \tag{2.2}$$

where $\nu_{\infty l}$ and δ_l are constants specific for the series of sharp, principal and diffuse lines and denote the series limit and quantum defect respectively. R_{Ryd} is the constant with assigned value $109721.6\,\text{cm}^{-1}$, which he assumed was identical for all chemical elements. This constant is today known as Rydberg constant. After rearranging his equation, Rydberg realized that the Balmer's formula was just a specific case of his result. However, both expressions provided only a formal description of spectra and their physical meaning was not understood yet.

In 1913 Danish physicist Bohr proposed a quantized shell model of an atom. The main assumption in his theory was that when an electron of mass m_e and negative charge e revolves around a heavy nucleus of positive charge Ze in a "stationary state" it

does not emit energy. The electron is held in a circular orbit of radius r by electrostatic interaction and obeys Newton's law of motion. The electron will gain or emit specific amount of energy only as it changes position from one stationary state to another (Bohr, 1913). One of the most important consequences of this theory was the relation it establishes between Rydberg and other fundamental constants:

$$R_{Ryd} = \frac{1}{4\pi\varepsilon_0}\frac{Z^2 e^4 m_e}{2\hbar^2}, \tag{2.3}$$

where ε_0 is the permittivity of free space, Z is the atomic number of an atom[1], e is the electron charge, m_e is the electron mass $m_e = 9.109 \times 10^{-31}$kg and $\hbar = 1.055 \times 10^{-34}$Js is the reduced Planck's constant[2]. Some physical quantities depending on n can be derived from Bohr's formulas, e.g. the size of the electron orbit. Thus the principal quantum number gives the information about the size and energy of the atom.

2.2 Properties of Rydberg atoms

Rydberg atoms are atoms in a high energy electronic state (n). The list of the most representative properties of Rydberg atoms is shown in Table 2.1 and are expressed as a function of n. Some of them can be derived directly from Bohr's theory, as for instance, the radius of the valence electron orbit which is given by:

$$r = \frac{(4\pi\varepsilon_0)n^2\hbar^2}{Ze^2 m_e}. \tag{2.4}$$

It is interesting to notice the scaling of r with n^2 as this implies that the size of a Rydberg atom can be large for high n e.g. $0.5\,\mu$m for $n = 80$. The atoms binding energy is also linked to n:

$$E_{bind} = -\frac{R_{Ryd}}{n^2}, \tag{2.5}$$

where all the constants are defined above, which shows how it decreases proportionately to $1/n^2$. Expressions for other physical quantities can be deduced using the radial matrix elements and energy separations (Gallagher, 1994). From Eq. (2.5), it follows,

[1]The atomic number Z gives the number of protons in the nuclei
[2]$\hbar = \frac{h}{2\pi}$, where h is Planck's constant, $h = 6.626 \times 10^{-34}$Js

that the energy spacing $(E_{bind}(n) - E_{bind}(n-1))$ scales as n^{-3}. The polarizability is proportional to the sum of the squares of the electric dipole matrix elements (which just like the orbital radius scale as n^2) divided by the energy difference between n and $n-1$ states (Bransden and Joachain, 2003), thus the polarizability scales as n^7.

The radiative lifetime τ_0 of an atomic state can be found by summing spontaneous decay rates Γ_i to all lower lying states (Gallagher and Cooke, 1979), $\tau_0 = 1/\Gamma_0$, and is proportional to n^3 which entails that Rydberg states of high n are long-lived. However, at room temperature the black body radiation[3] (BBR) affects atoms by inducing transitions and producing Stark shifts of energy levels. In most cases these effects can be ignored, however they become very important for highly excited atoms because transitions between close-lying energy levels are characterized by low frequencies which satisfy $h\nu \ll k_B T \sim 6\,\mathrm{THz}$. In addition, for high n the transitions between neighbouring Rydberg states possess large electric dipole matrix elements, such that at room temperatures ($T = 300\,\mathrm{K}$) Rydberg states are strongly coupled by the black body radiation. As a consequence of absorption (or stimulated emission) of the BBR photons, the atoms in the initial nl Rydberg state can be transferred to the higher (or lower) lying $n'l'$ Rydberg states or be directly photoionised. The black body induced redistribution of population of Rydberg states has a strong impact on the lifetimes of the excited states. Thus τ_0 has to be corrected for the contribution of the BBR, leading to an effective lifetime τ_{eff} which is determined by the sum of the spontaneous decay rate Γ_0 and BBR induced transitions rate Γ_{BBR}. For approximate calculations of effective lifetimes τ_{eff}, a semi-empirical formula $\tau_{eff} = \tau_0 (n^*)^\alpha$ is commonly used, where the coefficients τ_0 and α are found by numerical calculations and are different for each atomic species, and n^* is an effective quantum number (see Section 2.3). To obtain the effective lifetimes in Table 2.1 for rubidium, the values of $\tau_0 = 1.368$ and $\alpha = 3.0008$ were used, taken from Beterov *et al.* (2009).

In Rydberg atoms electrons orbit at a large distance from the atomic core (e.g. the orbital radius of $n = 80$ is $0.47\,\mu\mathrm{m}$ which is almost 9000 times bigger than the Bohr radius[4]) and are loosely bound. This results in very intriguing properties e.g. very

[3]In studying electromagnetic and thermal radiation, an idealized physical black body, which regardless of its temperature absolutely absorbs the incident radiation at all wavelengths (and thus is an ideal emitter as well), is used as a reference of an absorption or an emission of real physical bodies.

[4]Bohr radius, $a_0 = 5.292 \times 10^{-11}\mathrm{m}$ is a physical constant which characterizes the size of the orbit

Table 2.1: Scaling properties of Rydberg atoms and corresponding values for two S states of Rubidium 85

Property	n-dependence	Unit	Rb(10s)	Rb(80s)
Binding energy	n^{-2}	meV	288.62	2.3
Energy spacing n states	n^{-3}	GHz	25843	14.5
Orbital radius	n^2	a_0	68	8860
Geometric cross section	n^4	a_0^2	1.44×10^4	2.47×10^8
Polarizability	n^7	$\mathrm{MHzcm^2V^{-2}}$	5.75×10^{-4}	1.28×10^3
Radiative lifetime	n^3	μ s	0.41	500

large polarizabilities or electric dipole moments, and thus in the extreme sensitivity of Rydberg atoms to external electric fields. Relatively weak electric fields can shift the energy levels of Rydberg atoms or can even ionize them. This extreme sensitivity to the electric fields is reflected in strong interactions between pairs of Rydberg atoms, of van der Waals or dipole-dipole (Section 2.4.1) type. Atoms can be ionised by application of a small external electric field, which in case of Rydberg atoms is of order few meV. Furthermore, by employing selected values of the electric field strength one can ionise a specific Rydberg state, as different n states ionise at different field strengths, and subsequently by detecting electron and ion as a function of the ionizing field the population of a specific Rydberg state can be measured. This technique is called selective field ionisation(SFI).

Rydberg atoms can be produced in several ways: charge exchange, electron impact, photo-excitation or by combining collisional and optical excitation. In the first method, a Rydberg state of an initially ionic species is produced and energy is then transferred as the Rydberg ion captures an electron from a neutral atom during a collision process. Electron impact, where an electron beam hits the ground state atoms, allows one to excite high l states. However this technique is inefficient and not state-selective. In photo-excitation, the exciting photon is absorbed directly by the atom. As a consequence by tuning energy of the excitation photons one can access to specific Rydberg states. In zero electric field the attainable states depend upon the dipole selection rules ($\Delta l = \pm 1$) and thus only low angular momentum states l are achievable with optical excitation (Gallagher, 1994). There are several experimental methods to optically populate Rydberg states. The alkali atoms can be directly excited from the ground state

of the electron in the ground state in the hydrogen atom

s to the Rydberg state p using single-photon of ultra-violet wavelength (i.e. in case of rubidium $\lambda = 297\,\text{nm}$). Excitation of other atoms requires the use of intermediate resonant states, as the required wavelength of single-photon transition is not in an optical range of the spectrum. Optical excitation via a resonant state is often applied to alkali atoms as relatively low-power and cheap laser sources can be used. Using two-photon transitions with alkalis results in an s or d Rydberg state (see Section 4.2), while states p or f are accessed via three-photon transitions. The excitation to higher l states requires combined techniques which use e.g. optical and microwave fields in connection with linearly varying electric field to create Stark states[5]. Taking advantage of the recent development of narrow-linewidth, high power lasers, which can be tuned with high precision, well-defined Rydberg states can be produced. For instance the fine structure splitting of $90d$ state of rubidium is about 14 MHz, and it was demonstrated that this structure can be optically resolved using two-photon transition (Mohapatra *et al.*, 2007). The two-photon excitation scheme is also implemented in our experiment and it will be described in detail in Chapter 4.

2.3 Rydberg states of alkali atoms

Alkali-metals are atoms in the first group of the periodic table. Their ground state shells are closed, filled to capacity with electrons, with only one valence electron in the outer shell. The fact that all $N-1$ electrons fully fill internal shells, results in the nuclear charge being "screened" and the valence electron experiencing an effective charge of $Z_{eff} = +1$. Furthermore, the problem of describing the interaction of N electrons with the core can be simplified for highly excited states, to the well known one-electron model of hydrogen with some modifications. This is justified by the large separation between the core and the outer electron as well as the huge difference in binding energies of $N-1$ electrons in the ground state and the excited electron. As the core has an effective small charge $+e$ and its wavefunction is limited only to small space around the nuclei, the overlap of the core and outer electron wavefunction is negligible, leading to the problem of a single electron in a Coulomb potential. In other words, the

[5]In the presence of an external static electric field the energy levels of atoms shift and spilt. This is so called *Stark effect*.

core does not contribute to the orbital angular momentum l of the atom, and thus the state of the atom, is labelled only by the outer valence electron, which can be described by hydrogenic wavefunctions. In Rydberg states, in the case where the orbital angular momentum of the outer electron is small ($l \leq 3$), the orbit is elliptic and the electron can penetrate inside the core. The valence electron is therefore exposed to the unscreened, and hence more attractive nucleus. Furthermore, due to Coulombic interactions with other electrons in the inner shells, the shells can get polarized. This results in an increase of the binding energy compared to the binding energies of hydrogen states expressed by Eq. (2.5) for an electron in state n. The difference in energy can be treated by introducing quantum defect δ_{nlj}, which is used to replace n by an effective principal quantum number n^* in Eq. (2.2):

$$n^* = n - \delta_{nlj}. \tag{2.6}$$

Thus the binding energy is of form:

$$E_{bind} = -\frac{R_{Ryd} Z_{eff}}{(n - \delta_{nlj})^2}. \tag{2.7}$$

where l and j denote the orbital angular momentum and total angular momentum respectively. It is worth mentioning, that values presented in Table 2.1 were calculated using n^*. The quantum defect only weakly depends on n allowing values of δ_{nlj} to be used for states with different n but same l. It can be calculated using the extended Rydberg-Ritz formula:

$$\delta_{nlj} = \delta_0 + \frac{\delta_2}{(n - \delta_0)^2} + \frac{\delta_4}{(n - \delta_0)^4} + \frac{\delta_6}{(n - \delta_0)^6} + \dots \tag{2.8}$$

where the coefficients δ_i are obtained from Lorenzen and Niemax (1983) and Li *et al.* (2003*a*). These coefficients have been derived from experimentally measured energy levels of atomic species and fitted by Rydberg-Ritz formula. δ_i are specific for each element and for Rubidium are presented in Table 2.2. One can notice that for F state ($l = 4$) the quantum defect is close to zero and thus it can be neglected for $l \geqslant 4$.

Table 2.2: Quantum defect coefficients for Rubidium 85

State	δ_0	δ_2	δ_4	δ_6
$S_{1/2}$	3.1311804(10)	0.1784(6)	-1.8	-
$P_{1/2}$	2.6548849(10)	0.2900(6)	-7.904	116.4373
$P_{3/2}$	2.6416737(10)	0.2950(7)	-0.97495	14.6001
$D_{3/2}$	1.34809171(40)	-0.60286(26)	-1.50517	-2.4206
$D_{5/2}$	1.34646572(30)	-0.59600(18)	-1.50517	-2.4206
F	0.016312	-0.064007	-0.36005	3.239

2.4 Rydberg-Rydberg interactions in a frozen gas

In the ideal gas model particles do not interact with each other, however atoms are never truly ideal as they do attract or repel each other. These forces arise from Coulomb interactions between dipoles. Neutral atoms do not posses permanent dipole moments. Nevertheless, they do have instantaneous dipole moments due to fluctuations in an electron distribution within the orbitals. Even if the electron cloud is roughly spherical, due to the quantum nature of atoms, it is statistically possible that electrons spend some time grouped on one side of the atom, leaving it negatively charged while the other side, due to deficiency of electrons is positive. Both sides of this dipole can attract or repel neighbouring dipoles or even induce dipole moments in atoms in their vicinity. These temporary interactions are called van der Waals interactions and are the weakest interactions for neutral atoms. However due to large polarizabilities of Rydberg atoms the strength of the interactions can be increased by excitation to high n states. Atoms and molecules possessing permanent dipole moments can in addition, exchange state and transfer energy via dipole-dipole interactions. Permanent dipoles can be induced in the sample of Rydberg atoms by applying small electric field mixing states with different parity. The strength of the dipole-dipole interactions can be also increased by means of two-particle resonance exploiting the degeneracy of pair-states. These dipole-dipole interactions have on-resonant character while van der Waals interactions are off-resonant as they always occur.

According to the electrostatic theory, the potential created by a system of charges A and B (see Fig. 2.1), located at a distance R much greater than the dimension of the system ($|\boldsymbol{r}_A - \boldsymbol{r}'|, |\boldsymbol{r}_B - \boldsymbol{r}''| \ll \boldsymbol{R}$, $\boldsymbol{R} = \boldsymbol{r}_B - \boldsymbol{r}_A$), can be expressed as series in multipole moments of charge distribution. The first few terms of the expansion can be

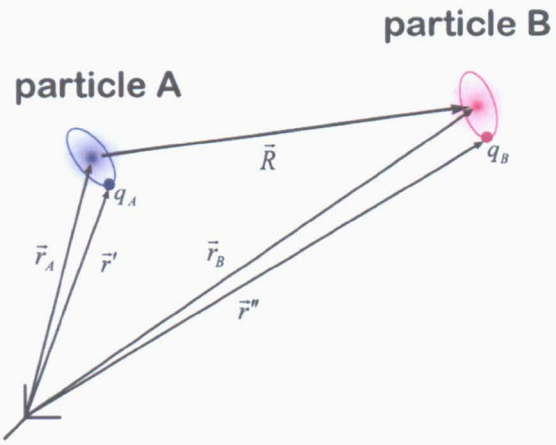

Figure 2.1: Interaction between two charged particles A and B, where q_A and q_B are the total net charges of particle A and B respectively.

written as follows:

$$V_{AB}(\boldsymbol{R}) = \frac{1}{4\pi\epsilon_0}\left[\frac{q_A q_B}{R} + \frac{q_A \boldsymbol{\mu}_B \cdot \boldsymbol{R}}{R^3} - \frac{q_B \boldsymbol{\mu}_A \cdot \boldsymbol{R}}{R^3} + \frac{R^2 \boldsymbol{\mu}_A \cdot \boldsymbol{\mu}_B - 3(\boldsymbol{\mu}_A \cdot \boldsymbol{R})(\boldsymbol{\mu}_B \cdot \boldsymbol{R})}{R^5} + \ldots\right] \tag{2.9}$$

where q_A and q_B are the total net charges of the particle A and B respectively, $\boldsymbol{\mu}_A$ and $\boldsymbol{\mu}_B$ are the dipole moment vectors given by $\boldsymbol{\mu}_A = q_A(\boldsymbol{r'} - \boldsymbol{r_A})$ and $\boldsymbol{\mu}_B = q_A(\boldsymbol{r''} - \boldsymbol{r_B})$. The first term, scaling as R^{-1}, represents strong long-range Coulombic interactions between two charges and is usually negligible for a pair of neutral atoms even for small interatomic distance. The second and third terms describe charge-dipole interactions, which are of shorter range as they scale as R^{-2}. They are non-zero if at least one of the systems possesses a net charge. The most important is the fourth term, which represents dipole-dipole interactions.

Rydberg atoms do not possess permanent dipole moments, however due to their strong polarizabilities they can interact strongly. Fig. 2.2, taken from Saffman *et al.* (2010), presents the interaction strengths of rubidium atoms and ions. It is straightforward to notice that the strongest interactions are between pair of ions (brass colour line). At short range, the interactions between ground state atoms, are governed by van der Waals forces (purple line) and for distances between atoms greater than 30 nm the system is dominated by magnetic dipole-dipole interactions (navy blue line). In comparison to ions, ground state atoms can be considered as non interacting due to

the extreme weakness of their interactions. This value can be changed over 12 orders of magnitude by simple excitation of the atoms to the $100s$ Rydberg state (red line). At short range the interactions have dipole-dipole character, which changes to van der Waals at the characteristic length scale of about $10\,\mu$m. An average interatomic distance $\sim 10\,\mu$m corresponds to densities of order $10^{13}\,{}^{\text{atoms}}/_{\text{cm}^3}$, which are attainable in a gas of laser-cooled alkali atoms. The investigation of Rydberg atoms in the ultra-cold regime has an additional advantage, mainly the atoms do not move significantly at a timescale of the experiment duration (i.e. ^{85}Rb atoms cooled down to $10\,\mu$K will move about $3\,\mu$m during 100 ns, which is less than the interaction range). This is why an ultra-cold Rydberg gas is referred to as "frozen". Here the dynamics of the system is dominated by the interactions between atoms rather then the kinetic energy of atoms, thus their interactions are easier to study in this regime.

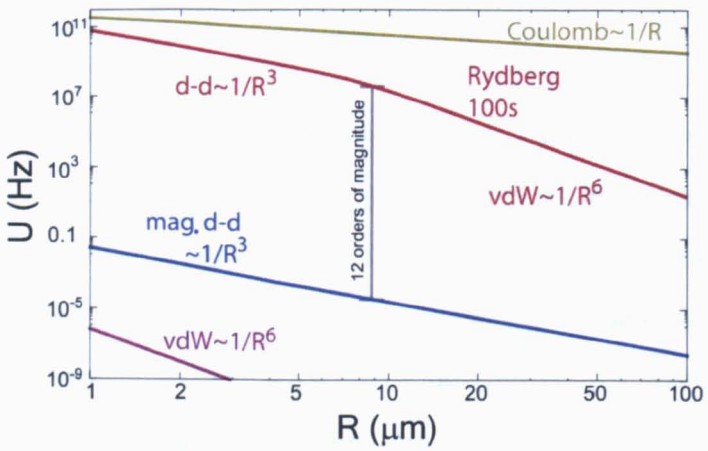

Figure 2.2: Two-body interaction strengths taken from Walker and Saffman (2005). Brass line shows two interacting ions, purple line shows ground state neutral Rb atoms interacting via van der Waals (vdW) interactions. Dipole-dipole (d-d) and vdW interactions of two Rb atoms excited to $100s$ state are marked with red line and magnetic dipole-dipole interactions (mag. d-d) with navy blue line.

Rydberg atoms offer a unique possibility to switch 'on' and 'off' their interaction, and moreover, to control its strength over a wide range. This extraordinary feature of Rydberg atoms makes them useful for quantum information processing (see Section 2.4.3).

2.4.1 Dipole - dipole interactions between two Rydberg atoms

We can derive the expression for the dipole-dipole and van der Waals interactions strength between Rydberg atoms using Eq. (2.9) for two interacting dipoles:

$$V_{dd}(\boldsymbol{R}) = \frac{\boldsymbol{\mu}_A \cdot \boldsymbol{\mu}_B}{R^3} - \frac{3(\boldsymbol{\mu}_A \cdot \boldsymbol{R})(\boldsymbol{\mu}_B \cdot \boldsymbol{R})}{R^5} \tag{2.10}$$

where $\boldsymbol{R}$ is the distance vector between two dipoles, and $\boldsymbol{\mu}_A$ and $\boldsymbol{\mu}_B$ are dipole moments of atom A and B (Fig. 2.3 (a)). To describe these interactions in a quantitative way, a simple quantum mechanical model is used, where the classical dipole moment is replaced by an electric dipole moment operator, $\hat{\mu} = e\hat{r}$. In general, if the wavefunctions $|\varphi\rangle$ and $|\varphi'\rangle$ of the initial and final atomic state are known, the necessary electric dipole matrix elements is of the form:

$$\langle\varphi|\hat{\mu}|\varphi'\rangle = \langle\varphi|e\hat{r}|\varphi'\rangle = \langle nljm_j|e\hat{r}|n'l'j'm'_j\rangle. \tag{2.11}$$

If two atoms in states $|\varphi_1\rangle$ and $|\varphi_2\rangle$ are considered, due to the interaction the atomic states couple creating pair states $|\varphi_1\varphi_2\rangle$ with an energy defect Δ. Thus, the interaction energy can be written as:

$$V_{dd}(R) \sim \frac{1}{R^3} \sum_{|\varphi'_1\rangle,|\varphi'_2\rangle} \langle\varphi_1|\hat{\mu}_1|\varphi'_1\rangle\langle\varphi_2|\hat{\mu}_2|\varphi'_2\rangle = \sum_{|\varphi'_1\varphi'_2\rangle} \langle\varphi_1\varphi_2|\frac{\hat{\mu}_1\hat{\mu}_2}{R^3}|\varphi'_1\varphi'_2\rangle, \tag{2.12}$$

where the sum indicates that all internal states of atoms are considered. If we investigate an atom in an initial state $|np\rangle$, then, for high n states, there should be a number of energetically close states nearby. However, the interactions are dominated by the coupling between $|np\rangle$ and $|ns\rangle$, as well as between $|np\rangle$ and $|(n+1)s\rangle$ states, as the energy difference between these states is small, leading to large dipole matrix elements. This situation is schematically depicted on Fig. 2.3 (b), where the initially populated states $|p\rangle$ and two dipole coupled $|s\rangle$ and $|s'\rangle$ give rise to pair states $|pp\rangle$ and $|s's\rangle$, $|ss'\rangle$ separated by $\Delta = E_{|s\rangle} + E_{|s'\rangle} - 2E_{|p\rangle}$. The Hamiltonian for this interaction is the sum

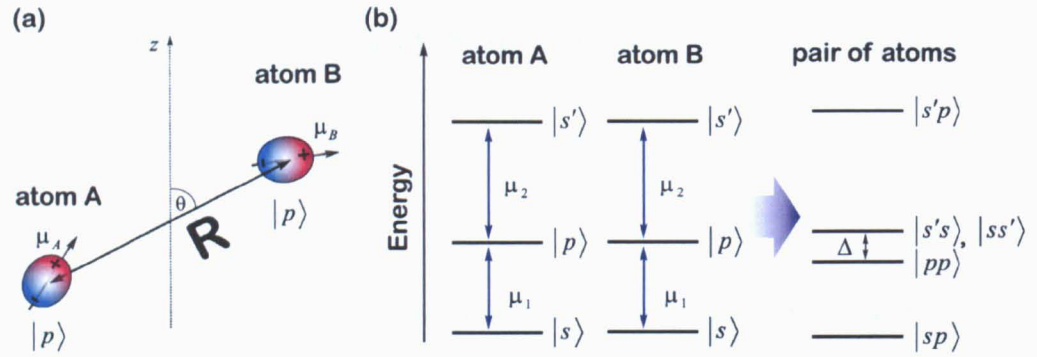

Figure 2.3: (a) Dipole-dipole interactions between two atoms at distance R, (b) single atom energy levels and energy levels of atomic pair states that are coupled by dipole-dipole interactions, Δ is an energy defect.

of the atomic Hamiltonian H_A and the interaction part H_{int}:

$$H = H_A + H_{int} = \begin{pmatrix} 0 & V_{dd}(R) \\ V_{dd}(R) & \Delta \end{pmatrix} = \begin{pmatrix} 0 & \frac{\mu_1\mu_2}{R^3} \\ \frac{\mu_1\mu_2}{R^3} & \Delta \end{pmatrix} \tag{2.13}$$

with eigenenergies:

$$E_{\pm} = \frac{\Delta}{2} \pm \sqrt{\left(\frac{\Delta}{2}\right)^2 + \left(\frac{\mu_1\mu_2}{R^3}\right)^2} \tag{2.14}$$

giving the spatial and Δ dependence of the energy of the pair states. It is possible to tune the relative position of energy levels of Rydberg atoms by employing an electric field. Thus two regimes of extremely large and small absolute value of the energy defect should be considered:

$|\Delta| \gg |\mu_1\mu_2/R^3|$ - long range, van der Waals interactions

In this case, expanding in series to Eq. (2.14) for $|\mu_1\mu_2/R^3| \ll |\Delta|$, the expression for the energy shift of the $|pp\rangle$ state takes form:

$$\Delta E_{|pp\rangle} = \frac{1}{\Delta}\frac{(\mu_1\mu_2)^2}{R^6} = -\frac{C_6}{R^6}, \tag{2.15}$$

where C_6 is the coefficient determining the strength of the (induced) van der Waals interaction. With $\mu \sim n^2$ and $\Delta \sim n^{-3}$, the C_6 scales as n^{11}. The sign of the detuning Δ governs whether the interaction is attractive or repulsive.

$|\Delta| \ll |\mu_1\mu_2/R^3|$ - short range, resonant dipole-dipole interactions

In this case, the Eq. (2.14) can be approximated by:

$$E_{\pm} = \pm\frac{\mu_1\mu_2}{R^3} = \pm\frac{C_3}{R^3}, \tag{2.16}$$

with the coefficient C_3 scaling as n^4. Usually this type of interaction is achieved by tuning the external electric field to remove the energy defect. However, there exist pairs of states (e.g. $58d_{3/2}$, $58d_{3/2}$ and $60p_{1/2}$, $56f_{5/2}$ (Walker and Saffman, 2008)) which are almost degenerate ($\Delta = 0$) in zero electric field. This phenomenon is usually referred to as Förster resonance.

The modelling of the atoms differs significantly in this two regimes, as the contribution of the surrounding atoms to the total interaction (Amthor, 2008) is different. In the case of the van der Waals interactions, it is adequate to consider only the interaction between nearest neighbours allowing the many-body system be treated as an ensemble of interacting pairs. In the dipole-dipole regime, the influence of all the atoms has to be taken into account, as the contribution from the surrounding atoms can be much larger than that from the nearest one. The characteristic length determining the boundary between these two regimes is called the van der Waals radius, $R_{vdW} = \sqrt[3]{C_3/\hbar\Delta}$, and it determines the region where the energy shift changes from the classic van der Waals form ($R \gg R_c$) to the resonant dipole-dipole form ($R \ll R_c$).

2.4.2 Dipole blockade effect and "super-atoms"

As already mentioned, the dipole-dipole interaction shifts the energy levels of the atoms. If the strength of the interaction is larger than other energy scales of the system (e.g. natural linewidth of the Rydberg state Γ or the linewidth of the an excitation laser $\Delta\nu$), then the dipole blockade effect occurs, where one atom excited to the Rydberg state prevents the excitation of other atoms located within a region, called blockade radius R_b (Lukin *et al.*, 2001).

Fig. 2.4 (a) illustrates the principle of the dipole blockade effect in the case of repulsive interaction for two atoms. The laser field with frequency $\omega = E_n/\hbar$ drives the transition from the ground state $|g\rangle$ to the Rydberg state $|r\rangle$ of the atom. If the

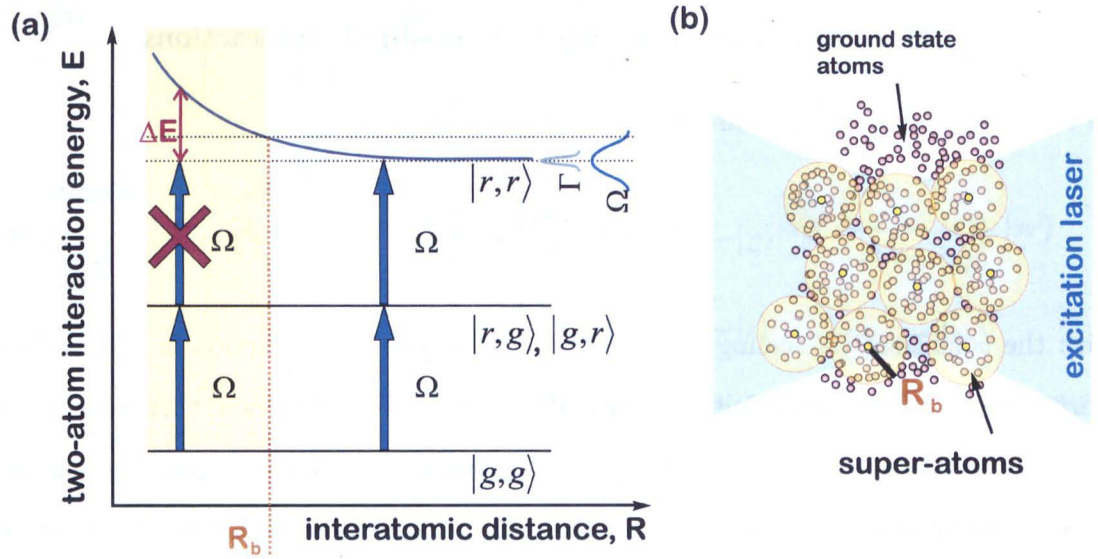

Figure 2.4: Principle of the dipole blockade: (a) Two-atom system is considered: a narrow band laser tuned to the atomic resonance cannot excite two atoms within the blockade radius to state $|rr\rangle$ due to energy level shift caused by the strong dipole-dipole interactions. (b) Illustration of collective excitation - all the atoms within the blockade radius share single Rydberg excitation creating so-called "super-atoms".

pair states are considered, four possible situations can occur: no excitation $|gg\rangle$, single excitation in either of states $|gr\rangle$ or $|rg\rangle$ and two simultaneous excitations $|rr\rangle$. Due to the dipole-dipole interaction, the energy level $|rr\rangle$ is shifted by ΔE which depends on the distance between two atoms, R. The energy levels of states $|gg\rangle$ and $|gr\rangle$ remain non-shifted as the polarizability of the ground state is small. In the case of non interacting atoms, a laser with frequency ω can drive both transitions: $|gg\rangle \rightarrow |gr\rangle$ and $|gr\rangle \rightarrow |rr\rangle$. However, for $R < R_b$, where R_b is blockade radius, the energy shift ΔE is larger than the greater of the two linewidths Γ or $\Delta\nu$, and thus the laser is no longer in resonance with the $|gr\rangle \rightarrow |rr\rangle$ transition, therefore this transition is suppressed. In this case, only one of the two atoms can be excited to the Rydberg state, and the two atoms share the excitation. This is a collective excitation as it is not possible to determine which of the atoms is excited.

The collective behaviour of many-body systems can be explained in similar way. For a group of N atoms within the blockade radius (Fig. 2.4 (b)), all states with two or more excited atoms will be shifted out of resonance with the excitation laser due to the strong interactions leaving only two states which can be populated (Stanojevic

and Côté, 2009), the ground state:

$$|\psi^{(N,0)}\rangle = |g_1 g_2 \dots g_n\rangle, \tag{2.17}$$

and only one excited state

$$|\psi^{(N,1)}\rangle = \frac{1}{\sqrt{N}} \sum_{i=1}^{N} |g_1 \dots r_i \dots g_N\rangle, \tag{2.18}$$

where r_i describes the Rydberg state. In other words, the whole system acts like a two-level system. A two-level atom in the presence of a resonant laser field will cyclically absorb and re-emit photons and thus will oscillate between the ground and excited state with a frequency Ω_0 called the Rabi frequency (Fig. 2.5 (a), see Section 3.1.1). The ensemble of N non-interacting atoms will undergo the same frequency Rabi oscillations, however the amplitude of the oscillations will increase by a factor of N (Fig. 2.5 (b)). In the case of an interacting N-body system only one excitation is present at any time in the system and it belongs to all atoms collectively. As all atoms share only one excitation, the system oscillates between the ground state and the excited state, where the excited state is a state with all atoms in the ground state except for a single excited one. Therefore the amplitude of the oscillations is equal to one, but the Rabi frequency of the system is enhanced by the factor of $\sqrt{N}$ (Fig. 2.5 (c)(blue line)). This system is sometimes referred to as a "super-atom".

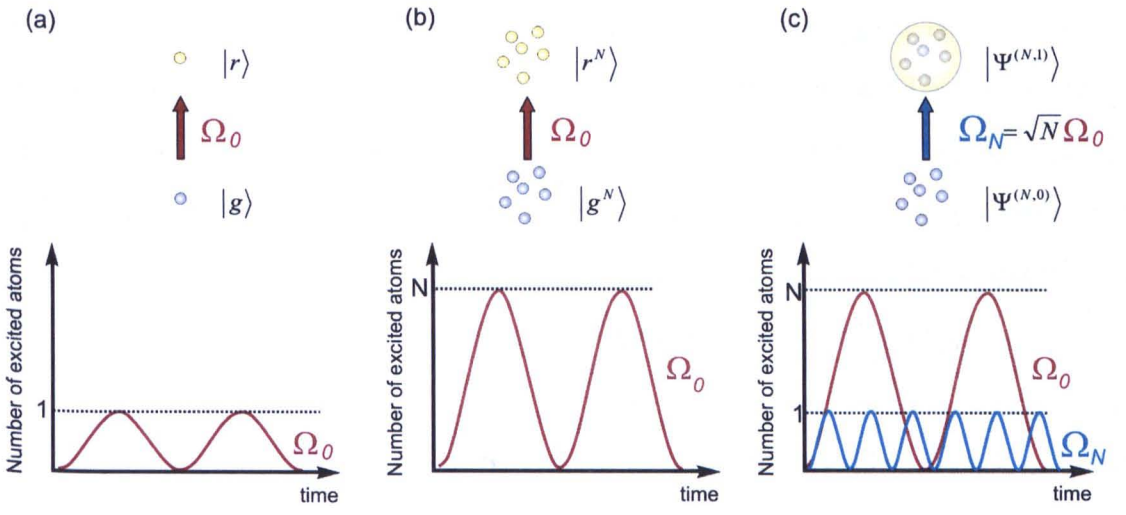

Figure 2.5: Different types of collective oscillations: (a) Rabi oscillations of single atom, (b) Rabi oscillations of N non-interacting atoms, (c) Rabi oscillations of a superatom.

The collective behaviour of a two-atom system has already been experimentally demonstrated by the group in Paris (Gaëtan *et al.*, 2009) and in Wisconsin (Urban *et al.*, 2009). They showed the Rydberg blockade within two atoms individually trapped in the micron sized optical dipole traps separated by a distance of 4 μm. They managed to record the oscillations, associated with the excitation of an entangled state between the ground state and the collective Rydberg state. These collective oscillations were sped up by the factor $\sqrt{2}$ relatively to the single atom excitation. Entanglement between two atoms trapped in individual dipole traps using Rydberg blockade was also demonstrated in the experiment of Wilk *et al.* (2010). The authors measured that at the end of an entangling sequence about 61% of the initial amount of atoms are still present in both traps and the fidelity of finding these pairs in the entangled state is 0.75. Although this results might seem not so impressive compared to the entanglement demonstrated with ions where the obtained fidelity was 0.9994 (Blatt and Wineland, 2008), by overcoming the loss of atoms from the system one can expect that significant improvements can be achieved.

A fully blockaded meso-scopic atomic ensemble has been demonstrated experimentally only very recently. The group of Kuzmich exploited the Rydberg blockade in a dense mesoscopic sample of Rb atoms for generation of a deterministic single-photon source (Dudin and Kuzmich, 2012). In a 1-D optical lattice they prepared a 15 μm long ultra-dense sample of a few hundred atoms which were excited to a high Rydberg state using two-photon transition. By tuning the geometry of the lattice and of the excitation beam, they manage to achieve a fully blockaded regime for $n > 70$. Probing such a collective Rydberg excitation with a read-out laser pulse tuned to the frequency of the intermediate state results in a single photon emission in a desired direction. This result is of great importance: not only as this is the first experimental realisation of a fully-blockaded meso-scopic sample but it also demonstrates non-linearity of an interacting Rydberg ensemble at a single photon level.

2.4.3 Applications of Rydberg atoms

The unique properties of Rydberg atoms result in a range of possible practical applications. For instance, they are used in the detection and amplification of millimetre-wave

radiation. Rydberg atoms coupled to a micrometer-wave cavity make up single-atom masers[6] (Haroche *et al.*, 1982). They also offer one of the most sensitive tools for detection of black body radiation, where the microwave photons trigger transitions of Rydberg atoms to higher n levels, which can be subsequently detected by selective field ionization (Tada *et al.*, 2006). Similar mechanism can also be applied to create an absolute quantum thermometer enabling the measurement of the room temperature with an accuracy of order 10 mK (Ovsiannikov *et al.*, 2011), which is of great importance in the precise operation of optical-frequency lattice clocks.

Rydberg atoms are very sensitive to electric fields and using the spectra of high Rydberg states of supersonic beam of krypton atoms it is possible to determine electric fields with a $20\mu V/cm$ accuracy (Osterwalder and Merkt, 1999). Taking advantage of the recent developments in micro-electromechanics, and of the optical detection of Rydberg states by exploiting the electromagnetically induced transparency (EIT) effect (see Section 4.4.1), one can produce a compact, chip-size electric field sensor (Bason *et al.*, 2008). Similarly, millimetre size optical magnetometers with picotesla sensitivity can be fabricated, which are based on the coherent population trapping (CPT) in alkali vapours (Schwindt *et al.*, 2004). Rydberg atoms also find the applications in the field of quantum computation.

Quantum computation with Rydberg atoms

According to Moore, the co-founder of *Intel*, the number of transistors on an integrated circuit that can be manufactured in an inexpensive way is doubled every two years (Moore, 1965). Nowadays, this law is reaching a fundamental limit, as the size of transistors is approaching the size of atoms. As a consequence, quantum mechanical effects begin to influence the efficiency of the electronic components and the presence of noise is limiting the power of classical computers. A solution to these problems is to bring on the computing to a different level, where the processing is performed by means of quantum mechanics (Nielsen and Chuang, 2000). In order to perform successful quantum computation, 5 fundamental requirements introduced by DiVincenzo (2000), have to be fulfilled. These criteria are: a **scalable** physical system with well defined

[6]Maser - a device producing coherent electromagnetic radiations exploiting stimulated emission phenomenon. MASER stands for Microwave Amplification by Stimulated Emission of Radiation

qubits, the ability to **initialize** qubits in a pure state, a **universal set of quantum gates**, **coherence times** much longer than gate operation time and finally the ability to **read-out** the output.

The qubit

A basic concept of classical computing is the *bit* which stores information. One bit can have only one of two possible values, which by convention are denoted by 0 and 1. In quantum computation, the bit is replaced by a *qubit*, which represents possible states of a quantum system and can be found not only in states $|0\rangle$ or $|1\rangle$ but also in any superposition of these states: $|\psi\rangle = \alpha|0\rangle + \beta|1\rangle$, where α and β are probability amplitudes and $|\alpha|^2 + |\beta|^2 = 1$. Thus a single qubit can exist in an infinite number of states (and therefore store an infinite amount of information) but upon being measured it can only give either 0 or 1. The main concept of quantum information is to make use of this hidden information, which grows exponentially with the number of qubits. To experimentally realize qubits, many different physical systems can be used e.g. the polarization of photons, the alignment of atomic, electronic or nuclear spins in a magnetic field or two states of an atomic system (e.g. ground and excited states of Rydberg atoms).

The idea to use Rydberg atoms as qubits was first proposed by Jaksch *et al.* (2000). Rydberg atoms have long lifetimes, they offer strong interactions and by changing the Rydberg state to which the atom is excited or by de-excitation to the ground state, the interactions between qubits can be switched off completely, as atoms in the ground state interact weakly with the environment. The interaction of Rydberg atoms with light enables fast performance of quantum gate operations.

Quantum logic gates

To perform operations on bits, classical computers use logic gates and the information is sent through the circuit wires as an electronic current. In quantum computation the "quantum wire" is represented by e.g a passage of time or a particle moving from one point in a space to other, and information is processed by quantum gates. An example of a two-qubit gate is the so-called *controlled-NOT* (or C-NOT) gate. The C-NOT

gate combined with any single qubit gate operations can generate any multiple qubit quantum logic gate. The C-NOT gate has two input qubits, a control and target one, and the gate operates in the following way; if the control qubit is in state 0 than the target remains unchanged, if the control is set to 1, then the state of the control qubit is flipped. This can be expressed as the truth table:

$$|00\rangle \rightarrow |00\rangle;\ |01\rangle \rightarrow |01\rangle;\ |10\rangle \rightarrow |11\rangle;\ |11\rangle \rightarrow |10\rangle. \tag{2.19}$$

The two-qubit gate for neutral atoms proposed by Jaksch *et al.* (2000) requires the qubit to be encoded in the two hyperfine levels of the ground state, labelled $|0\rangle$ and $|1\rangle$ and the interactions are switched on/off via excitations to the Rydberg state $|r\rangle$. A CNOT gate was first experimentally demonstrated by the group from Wisconsin (Isenhower *et al.*, 2010). They exploited the Rydberg blockade between two individually addressable atoms held in optical traps separated by about 8μm to create so-called *controlled-Z* (C_Z) gate. The experimental sequence involves three laser pulses Fig. 2.6: a π pulse[7] coupling $|1\rangle \rightarrow |r\rangle$ transition is applied to the control atom (1), then a 2π pulse $|1\rangle \rightarrow |r\rangle \rightarrow |1\rangle$ acts on the target atoms (2) and finally another π pulse $|r\rangle \rightarrow |1\rangle$ is applied to the control atom (3). When the initial two-qubit state is $|01\rangle$ Fig. 2.6 (a), the control atom is not coupled to the Rydberg level, thus there is no blockade effect, and the target atom is excited to the Rydberg state and subsequently de-excited by the second pulse. This corresponds to 2π rotation of the effective spin and results in a $\Delta\phi = \pi$ phase shift of the wave-function of the target atom. If the initial state is $|11\rangle$ as showed in Fig. 2.6 (b), the control atom gets exited to the $|r\rangle$ state and the blockade effect prevents an excitation of the target atom. As a result there is no phase change in its wave-function. The C_Z phase gate together with $\pi/2$ rotations between $|0\rangle$ and $|1\rangle$ gives the full C-NOT gate.

In summary, Rydberg atoms are very promising candidate for quantum information processing as they fulfil all 5 criteria given by DiVincenzo (2000). Taking advantage of laser manipulation, qubits can be easily initialized in a long lived hyperfine ground states. A set of universal quantum gates implementable with Rydberg atoms

[7]Pulse flip angle $\theta = \Omega t$, where Ω is Rabi frequency (see Section 3.1.1), determines the duration t of the laser pulse, e.g. applying π pulse results in the complete population inversion.

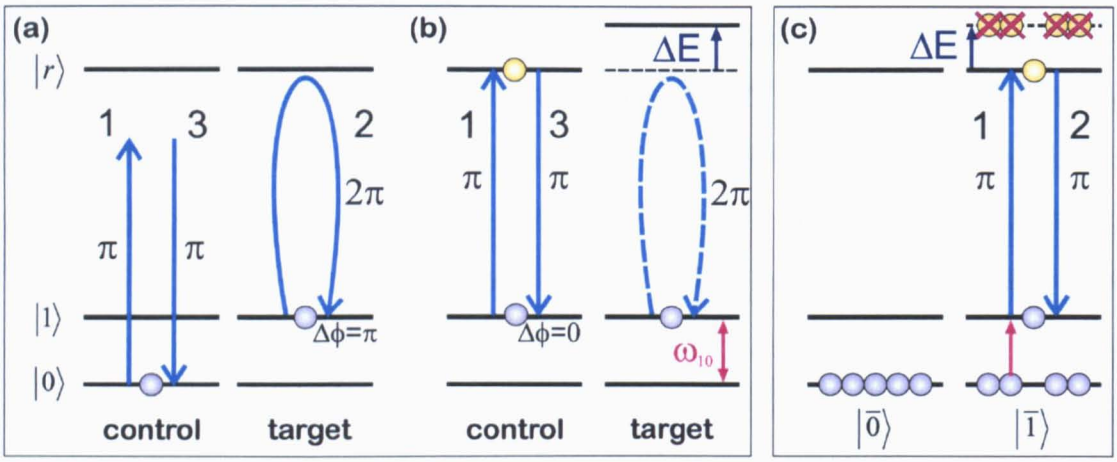

Figure 2.6: Implementation of Rydberg blockade for realization of a quantum logic gates with single atoms or atomic ensembles. Experimental sequence: (1) π pulse $|1\rangle \rightarrow |r\rangle$ is applied to the control atom, (2) 2π pulse $|1\rangle \rightarrow |r\rangle \rightarrow |1\rangle$ is applied to the target (3) π pulse $|r\rangle \rightarrow |1\rangle$ is applied again to the control atom. (a) initial state is $|01\rangle$ (b) initial state is $|11\rangle$ (c) quantum gate with an ensemble of atoms.

already exists as, for example a C-NOT gate between two individually addressed atoms, demonstrated in (Isenhower *et al.*, 2010). Such qubits offer long coherence times, much longer than the gate operation time. The last criteria, scalability, remains the most challenging to accomplish experimentally, e.g. to implement quantum algorithms for factorisation of numbers registers of thousands of qubits are required. To generate such registers arrays of dipole traps can be created using micro-lenses (Dumke *et al.*, 2002) or holographic techniques (Bergamini *et al.*, 2004). However, the efficiency of loading of a dipole trap with single atoms is of order 50% (Schlosser *et al.*, 2001) and therefore the probability of simultaneous loading of an array of independent dipole traps with single atoms drops exponentially with the number of traps. A different approach to create large qubit registers is to trap single atoms in an optical lattice. Recently, huge progress have been made in single-site addressing of an optical lattice, (Weitenberg *et al.*, 2011) which enables the possibility of performing two-qubit gate operations between selected pairs of atoms in the lattice. However, a loss of an atom from these systems results in the loss of a qubit and in failure of the gate operation. Lukin *et al.* (2001) proposed to extend the idea of single-atom qubit gates to many atom ensemble qubits, so called *meso-qubits*.

2.4.4 Our project: long term goal

The idea of using blockaded atomic ensembles for the preparation of meso-qubits has not been realized experimentally yet. The main goal of our research is to exploit long range dipole-dipole interactions between Rydberg atoms to generate multi-particle entanglement in interacting many atoms ensembles to create meso-qubit. We want to trap between 1-100 atoms in a tightly focused optical dipole trap and to exploit an off-resonant stimulated rapid adiabatic passage (Beterov *et al.*, 2011) technique to deterministically excite only one Rydberg atom out of a randomly loaded dipole trap to create and manipulate meso-qubit.

Meso-qubits

The idea of meso-qubit introduced by Lukin *et al.* (2001) relies on the collective excitation of a mesoscopic sample to Rydberg state. Using Eqs. (2.17) and (2.18), the ensemble states can be defined as $|\bar{0}\rangle = |00\ldots0\rangle$ and $|\bar{1}\rangle = \frac{1}{\sqrt{N}}\sum_{i=1}^{N}|0\ldots1_i\ldots0\rangle$ respectively, where N is the number of atoms in an ensemble (Fig. 2.6 (c)). Assuming that the shift of the energy levels due to the blockade effect ΔE is large enough to prevent excitation of a double Rydberg state, the ensemble can be then treated as a two-level system and the two qubit gates between ensemble-qubits can be performed in the same manner as in Fig. 2.6 (a) and (b). The entangled state $|\bar{1}\rangle$ is known as a coherent W state (Dür *et al.*, 2000).

The implementation of meso-qubits brings several advantages compared to the use of single-qubits for gate operations. To start with, loading the dipole traps with small atomic ensembles is much easier and more efficient than single atom trapping. Therefore, arrays of dipole traps can be used to create registers of meso-qubits. The interaction of meso-qubit and light is enhanced by $\sqrt{N}$, where N is the number of collectively interacting atoms, thus the quantum gate operations can be realized on a much faster time-scale than if single qubits are used, which results in also lower decoherence. Furthermore, meso-qubits are characterized by a high degree endurance against small number of atom losses from the system (Dür *et al.*, 2000; Chaves and Davidovich, 2010).

Investigation of multi-particle entanglement

We aim to investigate multi-particle entanglement within an ensemble confined within a μm-sized trap as well as between geometrically arranged meso-qubits. The goal is to demonstrate the validity of known single-qubit protocols to meso-qubits. Thus the meso-qubits will be prepared in arrays of micron-sized far-detuned dipole traps. Spatial distribution of the dipole traps can be easily manipulated using a programmable spatial light modulator (Bergamini *et al.*, 2004). This technique has an advantage that the symmetries in the geometrical arrangement of the traps can be broken leading to entirely arbitrary and controllable arrangement of traps. In addition by tuning the Rydberg state to which the ensemble is excited, different complex interaction patterns can be created. For example, by choosing the state of the electron non-isometric interactions can be achieved where the shape of the interaction changes in space (e.g. the dipole-dipole interaction range has a pattern similar to the radiation pattern of an antenna). Therefore an ensemble of few atoms can be spatially arranged in such a way that all the atoms will interact with one central atom but will not interact with each other. Furthermore by employing the scheme for deterministic single atom excitation (Beterov *et al.*, 2011), the multi-particle entangled states can be obtained with a single laser shot. This is so called *global addressing*. Enabling single-shot multi-particle entanglement generation will speed up quantum gate operations and thus reduce the total decoherence. Global addressing also allows one to overcome scalability issues as it should be possible to address hundreds of qubits stored in quantum register with a single laser pulse.

Summary

In this chapter I gave a review of unique properties of highly excited atoms with singe valence electron. The strong long-range Rydberg-Rydberg interactions and the resulting Rydberg blockade effect have been described. A range of possible applications, with particular emphasis to the quantum information with neutral atoms have been discussed. The possibility of implementing quantum information schemes with Rydberg atoms motivated this work, as the goal of our experiment is the investigation of collective behaviour of atoms and multi-particle entanglement between Rydberg atoms.

CHAPTER 3

LASER COOLING AND TRAPPING OF ALKALI ATOMS

The particle-like nature of light was suggested by Einstein in a 1905 paper on quantization of the radiation field, where he introduced the concept that light of frequency ν consists of a finite number of energy quanta $h\nu$, called *photons*[1]. However, the complete theory of the radiation was not published until 1917. Nevertheless, in his estimations, the damping force exerted by light on atoms was so small that it could be neglected. The first experimental demonstration of light pressure on atoms was carried out in 1933 by Frisch, who illuminated an atomic beam of sodium with resonant light and observed a slight deflection of atoms away from the light source (Frisch, 1933). Despite the much smaller momentum carried by photons compared to momentum of thermal atoms, many cycles of absorption and emission result in a noticeable force imposed by light. The manipulation of the atomic motion with light became possible half a century after Einstein's theory. The major breakthrough came after the invention of lasers, when Hänsch and Schawlow and independently Wineland and Dehmelt, suggested using laser light to slow down the atoms (Hänsch and Schawlow, 1975; Wineland and Dehmelt, 1975). In both cases, the proposed cooling mechanism was based on the Doppler effect (Section 3.1.3), and is known as Doppler-cooling.

[1]The name *photon* was devised in 1926 by physical chemist Gilbert Lewis

Laser cooling and trapping is nowadays an important and universal tool for investigation of the spectroscopic properties of atoms and for the active control and manipulation of the state of atoms. In this chapter the basic principles of laser cooling will be presented. A short review of atom-light interactions is provided in Section 3.1.1 in order to derive an expression for the scattering rate, an important parameter in laser cooling process. The light forces exerted on atoms are explained in Section 3.1.2, whilst the cooling mechanism based on Doppler cooling in 1D and cooling limits are elucidated in Sections 3.1 and 3.1.4. In general 3 pairs of counter-propagating laser beams are used to obtain 3D cooling and this configuration is called *optical molasses.* The cooling only reduces the temperature of atoms and increases their space density, but it does not confine them in space. To trap the atoms the so-called *magneto-optical trap* is commonly used, obtained by adding a magnetic field gradient to the molasses. The basic principles of the cooling and trapping mechanism taking place in such a trap are presented in Section 3.2. Finally the implementation of laser cooling for rubidium atoms is given, including a description of the laser source used in our experiment.

3.1 General principles of laser cooling

Laser cooling is a commonly used method for reducing the temperature of atomic gases. In this context the concept of temperature has a different meaning than in thermodynamics, where the temperature is defined as a state of a closed system being in equilibrium with its surrounding, which in turn requires the system to be in thermal contact with the environment. A laser cooled system is not closed as scattering of light is always active, thus it is inadequate to use the term temperature in this contest. However, for atomic gases, where the energy distribution of particles is characterized by the Maxwell-Boltzmann distribution, the average kinetic energy of atoms $\langle E_k \rangle$ is a measure of the temperature of the sample. The temperature T of the sample can be extracted from the expression $\langle E_k \rangle = {}^{k_b T}/_2$, where k_b is Boltzmann's constant. Following the fact that the interaction with light changes the momentum of atoms, and thus their kinetic energy, the term temperature is a convenient way of describing velocity and energy of atoms.

In order to properly describe the fundamental process of laser cooling, linked to the momentum exchange between an atom and a photon, the interaction between an atom and a light field should be considered. The atom-light interaction is a subject of many course books (e.g. Loudon (1973); Weiner and Ho (2003); Foot (2005); Steck (2007)) and in the following section only the main aspect of that question will be recalled.

3.1.1 Atom-light interaction

A two-level atom interacting with the light field can be described using the semi-classical approach where the atom is treated quantum-mechanically whilst the light is represented by a classical electromagnetic field. According to quantum mechanics, the state of a system is described by wave functions that obey the time-dependent Schrödinger equation given by:

$$\hat{H}\Psi(\boldsymbol{r},t) = i\hbar\frac{d\Psi}{dt}, \tag{3.1}$$

where the Hamiltonian, $\hat{H}$, is the energy operator[2] and $\Psi(\boldsymbol{r},t)$ is the atomic wave function. The total Hamiltonian of the system $\hat{H}$ is the sum of the isolated atom Hamiltonian $\hat{H}_A$ and the time-dependent atom-light interaction part $\hat{H}_{int}(t)$:

$$\hat{H} = \hat{H}_A + \hat{H}_{int}(t). \tag{3.2}$$

It is shown (e.g. in Atkins and Friedman (2005)), that the time dependent Schrödinger equation Eq. (3.1) for the Hamiltonian $\hat{H}_A$, which is time-independent, has solutions of the form:

$$\Psi_n(\boldsymbol{r},t) = \psi_n(\boldsymbol{r})e^{-iE_nt/\hbar} = \psi_n(\boldsymbol{r})e^{-i\omega_nt}, \tag{3.3}$$

where E_n represents the energy of a stationary state of the atom and $\omega_n = {}^{E_n}/_{\hbar}$ is the angular frequency of its wave representation. Thus, the time dependent wave function $\Psi(\boldsymbol{r},t)$ may be split into a time-independent wave function $\psi(\boldsymbol{r})$ and a time-

[2]Quantum mechanics provides a mechanical description of the time evolution of the state of a physical system. A particular quantum state is mathematically represented by a **wave function** and it is associated with information about the observables of the system formulated in terms of probability. An observable is a quantity which can be physically measured and it is mathematically represented in quantum mechanics by an **operator**.

dependent phase factor. In general, the wave function may be interpreted as a position probability amplitude, where the probability of finding an atom in a state $|\Psi_n\rangle$ is defined as $|\Psi_n|^2 = |\psi_n|^2$. This means, that if the atom is in a state with energy E_n, its probability density is independent of time, thus states $|\Psi_n\rangle$ are so called stationary states. A two-level atom $n = 1, 2$ has stationary states with energies E_1, E_2, which are labelled $|1\rangle$ and $|2\rangle$ for the ground and the excited state respectively (Fig. 3.1(a)). The energy difference $\omega_0 = (E_2 - E_1)/\hbar$ defines the atomic resonance frequency ω_0.

Substituting the solutions of Ψ_n back into Eq. (3.1) with the atomic Hamiltonian $\hat{H}_A$, the eigenenergies of an atom are derived, which are:

$$\begin{aligned} \hat{H}_A\psi_1 &= E_1\psi_1 = \hbar\omega_1\psi_1 \\ \hat{H}_A\psi_2 &= E_2\psi_2 = \hbar\omega_2\psi_2, \end{aligned} \tag{3.4}$$

with an associated atomic resonance frequency $\omega_0 = \hbar(\omega_2 - \omega_1)/\hbar = (E_2 - E_1)/\hbar$.

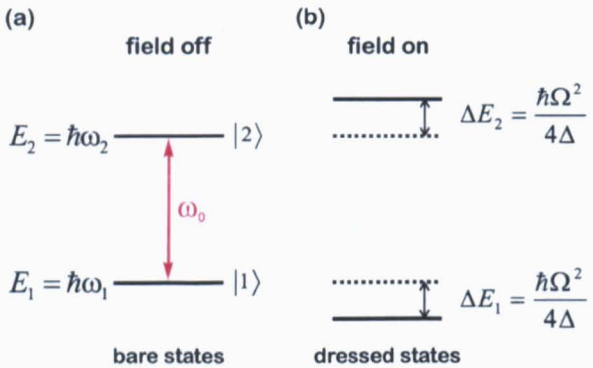

Figure 3.1: Energy levels of a two-level atom with the light field off (a), and energy levels shifted due to the atom-light interaction (b), Δ and Ω are defined in the text.

As the Schrödinger equation is linear, any linear combination of Eq. (3.3) gives another solution. $\hat{H}_{int}$ is the Hamiltonian which describes the interaction of atoms with light, whose electric and magnetic fields change with time and position, and therefore is time dependent. The most general solution of Eq. (3.1) with the total Hamiltonian $\hat{H} = \hat{H}_A + \hat{H}_{int}$, which is a linear combination of Eq. (3.3) is:

$$\Psi_n(\boldsymbol{r}, t) = \sum_{n=1}^{\infty} c_n(t)\psi_n(\boldsymbol{r})e^{-iE_n t/\hbar}, \tag{3.5}$$

where the complex expansion coefficient c_n is time dependent and represents an energy probability amplitude. Normalization requires that the coefficients satisfy $\sum_{n=1}^{\infty} |c_n(t)|^2 =$

1. Since the position-dependent probability density $|\Psi(\boldsymbol{r},t)|^2$ varies with time, the states $|\Psi_n\rangle$ are no longer stationary states.

By substituting back the time-dependent wave function (Eq. (3.5)) into the Schrödinger equation (Eq. (3.1)) with the total Hamiltonian $\hat{H}$, and by multiplying on the left by the conjugate $\psi_m^*(\boldsymbol{r})$ and integrating over the spatial coordinate $\boldsymbol{r}$, the general equation defining the time evolution of the state wave function can be obtained:

$$i\hbar\frac{dc_m(t)}{dt} = \sum_{n=1}^{\infty} c_n(t)\hat{H}_{mn}^{int}(t)e^{iE_{mn}t/\hbar}, \tag{3.6}$$

where the matrix elements of the interaction Hamiltonian $\hat{H}_{mn}^{int}$ in Dirac notation are expressed as $\hat{H}_{mn}^{int} = \langle\psi_m|\hat{H}_{int}|\psi_n\rangle = \int d^3\boldsymbol{r}\psi_m(r)\hat{H}_{int}\psi_n(r)$ and $E_{mn} = E_m - E_n$. It is worth noticing that in the presence of the light field, the eigenenergies E_n given by Eq. (3.4) are no longer eigenvalues of the total Hamiltonian. The new eigenstates are shifted by $\Delta E_{1,2} = \pm\frac{\hbar\Omega^2}{4\Delta}$, where $\Delta = \omega_l - \omega_0$ is the detuning of laser light of frequency ω_l from the atomic resonance ω_0 and Ω is the so-called Rabi frequency defined by Eq. (3.12). The shifted states are called 'dressed states' and are shown in Fig. 3.1 (b). The energy shift is proportional to the light intensity through Ω, and for atoms in an inhomogeneous light field it becomes spatially dependent.

Eq. (3.6) for an atom in a light field has not got an analytical solution. For an "ideal" two-level atom with states $|1\rangle$ and $|2\rangle$ coupled by a monochromatic resonant laser field, this set of coupled differential equations can be solved (Rabi, 1937). From Eq. (3.6) the amplitudes of the two coupled states are given by:

$$i\hbar\frac{dc_1(t)}{dt} = c_2(t)\hat{H}_{12}^{int}(t)e^{-i\omega_0 t} \tag{3.7a}$$

$$i\hbar\frac{dc_2(t)}{dt} = c_1(t)\hat{H}_{21}^{int}(t)e^{i\omega_0 t}. \tag{3.7b}$$

An electromagnetic wave oscillating with angular frequency ω_l is given by:

$$\boldsymbol{E}(t) = \hat{\boldsymbol{e}}E_0 cos(\omega_l t - kz) = \hat{\boldsymbol{e}}\frac{E_0}{2}\left(e^{-i\omega_l t + ikz} + e^{i\omega_l t - ikz}\right), \tag{3.8}$$

where E_0 and $\hat{\boldsymbol{e}}$ are the amplitude and the polarization of the wave, and $k = |\boldsymbol{k}| = 2\pi/\lambda$ is

the magnitude of the wave vector. If the wavelength of the radiation is large enough so that it is much larger than the size of the atom ($\simeq a_0 = 5.292 \times 10^{-11}$ and for rubidium atoms laser coupling ground and first excited state has a wavelength 780 nm), the spatial variation of the field over the atomic length is negligible and thus the dependence in kz can be omitted. The interaction energy between the atom and the field is given by the scalar product of the electric dipole moment $\boldsymbol{\mu} = -e\boldsymbol{r}$ and the electric field $\boldsymbol{E}$. Thus, the atom-light interaction Hamiltonian can be written as:

$$\hat{H}_{int} = -\hat{\boldsymbol{\mu}} \cdot \boldsymbol{E} = e\hat{\boldsymbol{r}} \cdot \hat{\boldsymbol{e}} E_0 cos(\omega_l t), \tag{3.9}$$

where $\boldsymbol{r}$ denotes the position of an electron with respect to the center of mass of the atom. The matrix elements coupling ground and excited state are given by:

$$\hat{H}_{12}^{int} = \langle 1|\hat{H}_{int}|2\rangle = -\frac{1}{2}\langle 1|\boldsymbol{\mu} \cdot \boldsymbol{E}|2\rangle \left(e^{-i\omega_l t} + e^{i\omega_l t}\right). \tag{3.10}$$

The coupled differential equations Eq. (3.7) might then be written in the form:

$$\frac{dc_1(t)}{dt} = \frac{-i\Omega}{2}\left(e^{i\omega_l t} + e^{-i\omega_l t}\right) e^{-i\omega_0 t} c_2(t) \simeq \frac{-i\Omega}{2}\left(e^{i\Delta t}\right) c_2(t) \tag{3.11a}$$

$$\frac{dc_2(t)}{dt} = \frac{-i\Omega^*}{2}\left(e^{i\omega_l t} + e^{-i\omega_l t}\right) e^{i\omega_0 t} c_1(t) \simeq \frac{-i\Omega^*}{2}\left(e^{-i\Delta t}\right) c_1(t), \tag{3.11b}$$

where the Rabi frequency Ω is defined as:

$$\Omega = -\frac{\langle 1|\boldsymbol{\mu} \cdot \boldsymbol{E}|2\rangle}{\hbar}. \tag{3.12}$$

The Rabi frequency gives information about how strongly two atomic states $|1\rangle$ and $|2\rangle$ with a dipole moment $\mu_{21} = -e\langle 2|\hat{\boldsymbol{r}}|1\rangle$ are coupled by the light field with an amplitude E_0. The approximation made in Eq. (3.11) is known as a the rotating wave approximation (RWA). It states that for small detuning Δ, $|\omega_l - \omega_0| \ll \omega_l + \omega_0 \simeq 2\omega_0$, terms with $e^{\pm(\omega_l+\omega_0)}$ oscillate rapidly compared to slow terms $e^{\pm i\Delta t}$ and in general they can be neglected as they average to zero on the interaction time-scale (e.g. for rubidium atoms $\omega_0 \sim 8\times10^{14}$ Hz while the detuning is usually of order of tens MHz).

To solve the system Eq. (3.11), the equations are decoupled by differentiating the

first one and substituting by c_2. We assume that only the ground state is populated at $t = 0$ ($c_1(0) = 1$ and $c_2(0) = 0$), therefore:

$$c_1(t) = \left[cos\left(\frac{\tilde{\Omega}t}{2}\right) - i\frac{\Delta}{\tilde{\Omega}} sin\left(\frac{\tilde{\Omega}t}{2}\right)\right] e^{i\Delta t/2} \tag{3.13a}$$

$$c_2(t) = -i\frac{\Omega}{\tilde{\Omega}} sin\left(\frac{\tilde{\Omega}t}{2}\right) e^{-i\Delta t/2}, \tag{3.13b}$$

where $\tilde{\Omega} = \sqrt{\Omega^2 + \Delta^2}$ is the generalized Rabi frequency. The above equations indicate that the probabilities of finding the atom in the ground or excited state $|c_1(t)|^2$, $|c_2(t)|^2$ oscillate at the generalized Rabi frequency $\tilde{\Omega}$ and the amplitude of the oscillations decreases as $\Omega^2/\tilde{\Omega}^2$ as the detuning Δ increases Fig. 3.2.

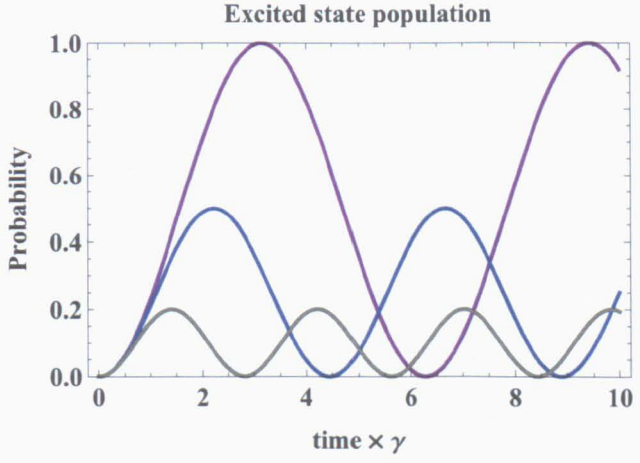

Figure 3.2: Excitation probability $|c_2(t)|^2$ of a two-level atom for different values of detuning: $\Delta = 0$ (purple line), $\Delta = \gamma$ (blue line) and $\Delta = 2\gamma$ (gray line), $\Omega = \gamma$.

The discussion above takes into account transitions resulting from absorption and stimulated transition processes only. However, atoms also emit photons with random polarization and in random directions during spontaneous emission processes. It is therefore necessary to include spontaneous emission into the description of the time-evolution of the atom-light interaction and it is no longer correct to describe it in terms of probability amplitudes. A real atom is never a true two-level system and spontaneous emission has the effect of populating other atomic states, which implies an evolution from a pure state to mixture of states. A description of the problem cannot be done by a single wave function. Instead a distribution of wave functions is used and one can only find the probability of finding the system within that distribution of wave

functions.

One way to deal with this is to introduce the density operator ρ defined as:

$$\rho = \sum_i P_i |\Psi_i\rangle\langle\Psi_i|, \tag{3.14}$$

where the probability P_i determines statistical distribution of a complete orthonormal set of states $|\Psi_i\rangle = \sum_n c_n^i(t)|\psi_n\rangle$ and $\sum_i P_i = 1$. The matrix elements of the density operator in this representation take the form:

$$\rho_{nm}(t) = \langle\psi_n|\rho|\psi_m\rangle = \sum_i \sum_{n,m} P_i c_n^i(t)(c_m^i(t))^*, \tag{3.15}$$

where ρ_{nm} represent the values of the coefficients of eigenstate that are averaged over the mixture of states, $\rho_{nm} = \overline{c_n c_m^*}$. The diagonal elements represent the probabilities of an atom to be in a state $|\psi_n\rangle$, $\rho_{nn} = \overline{c_n c_n^*} = |c_n|^2$ and thus are called *populations*. The off-diagonal elements depend on the relative phase of different complex coefficients, $\rho_{nm} = \overline{c_n c_m^*} e^{-i\omega_{nm}t}$ and carry information about the coherent superposition, thus they are called *coherences*. Other useful properties of the density operator are: $\rho_{nm} = \rho_{mn}^*$ which means that the operator is self-adjoined[3], and the diagonal elements form the probability distribution, thus the trace[4] of the density matrix is equal unity, $\mathrm{Tr}[\rho] = \sum_n \rho_{nn} = 1$. As a result, the purity of the state, defined as $\mathrm{Tr}[\rho^2]$, can be easily determined. For a pure state $\rho^2 = \rho$, therefore $\mathrm{Tr}[\rho^2] = 1$, but for mixed states $\mathrm{Tr}[\rho^2] < 1$. Furthermore, using Eq. (3.6) it is possible to show, that the time evolution of the density operator satisfies:

$$\frac{d\rho(t)}{dt} = \frac{-i}{\hbar}\left[\hat{H}, \rho(t)\right], \tag{3.16}$$

where the square brackets denote the commutator[5] (Liouville-von Neumann equation).

Considered here a two-level system that is in a pure state, characterized by a wave

[3]A bounded operator $\hat{A}$ is called a hermitian operator, or self-adjoined operator if $\hat{A} = \hat{A}^*$

[4]A trace of a square matrix A is defined as the sum of its diagonal elements, $\mathrm{Tr}[A] = \Sigma_{i=1}^n a_{ii}$

[5]For two operators $\hat{A}$ and $\hat{B}$, a commutator is a third operator defined as: $\left[\hat{A}, \hat{B}\right] = \hat{A}\hat{B} - \hat{B}\hat{A}$

function $|\Psi\rangle = c_1(t)|1\rangle + c_2(t)|2\rangle$. The density matrix thus takes the form:

$$\rho = \begin{pmatrix} \rho_{11} & \rho_{12} \\ \rho_{21} & \rho_{22} \end{pmatrix} = \begin{pmatrix} |c_1|^2 & c_1 c_2^* \\ c_2 c_1^* & |c_2|^2 \end{pmatrix}. \tag{3.17}$$

Substituting Eq. (3.17) into Liouville-von Neuman equation with atom-light interaction Hamiltonian $\hat{H}_{int}$, differentiating and subsequently substituting for $\frac{dc_1}{dt}$ and $\frac{dc_2}{dt}$ with Eq. (3.11) leads to a set of equations describing the time evolution of the density matrix elements, known as *optical Bloch equations* (OBE). In order to add the effects of spontaneous emission, one has to add a damping term of form $\frac{-i\Gamma c_2}{2}$ to the expression for $\frac{dc_2(t)}{dt}$, where $\tau = 1/\Gamma$ is the excited state lifetime. This leads to a set of differential OBE equations, that include spontaneous emission:

$$\frac{d\rho_{11}}{dt} = \frac{i}{2}\left(\Omega^*\tilde{\rho}_{21} - \Omega\tilde{\rho}_{12}\right) + \Gamma\rho_{22} \tag{3.18a}$$

$$\frac{d\rho_{22}}{dt} = \frac{i}{2}\left(\Omega\tilde{\rho}_{12} - \Omega^*\tilde{\rho}_{21}\right) - \Gamma\rho_{22} \tag{3.18b}$$

$$\frac{d\tilde{\rho}_{12}}{dt} = \frac{i}{2}\Omega^*\left(\rho_{22} - \rho_{11}\right) - \left(\frac{\Gamma}{2} + i\Delta\right)\tilde{\rho}_{12} \tag{3.18c}$$

$$\frac{d\tilde{\rho}_{21}}{dt} = \frac{i}{2}\Omega\left(\rho_{22} - \rho_{11}\right) - \left(\frac{\Gamma}{2} - i\Delta\right)\tilde{\rho}_{21}, \tag{3.18d}$$

where the oscillatory factors have been eliminated by substituting $\tilde{\rho}_{12} = \rho_{12}e^{-i\Delta t}$ and $\tilde{\rho}_{21} = \rho_{21}e^{i\Delta t}$. It is interesting to derive the steady-state solutions by setting the derivatives to zero, which results in a solution for populations and coherences in the form:

$$\rho_{22} = \frac{|\Omega|^2}{4\Delta^2 + \Gamma^2 + 2|\Omega|^2} \tag{3.19a}$$

$$\rho_{12} = e^{i\Delta t}\frac{\Omega(\Delta - i\frac{\Gamma}{2})}{2\Delta^2 + \frac{\Gamma^2}{2} + |\Omega|^2}. \tag{3.19b}$$

Since Ω^2 is proportional to the intensity of laser light, it is convenient to express the steady state population of the excited state $\rho_{22}(t \to \infty)$ in terms of saturation intensity, defined as:

$$I_{sat} = \frac{\hbar\omega_0 A_{21}}{2\sigma_0}, \tag{3.20}$$

where A_{21} is the Einstein spontaneous emission coefficient, $A_{21} = \Gamma$, σ_0 is resonant

cross section, which for linearly polarized light, is equal $\sigma_0 = 3\lambda^2/2\pi$. By defining the saturation parameter as:

$$\frac{I}{I_{sat}} = \frac{2|\Omega|^2}{\Gamma^2} \tag{3.21}$$

and substituting into the Eq. (3.19a) (a), one can obtain an expression for the population of the excited level as a function of the light intensity and detuning:

$$\rho_{22}(t \to \infty) = \frac{1}{2}\frac{I/I_{sat}}{1 + 4\Delta_\nu^2/\Gamma_\nu^2 + I/I_{sat}}. \tag{3.22}$$

For the rubidium D2 transition (see Section 3.3) the parameters are as follows: $\Gamma = 2\pi\Gamma_\nu$ where Γ_ν=6.065 MHz, the laser detuning with respect to the resonance frequency ν_{D2}, $\Delta_\nu = \frac{\Delta}{2\pi} = \nu - \nu_{D2}$, where ν_{D2}=384.23 THz, and saturation intensity I_{sat}=1.67 $\mathrm{mW/cm^2}$. Considering, that the population of the excited state decays at a rate Γ and that, at equilibrium, the excitation and the decay rates are equal, one can determine the expression for the total scattering rate of an atom R_{sc} by multiplying Eq. (3.22) by Γ. At very high intensities, where the saturation parameter $I/I_{sat} \gg 1$, $\rho_{22} \sim 1/2$ and thus scattering rate $R_{sc} = \Gamma/2$. This quantity has important implications in the laser cooling process which will be described in the next section.

3.1.2 The light forces

When an atom absorbs or emits a photon carrying momentum $\hbar\boldsymbol{k}$ there is a momentum transfer between the photon and the atom (Fig. 3.3). As a result of that processes, the atom recoils so that the momentum of the system is conserved and its velocity $\boldsymbol{v}$ is changed by $\hbar\boldsymbol{k}/m$, where m is a mass of the atom. The recoil acquired from the incident photons of the laser beam is always in the direction of the laser propagation and if the atom moves towards the laser beam its velocity gets reduced. During re-radiation of the photon, the atom experiences a recoil as well, however due to the randomness of the direction of the emitted photon, after many absorption-emission cycles, the time averaged momentum gained due to emission equals zero and the overall effect of these processes is that the atom gets slower. The time averaged force is called the scattering force $\boldsymbol{F}_{sc}$ and is a resultant of both processes, the force exerted on atoms due to absorption, $\boldsymbol{F}_{abs}$, and spontaneous emission, $\boldsymbol{F}_{em}$, of photons, $\langle \boldsymbol{F}_{sc} \rangle =$

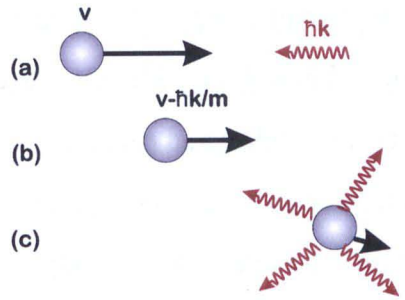

Figure 3.3: The result of the scattering force exerting on a moving atom, (a) an atom is travelling towards the laser beam with velocity $\boldsymbol{v}$, (b) absorption of a photon carrying a momentum $\hbar\boldsymbol{k}$ reduces the velocity of the atom, (c) re-emission of a photon happens in a random direction thus on average atom is slower than initially.

$\langle \boldsymbol{F}_{abs} \rangle + \langle \boldsymbol{F}_{em} \rangle + \delta \boldsymbol{F}_{em}$, where $\delta \boldsymbol{F}$ describes the fluctuations in the cooling force due to the random direction of spontaneous emission and has an influence on the cooling limit.

The scattering force is thus proportional to the number of scattered photons per unit time, which can be expressed by the scattering rate $R_{sc} = \Gamma \rho_{22}$ (Eq. (3.22)) and ultimately takes the form:

$$\boldsymbol{F} = \hbar \boldsymbol{k} R_{sc} = \hbar \boldsymbol{k} \frac{\Gamma}{2} \frac{\frac{I}{I_{sat}}}{1 + \frac{4\Delta_\nu^2}{\Gamma_\nu^2} + \frac{I}{I_{sat}}}. \tag{3.23}$$

The maximum acceleration experienced by atoms moving in a laser field $\langle a_{max} \rangle = \hbar k \Gamma / 2m$, happens when $R_{sc} = \Gamma/2$. One can estimate the deceleration of rubidium atoms due to the 780 nm laser beam, which is of order $10^4\,\mathrm{g}$, where g is acceleration due to gravity. This indicates that atoms can be significantly slowed down in a very short time. For example at room temperature the velocity of rubidium atoms is about 300 m/s. In order to bring the atom to rest, about 4×10^4 photons need to absorbed, which takes $\sim 1\,\mathrm{ms}$.

3.1.3 Doppler cooling

Using six counter-propagating orthogonal laser beams with frequency ν_L slightly detuned below the atomic resonance ν_a by Δ (Hänsch and Schawlow, 1975; Wineland and Dehmelt, 1975) it is possible to achieve 3-D cooling in a sample of atoms. The principal cooling mechanism is known as Doppler cooling and is schematically depicted in Fig. 3.4

(a) in the 1-D case. Due to the Doppler effect, the atom moving with velocity $\boldsymbol{v}$ 'sees' the laser frequency shifted by a factor $\boldsymbol{k} \cdot \boldsymbol{v}$. The atom sees the frequency of photons propagating against its direction as higher and closer to the resonance ($\Delta_2 < \Delta$), while the frequency of co-propagating photons is seen as shifted away from the resonance ($\Delta_1 > \Delta$). As a result an atom interacts more strongly with the counter-propagating beam and its velocity is reduced. The cooling force is thus proportional to the velocity

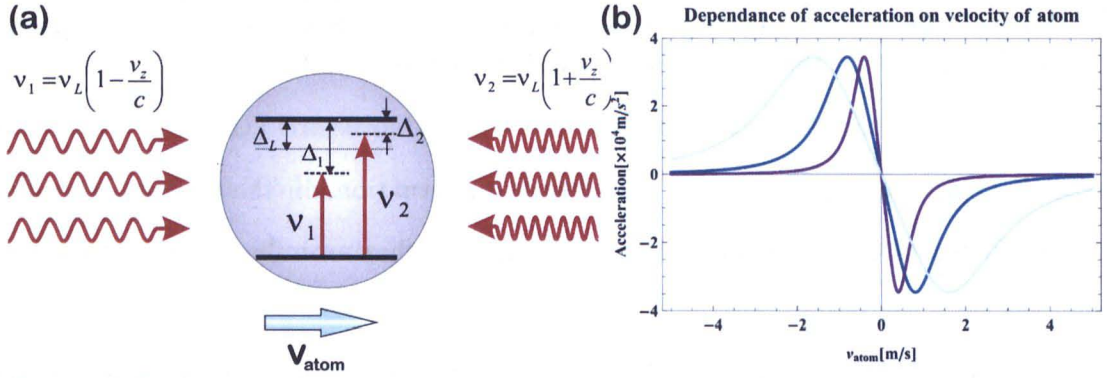

Figure 3.4: The principle of Doppler cooling in a one-dimensional situation(a) and the velocity dependent acceleration for ^{85}Rb calculated using Eq. (3.24) for different detuning: $\Delta = -0.5\Gamma$ (purple line), $\Delta = -\Gamma$ (dark blue line) and $\Delta = -2\Gamma$ (light blue line).

of the atoms and for each of two beams can be given by:

$$\boldsymbol{F}_{\pm} = \hbar \boldsymbol{k} \frac{\Gamma}{2} \frac{I/I_{sat}}{1 + I/I_{sat} + (2(\Delta \mp \boldsymbol{k} \cdot \boldsymbol{v})/\Gamma)^2}. \tag{3.24}$$

In a one-dimensional case, in the regime of low beam intensities, the resultant force is simply a sum of these two forces, $\boldsymbol{F}_{total} = \boldsymbol{F}_+ + \boldsymbol{F}_-$. Fig. 3.4(b) shows the total acceleration $\boldsymbol{a} = \boldsymbol{F}_{total}/m_{atom}$, exerted on ^{85}Rb atoms by two counter-propagating red-detuned ($\Delta \leq 0$) 780 nm laser beams with intensities close to the saturation intensity, I =2.4 mW/cm^2 as a function of the atoms velocity. Three different detunings are considered: $\Delta = 0.5\Gamma, \Gamma, 2\Gamma$. One can notice that by changing the detuning, the atoms with different range of velocities can be efficiently accelerated or decelerated. Furthermore, in the limit of small velocities ($kv \ll \Gamma$), the radiation force varies linearly with the velocity, $\boldsymbol{F}_{total} \simeq -\alpha \boldsymbol{v}$, where the coefficient α is referred to as a friction coefficient in viscous media and is given by $\alpha = 4\hbar k^2 \frac{-2\Delta}{\Gamma} \frac{I/I_{sat}}{(1+I/I_{sat}+(2\Delta/\Gamma)^2)^2}$. As the damping force requires positive α, the detuning Δ needs to be < 0. The cooling technique involving

counter-propagating laser beams red detuned from resonance is called *optical molasses*. The first experimental demonstration of a three-dimensional optical molasses was carried out in 1985 by Chu and co-workers, who managed to cool sodium atoms to a temperature of approximately $240\mu K$ (Chu *et al.*, 1986).

3.1.4 Cooling limits

In the absence of other factors influencing the motion of atoms, the damping force still cannot decelerate the atoms to zero velocity. This is because an additional heating process, not taken into account so far, caused by the laser beams limits the final temperature obtainable. Due to the discrete size of the momentum steps $\hbar k$, the atom undergoes a random walk in the momentum space, a process similar to the Brownian motion of particles in a liquid, with a step frequency $2R_{sc}$ (where the factor 2 is introduced because we have two beams). As a consequence atoms can diffuse out of the molasses region and hence in the momentum space, with the diffusion coefficient given by $D_0 \equiv 2(\Delta p)^2/\Delta t = (\hbar k)^2 2R_{sc}$ (e.g. for an atom it takes about 30 s and 10^7 steps to diffuse a distance of 1 cm (Metcalf and van der Straten, 2003)). The steady state temperature is reached when the cooling and the heating process due to the diffusion of momentum equilibrate. This temperature determines the the Doppler cooling limit and in the case of $\Delta = -\Gamma/2$, is given by:

$$T_D = \frac{\hbar\Gamma}{2k_B}. \tag{3.25}$$

There are other ways to determine minimum temperature obtainable in the Doppler limit, i.e. by equating the heating rate $4\hbar\omega_{recoil}R_{sc}$ (estimated from the losses of energy of the light field using the recoil kinetic energy) and the cooling rate $\boldsymbol{F}\cdot\boldsymbol{v}$, yields the same expression for Doppler temperature, T_D.

For rubidium, the minimum temperature obtainable in the Doppler limit is T_D =146 μK. The first experiments in laser cooling provided temperatures comparable with T_D. However, in 1988 Phillips and Metcalf managed to cool sodium atoms to a temperature 6 times below Doppler limit, $40\mu K$ (Lett *et al.*, 1988), which indicated that the so far assumed two-level model of an atom is not accurate enough for alkali atoms

which have a hyperfine structure. The first explanation of the mechanism leading to the sub-Doppler cooling was proposed by Dalibard and Cohen-Tannoudji in 1989. The sub-doppler cooling is linked to light polarization gradients and optical-pumping between atomic ground state sub-levels. To properly elucidate this phenomenon the hyperfine structure of atoms and the polarization of light must be taken into account, as we will see in the next section.

3.2 The magneto-optical trap

In optical molasses atoms are significantly slowed down and they accumulate in the region where the laser beams overlap, however they are still diffusing out of that space. In 1987 Pritchard implemented the first magneto-optical *trap* for atoms by adding a weak quadrupole magnetic field, which is zero at the center of the trap and grows linearly as the atoms move away from the zero field region ($\boldsymbol{B} = B_0(x, y, -2z)$), and using circularly polarized laser beams for the optical molasses - hence the commonly used name of magneto-optical trap (MOT) (Raab *et al.*, 1987). An optical molasses provides a velocity-dependent damping force by creating an imbalance in the scattering forces generated by two laser beams. The magnetic field makes the radiation pressure imbalance spatially dependent as a result of the space dependent shift of the atomic sub-levels because of the Zeeman effect[6]. In this way, the radiation force cools and at the same time confines the atoms creating cold and dense samples. The typical configuration of the magnetic field and laser beams in the MOT is shown in Fig. 3.5 (b).

Because of the Zeeman splitting of the excited state, a four level system has to be considered (Fig. 3.5 (a)). The energy levels are characterized by quantum numbers F and m_F which represent the total angular momentum and the projection of the total angular momentum onto the quantization axis respectively. Thus the ground state is given by $|F, m_F\rangle = |0, 0\rangle$ and the degenerate excited states are $|F', m_{F'}\rangle = |1, -1\rangle, |1, 0\rangle, |1, 1\rangle$. If the magnetic field is relatively weak, the Zeeman splitting of the energy levels is given by $E_Z = g_F \mu_B m_F |\boldsymbol{B}|$, where g_F is a coupling constant, so-called

[6]In the presence of the magnetic field, atomic energy levels split into several sub-levels and the splitting is proportional to the strength of the magnetic field $|\boldsymbol{B}|$

Landé g-factor (see Section 3.3), μ_B is Bohr magneton[7], and B is the magnitude of the magnetic field. Thus the new resonance frequencies are $\nu'_a = \nu_a + E_Z/h$.

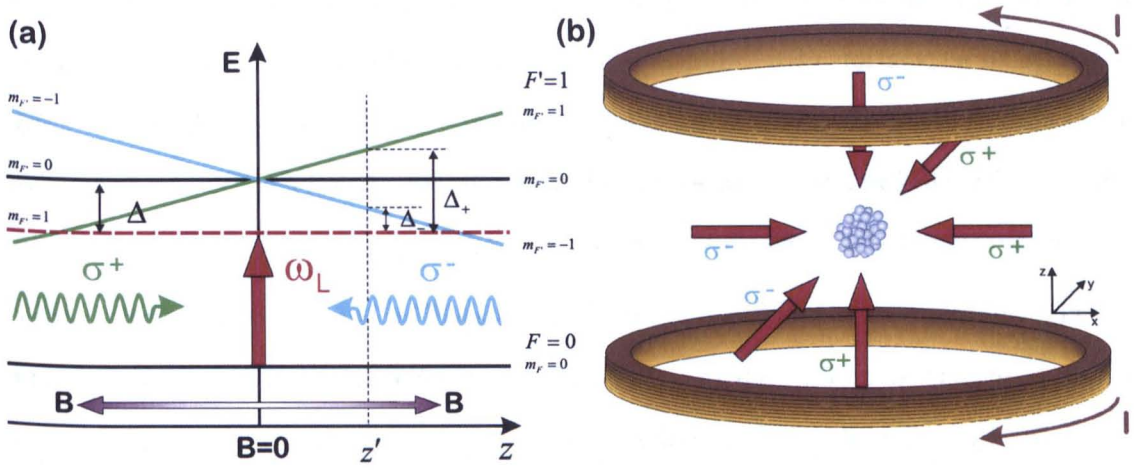

Figure 3.5: The mechanism of a magneto-optical trap: (a) a one-dimensional MOT: energy levels of an atom in a linearly varying magnetic field (the scale is exaggerated), red dashed line represents laser detuned below the atomic resonance. The atom placed at point z' is pushed back to the center of the trap by a net restoring force resulting from the imbalance in the radiation force caused by the Zeeman effect. (b) the arrangement of the magnetic field coils and laser beams polarisations in a MOT. The quantisation axes of the atom are chosen to be in a fixed direction in space, e.g. z direction in figure (a), in figure (b) they are marked by black arrows. Labels $\sigma^{\pm}$ refer to the transitions of atom.

The polarization of the light has so far been omitted in the description of the atom-light interaction, but it plays an important role in the case of a multilevel alkali atoms and it must be considered. The polarization in general means *orientation*, and by convention in the case of light it specifies the orientation of the oscillating electric field vector $\boldsymbol{E}_L(\boldsymbol{r}, t)$ along the light propagation direction given by $\boldsymbol{r}$ the position vector in a three dimensional space, $\boldsymbol{r} = (x, y, x)$. If the electric field vector $\boldsymbol{E}_L$ oscillates in one plane, perpendicular to $\boldsymbol{r}$, than the light is said to be linearly or π polarized (e.g. a plane wave has a linear polarization). If $\boldsymbol{E}_L$ has a constant magnitude but the tip of the vector rotates as the wave propagates, e.g. clockwise (anticlockwise) as seen by an observer looking in the source direction, then the light is said to be left-circularly or σ^+ (right-circularly or σ^-) polarized. A linear combination of two circularly polarized waves, can give rise to any linearly or elliptically polarized wave. In the quantum mechanical description, circularly polarized light consists of photons

[7]Bohr magneton μ_B is a physical constant and a unit used to express electron magnetic dipole moment

carrying the angular momentum $\pm 1\hbar$, also called spin of photons $\boldsymbol{s}_{ph}$, in particular σ^+ represents photons with $\boldsymbol{s}_{ph} = +\hbar\boldsymbol{k}/|\boldsymbol{k}|$ pointing into the propagation direction, while σ^- represents photons pointing opposite $\boldsymbol{s}_{ph} = -\hbar\boldsymbol{k}/|\boldsymbol{k}|$. Linearly polarized light, as it is the superposition of σ^+ and σ^- has an average photon spin $\boldsymbol{s}_{ph} = \boldsymbol{0}$. For an atom placed in an external magnetic field, from the selection rules it follows that only transitions with $\Delta m_F = -1, 0, +1$ are allowed between Zeeman levels, and they are induced in case of absorption by σ^-, π and σ^+ light respectively.

The physics of the MOT can be easily explained in a one-dimensional situation, which is presented in Fig. 3.5 (a). For an atom placed in a magnetic field gradient generated by a pair of anti-Helmholtz coils[8], the Zeeman splitting of the energy sublevels depends on the position of the atom with reference to the centre of the trap, where $\boldsymbol{B} = 0$. The counter-propagating beams are red detuned to provide the optical molasses, but they are also appropriately circularly polarized to take advantage of the selection rules. Thus for an atom displaced from the center of the trap at a position $z = z'$ is considered, the $\Delta m_F = -1$ transition is closer to the resonance while $\Delta m_F = +1$ is shifted away. If the beam propagating in the $-z$ direction is σ^- polarized (light green colour) and for the opposite is σ^+, (light blue colour) the atom scatters more σ^- light and is pushed by that beam towards the center of the trap. A similar process takes place in other directions. Thus the atoms experience a net restoring force which always pushes them back to the center of the trap.

The total force experienced by the atoms in a MOT, $\boldsymbol{F}_{MOT} = \boldsymbol{F}_{\sigma+} - \boldsymbol{F}_{\sigma-}$, is obtained by substituting the Zeeman shifted energy ν_a' into the Eq. (3.24), which leads to expressions for $\boldsymbol{F}_{\sigma\pm}$ of the form:

$$\boldsymbol{F}_{\sigma\pm} = \hbar\boldsymbol{k}\frac{\Gamma}{2}\frac{I/I_{sat}}{1 + I/I_{sat} + (\frac{2}{\Gamma})^2(\Delta \mp \boldsymbol{k}\cdot\boldsymbol{v} \pm \beta z)}, \tag{3.26}$$

where $\beta z = \frac{g\mu_B}{\hbar}\frac{dB}{dz}$ describes the Zeeman shift at distance z, the Lande-g factor is given by $g = (g_F m_F - g_{F'} m_{F'})$, and for most of the cooling transitions $g \simeq 1$. In the limit of small velocities and small Zeeman shift, the total force acting on the atoms in the

[8] A pair of identical coils connected in series and placed symmetrically along a common axis in such a way that the current is flowing through the two coils in opposite direction is called anti-Helmholtz configuration and it produces a quadrupole magnetic field.

MOT can be written as:

$$\boldsymbol{F}_{MOT} \simeq -\alpha \boldsymbol{v} - \frac{\alpha\beta}{k}\boldsymbol{z} = -\alpha \boldsymbol{v} - \kappa \boldsymbol{z} \tag{3.27}$$

where κ is denoted as a spring constant. This indicates that the atoms in the MOT undergo a damped harmonic motion. The big advantage of the magneto-optical trap is that it confines the atoms while still providing a strong damping force.

3.2.1 Sub-Doppler cooling

As noted in the previous section, the two-level model of an atom is not accurate enough to explain cooling below Doppler limit of alkali atoms. In 1989 two independent works Dalibard and Cohen-Tannoudji (1989) and Chu (Ungar *et al.*, 1989), proposed two newly identified mechanisms explaining the sub-Doppler cooling. These new models take into account the existence of the Zeeman structure in the ground level of alkali atoms and the polarization gradients of the light. The main difference between these models consists on the type of polarization gradient in a one-dimensional molasses. Two plane waves, which have the same frequency ω_l and are counter-propagating along axis z create a standing wave. As a result of the superposition of two fields, the total electric field vector varies along z. There are two important cases from the point of view of laser cooling, which are considered below.

Gradient of ellipticity - the *lin* $\perp$ *lin* configuration

If counter-propagating waves have orthogonal linear polarizations and equal amplitudes, then the ellipticity of the resultant vector changes over the distance $\lambda/2$, from linear at 45° to the polarization of two beams ($z = 0$), through σ^- ($z = \lambda/8$), to linear again but orthogonal to the previous direction ($z = \lambda/4$), through σ^+ ($z = 3\lambda/8$) to opposite linear ($z = \lambda/2$), and so on... Alkali atoms have two sub-levels in the ground state, which are coupled to the $\sigma^\pm$ light with different strengths. As a result of the light shift, the energy of the magnetic ground state sub-levels varies periodically with z as well. The transition rates associated with the absorption of $\sigma^\pm$ followed by spontaneous emission are always highest from the higher sub-level of the ground state to

the lower sub-level of the ground state and the internal time in which the population is transferred between these two sub-levels is called optical-pumping time, τ_{int}. In other words, as an atom moves through the polarisation gradient with velocity v and if $v\tau_{int} \simeq \lambda/2\pi$, it has enough time to climb the potential hill, loosing its kinetic energy for the benefit of potential energy, before being optically pumped back to the potential well dissipating its potential energy via spontaneous emission (Fig. 3.6). The atom thus keeps climbing up the hill loosing its velocity until it ends up at the bottom of the well. The equilibrium temperature is then reached and it is proportional to the well depth U_0, and it is related to the intensity and the detuning of the light through the expression:

$$k_B T \simeq U_0 = \frac{\hbar\Omega^2}{|\Delta|}. \tag{3.28}$$

In an analogy to Greek myth, this process is called *Sisyphus cooling.*

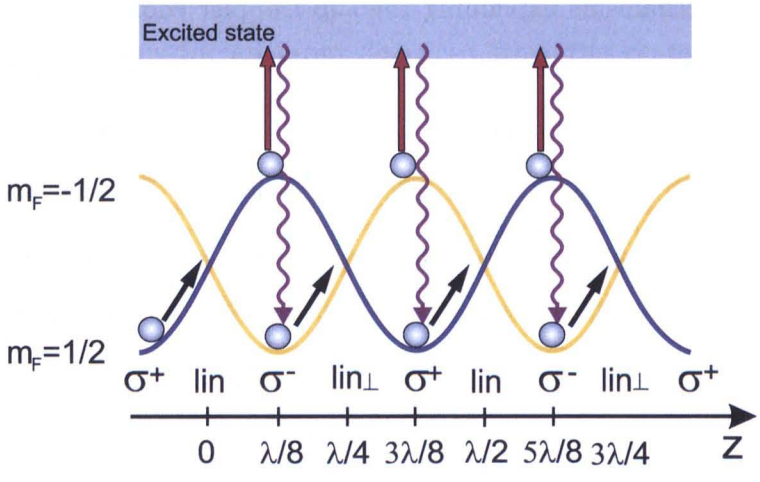

Figure 3.6: Details of the Sisyphus cooling. Two counter-propagating laser beams in the *lin* ⊥ *lin* configuration generate a spatially varying light shift of the ground state magnetic sub-levels. An atom moves along the polarisation gradient and when reaches the top of the potential can absorb a photon and subsequently spontaneously decay to a different magnetic sub-level losing the energy.

Rotation of polarization - the $\sigma^+ - \sigma^-$ configuration

If two counter-propagating waves have opposite circular polarization and equal amplitudes, then the total electric field vector has linear polarization and rotates around the z axis with a period determined by the laser wavelength. In this case, the light shift of the two sub-levels of the ground state is constant and equal along z and the

stationary atom has a symmetrically distributed population of these states. However, an atom moving in a non-adiabatic way sees the change of the electric field which leads to a population difference in the ground state sub-levels, in other words there is an atomic orientation along the beam axis. As a consequence of the breaking of symmetry, the difference in absorption of light from two beams is enhanced and the beam opposing the motion of atoms is scattered at a higher rate, which in turn leads to a stronger damping force. This technique is called *motion-induced orientation* (Dalibard and Cohen-Tannoudji, 1989).

Each pair of counter-propagating beams with opposite circular polarization generates linearly polarized electric field vectors with strongly position dependent orientation, thus 3 orthogonal pairs of beams which form the optical molasses in a MOT, create a complex polarization pattern. Therefore in a real MOT experiment a combination of sub-Doppler cooling mechanism occurs. The ultimate limit of the temperature is determined by the recoil kinetic energy given by:

$$T_{rec} = \frac{\hbar^2 k^2}{k_B M}, \tag{3.29}$$

where M is the mass of the atom. For ^{85}Rb the recoil temperature is about $0.37\mu K$ and experimentally achievable temperatures are around 15 times larger.

3.3 Implementation of laser cooling for rubidium

The first laser cooled atoms were alkali atoms, mainly because the frequency of the excitation from the ground to the first excited state is found in the visible region of the spectra, which is easily accessible by commercial lasers. Furthermore, atomic vapour reservoirs are also relatively easy to produce in the case of alkali-metals. In this section the experimental implementation of laser cooling of rubidium atoms will be described.

The electron configuration of rubidium is $1s^2 2s^2 2p^6 3s^2 3p^6 3d^{10} 4s^2 4p^6 5s^1$, thus, as already indicated in Section 2.3, it has a closed shell with only one valance electron. The state of an electron is determined by its orbital angular momentum $\boldsymbol{l}$ associated with the orbital motion of the electron around the atomic core, and an additional

intrinsic angular momentum of the electron around its own axis called the spin angular momentum $\boldsymbol{s}$. The spin has two possible spatial orientations, hence $s = \pm 1/2$, and it is also related to the magnetic spin moment of the electron by $\boldsymbol{\mu}_s = -g_s(\mu_B/\hbar)\boldsymbol{s}$, where $g_s \approx 2$ is the *Landé g-factor*. The interaction between μ_s and the internal magnetic field $\boldsymbol{B}_l$ resulting from the orbital motion of the electron, known as the spin-orbit (or l-s) coupling, leads to the Zeeman splitting of the energy levels E_n of an atom (given by Eq. (2.5)) into two components. This comprises to the so-called *fine structure*, and the energy levels are $E_{n,l,s} = E_n - \boldsymbol{\mu}_s \cdot \boldsymbol{B}_l$.

Since the core does not have an impact on the total angular momentum of the atom $\boldsymbol{L} = \boldsymbol{l}$ and the total spin angular momentum $\boldsymbol{S} = \boldsymbol{s}$, which determine the total non-nuclear angular momentum of the atom $\boldsymbol{J}$, $\boldsymbol{J} = \boldsymbol{L} + \boldsymbol{S}$, and the corresponding values of quantum number $\boldsymbol{J}$ lie in the range $|L - S| \leq J \leq |L + S|$. In spectroscopic notation, the state of the atom for $L - S$ coupling is written in the form $(n)^{2S+1}L_J$, where $L = 0, 1, 2 \ldots$ for historical reasons it is appropriately substituted by $S, P, D, F \ldots$. Following the above, the ground state of rubidium is characterized by quantum numbers $n = 5$, $L = 0$, $S = 1/2$ and $J = 1/2$, is written as $5^2S_{1/2}$. As fine structure is revealed for $L > 0$, the first excited state of rubidium P, splits into into $5^2P_{1/2}$ for $J = 1/2$ and $5^2P_{3/2}$ for $J = 3/2$, and the transitions which link these states with the ground state are called D_1 and D_2 lines respectively.

The atomic nucleus possesses its own mechanical angular momentum I and associated with it a nuclear magnetic moment $\boldsymbol{\mu}_N$. The interaction between $\boldsymbol{\mu}_N$ and the magnetic field generated by electrons leads to further splitting of $E_{n,l,s}$ into so-called *hyperfine structure*. The coupling between the nuclear angular momentum $\boldsymbol{I}$ and the total electronic angular momentum $\boldsymbol{J}$, known as the nuclear spin-spin coupling, determines the total angular momentum of the atom $\boldsymbol{F}$, $\boldsymbol{F} = \boldsymbol{J} + \boldsymbol{I}$, and the corresponding values of quantum number $\boldsymbol{F}$ lie in the range $|J - I| \leq F \leq |J + I|$.

Naturally occurring rubidium has two isotopes 72% ^{85}Rb and 28% ^{87}Rb, which are characterized respectively by quantum numbers $I = 5/2$ and $I = 3/2$. Therefore two isotopes have different hyperfine structures. Rubidium, similarly to all alkali atoms, has the ground state $5S_{1/2}$ and $5P_{1/2}$ state split into two F levels ($F(I, J) = I \pm \frac{1}{2}$), while the $5P_{3/2}$ state has four F levels ($F(I, J) = I - \frac{3}{2}, I - \frac{1}{2}, I + \frac{1}{2}, I + \frac{3}{2}$). In addition,

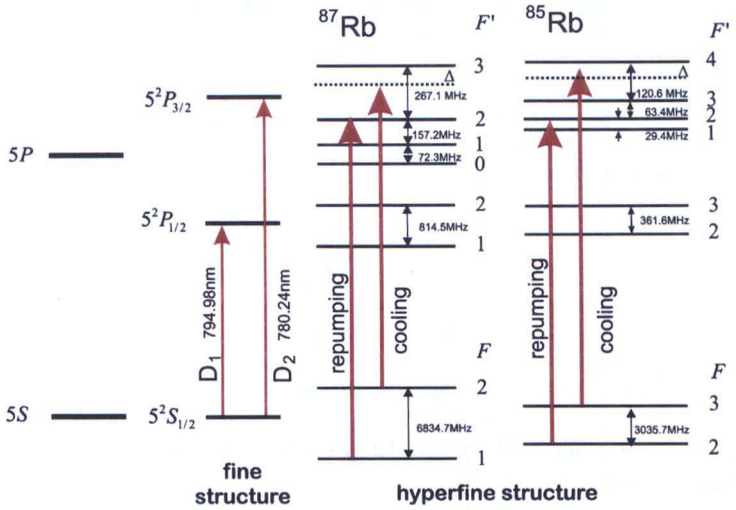

Figure 3.7: Fine and hyperfine structure of ^{85}Rb and ^{87}Rb. Δ is the detuning of the laser from the cooling transition.

each F state has its magnetic sub-levels $m_F = -F, -F+1, \ldots, F$, thus the number of m_F levels equals $2F+1$. The energy levels of rubidium 87 and 85 are shown in the Fig. 3.7.

The cooling transition from Fig. 3.5 (a) is a red detuned transition from $F = I + \frac{1}{2}$ to $F' = I + \frac{3}{2}$ state, which is $F = 2 \rightarrow F' = 3$ for ^{87}Rb and $F = 3 \rightarrow F' = 4$ for ^{85}Rb. The general selection rules for the light absorption impose $\Delta F = 0, \pm 1$ and $\Delta m_F = 0, \pm 1$, however due to the circular polarization of light the transition $\Delta F = 0$, $\Delta m_F = 0$ is forbidden. An atom in $F' = I + \frac{3}{2}$ state decays only to $F = I + \frac{1}{2}$, thus an atom oscillates between these two states, and the cooling transition is called a *closed transition*. However, the energy levels are homogeneously broadened and there is small overlapping between neighbouring hyperfine levels. As the cooling laser is blue detuned to $F' = I + \frac{1}{2}$, there is a probability that $F' = I + \frac{1}{2}$ state is populated as well, although at smaller rate. This state can only decay to $F = I - \frac{1}{2}$. Therefore, after many absorption-emission cycles, all population will end up in the ground state $F = I - \frac{1}{2}$, which is out of frequency range of the cooling laser. To prevent this situation to happen, a second laser tuned to $F = I - \frac{1}{2} \rightarrow F' = I + \frac{1}{2}$ transition (^{87}Rb $F = 1 \rightarrow F' = 2$ and ^{85}Rb $F = 2 \rightarrow F' = 3$), is overlapped with the cooling laser and it has the effect of re-populating the $F = I + \frac{1}{2}$ ground state, making the cooling process effective again. This laser is called *re-pumper*.

For an efficient cooling experiment the laser light employed has to fulfil two major

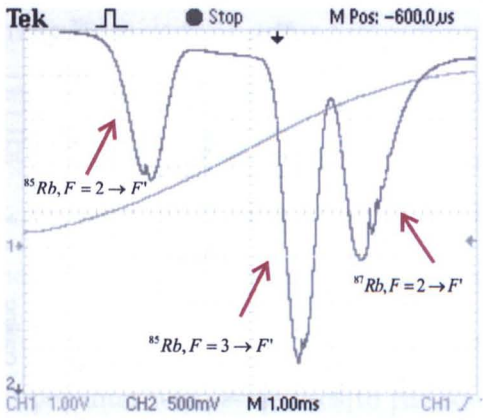

Figure 3.8: Saturated absorption spectrum of the rubidium D_2 line (transition $F = 2 \rightarrow F'$ ^{87}Rb is not visible.

requirements. First, the linewidth of the laser has to be narrower then the natural linewidth of the hyperfine transition used for the cooling. Second is the stability of the laser, so the frequency drift will be less than a fraction of that linewidth during the time of the experiment. The natural linewidth of the D2 transition is 6 MHz, thus the cooling laser should be narrower then 1 MHz. The linewidth of the re-pumper laser is not so critical though. The central frequency of the laser should stay stable at 1 MHz during at least an hour for both lasers. The laser system employed in our cooling experiment will be described in detail in the next chapter. In Fig. 3.8 the absorption profile of rubidium atoms probed by cooling laser tuned to the D2 line frequency and scanned over the cavity range (~5 GHz) is shown. The lines measured by the detector are Doppler broadened and hide the hyperfine structure, however, this also can be revealed using Doppler-free spectroscopy which will be described in detail in Section 4.1.1.

3.3.1 Apparatus for laser cooling

As we will see in Fig. 4.1 the highest detected peaks in the spectra used for locking of rubidium are the "cross-over peaks" (see Section 4.1.2), and these are used in our experimental set-up as reference points for laser locking. The techniques used for locking will be explained in the next chapter. In case of ^{85}Rb it is the $F = 3 \rightarrow F' = 2, 4$ cross-over which is 92 MHz away from the cooling transition, and for ^{87}Rb the locking peak is $F = 2 \rightarrow F' = 2, 3$ at 133.2 MHz away from the resonance. To red detune

the laser by approximately $\sim 1.5\Gamma_\nu$, its frequency is shifted using a device called an acousto-optic modulator (AOM)[9].

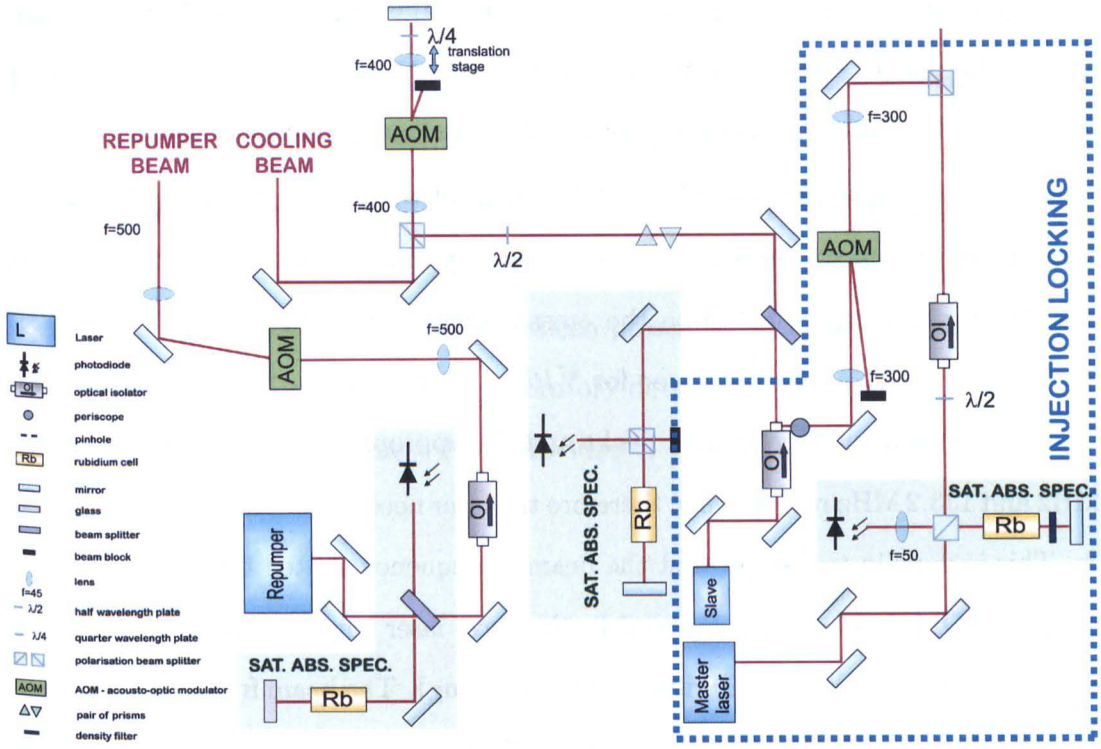

Figure 3.9: Layout of the optics for laser cooling and trapping. With green background the saturated absorption spectrometers have been highlighted and the dotted blue lines mark out the injection locking part.

All lasers used for cooling purposes in our laboratory are semiconductor lasers, with the typical output power of the diode up to 70 mW. As the lasers are operating in an extended cavity, which uses the feedback from the diffraction grating (Section 4.2.1), the output power is reduced to about 30 mW. Furthermore, some of the power is used for the saturated absorption scheme and other losses are due to coupling of the laser beam to the AOM. Thus, it is necessary to increase the power available in the experiment and a second laser is added to the set-up, whose frequency is controlled using the *injection locking* technique. This technique allows us to obtain a high power output source characterized by a low phase noise using a low intensity injecting beam. The main concept is as follows: one laser is producing a stable and single-mode output beam, but is usually operating at a low power - this is the so-called *master* laser. That beam is subsequently injected to the resonant cavity of the second high-power laser - so called

[9] AOM- acousto-optic modulators are devices which enable to modify the frequency, intensity and the direction of propagation of the laser light, making use of Bragg diffraction of light off acoustic wave-front propagating through a crystal

slave. If the frequencies of both lasers are close enough, the injection forces the high power laser to operate exactly at the frequency of the master laser and with relatively low noise. In our setup both lasers are built with Sanyo DL-7140-201S diodes. The output of the master laser is 15 mW, but only about 2.5 mW is used for the injection locking. The slave laser gives around 40 mW of the output power. The frequency after the injection locking is controlled by monitoring a saturated absorption spectrum.

In our experiment we can easily switch between working with ^{85}Rb and ^{87}Rb. The master laser is frequency locked to the cross-over peak (see Fig. 4.1 and Fig. 4.2), in ^{85}Rb it is $F = 3 \rightarrow F' = 2,4$ or for ^{87}Rb $F = 2 \rightarrow F' = 2,3$ transition. The separation between these cross-over peaks and the appropriate cooling transitions are 92 MHz and 133.2 MHz respectively, therefore the laser needs to be subsequently shifted back. This is done in two steps, first the beam is frequency shifted by 80 MHz using a single-pass AOM, before being injected to the slave laser through the optical isolator (this arrangement results in an additional power saving). The beam from the slave laser passes twice through the AOM (double-pass configuration), operating at 160 MHz when working with ^{85}Rb, which results in the frequency shift equals to 10 MHz. An available power for the cooling experiment with ^{85}Rb is 17 mW and the frequency is shifted by $\sim 1.5\Gamma_\nu$ towards the red. By changing the frequency of the double-pass AOM to 200 MHz, the cooling of ^{87}Rb can be easily achieved with the laser detuned by 13 MHz towards the red. To close the cooling transition a repumping laser is used. For ^{85}Rb it is locked to $F = 2 \rightarrow F' = 1,3,4$ cross-over peak or ^{87}Rb $F = 1 \rightarrow F' = 1,2$, so we can use a single pass AOM which shifts the beam by 60 MHz. It is not necessary to dynamically shift the frequency of the repumper laser, however we use AOM to quickly switch on/off the laser beam in the experiment with the dipole trap. The configuration of the injection locking lasers, as well as the arrangement of the rest of the optics used for the laser cooling together with re-pumping beam set-up is schematically depicted in Fig. 3.9.

Summary

During the absorption and emission of photons a momentum transfer occurs, which changes the velocity of a moving atom. Although the light force exerted on atoms is

rather small, many cycles of absorption and emission can reduce the temperature of the atoms in a short time. In this chapter the basic principles of atom-light interactions have been described. The expression for the scattering force has been derived. The principles of the Doppler and sub-Doppler cooling mechanism as well as magneto-optical trapping have been described. The cooling and trapping techniques developed in recent years enable us to manipulate atoms in a completely new regime. As an introduction to the material included in this thesis, the mechanisms behind the realisation of MOT with rubidium atoms have been presented. A detailed description of the experimental implementation in our laboratory developed for investigation of Rydberg atoms in the ultra-cold regime will be provided.

BLANK PAGE IN ORIGINAL

CHAPTER 4

LASER SYSTEM

Since the invention of tunable lasers, which can continuously change the frequency of the emitted light in a given spectral range, a lot of effort has been put into reducing the laser linewidth[1]. Other important parameters characterizing the good performance of a laser system are the coherence and the phase stability, as they are very critical for the majority of quantum optical experiments. Laser cooling experiments require a laser linewidth $\Delta\nu$ to be much narrower than the natural linewidth of the atomic transition involved Γ, as well as stable and reproducible laser frequencies which can be detuned continuously in a range of several Γ. The excitation to Rydberg states for applications to quantum information processing, which is based on the coherent control and manipulation of the quantum state of atoms, also requires a coherent and very stable laser excitation system.

The effective performance of each laser system is affected by quantum noise and is often limited by electronic noise or mechanical instabilities. Thus the reduction of the noise and the stabilization of the laser frequency to a reference point, which is typically chosen to be a strong optical transition, are necessary for good experimental performance. An active stabilisation requires the conversion of fluctuations of numerous parameters which influence the performance of the laser such as its temperature, air

[1]The linewidth of a single-frequency laser is the width of its optical spectrum typically expressed as the full width at half maximum (FWHM)

pressure and driving current into an electronic signal which is subsequently fed back into the laser control system. Such a signal can be generated in many different ways, some of them will be introduced in Section 4.1.

This chapter is devoted to all the lasers developed in our laboratory for the cooling and excitation of atoms to Rydberg states. In Section 4.1 the arrangement of cooling lasers together with their stabilisation technique is presented. Section 4.2 describes the technique used for coherent excitation of atoms to Rydberg states using a two-photon excitation scheme. A home-built 780 nm extended cavity laser system along with commercial 480 nm SHG laser, providing photons for both transitions are described. A lot of effort was devoted to the frequency stabilisation of the two lasers which are also frequency locked to each other. The techniques used to generate the locking signals for both lasers, mainly the modulation transfer spectroscopy and stabilization using electromagnetically induced transparency feature are explained in Sections 4.3.1 and 4.4.

4.1 The cooling lasers

Over the time the set frequency of the laser will drift, in the case of a semiconductor laser this is mainly due to the temperature and current fluctuations as well as mechanical effects. This problem can be solved by implementing active control techniques, which usually rely on the control of the lasers output using closed servo-loops[2]. An electronic frequency-dependent signal, the so-called *error signal*, is fed back to the laser control device. The error signal discriminates whether the laser frequency is too high or too low compared to the locking point, thus it should be monotonic and cross zero at the resonance, so that the servo-loop counteracts the shifts and brings the laser back to the central frequency. The technique of frequency stabilisation by means of closed servo-loops is called *laser locking.* A dispersive or absorptive feature of an appropriate resonance frequency are used as a reference, and they can be provided exploiting the interaction of lasers with macroscopic structures e.g. optical resonators or microscopic structures such as atoms and molecules (Riehle, 2004).

[2]Servomechanism relays on an automatic correction of the performance of a device. The correction loop is a closed system, where the error in the performance of the device is detected by some sensor and subsequently a negative feedback is sent to the device control system, which adjusts the operation of the device.

Techniques based on polarization spectroscopy (Hänsch and B., 1980) or radio-frequency (rf) phase modulation spectroscopy Drever *et al.* (1983) in combination with an optical resonator offer a very simple and relatively cheap method and provide a sensitive stabilisation of the laser. However, the resonance frequencies of macroscopic structures depend on their dimensions, which are affected in general by temperature, air pressure and mechanical vibrations. Thus the stability of the laser relies on how well these parameters can be controlled. Usually pre-stabilisation of the laser and narrowing down of the linewidth is achieved using the Pound-Drever-Hall method, which is also the technique used to control the frequency of the Toptica TA/DL-SHG 110 laser. The influence of the environment is much less significant when atoms or molecules (micro-structure resonators) are used, as they have well defined frequencies. Another advantage of using atoms as reference oscillators is that their transition frequencies are constant, so one can copy a frequency standard an unlimited number of times. All cooling lasers in our experiment are stabilized to an atomic transition.

4.1.1 Laser frequency stabilisation to an atomic transition

For efficient locking, some electronic manipulation of the emission and absorption spectra must be performed to obtain an useful error signal. Dispersive-like signals can be either optically generated and further processed by means of electronics or the information is first encoded electro-optically and the decoding is done electronically, so-called *optical heterodyne detection.* The first group of techniques includes: polarisation spectroscopy (Hänsch and B., 1980), Dichroic atomic vapour laser locking (DAVLL) (Chéron *et al.*, 1994) or "tilt locking" (Shaddock *et al.*, 1999) and the second is constituted by frequency modulation spectroscopy techniques (Drever *et al.*, 1983).

In polarization spectroscopy (Hänsch and B., 1980; Pearman *et al.*, 2002) a circularly polarized beam induces a birefringence in a medium which is then interrogated by a probe beam. This technique is characterized by a broad capture range, the maximum frequency drift which can be corrected using the generated error signal, and simple electronics are required to build up the servo-loop. However, a disadvantage of this method is that the zero crossing of the error signal depends on the power of the pump beam, thus it might not coincide with the peak of the absorption profile. The

DAVLL technique relies on the differential absorption of σ^+ and σ^- polarized beams by atoms in a magnetic field, the so-called *circular dichroism.* Single beam DAVLL (Chéron *et al.*, 1994) also offers a large capture range, but has the downside of low frequency resolution. This can be improved by combining DAVLL with Doppler-free spectroscopy (Wasik *et al.*, 2002), which results in error signals with a steeper gradient and thus a higher accuracy of the laser locking. The shape of the signals obtained is however very sensitive to stray magnetic fields and the power of the pump beam. The tilt locking method based on spatial modes interference (Shaddock *et al.*, 1999) or two-beam interference in a Sagnac interferometer (Robins *et al.*, 2002) also provides a simple, inexpensive, highly sensitive locking system. All these techniques rely on the detection of DC signals, thus they are affected by the current noise and fluctuations, which might result in an overall frequency offset.

4.1.2 Frequency modulation spectroscopy

The frequency modulation (FM) spectroscopy technique was invented in 1979 by Bjorklund (1980) and independently by Drever *et al.* (1983). Drever and Hall suggested to use optical heterodyne detection for the frequency locking of lasers to an optical resonator by means of servo-loops. This method was experimentally demonstrated by Drever *et al.* (1983) and Prentiss *et al.* (1981). Bjorklund (1980) applied this technique to measure weak absorption and dispersion features.

The main concept of FM spectroscopy is as follows: a single mode laser oscillating at a frequency ω_c is externally modulated at a frequency ω_m to produce a pure frequency modulated optical spectrum, which consists of a strong carrier at ω_c and weak sidebands at $\omega_c \pm \omega_m$. If ω_m is large compared to the width of the spectral line, the sidebands are well separated and the transition feature can be probed by a single sideband. The spectral feature, here the atomic transition spectral line or the cavity resonance feature in the Pound-Drever-Hall method, affects the sideband of the FM signal and thus the FM spectrum is distorted. The rf (radio-frequency) heterodyne beat signal is detected by a photodiode. By observing the phase and amplitude of the registered and demodulated electrical signal it is possible to recover information about the absorption and dispersion (Bjorklund *et al.*, 1983).

The analysis of the signal is done electronically by means of lock-in amplifiers (phase sensitive detectors) and will be described in detail in Section 4.3.2. The demodulated signal acquires a dispersion-like shape and can be used for the frequency locking of the laser. The great advantage of the FM technique is that the lasers have a low noise level in the radio-frequency regime, thus the rf modulated signal can be detected with high sensitivity.

Doppler free saturated absorption spectroscopy

To lock the lasers to an atomic transition, suitable spectral lines to build the reference signal have to be obtained. When a laser beam of frequency ω_l is propagating through an atomic cloud, only atoms whose velocity meet the Doppler condition $\omega_l = \omega_0 + \boldsymbol{k} \cdot \boldsymbol{v}$, absorb the light. The stationary detector recording the loss of the light propagating through the sample measures the Doppler-broadened profile, thus each 'dip' in Fig. 3.8 represents the Doppler-broadened absorption profile of ^{85}Rb $F = 2 \rightarrow F'$, ^{85}Rb $F = 3 \rightarrow F'$ and ^{87}Rb $F = 2 \rightarrow F'$ transitions. From the selection rules it follows that $\Delta F = 0, \pm 1$ therefore, for both isotopes, ^{85}Rb and ^{87}Rb, there are only three allowed transitions for each ground state sub-level. As the hyperfine sub-levels are separated by ~100 MHz and the Doppler-broadened absorption profile of each line is ~500 MHz, each 'dip' is composed of three overlapping lines with frequencies $[\nu_1, \nu_2, \nu_3]$. Therefore to resolve the hyperfine structure a Doppler-free spectroscopy technique has to be used.

The saturated absorption (SA) technique is used to minimize the Doppler-broadening effect. A laser beam is split into two beams, the pump and the probe beam, which counter-propagate through the atomic vapour cell and overlap at some point in it. The intensity of the pump beam needs to be higher then the saturation intensity while the probe beam is much weaker, usually it has 5-10% of the power of the pump beam. When the frequency of the laser is tuned to the atomic resonance, both beams interact with the same group of atoms whose velocity along the beam axis is "zero". The strong pump beam depletes the number of atoms in the initial state, which leaves only a few atoms for the probe beam to interact with, so the probe passes through the cell without being absorbed. Fig. 4.1 presents saturated absorption spectra of rubidium with resolved hyperfine structure of Rb atoms, which appears as a reduced absorption

in the Doppler-broadened line profile. In addition $[\nu_1, \nu_2, \nu_3]$ lines are accompanied by so-called *cross-over peaks* at midway frequencies given by $[\frac{\nu_1+\nu_2}{2}, \frac{\nu_2+\nu_3}{2}, \frac{\nu_1+\nu_3}{2}]$.

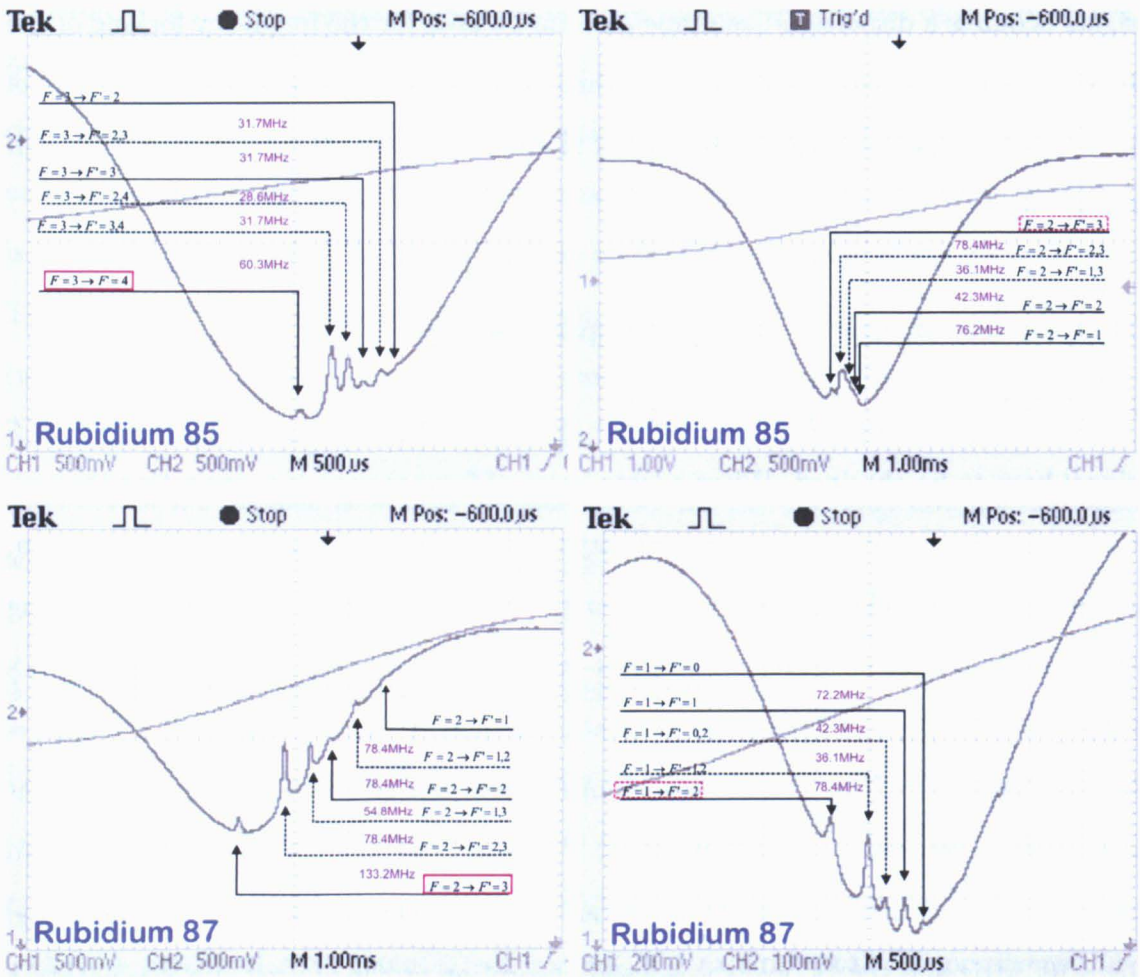

Figure 4.1: Saturated absorption spectra of ^{85}Rb $F = 3 \rightarrow F'$, ^{85}Rb $F = 2 \rightarrow F'$, ^{87}Rb $F = 2 \rightarrow F'$ and ^{87}Rb $F = 1 \rightarrow F'$ with revealed hyperfine structure. The cooling transitions for both isotopes are marked out by red boxes and appropriate re-pumping transitions by dashed red boxes.

FM saturated absorption spectroscopy

A modulation of the current driving the diode can be added via locking electronics, which in turn modulates the laser frequency at a slow rate compared to Γ. The signal from the photo-diode recording the saturated absorption spectrum is thus also frequency modulated, but it is subsequently electronically demodulated by a lock-in amplifier, tuned to the modulation frequency. The resulting signal is proportional to the first derivative of the saturated absorption peaks and is used as an error signal, as the derivative has a linear response near the the top of the transitions peaks.

Fig. 4.2 shows error signals observed with FM spectroscopy. The amplitude of the error signal is proportional to the strength of the signal detected by the photodiode. Due to residual linear absorption experienced by the probe beam, the error signal has a background slope proportional to the derivative of the Doppler broadened absorption profile. This offset can be partially tuned by adjusting the phase of the lock-in amplifier (see Section 4.3.2). In this way the 'zero' level of the error signal, indicated by the purple lines, can be tuned to cross the top of the resonance peak to which the laser is being locked. The offset in the detected signal limits the accuracy of the laser locking, as it shifts the locking point away from the top of the reference peak.

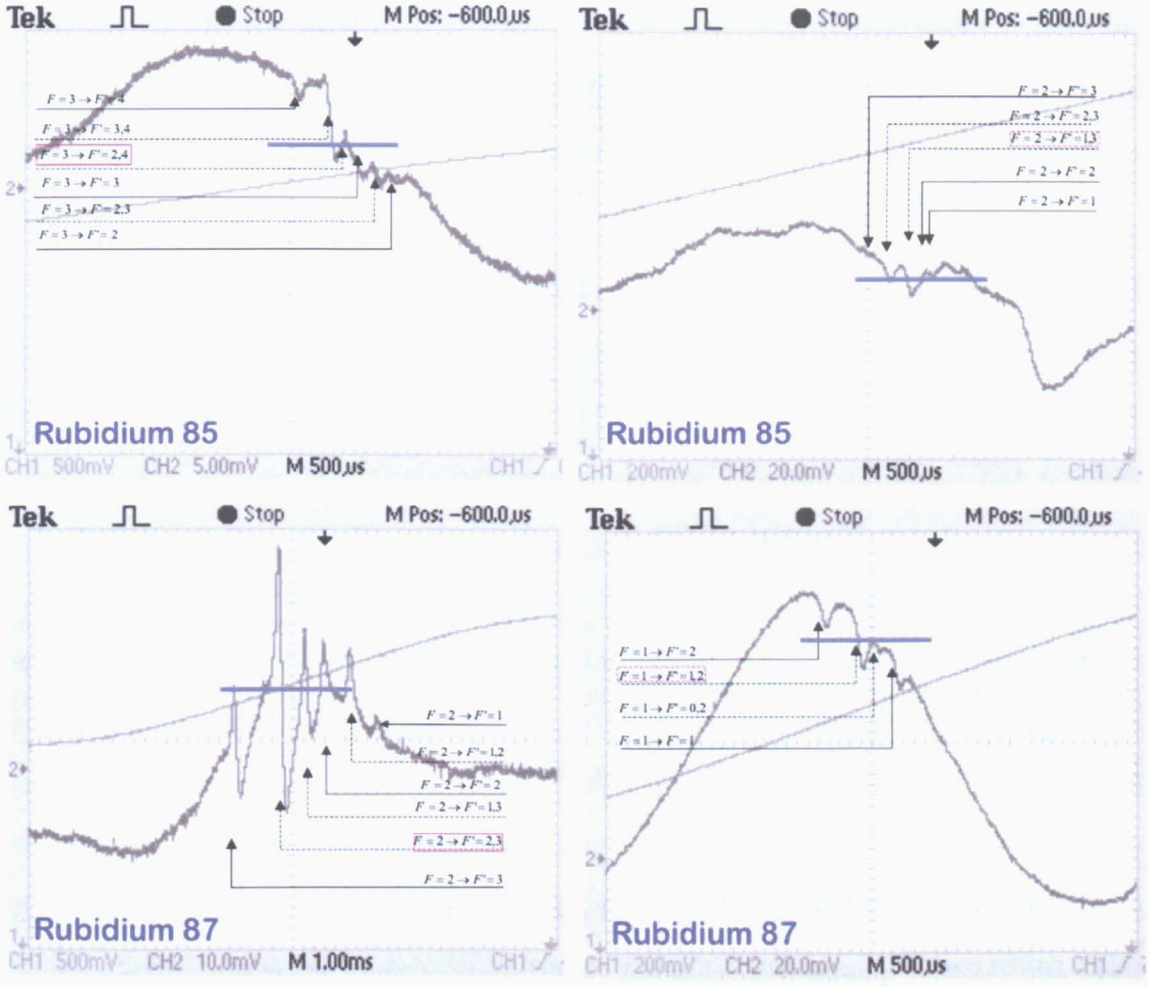

Figure 4.2: Error signals recorded with FM saturated absorption spectroscopy, obtained for transitions $^{85}Rb\ F = 3 \rightarrow F'$, $^{85}Rb\ F = 2 \rightarrow F'$, $^{87}Rb\ F = 2 \rightarrow F'$ and $^{87}Rb\ F = 1 \rightarrow F'$. The dispersion features are revealed for hyperfine structure peaks. Red boxes indicate the reference frequency used to lock the lasers. Horizontal purple lines indicate 'zero' level of error signal, corresponding to the top of the locking peaks.

We use this method to frequency lock our laser sources for the cooling and trapping of atoms.

4.2 Excitation of Rubidium atoms into Rydberg states

Amongst the numerous methods for excitation of alkali atoms to Rydberg states (Gallagher and Cooke, 1979), a technique commonly used is photo-excitation via one resonant level, so called *two-photon excitation*. Fig. 4.3 shows the energy level diagram of the two-photon transition for rubidium atoms, that we use for excitation to a Rydberg state - a three-level ladder system. In our experiment the intermediate state $|2\rangle$ is chosen to be $5P_{3/2}$ and thus the two laser fields coupling it to the ground $|1\rangle$ and Rydberg state $|3\rangle$ require wavelengths of 780 nm and 480 nm respectively. The couplings are characterized by Ω_1 and Ω_2 - the one-photon Rabi frequencies given by Eq. (3.12).

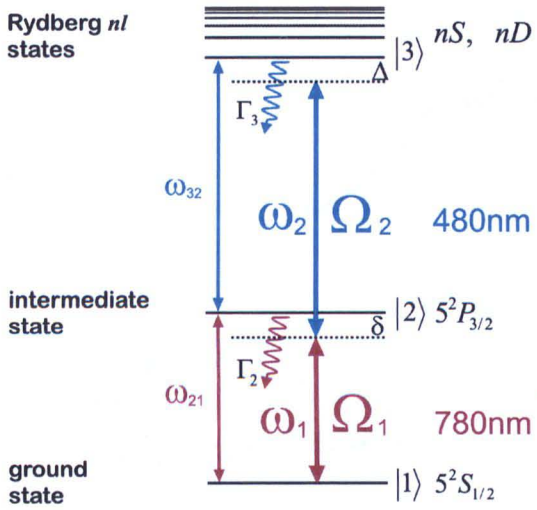

Figure 4.3: A three-level ladder system - simplified scheme of a two-photon transition in rubidium. $\hbar\omega_{21}$ is the energy difference between states $|1\rangle$ and $|2\rangle$, and $\hbar\omega_{32}$ between $|2\rangle$ and $|3\rangle$ respectively. The 780 nm laser has a frequency ω_1 which is far detuned from the $|1\rangle \rightarrow |2\rangle$ transition by δ while the 480 nm laser of frequency ω_2 is detuned by $\Delta = \omega_1 + \omega_2 - \omega_{31}$, on the two-photon resonance $\delta + \Delta = 0$.

In certain circumstances a three-level atom can be considered as an effective two-level one, so the quantum mechanical description of the system can be simplified (Saffman *et al.*, 2010). If the detuning of the first transition from the intermediate level $\delta = \omega_1 - \omega_{21}$ is much larger than the width of the level $|2\rangle$, and if the decay rate of that state to state $|1\rangle$, Γ_{21}, is large compared to Γ_{32}, than the population of state $|2\rangle$ might be considered as negligible. With these conditions met and $\Omega_1 \ll \Gamma$, in the case of a two-photon resonance, the population oscillates between the ground and the Rydberg state with an effective Rabi frequency given by $\Omega_{eff} = \Omega_1\Omega_2/2\delta$. Any fractional

population of the state $|2\rangle$ leads to a decrease of the coherence due to the spontaneous emission from that state. There is a finite probability of populating intermediate state and thus there is a probability of spontaneous emission from this state, P_{se}, which is inversely proportional to the detuning δ and depends on the factor $|\Omega_2/\Omega_1|$. The spontaneous emission is minimized if $|\Omega_2/\Omega_1| = 1$, taking this into account that the effective Rabi frequency may be expressed as $\Omega_{eff} = {}^{P_{se}|\Omega_2|}/_{\pi\Gamma_2}$ (Saffman *et al.*, 2010). This means that in order to quickly excite the atoms, Ω_2 has to be sufficiently large. As the Rabi frequency is proportional to the dipole matrix element of a given transition (Eq. (3.12)), which scales as $\sim n^{-3/2}$, for high lying Rydberg states the laser power necessary for efficient excitation to state n scales as n^3. Typically in order to keep the ratio $|\Omega_2/\Omega_1|$ close to 1, the power of the 780 nm laser is of the order μW while the power of the 480 nm laser is up to a few hundreds of mW and the beam is focused to a few μm spot size.

There are two sorts of uncertainties for the detuning of both lasers. The first arises from the Doppler effect. The recoil velocity resulting from the absorption of a 780 nm photon by ^{85}Rb atom is about $0.6\,{}^{\mathrm{cm}}/_{\mathrm{s}}$ and it gives a Doppler broadening of 48 kHz, while for the 480 nm light these parameters are $0.97\,{}^{\mathrm{cm}}/_{\mathrm{s}}$ and 127 kHz. The Doppler broadening can be partially reduced to about 30 kHz by using counter-propagating excitation beams. However, in the case of two-photon of different wavelengths it is impossible to cancel it out completely. The excitation could be made Doppler-free using two counter-propagating beams at 594 nm, however the lack of a close intermediate level makes this solution infeasible. The second cause of detuning errors is the Stark shifts of the energy levels caused by the excitation lasers. The main contributions arise from the interaction of the red laser with the ground state and the blue laser with the Rydberg state. States $|1\rangle$ and $|3\rangle$ are thus shifted by $\delta_1 = {}^{|\Omega_1|^2}/_{4\delta}$ and $\delta_3 = -{}^{|\Omega_2|^2}/_{4\delta}$, which again implies to keep $|\Omega_2/\Omega_1| = 1$ so that the Stark shift is reduced (Saffman *et al.*, 2010). Finally it is important to retain the detuning Δ small compared to the effective Rabi frequency.

The next sections describe laser sources used in our experiment for the two-photon excitation scheme and the methods developed to overcome the obstacles described above and obtain stable laser sources to access Rydberg states with high precision.

4.2.1 Extended cavity diode laser (red laser source)

As mentioned in the previous sections, in our experiment we make use of semiconductor lasers. The essential requirements for any laser system are an excitation source, an active medium and an optical resonator. In a laser diode these are achieved by employing layers of different semiconductor materials, which are usually based on a combination of elements from the group III and V of the Periodic Table, depending on the desired wavelength. Infra-red light is emitted by AlGaAs diodes, where a p-n junction[3] is made of an aluminium gallium arsenide crystal. The excitation mechanism is the flow of the current across the p-n junction. In order to obtain coherent laser light stimulated emission has to dominate in the system. This is achieved when the applied forward bias is high enough so that population inversion occurs in the junction[4]. The typical laser diode has a heterostructure where an active GaAs medium lies between p- and n- doped layers of AlGaAs. This provides the photon confinement, due to the difference in the refractive indices of these materials which enables the total internal reflection. Furthermore, the facets of the crystal are cleaved to form reflecting surfaces of a resonator.

It is desirable to have a single mode tunable laser, which can be continuously adjusted over the cavity range without losing the output power, however usually many modes can oscillate in the resonator cavity simultaneously. A typical AlGaAs diode has a cavity length of 250 μm and refractive index $n_{ref} = 3.5$, thus the free spectral range[5] $\Delta\nu_{FSR}$, the range in which the frequency can be tuned, is about 170 GHz and the modal linewidth $\Delta\nu_{FWHM}$ is of order 100 GHz. The high order modes can be removed by the use of a gain medium, which in the case of semiconductor lasers has a sharp exponential profile. The coupling between cavity modes and the exponential gain factor has the effect that the emission at the frequency with highest gain gets enhanced and other modes are suppressed. As a result the emission linewidth is reduced by about a 1000

[3] A p-n junction is formed of two semiconductors with different band structure: on the p-doped side there is an excess of holes while on the n-doped side there is an excess of electrons. In equilibrium a potential barrier (so called built-in voltage) is created across the junction which prevents the electron-hole recombination. Applying an external voltage lowers the built-in barrier allowing electron-hole recombination accompanied by the release of energy - spontaneous emission of photons. The first semiconductor laser was experimentally demonstrated by Hall *et al.* (1962)

[4] The population inversion occurs when there are more electrons injected to the higher energy conductive band then there are electrons in a lower energy valance band.

[5] The free spectral range of an optical resonator is the spacing between its adjacent axial modes.

times down to a few MHz. The gain medium, in the case of a semiconductor laser is the injection current. The diode laser operates in multi-longitudinal modes until the injection current exceeds the threshold value starting single mode operation.

In the specific case of diode lasers, the spectral linewidth is an interesting property as its measured values are greater by about 30 times than the theoretical predictions, based on Schawlow - Townes formula, e.g for 1 mW beam the measured measured width is 114 MHz instead of few MHz (Henry, 1982). The line broadening arises from the fluctuations in the refractive index of the crystal, as well as the phase and intensity fluctuations caused by the spontaneous emission. To reduce the influence of these factors a dispersive element such as a grating or an etalon is added to the cavity inside or outside the gain medium, which works as a filter of unwanted modes as it provides selective feedback and forces the single mode operation. These elements can be either micro-fabricated on the diode or the cavity can be externally extended (Ye, 2004). The first experimental demonstration of semiconductor lasers coupled to an external cavity was carried out by Crowe and R. M. Craig (1964), and nowadays extended cavity diode lasers (ECDLs) are commonly used in telecommunications as well as in research as tunable coherent laser sources.

Littrow configuration

The 780 nm diode lasers used in our experiment (see Fig. 4.5) are built with an extended cavity (ECDL). The external cavity is created between a diffraction grating and an anti-reflection coated facet of the diode. From the grating equation it follows that $m\lambda = d(\sin\theta_1 + \sin\theta_2)$, where d is the grove spacing, m is an integer and θ_1, θ_2 are the incidence and diffraction angles respectively, it follows that for a given spectral order $m > 0$ the diffracted wavelengths are separated, $\theta_2(\lambda, \theta_1)$ (Fig. 4.4 (b)). Thus changing the incidence angle by rotating of the grating allows us to choose a wavelength, different than the one the laser is currently operating at. The selected mode is amplified in the lasing medium, forcing single mode operation of the laser at the selected frequency. In the so called *Littrow configuration* the first order diffracted beam is sent back to the lasing cavity, which imposes $\theta_1 = \theta_2$, and the reflected zero order provides the output beam.

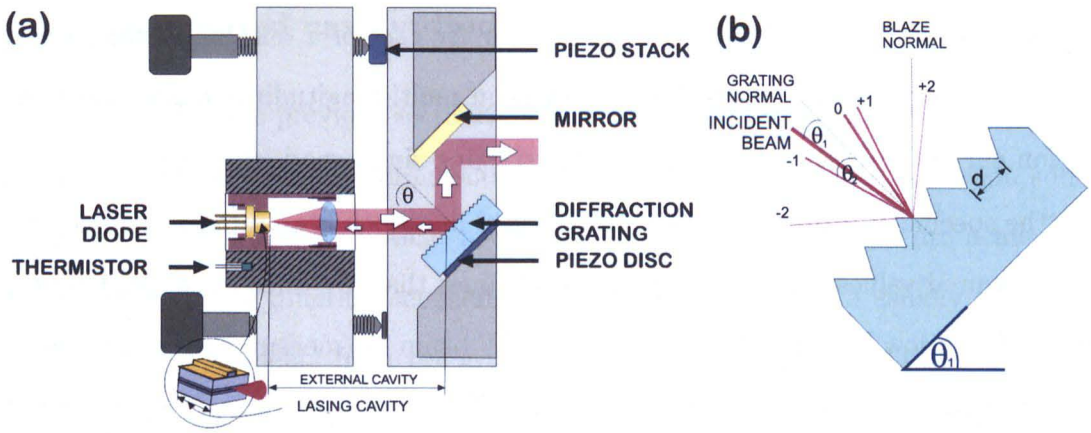

Figure 4.4: (a) Schematic diagram of the ECDL designed by Arnold *et al.* (1998) with fixed output beam direction - top view after Hawthorn *et al.* (2001). (b) Diffraction by a plane blazed reflection grating.

Fig. 4.4 (a) presents the design of a cavity implemented in our set-up based on the original work of Arnold *et al.* (1998). The direction of the reflected zero order beam depends on the wavelength, thus a modification has been made by adding a fixed mirror mounted parallel to the grating surface (to form a retro-reflector) (Hawthorn *et al.*, 2001). Simultaneous rotation of the mirror and the grating allows to keep the constant direction of the output beam. As the light emitted from the diode is strongly diverging ($\Theta_\perp = 17°$, $\Theta_\parallel = 8°$), a high numerical aperture (NA ~ 0.5) aspheric lens is mounted with the diode in a collimation tube, which has a twofold role: it collimates the output beam and focuses the feedback beam to a spot size of the order of the active region of the diode. The diffraction grating is gold coated, reflects about 40% of the incident light and is mounted on a $12.7 \times 12.7 \times 6\,\text{mm}$ substrate. As it has $1800\,^{\text{groves}}/_{\text{mm}}$, for 780 nm light the Littrow angle is $\theta = 44.6°$. The grating is glued to the 1 mm thick piezoelectric transducer[6] (PZT) disk fixed to a modified mirror mount. The mount provides a vertical and horizontal grating alignment and thus rough wavelength adjustment. A second PZT is mounted with a screw to tilt the grating around a vertical axis. The PZT also contracts and extends according to the applied voltage, which enables a fine adjustment of the cavity length and thus the electric control of the laser frequency.

[6]A piezoelectric transducer is a certain solid state material e.g. crystal or ceramic which exhibits piezoelectric effect i.e. they accumulate an electric charge in response to applied stress. This effect is reversible, the electric energy can be converted to mechanical vibrations to build high resolution actuators.

The length of the external cavity is about 2 cm, which results in 7.5 GHz of free spectral range of the laser. The linewidth is reduced to few hundreds of kHz. Fig. 4.5 shows the 780 nm ECDL laser used for the two-photon excitation. The aluminium parts were manufactured in the S&T Workshop. The maximum power of a free running diode is 100 mW, and the maximum output from the extended cavity is 70 mW. The loss is due to reflecting the first order beam back into the diode. During the experiment the laser is operated at 60 mA which gives a laser power of 20 mW.

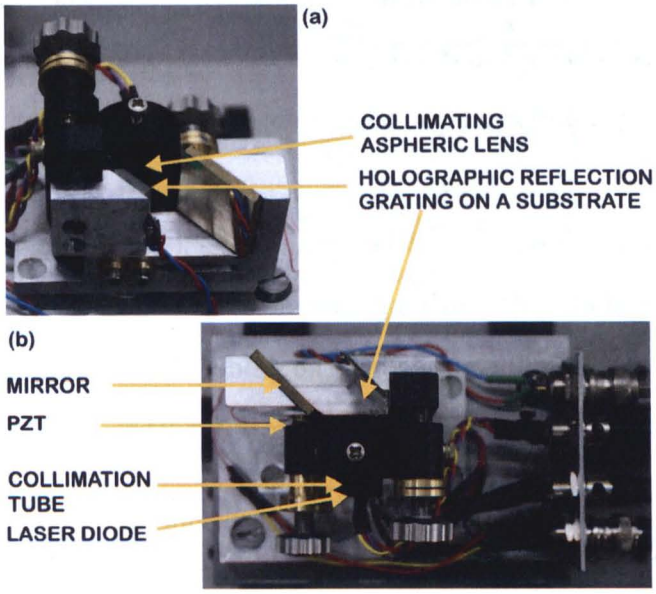

Figure 4.5: Extended cavity diode laser built in our laboratory.

Temperature and current control

The central wavelength of the laser output is strongly related to the energy of the band gap of the semiconductor, which in turn depends on the temperature and the injection current. Thus for a stable operation of diode lasers the temperature and the current need to be controlled. In the experiment we use a commercial *Thorlabs ITC 502* driver, which allows to stabilize the temperature and current of the diode.

The temperature of the laser is monitored by a 100 kΩ thermistor[7], placed close to the diode in a small hole drilled in the mount and it is regulated using a commercial thermoelectric cooler[8] (TEC) installed under the mirror mount. One side of the cooler

[7] A temperature sensitive resistor which serves as a temperature sensor.

[8] If the current flows through the junction of two semiconductors with opposite doping, the junction will be cooled or heated depending on the current direction - so called *Peltier* or *thermoelectric* effect.

is connected to a heat sink - a heavy thick metal base which also provides damping of the tabletop vibrations. The control feedback loop is based on a standard PID (proportional-integral-derivative) algorithm. To avoid a delay in the loop the sensor should be placed near to the cooler and at the same time for an accurate measurement of the diode temperature it has to be in the close vicinity of the diode. In some cases, especially involving small thermal loads, the procedure of adjusting of PID controller will not work and the temperature of the diode will not stabilize. It happened in our case probably due to a small delay in the servo loop. Therefore, to enable fast temperature stabilisation the integrator part in the control unit had to be disconnected. As a result of using proportional-derivative controller the temperature stabilises a bit below the set-point.

A low noise current source is essential for an efficient performance of the diode. The current controller stabilizes the driving current at the level of $\pm 10\,\mu$A, which is less than 0.02% of the typical value applied to the diode. Without changes in the ambient temperature the current stays stable at this level for 24 h. The driver also contains a current limiting resistor which protects the diode against unwanted transients. The current driver enables high-speed modulation which is important for laser locking.

4.2.2 SHG laser system (blue laser source)

The second step in the two-photon excitation requires ~480 nm light. Although this wavelength lies in the range of semiconductor lasers, operating the diode in an external cavity significantly reduces the output power of the laser. As it was explained earlier, it is essential to keep the Rabi frequency of the upper transition large by employing high power lasers, thus low power diode lasers are not efficient enough for our purpose. Other systems providing this wavelength are dye lasers, however they are usually expensive and difficult to operate. A good alternative is to use non-linear optic crystals to halve the wavelength of a reliable, high power, a narrow linewidth infra-red light emitted by an amplified semiconductor laser. This technology is offered by a commercial SHG (second harmonic generation) lasers manufactured by Toptica.

The scheme of the TA-DL SHG 110 laser system, which is used in our experiment, is presented in Fig. 4.6. It is composed of three main parts: master oscillator, amplifier

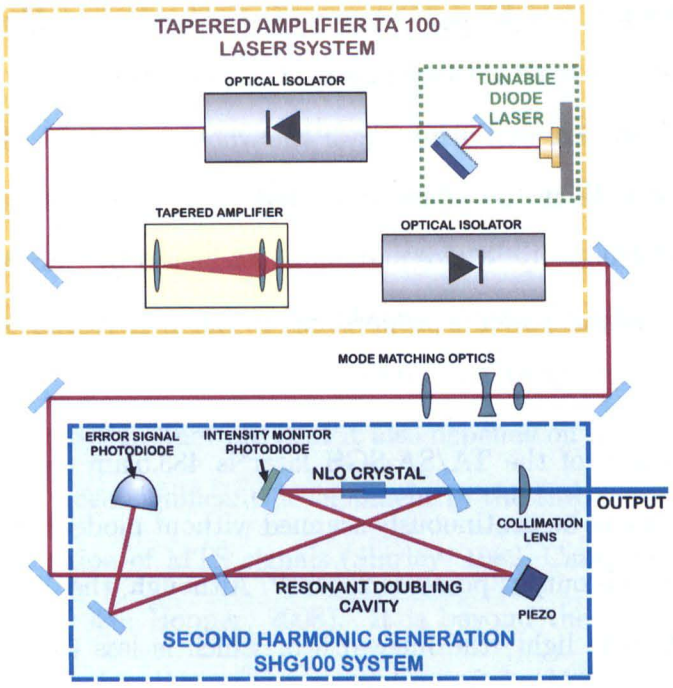

Figure 4.6: Scheme of the frequency doubled high power laser system TA/DL-SHG 110 by Toptica.

and doubling cavity. A tunable grating stabilized diode laser provides the fundamental wavelength of 956 nm and an output power of 50 mW. The output of the master laser is coupled to a high power semiconductor amplifier with a tapered gain region, *tapered amplifier* (TA), which gives 1 W output beam. To avoid optical damage of both diode lasers, they are secured with high extinction optical isolators. The TA output beam is adapted to a resonant cavity by mode matching optics. The resonant doubling cavity is designed as a folded ring cavity, in a *bow-tie* configuration, with the NLO (non-linear optic) crystal placed in a beam waist between two confocal mirrors. To adjust the cavity length one of the mirrors is mounted on a PZT controlled by the stabilization unit which uses the Pound-Drever Hall method of error signal generation (see Section 4.1.2).

Second harmonic generation within NLO crystal provides the doubling of the frequency of the input beam. In our case a potassium niobate ($KNbO_3$) crystal is used which works for a wavelength of ~970 nm. When an electro-magnetic wave with frequency ω_I propagates through a non-linear optic medium, the electric field induces electric dipole moments in the medium, which oscillate at frequency $\omega_{II} = 2\omega_I$. This induced polarization radiates and emits an optical field at frequency $2\omega_I$, so called sec-

ond harmonic frequency, which was not present in the fundamental beam. The induced dipoles radiate a rather weak electromagnetic field, however, as the phase and amplitude of the input beam are well defined over the whole crystal, all the induced dipoles have fixed phase as well, the so-called *phase-matching*. Thus the radiation from each dipole adds up constructively. Phase matching is achieved by tuning the temperature of the crystal. The output power is proportional to the intra-resonator power enhanced by the cavity.

The set wavelength of the TA/SA-SGH laser is 483.5 nm and the coarse tuning range is ±4.5 nm. It can be continuously scanned without mode hops in a range about 35 GHz. The maximum output power is 250 mW. Although, the cavity locking system gives highly stable blue light, the linewidth of which is less than 2 MHz, to access specific Rydberg states it has to be further reduced and stabilized using additional techniques which will be described in Section 4.4.2.

4.3 Laser frequency stabilisation using MTS

Similarly to the saturated absorption, MTS (modulation transfer spectroscopy) is a pump-probe technique which produces sub-Doppler line-shapes useful for the laser locking. This technique differs from the standard FM spectroscopy, as the modulation is applied to the pump beam instead of the probe. The unmodulated probe obtains sidebands via the interaction with the modulated pump beam within a saturable medium. The modulation transfer process is an example of the so-called *four-wave mixing* phenomenon, which was first observed in iodine by Snyder *et al.* (1980) and explained by Shirley (1982). As the four-wave mixing is a non-linear process, the great advantage of using MTS for laser locking, is that this method is insensitive to the background absorption of the medium and it produces a flat Doppler-free error signal (Fig. 4.9 (b)). As a consequence, the fluctuations and the background noise resulting from the saturated absorption signal, which can shift the baseline of the locking point, are eliminated. The theory of the MTS signals will be presented in the next sections.

4.3.1 Basic theory of modulation transfer

Alike a standard saturated absorption technique (Section 4.1.2), in MTS two collinear laser beams (here also called *the pump* and *the probe*) propagate in opposite directions through the atomic vapour cell. Similarly to SA the magnitude of the obtainable signals depends on parameters such as the pressure of the medium, the length of the interaction of the two laser fields within the cell, the medium saturation intensity, absorption coefficient and the transition linewidth but it also depends on modulation parameters. Since 1980 there has been significant development in the theoretical analysis and the experimental optimisation of MTS signals (Shirley, 1982; Camy *et al.*, 1982; Ma and Hall, 1990; Jaatinen, 1995; Hopper, 2008). It is beyond the scope of this thesis to provide the detailed explanation of the generation of the MTS signal, however some basic theory will be provided below.

Following Eq. (3.8), the electric field amplitude of a monochromatic laser beam, in this case the probe beam, propagating in the direction of the laboratory z (Fig. 4.7) axis is described by:

$$E_{probe}(z,t) = \frac{1}{2}\widetilde{E}_{probe}e^{i(\omega_c t - kz)}, \tag{4.1}$$

where ω_c is the carrier frequency. The counter-propagating pump beam goes through the electro-optic modulator where it is phase modulated and acquires sidebands at frequency ω_m:

$$E_{pump}(z,t) = \frac{1}{2}\widetilde{E}_{pump}e^{i(\omega_c t + kz)}e^{i\delta cos\omega_m t}, \tag{4.2}$$

where δ is the modulation index which determines the difference between the phase of the unmodulated and modulated beam $\Delta\omega = \omega_m\delta$. By expanded into Fourier components this gives:

$$E_{pump}(z,t) = \frac{1}{2}\widetilde{E}_{pump}\sum_{n=-\infty}^{+\infty} J_n(\delta)e^{i[(\omega_c + n\omega_m)t + kz]}, \tag{4.3}$$

where J_n is the Bessel function of order n and n is an integer.

According to Shirley (1982) there are two physical mechanisms responsible for the transfer of modulation, the so-called *modulated hole burning* and the reflection. When the phase or amplitude modulated pump beam is propagating through the atomic

sample it burns holes of modulated depth into the velocity distribution of atoms. The second resonant beam propagating through this sample, the probe beam, interacts with these generated holes which results in a modulated absorption and dispersion sensed by the beam. As a consequence the probe beam gains the modulation.

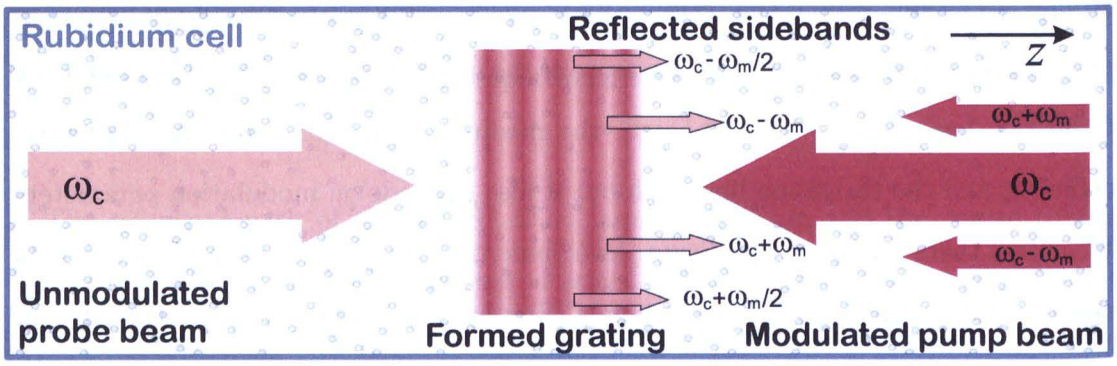

Figure 4.7: Illustration of the modulation transfer process via reflection of sidebands from the spatial grating created as a result of the interference of the pump and the probe beams.

The second mechanism of the modulation transfer is reflection, shown in Fig. 4.7. The modulated pump beam and unmodulated probe are counter-propagated through the atomic vapour cell. The pump and probe beams interfere, generating a partial standing-wave field pattern, which due to saturation is transferred into the population of the resonant states of the medium. This imposes a spatial periodicity in the transparency of the atomic sample which mimics a diffraction grating. As a consequence, a part of each beam is Bragg reflected in the opposite direction to the propagation. Following that, each of the two arbitrary sidebands of the pump beam (described by the Fourier components $\omega_c + n\omega_m$ and $\omega_c + n'\omega_m$) is reflected on the grating. The re-radiated field travels in the direction of the probe carrier, thus the probe field gains two sidebands at frequencies $\omega_c \pm (n - n')\omega_m$. This process is the already mentioned four-wave mixing process, where two fields interfere creating a grating which reflects a third field in order to produce a fourth field.

The sidebands of the pump beam can interfere with the probe as well, however as their frequency is shifted compared to the carrier frequency, this interference induces a moving spatial grating. The pump beam carrier reflected from this induced grating is Doppler shifted by the frequency of the moving grating, which results in two extra components for the probe, however these components are usually neglected in the

theoretical analysis of the resultant signal.

In order to detect the modulation transfer signal the optical heterodyne detection technique has to be used. The optical frequencies oscillate too fast to measure the phase of the electric field electronically. Employing this technique allows shifting of the optical band to the detectable radio-frequency range and reveal spectral features of interest. Also, the modulation transfer signals are very weak and this method allows one to extract feeble signals from the extremely noisy background. The principle of the heterodyne detection in connection with the MTS method will be described in the next section.

4.3.2 Frequency modulated signal generation and demodulation

The key concept of modulation spectroscopy is to modulate the laser beam at radio frequency, which is detectable electronically and is large compared to the width of the investigated atomic levels. High frequencies are especially attractive for two reasons. First, if the side-bands are widely separated (by a few Doppler-free linewidths) the spectral lines can be probed by a single side-band. Second, the laser amplitude and phase noise are smaller in the rf regime thus heterodyne detection improves the signal to noise ratio, offering highly sensitive signal detection.

The probe and the side-bands beat at the fast photo-detector. When the modulated signal is distorted by the resonance feature, the absorption and dispersion spectra can be extracted from the phase and amplitude of the rf heterodyne beat signal. At the resonance the frequency modulated probe beam is balanced as a pair of n^{th} order side-bands have equal amplitudes, but opposite phase and simply cancel out. Off-resonance the balance is disturbed as the side-bands have unequal amplitudes leading to an non-vanishing sinusoidal signal with a Lorentzian absorption or dispersion shape. The amplitude and phase of the beat note signal Sig_{FM} depend on the frequency detuning

Δ (Shirley, 1982):

$$\begin{aligned} Sig_{FM}(\Delta,t) = & \frac{C}{\sqrt{\Gamma^2+{\omega_m}^2}} \sum_{n=-\infty}^{+\infty} J_n(\delta)J_{n-1}(\delta) \\ & \times [(L_{(n+1)/2} + L_{(n-2)/2})\cos(\omega_m t+\phi) \\ & + (D_{(n+1)/2} - (D_{(n-2)/2})\sin(\omega_m t+\phi)], \end{aligned} \tag{4.4}$$

where ϕ is the detector phase with respect to the modulation applied to the laser beam and

$$L_n = \frac{\Gamma}{\Gamma^2+(\Delta-n\omega_m)^2} \quad \text{and} \quad D_n = \frac{\Gamma(\Delta-n\omega_m)}{\Gamma^2+(\Delta-n\omega_m)^2}. \tag{4.5}$$

The L_n and D_n are known as absorptive and dispersive Lorentians respectively and Γ is the natural linewidth. The constant C represents all other properties of the medium and radiation such as laser field amplitudes or electric dipole moments and other physical properties.

The modulation of the laser beam in the case of semiconductor lasers can be either done internally, by modulation of the diode current, or externally by means of optical modulators such as acousto-optic or electro-optic modulator (EOM). The former are typically used for amplitude modulation while the latter for phase modulation. For the locking of the 780nm laser in the two-photon transition scheme, we employ EOM to modulate a portion of the beam, which allows to leave the main beam unaffected. This method allows one to achieve relatively small modulation indices, usually $\delta < 1$ and taking into consideration that modulation transfer occurs for frequencies $\omega_c \pm \omega_m$ and $\omega_c \pm \omega_m/2$, only first order sidebands are considered. Eq. (4.4) simplifies to:

$$\begin{aligned} Sig_{FM}(\Delta,t) = & \frac{C}{\sqrt{\Gamma^2+{\omega_m}^2}} J_0(\delta)J_1(\delta) \\ & \times [(L_{-1} - L_{-1/2} + L_{1/2} - L_1)\cos(\omega_m t+\phi) \\ & + (D_1 - D_{1/2} - D_{-1/2} + D_{-1})\sin(\omega_m t+\phi)]. \end{aligned} \tag{4.6}$$

The signal produced by the fast photo-detector needs to be demodulated. The demodulation is done electronically and is carried out in a *lock-in amplifier*. This is an amplifier which responds only to the part of the input signal which occurs at the

supplied reference frequency with a fixed phase while the rest of the signal is averaged to zero. This is done in a process called frequency *mixing* mathematically corresponding to multiplication of the input signal by the reference signal. Here, the signal from the photo-detector described by Eq. (4.6) is multiplied by $\cos(\omega_m t + \Phi)$ and applying simple trigonometric identities, the output of the frequency mixer can be written as:

$$\begin{aligned} Sig_{mixer}(\Delta, t) = A(\Delta)cos(\Phi') - B(\Delta)\sin(\Phi') + N(t)\cos(\omega_m t + \Phi) \\ + A(\Delta)\cos(2\omega_m t + \Phi'') + B(\Delta)\sin(2\omega_m t + \Phi''), \end{aligned} \tag{4.7}$$

where $N(t)$ describes noise and Φ' and Φ'' are resultant phases. The last step is to time average the above equation using a low-pass frequency filter[9]. The time dependent parts in the Eq. (4.7), the two terms oscillating at $2\omega_m$ and the noise term, will be removed by the filtering. The frequency mixing and filtering produces a demodulated signal of the form:

$$Sig_{demodulated}(\Delta, t) = A(\Delta)\cos(\Phi') - B(\Delta)\sin(\Phi') \tag{4.8}$$

which is known as the error signal. The signal consists of two components: the in-phase term described by the cosine element and the quadrature term described by the sine. By changing the phase of the lock-in amplifier, either of the terms can be recovered or a weighted sum of both components can be created for the desired optimisation of the error signal. The experimental implementation of the above technique is presented in the next section

4.3.3 780nm laser frequency stabilisation system

Fig. 4.8 shows the experimental set-up for the frequency stabilisation of the lasers used in the two-photon excitation scheme adapted from McCarron *et al.* (2008) and Abel *et al.* (2009). The red highlighted area represents the modulation transfer spectroscopy which is a part of the locking scheme used to stabilize the 780 nm laser. The red light is provided by the diode laser operating in extended cavity, which gives an output power

[9] A low-pass filter is an electronic device which allows signals with low frequency to pass and attenuates signals at frequencies higher than a corner frequency.

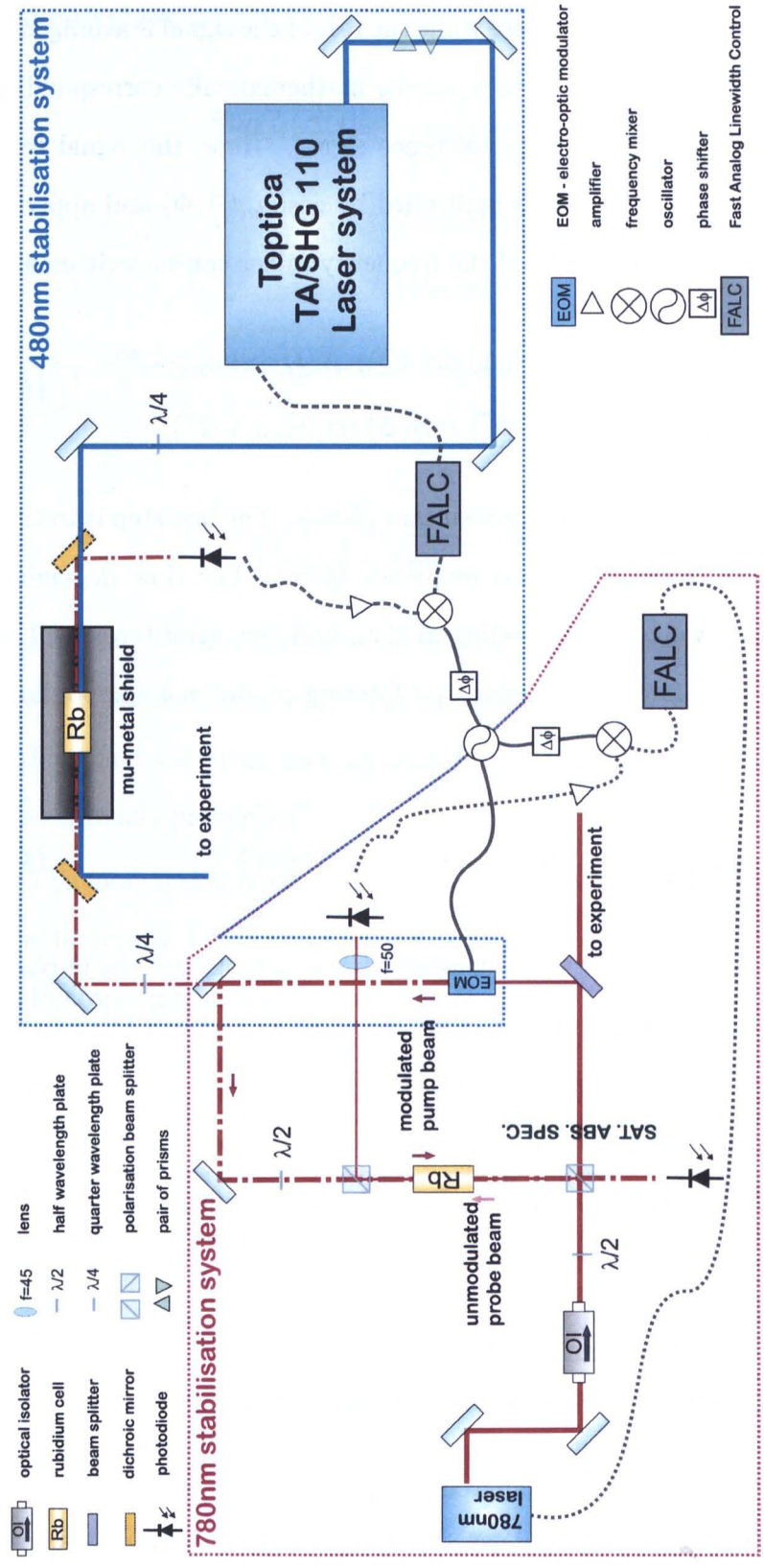

Figure 4.8: Experimental realisation of the laser stabilisation system for the two-photon excitation scheme using frequency modulation technique. The reference signal for the locking of 780 nm laser is obtained using MTS technique and for the 480 nm the EIT signal is exploited. The dashed red line represents frequency modulated red laser beam and the gray solid and dashed lines indicate cable connections.

of 30 mW. In the standard operation mode a beam of power 12.5 mW passes through the optical isolator (to prevent back-reflection to the diode) and is split on a polarizing beam splitter into probe and pump beams. The pump beam is further divided on a 20%/80% optical glass beam splitter to provide an unmodulated beam which can be

used in the experiment. The power ratio between the pump and the probe is adjusted to achieve a high amplitude error signal without power broadening. Typically the power of the probe beam is of order 0.9 mW and the pump beam 0.2 mW.

The pump beam is phase modulated at 9.8 MHz using an EOM-01 Photonics Technologies electro-optic modulator driven by a TG-120 function generator manufactured by Thurlby Thandar. The EOM consists of a nonlinear crystal, lithium niobate ($LiNbO_3$), mounted between two electrodes. Supplying a voltage to the electrodes modifies the refractive index of the crystal and thus the phase delay of the laser beam propagating through it. Controlling the strength of the electric field the power ratio between the carrier and the side-bands can be adjusted. In the experiment the ratio is adjusted so that only first order side-bands are generated. After modulation, the pump beam is further split into two components, one used in the MTS scheme and the other in the EIT scheme (see Section 4.4). In the MTS set-up, the modulated pump and the unmodulated probe beam are counter-propagated through the 10 cm long rubidium cell and aligned colinearly. After passing the cell the probe beam is focused onto a fast photo-diode, ET-2030A from Electro-Optics Technology. Additionally, the pump beam is detected by a pre-amplified photo-diode built in the Electronics Workshop, providing a saturated absorption signal for monitoring purposes. Fig. 4.9 (a) shows traces of saturated absorption of $^{85}Rb\ F = 3 \rightarrow F'$ and $^{87}Rb\ F = 2 \rightarrow F'$ recorded by the detection of the pump (blue) and the probe (pink) beams. As the pump and the probe have similar intensities, the peaks of hyperfine structure exhibit power broadening.

To obtain the error signal, the modulation transfer signal is first amplified using a low noise voltage controlled amplifier ZFL-500LN-BNC+ (Mini-Circuits), which gives a gain of about 30 dB at 14 V, and then sent to the RF input of the double balanced frequency mixer (DBM) ZAD-6+ (Mini-Circuits). The LO input (local oscillator) is fed with the reference signal. The output of the TG-120 unit is split to drive the EOM and further divided using a 50 Ω power splitter to provide reference signals for two DBM's. The phase of the reference signal can be adjusted either by altering the length of the cables connecting DBM and the function generator or by using voltage variable phase shifter JSPHS-12+ (Mini-Circuits).

The output signal of the mixer is sent to FALC (fast analog linewidth controller) a

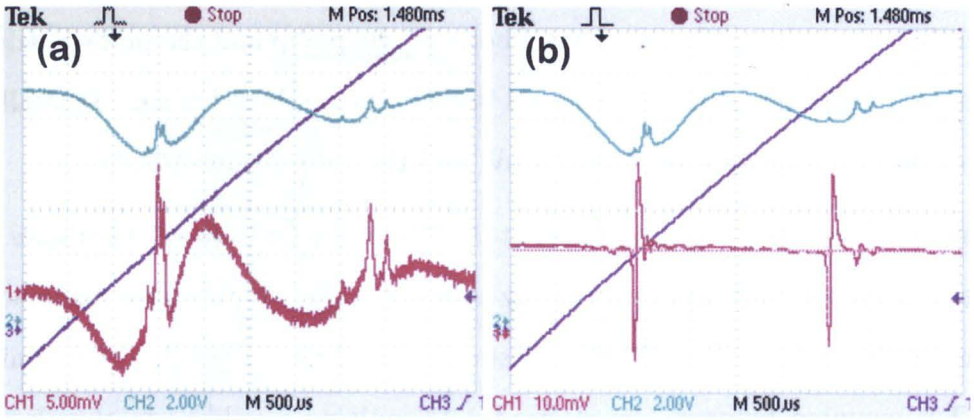

Figure 4.9: Piezo scan over ^{85}Rb $F = 3 \rightarrow F'$ and ^{87}Rb $F = 2 \rightarrow F'$ (a) saturated absorption spectra recorded by the detection of the pump (blue) and the probe (pink) beams, (b) corresponding error signal obtained using MTS. The purple line is the voltage applied to piezo-electric transducer.

commercial servo amplifier unit manufactured by Toptica. We use model FALC 110. A schematic diagram of FALC is shown in Fig. 4.10. Within the unit the signal is amplified and split into two regulator branches: a fast circuit branch which is used to control the diode current, and a slow unlimited integrator branch for correction of the PZT signal to compensate for the slow drifts. The fast section consist of three lag-lead filters and one lead-lag filter connected in series, which are active loop low- and high-pass filters respectively. The response of the loop filter is matched to the phase input. Extra Slow Limited Integrator (XSLI) covers the lowest frequencies and enables adjusting of the corner frequency in a range 0.9 Hz-90 Hz yielding gain of 26 dB. Slow Limited Integrator (SLI) covers the frequencies range 11 Hz-5 kHz with a gain of 36 dB, and the high frequencies are controlled by Fast Limited Integrator (FLI) between 1.4 kHz and 650 kHz and attenuation 15 dB. The lead lag filter - Fast Limited Differentiator (FLD) covers the highest frequencies with the upper corner frequency operating between 100 kHz-4.8 MHz and attenuation 15 dB. Each of the filters offers a flat response option as well. The Unlimited Integrator branch consists of a slow integrating amplifier and integration speed selector. There is no extra low-pass filter in our experimental set-up, thus the demodulation is done by frequency mixer in connection with FALC.

The four stages of error signal generation for ^{85}Rb $F = 3 \rightarrow F'$ transition are presented in the Fig. 4.11. The noisy output of the frequency mixer (averaged 4 times)

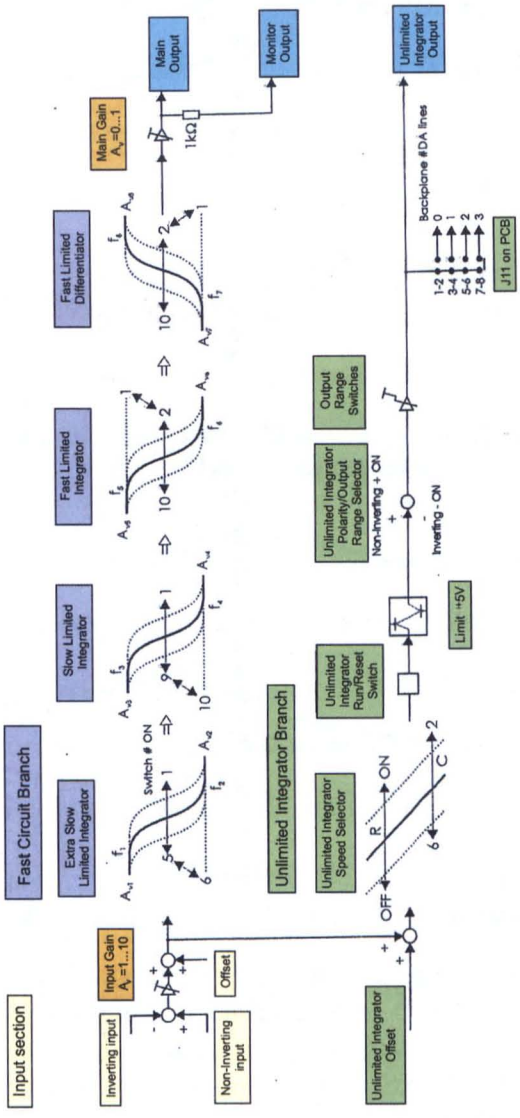

Figure 4.10: Block diagram of FALC 110 adapted from Photonics (2007).

is presented in part (a), the signal has amplitude about 12 mV V_{pp} when it reaches the non-inverted input of the FALC. Scans (b-d) show the monitor output of the FALC with different filters settings and with low main gain (MG=0.1). Trace (b) is a single scan recorded with flat response of all filters (settings: SLI=10, FLD=1, FLI=1, XSLI=6), thus the amplitude of the signal decreases significantly, as there is no gain due to filtering and the signal is attenuated. The single trace (c) shows the error signal generated for optimized FALC settings (SLI=1, FLD=1, FLI=6, XSLI=6) used for frequency locking. The signal is amplified about 50 times due to the filtering. The peak-to-peak amplitude of the error signal can be increased by adjusting the main gain of the FALC, however if the gain is too high the signal can oscillate. In our

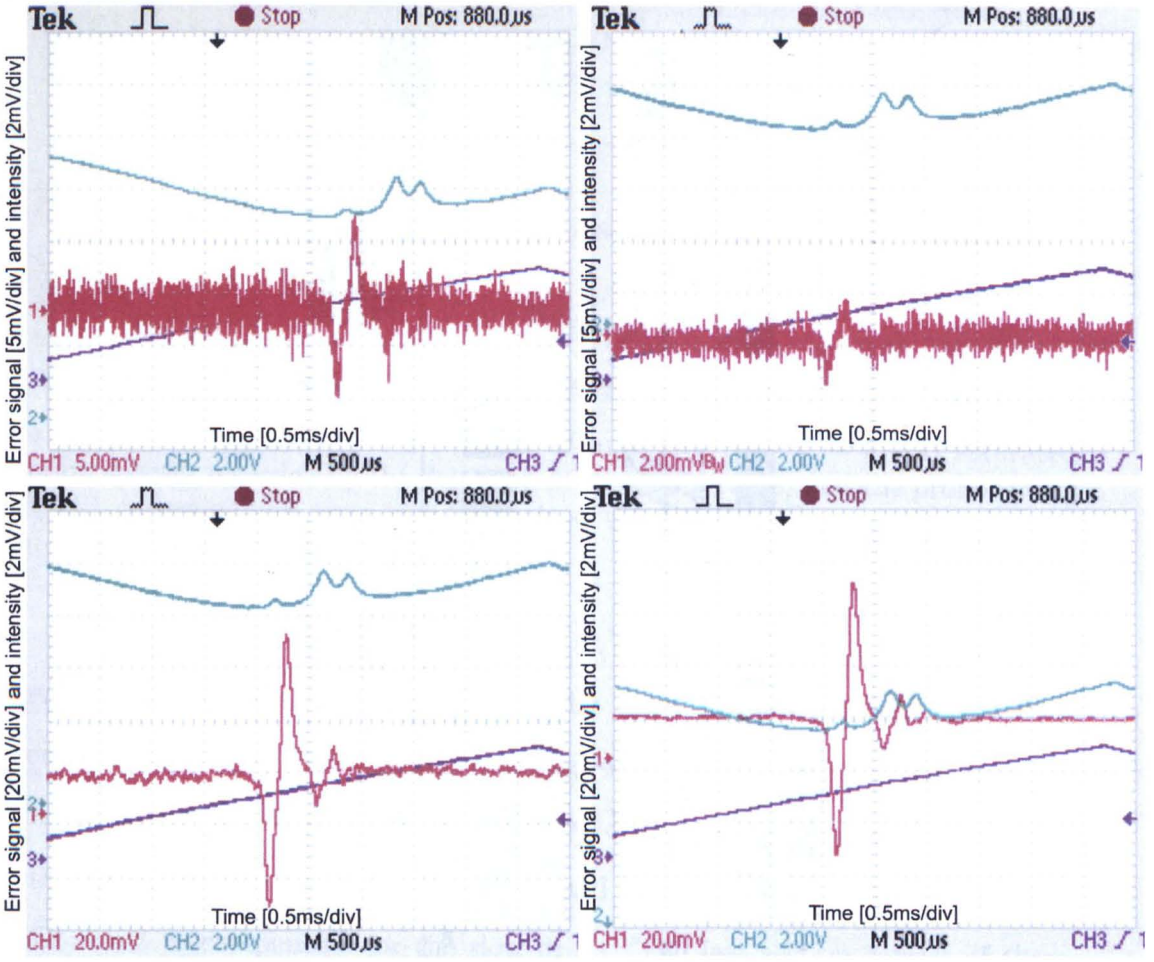

Figure 4.11: Typical traces obtained during different stages of the error signal generation (pink colour) for $^{85}RbF = 3 \rightarrow F'$ transition using MTS technique:(a) output of the frequency mixer (averaged 4 times), (b-d) monitor output of the FALC: (b) filters off: SLI=10, FLD=1, FLI=1, XSLI=6 (single scan), (c) filters on: SLI=1, FLD=1, FLI=6, XSLI=6 (single scan), (d) error signal overlapped with the saturated absorption spectrum (blue colour) (averaged 4 times). The purple line represents the scan of the PZT.

set-up we adjust parameters to get the error signals with amplitude about 50-100 mV. Typically the gradient we achieve is 5 mV/MHz. The last figure (d) contains the error signal averaged 4 times overlapped with the error signal of the saturated absorption spectrum recorded with the control photo-diode. One can notice that the center of the absorption peak overlaps well with the zero level of the signal, thus enabling good locking to the top of the peak.

Another important feature of the error signals obtained with the MTS is that the signal is not proportional to the intensity of the detected peaks like in case of SAS. The highest amplitude has a feature corresponding to the ^{85}Rb $F = 3 \rightarrow F' = 4$ transition. This is because the signal is always stronger for closed transitions, however, if desired,

the locking to the cross-over peaks can be achieved. To do this the error signal can be amplified and the phase has to be re-adjusted. The 780 nm laser locked using MTS technique presented above stays stable for hours.

4.4 Laser frequency stabilisation using EIT signal

The stabilisation of the blue laser used in the two-photon excitation scheme operating at 480 nm becomes more complicated as for rubidium atoms there is a lack of transitions from the ground state available at this wavelength which could be used for obtaining the error signal. One of the solution is to use a frequency comb[10] or a reference cavity. The first method is extremely complex and expensive, whilst the stability of the cavity is influenced by various environmental factors limiting the stability of the laser. In 2008 a new technique for laser stabilisation to an excited state was proposed by the group from Durham (Abel *et al.*, 2009). This method exploits the phenomenon known as the electromagnetically induced transparency in a cascade system. They used a reference atomic vapour cell at room temperature to generate the error signal. This scheme allows the frequency locking to any excited Rydberg state, even in the absence of a strong transition. In the next section, the EIT phenomenon is explained and the experimental implementation of the EIT-based technique in our experimental set-up is presented in Section 4.4.2.

4.4.1 Electromagnetically Induced Transparency

Electromagnetically induced transparency (EIT) is a phenomenon whereby the effect of the medium on resonant light is modified in the presence of a second resonant light source, due to quantum interference between possible excitation paths of an atom. In order to describe EIT, the atom-light interaction of a two-level atom presented in Section 3.1.1 has to be extended to the case of a three-level system interacting with two resonant light fields.

Fig. 4.12 (a) shows a three-level cascade system with a ground state $|1\rangle$, interme-

[10] An optical frequency comb is a technique which exploits short laser pulses to mimic a regularly spaced series of different frequencies. With ultra-short pulses the entire visible spectrum can be covered, generating a âĂIJcombâĂİ of coloured lines on a traditional spectrometer.

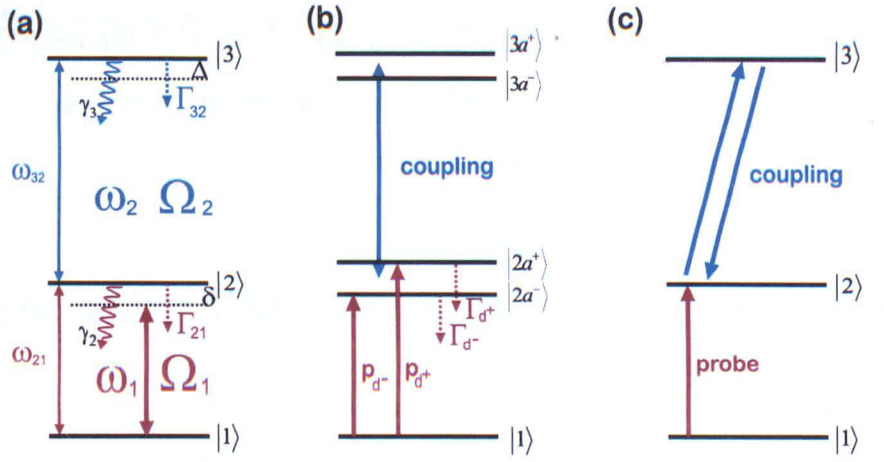

Figure 4.12: Electromagnetically induced transparency in a cascade system: (a) Energy scheme of a three-lever atom in a cascade system interacting with probe Ω_1 and coupling Ω_2 laser fields with detuning δ and Δ, decay rates from states $|2\rangle \rightarrow |1\rangle$ and $|3\rangle \rightarrow |2\rangle$ given by Γ_{21} and Γ_{32} respectively and γ_2, γ_3 representing all other dephasing of levels $|2\rangle$ and $|3\rangle$. (b) coherent coupling of the state $|2\rangle$ to stable state $|3\rangle$ generates dressed states $|na^{\pm}\rangle$, the interference of the decay channels of state $|2^{\pm}\rangle$ leads to cancellation of absorption. (c) interference between pathways of excitation of state $|2\rangle$.

diate state $|2\rangle$ and excited state $|3\rangle$, where the direct transition $|1\rangle \rightarrow |3\rangle$ is dipole forbidden. The system is interacting with two resonant laser fields: the weak probe beam, characterized by the parameters ω_1 and Ω_1, and the strong coupling beam with ω_2, Ω_2. The detuning of the lasers from the transitions $|1\rangle \rightarrow |2\rangle$ and $|2\rangle \rightarrow |3\rangle$ are given by $\delta = \omega_{21} - \omega_1$ and $\Delta = \omega_{32} - \omega_2$ respectively. If the probe is tuned to the atomic resonance, the optical response of the medium is the same as in the two-level system and the atoms will absorb the radiation. However, in the presence of the strong coupling beam, the atomic eigenenergies are shifted (Fig. 4.12 (b)). The new eigenstates $|2a^{\pm}\rangle$ decay to the same continuum and the destructive interference of the decay channels leads to the cancellation of the absorption of the probe beam. This phenomenon was proposed independently by Kocharovskaya and Khanin (1988) and Harris (1989) and observed experimentally by the latter group in strontium atoms (Boller *et al.*, 1991). Boller in his paper pointed out that there is also a second mechanism which can explain cancellation of absorption, mainly that the contribution to the linear susceptibility[11] due to two resonant fields is equal in magnitude but opposite in sign which

[11]The response of a dielectric (here atoms of the medium) to an external electric field is expressed as the electric polarisation $\mathbf{P}$ and is given by $\mathbf{P} = \epsilon_0 \chi(\omega)\mathbf{E}$. $\chi(\omega)$ is a constant of proportionality and is called susceptibility. The first order susceptibility $\chi^{(1)}$ describes the linear response of an atom to the resonant light. It is a complex number of which the imaginary part determines the dissipation of the light by atoms (absorption) while its real part determines the refractive index

leads to the cancellation of the response of the probe beam at zero-field resonance. The equivalent description (Fleischhauer *et al.*, 2005) is presented in Fig. 4.12 (c). State $|2\rangle$ can be excited via two pathways the direct one $|1\rangle \rightarrow |2\rangle$ and the indirect route $|1\rangle \rightarrow |2\rangle \rightarrow |3\rangle \rightarrow |2\rangle$. As the coupling beam has higher intensity than the probe, the probability amplitude of both pathways is equal in magnitude but opposite in signs leading to cancellation.

In Fleischhauer *et al.* (2005) the interaction Hamiltonian for a three-level cascade system is of form:

$$H_{Int}^{RWA} = -\frac{\hbar}{2}\begin{pmatrix} 0 & \Omega_{12} & 0 \\ \Omega_{12} & -2\delta & \Omega_{23} \\ 0 & \Omega_{23} & -2(\Delta+\delta) \end{pmatrix}. \tag{4.9}$$

The 2x2 part of the matrix in the top left corner refers to the probe beam transition alike in a two-level system and the rest of the matrix components represent the energy of the state $|3\rangle$ and the coupling of states $|2\rangle$ and $|3\rangle$. The eigenstates can be expressed in terms of mixing angles θ and ϕ which for the two-photon resonance ($\delta = \Delta$ are defined as $\tan\theta = {}^{\Omega_1}/_{\Omega_2}$, $\tan 2\phi = \frac{\sqrt{\Omega_1^2+\Omega_2^2}}{\delta}$. Thus the three eigenstates are (Fleischhauer *et al.*, 2005)

$$\begin{aligned} |a^+\rangle &= \sin\theta\sin\phi|1\rangle + \cos\phi|2\rangle + \cos\theta\sin\phi|3\rangle \\ |a^0\rangle &= \cos\theta|1\rangle - \sin\theta|3\rangle \\ |a^-\rangle &= \sin\theta\cos\phi|1\rangle - \sin\phi|2\rangle + \cos\theta\cos\phi|3\rangle, \end{aligned} \tag{4.10}$$

where states $|a^\pm\rangle$ are shifted up and down by an amount $\Delta E^\pm = \frac{\hbar}{2}(\delta \pm \sqrt{\delta^2+\Omega_1^2+\Omega_2^2})$. Since there is a lack of the component of the state $|2\rangle$ in the state $|a^0\rangle$, if the atom is prepared in $|a^0\rangle$ there is no possibility of excitation to the state $|2\rangle$ and subsequent spontaneous emission is suppressed: this state is called a *dark state*. In the case of a weak probe beam, $\Omega_1 \ll \Omega_2$ and $\theta \rightarrow 0$, thus the ground state $|1\rangle$ becomes the dark state and the population is trapped in state $|1\rangle$ or $|3\rangle$. To determine how much these states are populated one needs to solve OBE equations for a three-level system (Section 3.1.1). As seen in Section 3.1.1 OBE can be derived from Eq. (3.16), however

the decay rates and the dephasing should be included by adding the decay matrix $\hat{\Gamma}(\rho)$, leading to

$$\frac{d\rho(t)}{dt} = -\frac{i}{\hbar}[\hat{H}, \rho] + \hat{\Gamma}(\rho). \tag{4.11}$$

The decay matrix has the form:

$$\Gamma(\rho) = \begin{pmatrix} \Gamma_{21}\rho_{12} & -\frac{\Gamma_{21}+\gamma_2}{2}\rho_{12} & -\frac{\gamma_3}{2}\rho_{13} \\ -\frac{\Gamma_{21}+\gamma_2}{2}\rho_{21} & -\Gamma_{21}\rho_{21} & -\frac{\Gamma_{21}+\gamma_2+\gamma_3}{2}\rho_{23} \\ -\frac{\gamma_3}{2}\rho_{31} & -\frac{\Gamma_{21}+\gamma_2+\gamma_3}{2}\rho_{32} & 0 \end{pmatrix}, \tag{4.12}$$

where Γ_{21} is the usual D2 linewidth, $\gamma_{1,2,3}$ represents the dephasing of level 1,2 and 3 and the lifetime of the Rydberg state has been neglected (Fleischhauer *et al.*, 2005). From the evolution of the density matrix six OBE for the populations and coherences can be derived, which can be found in the literature (i.e. (Loudon, 1973)). Solving these OBE equations for the steady state ($d\rho/dt = 0$) and assuming that populations of states $|2\rangle$ and $|3\rangle$ are negligible ($\rho_{11} = 1$, $\rho_{22} = 0$, $\rho_{33} = 0$), the coherence $\tilde{\rho}_{12}$ can be found (Gea-Banacloche *et al.*, 1995):

$$\tilde{\rho}_{12} \simeq \frac{i\Omega_1}{\Gamma_{12} - 2i\delta + \frac{\Omega_2^2}{\gamma_3 - 2i(\Delta+\delta)}}. \tag{4.13}$$

The off-diagonal elements of the density matrix are related to the atomic dipole moment, which in turn can be used to calculate the polarization of the sample and thus the susceptibility. The probe absorption and dispersion are proportional to $Im[\tilde{\rho}_{12}]$ and $Re[\tilde{\rho}_{12}]$ respectively. A typical absorption profile of the probe beam propagating through rubidium vapour at room temperature with frequency scanned around ^{85}Rb $F = 3 \rightarrow F'$ transition, recorded in the presence of strong coupling field tuned to $30D_{5/2}$ transition, is presented in Fig. 4.13. The characteristic dip in the absorption profile is the EIT feature. The EIT signal can be exploited to stabilize the frequency of the coupling laser, which will be discussed in the next section.

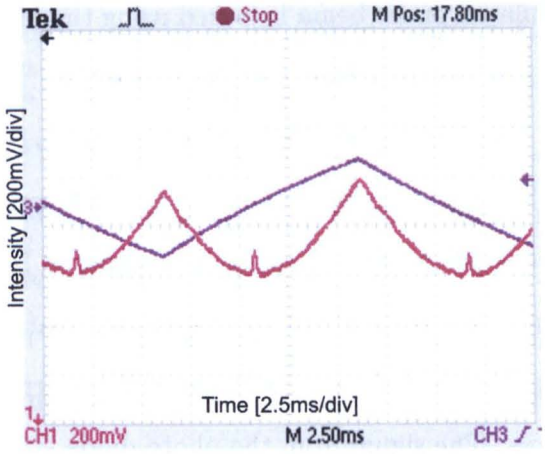

Figure 4.13: Oscilloscope trace of the EIT signal with the blue laser locked to $30D_{5/2}$ transition and the red scanned over ^{85}Rb $F = 3 \rightarrow F'$ transition.

4.4.2 480nm laser frequency stabilisation system

The blue highlighted area in Fig. 4.8 represents the frequency stabilisation system of the Toptica laser, that provides an output at 480 nm which is used in two-photon excitation scheme. The technique was pioneered by Abel *et al.* (2009) and in contrast to other methods of frequency stabilisation it uses a laser at one wavelength λ_p=780 nm to stabilize a second laser operating at a completely different wavelength λ_c=480 nm. It exploits a standard FM method to generate the error signal from an EIT feature as a frequency reference.

The experimental arrangement is as follows: the blue laser light is provided by the TA-DL SHG 110 laser system described in Section 4.2.2. The typical output power is of the order 150-200 mW. The beam is sent through a magnetically shielded rubidium vapour cell where is aligned collinearly with the 780 nm beam, and subsequently reflected on a dichroic mirror to the experiment. The shield is a cylinder shaped can of diameter 12 cm and length 22 cm and has caps at both ends with machined 15 mm holes in the center to allow the laser beams to go through. It is made of mu-metal[12] and attenuates a magnetic field by about 200 times at the center where a 10 cm long glass rubidium vapour cell is mounted. The 780 nm laser beam is taken after modulation with EOM at 9.8 MHz (as used in the MTS set-up). To be consistent with the EIT description this beam will be called the *probe beam* in this section.

[12]Mu-metal is a nickel-iron alloy, which is characterized by high magnetic permeability. It is exploited in shielding against static or low-frequency magnetic fields.

The frequency modulated probe beam is locked using the MTS set-up (described in the Section 4.3.3) to a desired transition, usually it is either $^{85}Rb\ F = 3 \rightarrow F' = 4$ or $^{87}Rb\ F = 2 \rightarrow F' = 3$. The blue laser is scanned across the nD or nS EIT resonance. The EIT feature is probed by the sidebands of the probe beam and the rf heterodyne beat signal of the probe sideband and the carrier is recorded by the fast photo-diode. Similarly, the phase and the amplitude of the registered beat note contain the information about the absorption and dispersion of the EIT feature, which is extracted via the demodulation process. The signal from the photo-diode is first intensified using an amplifier which has low noise at 10 MHz. Again the demodulation is done by employing DBM mixer ZAD-6+ (Mini-Circuits). The LO input (local oscillator) is fed with the portion of the reference signal generated by the TG-120 function generator and the phase of the reference signal is adjusted either by altering the length of the cables or using voltage variable phase shifter JSPHS-12+ (Mini-Circuits). The output of the mixer is fed to the non-inverting input of the FALC unit to complete the demodulation process using its SLI filter.

The four stages of error signal generation for Rydberg state $30S_{1/2}$ are presented in the Fig. 4.14. The probe is locked to the $^{85}RbF = 3 \rightarrow F' = 4$ transition. The averaged output of the frequency mixer is presented in part (a), where the signal has an amplitude about 60 mV V_{pp}. Scan (b) shows the monitor output of the FALC with flat response off all filters (settings: SLI=10, FLD=1, FLI=1, XSLI=6) which results in the signal being attenuated 4 times. Scan (c) presents the demodulated error signal generated for the optimized FALC settings (SLI=1, FLD=1, FLI=6, XSLI=6) used for frequency locking, which is amplified about 30 times due to the filtering. Typically in our set-up we adjust parameters to obtain the error signals with an amplitude about 200-300 mV. The gradient we achieve is 100 mV/MHz. Fig. (d) contains the error signal averaged 4 times, overlapped with the absorption spectrum of the EIT line recorded with the same photo-diode, thus the V_{pp} of the signal is halved due to the signal splitting. One can notice that the center of the absorption peak overlaps exactly with the zero level of the signal thus enabling good locking to the top of the peak. For a comparison scan over the $30D_{5/2}$ line (e) and both $30D_{5/2}$ and $30D_{3/2}$ resonances are presented in (f) revealing the fine structure of the D state. The lines are separated by

about 200 MHz. The $30D_{3/2}$ has lower amplitude, however adjusting FALC settings makes it possible to lock to this state as well.

The above technique is suitable to lock a laser to transitions characterized by small Einstein A-coefficients such as high Rydberg states. The error signal amplitude is proportional to the power of the coupling laser, thus in our set-up we sent the whole available power through the EIT reference cell. This results in high amplitude error signals suitable for locking the laser up to $n = 90$ states. The 480 nm laser locked using the presented above stays stable for hours.

The EIT experiments provide useful tool for the investigation of the properties of Rydberg atoms. Direct non-destructive measurements of Rydberg states can be achieved by analysis of the shape of EIT spectra, which are very sensitive to even small changes in the interaction strength and can be used for coherent optical detection of highly excited states (Mohapatra *et al.*, 2007; Weatherill *et al.*, 2008). A recent proposal of Günter *et al.* (2012) is to exploit interaction induced shifts on Rydberg states and spatially resolve them via EIT resonance, providing a new all optical detection method of individual Rydberg atoms.

We have taken advantage of EIT spectrometry to measure the electric dipole moments for ^{87}Rb $5P_{3/2} \rightarrow nD_{5/2}$ transitions (Piotrowicz *et al.*, 2011). This experiment will be described in detail in the next chapter (Chapter 5). However, by observation of the variation of the position of the EIT feature during data acquisition, it was possible to estimate the stability of the locking of the 480 nm laser. The blue laser stays stable within less than 1 MHz for a few hours (Piotrowicz, 2010).

Summary

In this chapter the laser system for experiments with Rydberg atoms have been described. The laser system employed for cooling the atoms, together with the FM stabilisation technique used to stabilize the cooling and re-pumping laser have been presented. The second part was devoted to the detailed description of the two-photon excitation scheme used in our experiment. The home-built diode laser operating in the external cavity which provides 780 nm light for the first step in the excitation scheme has been described. The stabilisation of this laser is based on FM in connection with

modulation transfer spectroscopy, resulting in a steep gradient error signal perfectly suitable for laser locking being obtained. The advantage of this technique is its insensitivity to the background absorption of atoms, thus providing flat background error signals with zero-crossing, exactly at the top of the reference peak. The laser light for the second transition was delivered by a commercial SHG laser at 480 nm. The FM stabilisation set-up has been built and the reference signal was obtained using EIT spectroscopy. This technique allows us to achieve reference frequencies for excitation of rubidium atoms to n as high as 90.

The laser system described in this chapter for two-photon excitation was proved to work efficiently during experiments involving the measurement of electric dipole moments, which will be presented in the next chapter. The main purpose is to exploit two-photon excitation for deterministic excitation of one Rydberg atom from randomly loaded tightly focused dipole traps to create multi-particle entangled states. An excitation scheme, which exploits the two-photon transition scheme and guarantees the deterministic preparation of a collective excited states of N atoms was proposed recently in Beterov *et al.* (2011).

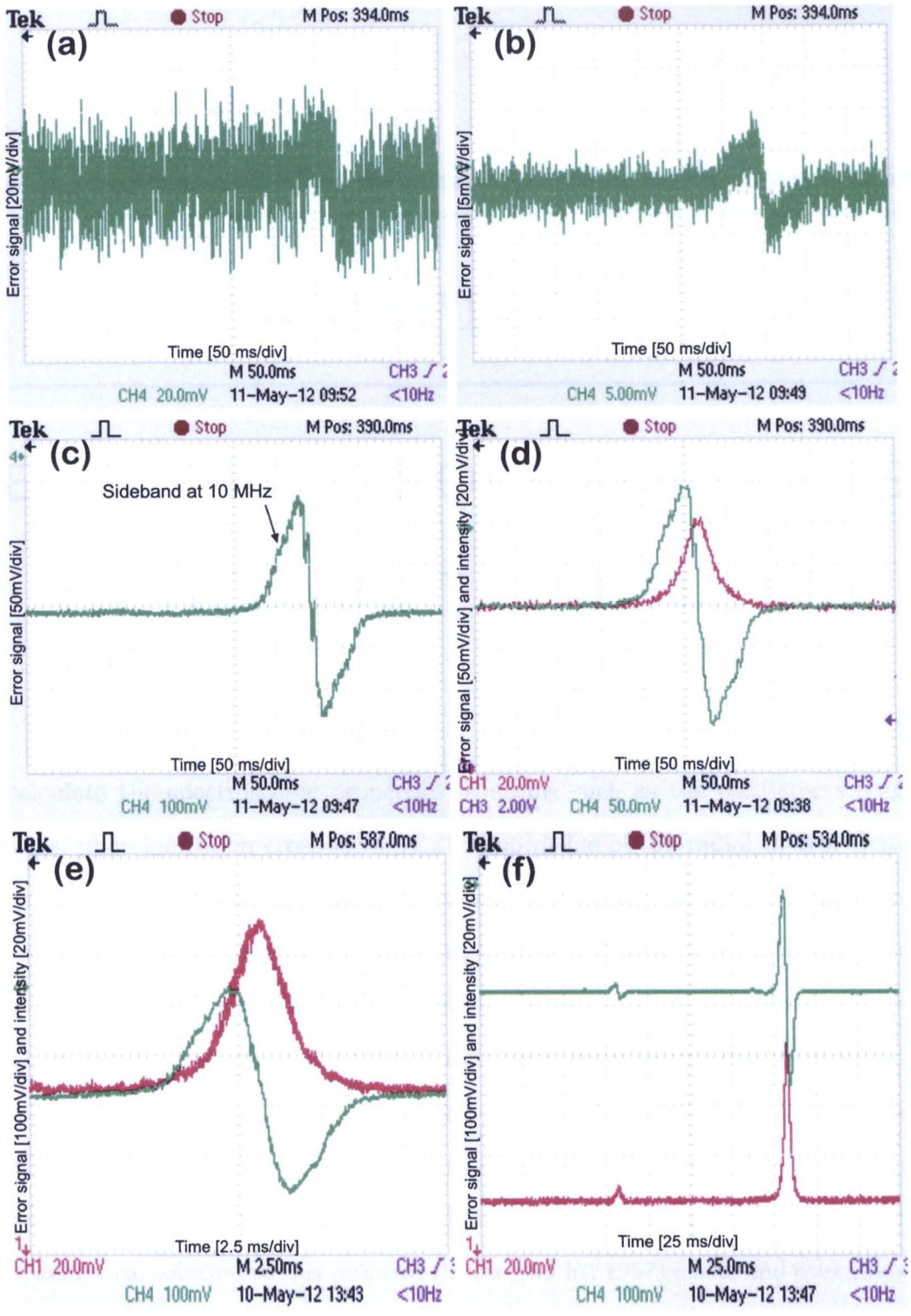

Figure 4.14: Typical traces obtained during different stages of the error signal generation (green colour). The probe was locked to $^{85}Rb\ 5s^2S_{1/2}\ F = 3 \rightarrow F' = 4$ transition. Fig (a-d) the coupling beam was scanned across $30S_{1/2}$ Rydberg state resonance: (a) output of the frequency mixer (averaged 4 times), (b-d) monitor output of the FALC: (b) filters off: SLI=10, FLD=1, FLI=1, XSLI=6 (single scan), (c) filters on: SLI=1, FLD=1, FLI=6, XSLI=6 (single scan), (d) error signal overlapped with the EIT absorption profile (pink trace) (averaged 4 times). The purple line represents the scan of the PZT. (e) the coupling beam was scanned across $30D_{5/2}$ resonance, (f) the fine structure splitting revealed with EIT scan across $30D_{5/2}$ and $30D_{3/2}$ lines.

BLANK PAGE IN ORIGINAL

CHAPTER 5

ELECTRIC DIPOLE MOMENTS OF ATOMIC TRANSITIONS

To calculate the spectroscopic properties of atoms such as the oscillator strengths, lifetimes, photoionization cross-sections, the knowledge of the radial matrix elements of the atomic transitions is required. As it was mentioned in Section 2.2, alkali-metal atoms possess a single valence electron and thus lots of their basic properties can be estimated using analytical formulas existing for hydrogen atom. However, only states with high angular quantum number $l > 4$ and thus small quantum defects exhibit truly hydrogen-like behaviour. Thus the accurate calculation of radial matrix elements for transitions S, P and D states remains a challenging task, because the interaction of the valence electron with the atomic core has to be taken into account. At present no exact analytical solution to this problem (Bethe and E., 1957) exists and over the years many theoretical models for calculation of dipole matrix elements have been developed (Gallagher, 1994; Safronova *et al.*, 2004). However, verification of the models with experiment is very difficult as very few experimental measurements for alkali atoms are available.

In this chapter a method for the direct measurements of electric dipole moments between first excited and Rydberg $nD_{5/2}$ levels of rubidium is presented. The method relying on the spectroscopic observation of the Autler-Townes splitting (Section 5.1.1)

in a cascade system, is presented (Piotrowicz *et al.*, 2011). Section 5.1.1 gives details of this method and describes the experimental set-up. The method used for derivation of the dipole moments from the measured spectra is presented in Section 5.1.2. The results obtained were compared to existing theoretical models and have been found to be in a good agreement with the model by D'yachkov and Pankratov (1994).

The mentioned semi-classical model by D'yachkov and Pankratov (1994) has been used to calculate the radial matrix elements of transitions between S, P, D and F of alkali atoms. Section 5.2 shows numerical calculations of relative matrix elements presented as density plots revealing Cooper minima for rubidium atoms, a remarkable feature of alkali-metal Rydberg atoms that leads to minima in the transition probabilities, oscillator strengths or photo-ionization cross-sections (Bates, 1947; Aymar, 1978; Cooper, 1962).

5.1 Measurements of electric dipole moments

As mentioned earlier, several numerical models for calculations of radial matrix elements exists and it is of great importance to verify them empirically. However, the experimental work in this direction has been lagging behind and, due to the complexity of this task, only few experiments for alkali atoms have been carried out. The oscillator strengths of the lines of the principal series of rubidium (Shabanova and Khlyustalov, 1984), lithium and sodium (Nawaz *et al.*, 1992*b*; Baig *et al.*, 2007; Hussain *et al.*, 2007) and potassium (Nawaz *et al.*, 1992*a*) have been measured, however strong discrepancies between these results and theoretical values have been observed. The indirect confirmation of the quasi-classical theory has been accomplished by measurement of the effective lifetimes of Rydberg states (Marcassa, 2009; Branden *et al.*, 2010), however this method cannot reveal the spectroscopic features of each particular transition. Therefore further experimental verification of the numerical models is necessary. Recently we have measured for the first time the electric dipole moments for Rb $5P_{3/2} \rightarrow nD_{5/2}$ transitions with high accuracy (Piotrowicz *et al.*, 2011).

5.1.1 The method and the experiment

Our method relies on the observation of the EIT spectra and Autler-Townes splitting in a three-level ladder system (Teo *et al.*, 2003; Weatherill *et al.*, 2008), recorded in a sample of ultracold rubidium atoms. The EIT phenomenon has been described in details in Section 4.4.1. The spectra are obtained by measuring the absorption profile of a weak probe laser beam scanned across $5S_{1/2} \rightarrow 5P_{3/2}$ resonance in the presence of a strong coupling laser field tuned to the $5P_{3/2} \rightarrow nD_{5/2}$ transition.

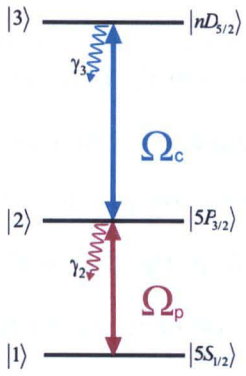

Figure 5.1: Three-level ladder scheme. Ω_c and Ω_p are the Rabi frequencies of the coupling and probe lasers respectively.

A three-level cascade system with energy levels relevant in this experiment is showed in Fig. 5.1. We assume that the long-lived states $|1\rangle$ and $|3\rangle$ are not coupled by electric dipole transition, however they are coupled to a short-lived state $|2\rangle$ by a weak probe and an intense coupling laser fields. Ω_c and Ω_p are the Rabi frequencies associated with these laser fields.

As mentioned in Section 3.1.1, the Rabi frequency characterizes the strength of the coupling between the atoms and the light field. For an atomic transition from state $|1\rangle$ to state $|2\rangle$, with a dipole moment μ_{12} it is given by:

$$\Omega = -\frac{\mu_{12} E_0}{\hbar}. \tag{5.1}$$

The optical intensity I is related to the electric field amplitude E_0 by $I = \frac{c\epsilon_0 n_{ref}}{2}|E_0|^2$, where c is the vacuum velocity of light, ϵ_0 is vacuum permittivity and n_{ref} is the refractive index, The intensity of a Gaussian beam of waist w_0 can be related to its optical power P by relation $I = \frac{2P}{\pi w_0^2}$. Substituting it in Eq. (5.1) the Rabi frequency

Ω can be written as:

$$\Omega = -\mu_{12}\frac{2}{\hbar\sqrt{\pi w_0^2 c\epsilon_0}}\sqrt{P} = a\mu_{12}\sqrt{P}. \tag{5.2}$$

This formula reveals the linear dependence of the Rabi frequency on the square root of the coupling laser power and the coefficient of proportionality is related to the electric dipole moment of the transition. To derive the dipole moments from the gradient of Eq. (5.2) the Rabi frequency for different intensities of coupling laser is measured exploiting the Autler-Townes effect.

If the atoms initially populate state $|1\rangle$ and the coupling laser is tuned to the $|2\rangle$ to $|3\rangle$ resonance, then while scanning the probe laser across $|1\rangle$ to $|2\rangle$ transition on the EIT a dip appears in the absorption profile of the probe beam. As described in the previous chapter, EIT results from the destructive interference between excitation pathways. The width of the transparency dip increases with increasing intensity of the coupling laser until it eventually separates into two individual lines, this effect is known as the Autler-Townes splitting (Autler and Townes, 1955). It originates from the dynamic splitting of the middle energy level due to the strong coupling field and becomes visible when Ω_c is larger then the natural linewidth of the probe transition. By modelling the absorption lineshape and fitting the recorded spectrum the Rabi frequency can by extracted.

The expression for the absorption lineshape of the probe beam is obtained by solving the optical Bloch equations (Sections 3.1.1 and 4.4.1) for the three-level system coupled by two laser fields. The intensity of the probe field is kept in the regime $I_p \ll I_{sat}$, this allows to treat the probe laser as a weak perturbation and set the population of the the two states $|2\rangle$ and $|3\rangle$ to 0. As discussed in Weatherill *et al.* (2008) in this limit, the population of the Rydberg state is negligible, so that any effects arising from level shifts induced by the interaction between Rydberg atoms are insignificant. As a result, the absorption cross-section σ_p for the fixed intensity of the probe laser is given by:

$$\sigma_p = \sigma_0\left[\left((\Gamma + 2i\delta) + \frac{\Omega_c^2}{\gamma_3 + 2i\,(\delta + \Delta)}\right)^{-1} + c.c\right] \tag{5.3}$$

where σ_0 is the cross-section for absorption in the absence of the coupling laser, Γ is

the width of the $|2\rangle$ state, δ and Δ are the detunings of the probe and the coupling beams respectively and γ_3 is the dephasing rate of the $|3\rangle$ state.

In our experiment, state $|1\rangle$ corresponds to the $5S_{1/2}F = 2, m_F = 2$ state, $|2\rangle$ to $5P_{3/2}F = 3, m_F = 3$ and the state $|3\rangle$ to one of the Rydberg states $nD_{5/2}, F = 4, m_F = 4$, where n lies between 20 and 48. The spectra $\sigma_p(\delta)$ are obtained by scanning the frequency of the probe beam around the $|1\rangle \rightarrow |2\rangle$ resonance. Ω_c is determined by fitting the line-shapes to the measured profiles. The dependence of Ω_c on the power of the coupling beam for a variety of Rydberg states was investigated, which allowed us to determine experimentally transition dipole moments of the states in question.

Experiment

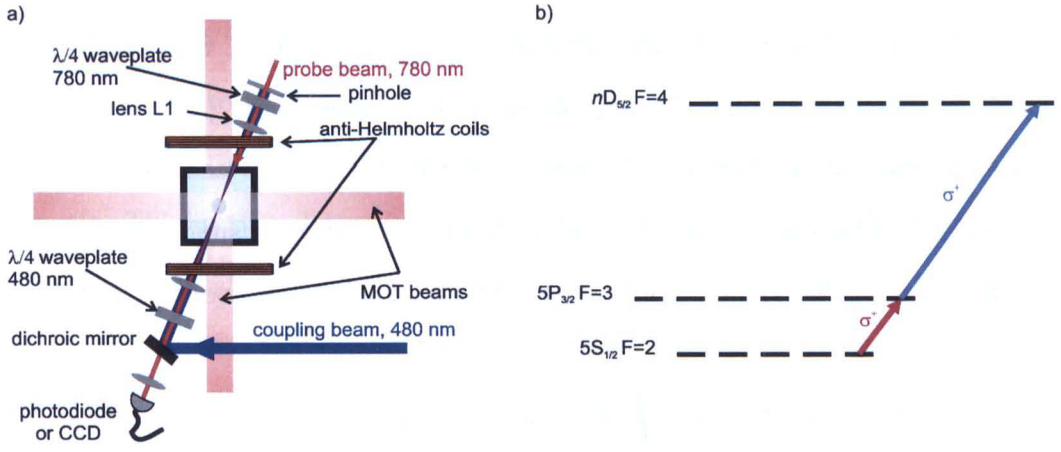

Figure 5.2: Experimental set-up: (a) scheme of the experimental apparatus showing the MOT vacuum chamber as well as the probe and coupling beams arrangement, (b) diagram of the tuning of the probe (red) and coupling laser (blue), showing the $|5S_{1/2}\rangle$, $|5P_{3/2}\rangle$, $|nD_{5/2}\rangle$ states and the hyperfine structure (including magnetic sublevels)

In Fig. 5.2 (a) the scheme of the experimental set-up is presented. The apparatus and the experimental sequence is described in details in Piotrowicz (2010). The ultra-cold sample of atoms was prepared in a standard magneto-optical trap by collecting 3×10^6 atoms from the background vapour and further cooling them in optical molasses which allowed to reach a temperature of 10 μK and a density of 6×10^9 cm^{-3}. The atoms are subsequently illuminated for 1 ms by an intense 480 nm coupling laser and a counter-propagating weak 780 nm probe laser, which are σ^+/σ^+ polarized. Both beams are focused onto the atom cloud in order to maximize its influence on the atomic sample.

Our laser system is not able to resolve the hyperfine structure of nD_j states, thus, in general, we do not have a true three level system. However, as the atoms are initially prepared in $|5S_{1/2}, F = 2, m_F = 2\rangle$ state, by choosing σ^+ polarization for both laser beams, we drive only $\Delta m_F = 1$ transitions, which selects the $nD_{5/2}$ F = 4, $m_F = 4$ sub-level (Fig. 5.2(b)). During this 1 ms the probe beam is swept through the resonance using AOM in a range of 50 MHz. The intensity of the probe was set to $0.012\, I_{sat}$ to minimize the population of state $|2\rangle$. After passing through the sample, the probe beam is imaged by a system of lenses on a photo-diode and recorded on a digital oscilloscope, however the set-up also enables absorption imaging using a CCD camera.

5.1.2 Spectra analysis

To obtain the absorption cross section σ_p, the transmission of the probe beam was recorded in the presence of the atomic sample, I_{sig}, and without the atoms I_0. The transmitted signal, detected by the photo-diode is processed using the Lambert-Beer law, which describes the relation between the concentration of the sample and the amount of light reaching the detector, as the intensity of the transmitted signal decays exponentially (see Section 7.2.2 for more details). The photo-diode signal takes the form:

$$I_{sig}(x, y) = I_0(x, y) \int dx\, dy\, dz \exp(-\sigma_p(x, y) n_{dens}(x, y, z)), \tag{5.4}$$

where n_{dens} is the spatial distribution of atoms. Integrating over z gives the absorption cross section multiplied by the 2-D cloud profile, however the photo-diode records the signal integrated over x and y, thus the obtained signal is:

$$\ln \frac{I_{sig}}{I_0} = -\int \sigma_p(x, y) n_{dens}(x, y)\, dx\, dy. \tag{5.5}$$

Due to the inhomogeneity of the coupling laser and the atomic density distribution, the absorption cross-section is a function of x and y, $\sigma_p(x, y)$. To account for that, the size of the cloud as well as the waist sizes of the coupling beam have been measured using an absorption imaging technique (see Section 7.2.2) and are used as input parameters.

Due to the Gaussian profile of the coupling beam, the Rabi frequency Ω_c is in

general a function of the position as well, thus $\Omega_c \rightarrow \Omega_c(x, y)$. Our method does not allow us to resolve the spatial distribution of the coupling Rabi frequency due to the intensity profile, as it provides an integrated signal and an 'average' cross-section $\sigma_p(\delta)$ across the spatial profile $E(x, y)$ of the coupling laser. Thus the recorded signal is numerically evaluated by considering the contributions from areas of equal intensity and integrating over the beam profile determined using an absorption imaging. By taking into account the spatial profile $E(x, y)$, and therefore $\Omega_c(x, y)$, from each scan a value for Ω_c^{max}, corresponding to the peak value of $E(x, y)$, is extracted.

The first set of data is taken without the coupling beam on. From fitting a Lorentzian profile to the absorption spectrum of the probe beam, initial parameters which characterize $|1\rangle \rightarrow |2\rangle$ transition such as amplitude, Γ and the central frequency are derived. The measured linewidth Γ is about 9 MHz which is much larger than the expected value of 6.065 MHz obtained with high-precision experiments. The observed broadening is due to instrumental limitations. Working with very low probe intensity imposed lowering the bandwidth of the photo-diode to 35 kHz, to improve signal to noise ratio. This in turn determines the width of the observed EIT dip. Nevertheless, the effect of this instrumental broadening on the recorded EIT/AT spectra have been studied. It was found that the fitting procedure we employ do not forge the obtained values of Ω_c. Fig. 5.3 shows exemplary EIT scans averaged using oscilloscope and measured for the upper state $44D_{5/2}$ and $22D_{5/2}$ with fitted lineshapes. The employed method of modelling of the lineshapes well adapts to the measured spectra.

5.1.3 Results

Sets of EIT spectra were recorded for the transitions to the following n states: 20, 22, 26, 28, 30, 35, 37, 40, 44, 48 using the method described above. The measurements were repeated for each n state at different coupling laser powers, ranging from 5 mW to 90 mW. Additionally, for each n the background scan of the $|1\rangle \rightarrow |2\rangle$ transition without coupling laser on was recorded in order to extract initial fitting parameters. Then by modelling the absorption cross-section lineshape using Eq. (5.3), the Ω_c^{max} value was determined as a function of $\sqrt{P}$. Example results obtained for $n = 22$ and $n = 44$ are showed in Fig. 5.4.

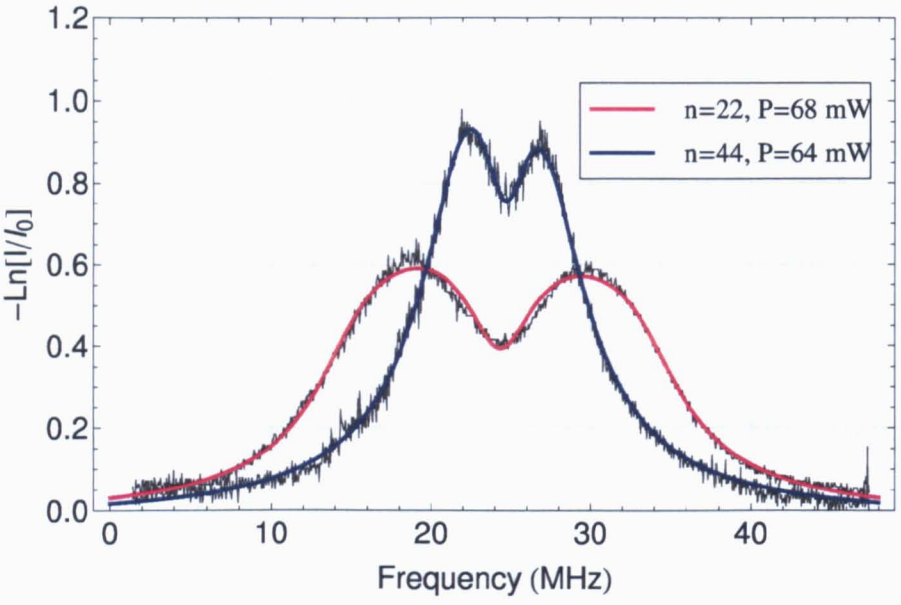

Figure 5.3: Typical AT spectra recorded for the upper state $44D_{5/2}$ and $22D_{5/2}$. Solid lines show the modelling of the lineshape.

This allowed us to obtain a linear trend of Ω_c^{max} against $\sqrt{P}$. Following $\Omega = -\mu_{12}\frac{2}{\hbar\sqrt{\pi w_0^2 c\epsilon_0}}\sqrt{P}$ we were able to extract a value for the dipole moment for each $|5P_{3/2}, F = 3, m_F = 3\rangle \rightarrow |nD_{5/2}, F = 4, m_F = 4\rangle$ transitions for a given n, directly from the gradients. Accurate values of w and P were measured with high precision. The uncertainty on the gradient in Fig. 5.4 is obtained from the statistics of the fitting procedure and is less than 2 % in most cases with a maximum of 4 % for n=44. A good linear trend can be observed, which indicates that the inhomogeneity of the coupling laser has been correctly accounted for. Estimating the uncertainties of the measured dipole moments μ_n involves taking into account the uncertainties on the measurements of w and P, thus the resulting total uncertainty on the measured dipole moments was determined to be of less than 10% for all n.

The reduced matrix elements

As described above, the electric dipole moments of the $|5P_{3/2}, F = 3, m_F = 3\rangle \rightarrow |nD_{5/2}, F = 4, m_F = 4\rangle$ transition were measured, so the matrix element is of the form:

$$\mu^{exp} = \langle 5P_{3/2}, F = 3, m_F = 3|er_q|nD_{5/2}, F = 4, m_F = 4\rangle. \tag{5.6}$$

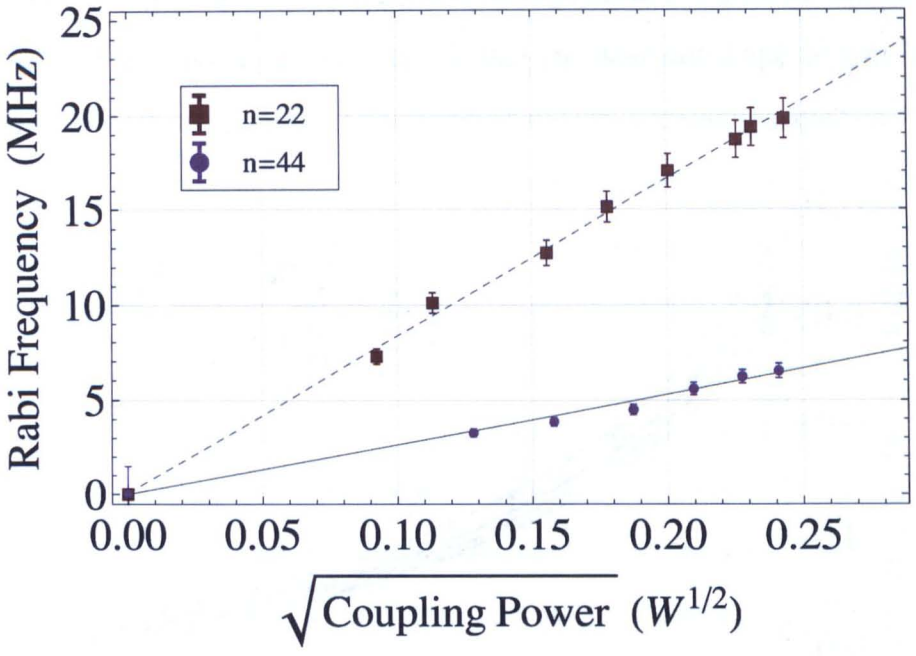

Figure 5.4: The dependence of the Rabi frequency Ω_c on the square root of the coupling power $\sqrt{P}$. Error bars represent the uncertainty in the value of Ω_c obtained from the fit.

To calculate the matrix elements coupling two hyperfine sub-levels one needs to factor out the angular m_F dependence by writing the matrix elements as a product of reduced matrix element and a Wigner three-J symbol related to Clebsch-Gordan coefficient. Using the Wigner-Eckart theorem (Brink and Satchler, 1994):

$$\langle Fm_F|er_q|F'm'_F\rangle = \langle F||e\boldsymbol{r}||F'\rangle\langle Fm_F|F'1m'_Fq\rangle, \tag{5.7}$$

where the double bars indicate the reduced matrix element and $q = 0, \pm 1$ is an index labelling $\boldsymbol{r}$ in the spherical basis. This matrix element can be further simplified by factoring out the F dependence using Wigner six-J symbol, which leads to the final expression:

$$\langle 5P_{3/2}, F, m_F|er_q|nD_{5/2}, F', m'_F\rangle = (-1)^{2F'+J+I+m_F}\sqrt{(2F+1)(2F'+1)(2J+1)} \times \\ \times \begin{Bmatrix} J & J' & 1 \\ F' & F & I \end{Bmatrix} \begin{pmatrix} F' & 1 & F \\ -m'_F & q & m_F \end{pmatrix} \langle 5P_{3/2}||e\boldsymbol{r}||nD_{5/2}\rangle. \tag{5.8}$$

In our case the quantum numbers are: $J = 3/2$, $J' = 5/2$, $F = 3$, $F' = 4$, $I = 3/2$,

$m_F = 3$, $m'_F = 4$ and $q = 1$ which gives an angular coefficient of $\sqrt{\frac{2}{3}}$. In Fig. 5.5 the measured electric dipole moments are therefore plotted, after rescaling using the above procedure as reduced matrix elements representing the $|5P_{3/2}\rangle \rightarrow |nD_{5/2}\rangle$ transition.

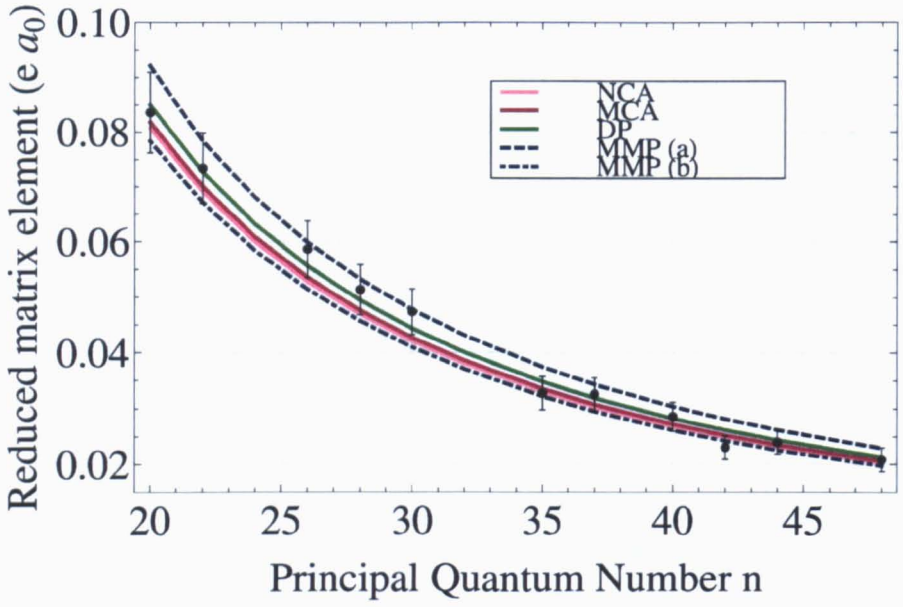

Figure 5.5: Obtained reduced matrix elements μ versus principal quantum number n and their comparison to theoretical models.

Comparison of results to theoretical models

To demonstrate the validity of our measurement method, the experimental results have been compared to existing theoretical models. As already mentioned, although the alkali-metal atoms have a single valence electron, the calculation of the radial matrix elements is complicated. Only the states with small quantum defects can be treated as hydrogen atoms for which analytical solutions are available. For transitions between states with small angular momentum the calculations are challenging due to the interaction of the valence electron with the atomic core. Two methods are commonly used, which allow an approximate calculation of the radial integral. The first group exploits the Coulomb approximation first introduced by (Bates and Damgaard, 1949), which takes advantage of the fact that the Rydberg electron orbits mostly outside the atomic core, where the potential is assumed to be Coulombic. One of the most popular methods is the the Numeric Coulomb Approximation (NCA) (Zimmerman *et al.*, 1979), where the radial wavefunctions are obtained by numerical integration of the

Schrödinger equation with the exact energies of the Rydberg states, using quantum defects as input parameters, and the integration is truncated at the inner core radius. The Modified Coulomb Approximation (MCA) method was developed by Klarsfeld (1989). The radial matrix elements are calculated by extrapolation of the analytical expression of the radial integral, known for the hydrogen atom, to non-integer quantum numbers. Avoiding the numeric integration allows the direct calculation of the radial matrix elements. The calculations in the Coulomb approximation can be simplified further by extension of the quasiclassical approximation to states with low principal quantum numbers. These models have been developed by Kaulakys (1995) and D'yachkov and Pankratov (1994). The second kind of methods is based on the use of the realistic model potentials MMP (Method of Model Potential) . Similarly to the Coulomb approximation the potential outside the atomic core is assumed to be nearly Coulombic, however this method allows to model the change of the potential within the atomic core. The method takes into account the effect of the induced core electron moments on the valence electron and corrections for spin-orbit interaction (Marinescu *et al.*, 1994).

The methods described above (NCA, MCA, DP and MMP) have been used to calculate reduced dipole matrix elements. The quantum defects for rubidium atoms given in Salvat *et al.* (1995) were used, and the energy of $5P_{3/2}$ state was taken from from Sansonetti (2006). Program RADIAL Salvat *et al.* (1995) was used for MMP calculations, which have been performed without (MMP(a)) and with (MMP(b)) correction for core polarization (Bersuker, 1957)

The comparison of these calculations to the measured values is presented in Fig. 5.5. A 'chi-squared' statistical test has been used to estimate the agreement between the models and our results. A good agreement is observed for DP, MCA and NCA models, for which the P-value[1] is 0.97, 0.92 and 0.83, respectively. Whilst MMP calculations without taking into account the ion-core polarization (MMP(a)) result in a P-value of 0.28, a substantial improvement to a P-value of 0.48 can be achieved by including the correction for the core polarization (MMP(b)).

[1] P-value is associated with test statistics and is a calculated probability which is used to verify how well the data are consistent with theoretical predictions, called null hypothesis. Low P-value indicates that the data do not support the null hypothesis.

These results show that the non-relativistic models can be used for calculation of radial matrix elements for transitions involving low-excited and Rydberg states of alkali-metal atoms.

5.2 Cooper minima

While investigating the photo-ionization cross sections from outer atomic shells Cooper (1962) came across an extraordinary property of atoms which was the presence of minima in the distribution of interrogated oscillator strengths, known as *Cooper minima* (Cooper, 1962; Fano and Cooper, 1968). Such remarkable features have been also found in spectral lines of alkali-metal Rydberg atoms. The minima have been reported in photo-ionization cross sections (Aymar, 1978; Msezane and Manson, 1982), emission (Theodosiou, 1980) and absorption (Hudson and Carter, 1967) oscillator strengths of excited Rydberg states. For some transitions such a minimum appears when the dipole matrix element between two states becomes very small, negligible. The matrix element depends on the overlap between the wavefunctions of the initial and final state of the atom. At some n the contributions to the matrix element from positive and negative lobes of wavefunction cancel each other out during integration, thus the minimum appears (Theodosiou, 1980).

As an example of Cooper minima, in Fig. 5.6 the calculated radial matrix elements and their dependence on the principal quantum number n for transitions from state $n = 60$ in rubidium, caesium, potassium and lithium are shown. Sharp minima can be observed in each distribution. The radial matrix elements vanish for the following transitions: $60F \rightarrow 57D$ in rubidium, $60F \rightarrow 19D$ in caesium, $60D \rightarrow 11P$ in potassium and $60P \rightarrow 25S$ transitions in lithium.

5.2.1 Applications

Alkali-metal atoms are nowadays commonly used in laser cooling experiments with Rydberg atoms, thus the understanding of the electronic structure of the atoms is of great importance. Knowing the Cooper minima can be relevant for calculations of lifetimes of Rydberg states, BBR induced photo-ionization rates (Beterov *et al.*, 2009)

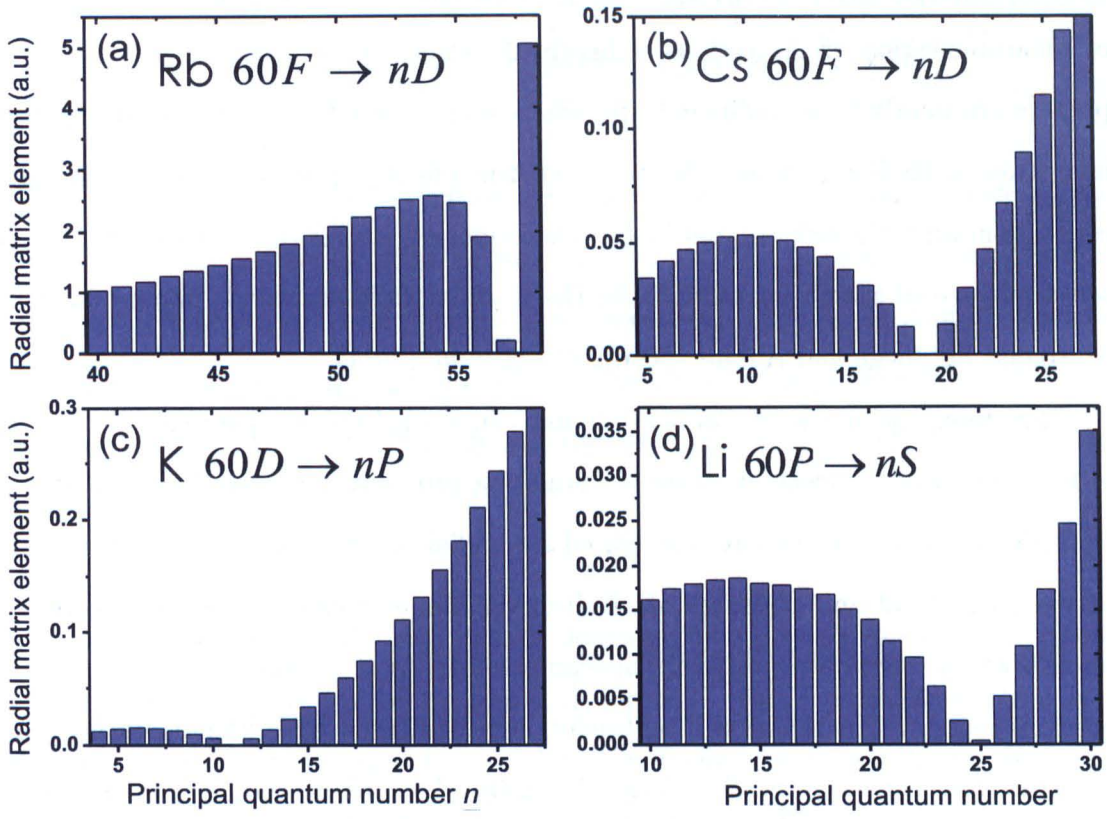

Figure 5.6: The calculated radial matrix elements for bound-bound (a) $60F \rightarrow nD$ transitions in rubidium; (b) $60F \rightarrow nD$ transitions in caesium; (c) $60D \rightarrow nP$ transitions in potassium; (d) $60P \rightarrow nS$ transitions in lithium.

or collisional ionization cross-sections of cold atoms (Amthor *et al.*, 2009).

Informations about the oscillator strengths, transitions probabilities and photo-ionisation cross section are extremely important also from the experimental point of view. A variety of existing theoretical models for the calculation of spectroscopic properties of atoms and molecules can be verified by experiments investigating Cooper minima.

Usually Cooper minima are observed as a suppression of the photo-ionisation cross section (Fano and Cooper, 1968) or a remarkable decrease in the emission oscillator strengths (Theodosiou, 1980). Photo-ionisation spectroscopy plays an important role in many experiments with ultra-cold atoms. For example, the presence of Cooper minimum in the lithium spectrum for transitions $ns \rightarrow n'p$ (Fig. 5.6 (d)) resulted in the suppression of the two-photon photo-ionization of Li atoms to np Rydberg states (Hoogenraad and Noordam, 1998). To avoid this problem, theoretical studies of Cooper minima have been performed and different channels of multi-photon ionisation had

to be found. Also in experiments with far-of-resonance dipole traps the knowledge of photo-ionisation cross sections is highly desirable. Ultra-cold samples are often prepared in tightly focused dipole traps, where very intense laser field can cause photo-ionisation of Rydberg atoms. In most experiments it is important to remove such effect. Knowing Cooper minima in the photo-ionisation cross-section would allow to select a so called *magic-wavelengths* for the trapping light, for which photo-ionisation is avoided Potvliege and Adams (2006); Zhang *et al.* (2011).

Therefore, the maps of Cooper minima can be helpful in spectroscopic studies of Rydberg atoms, especially when investigating processes involving large number of transitions. Therefore, we have calculated the radial matrix elements , for transitions between S, P, D and F states of alkali-metal atoms, using one of the theoretical models which have been positively benchmarked in the experiment described in the previous section. The model will be briefly described below and the numerical results are presented in Section 5.2.3 in form of density plots, where the Cooper minima in bound-bound[2], bound-free[3] and free-free[4] transitions can be observed.

5.2.2 Dyachkov and Pankratov model

The Cooper minima shown in Fig. 5.6 have been calculated using the Dyachkov-Pankratov model. This theory is based on the Coulomb approximation method introduced by Bates and Damgaard (1949), briefly mentioned in Section 5.1.2, which implies that the main contribution to the radial integral comes from the region outside the atomic core where the interaction between the electron and the core is Coulombic. This method originally could not be applied for states of large principal quantum number $n, n' < 20$. Although quasi-classical models developed later for non-hydrogenic case extended the range of n over which this models are valid, they remained restricted only to neighbouring transitions (Davydkin and Zon, 1981). The model derived by D'yachkov and Pankratov (1994) overcomes the $|n' - n| < n$ restrictions, enables extension to

[2]Bound-bound transition is referred to a transition where the initial and final state of the atom is a bound state, the electron absorbs or emits the photon but it is "bound" to the atom.

[3]In a bound-free transition electron absorbs the photon and is ejected out of the atom completely into an unbound state, a continuum state, as a result the atom is ionized atom. Free-bound transition describes the recombination.

[4]In a free-free transition the electron gains or looses the energy by absorbing or emitting a photon as it passes an ion. This process is called Bremsstrahlung (braking radiation).

the bound-free transitions, and provides more accurate values of the wavefunctions of Rydberg and continuum states compared to other semi-classical models.

The formula developed by D'yachkov and Pankratov (1994) is applied for the calculation of the radial matrix elements between $|E, L\rangle$ and $|E', L'\rangle$ states, where E' and E are the energies of the upper and lower states respectively, $E' > E$. To simplify the calculation of the radial integral, an intermediate state with mean energy $E_c = \frac{E+E'}{2}$ was introduced. By the choice of mean value n_c, the formula can be extended to investigate transitions to the continuum states.

Using the DP model the radial matrix elements for the bound-bound, bound-free and free-free transitions can be expressed in terms of relative matrix elements R_{rel} multiplied by appropriate scaling factors. The formula for calculation R_{rel} can be found in Beterov *et al.* (2012); D'yachkov and Pankratov (1994) The radial matrix elements in Fig. 5.6 have been calculated using DP model. They show good agreement with the known Cooper minima in alkali-metal atoms spectra for $nD \rightarrow n'F$ in Cs, $nD \rightarrow n'P$ in K and $60P \rightarrow nS$ in Li (Theodosiou, 1980; Hoogenraad and Noordam, 1998). The validity of this model has been also confirmed by our experimental data on the electric dipole moments measurements in rubidium described in the previous section, and with the results of the experiments investigating photo-ionisation in rubidium (Nadeem and Haq, 2011) and in caesium (Fabry and Cussenot, 1976; Nadeem and Haq, 2010). The DP model fits very well rubidium data, however a discrepancy by a factor of 2 is observed for the data of caesium in the limit of high n. This disagreement can be explained by improper account for the heavy caesium core (Beterov *et al.*, 2012), however the calculations are consistent with the theoretical results of Fabry and Cussenot (1976). Furthermore, the DP model is also consistent with the experimental results on the measurements of lifetimes of Rydberg atoms (Feng *et al.*, 2009; Branden *et al.*, 2010).

Therefore we have concluded that DP model is suitable for the calculations of radial matrix elements.

5.2.3 Maps of the Cooper minima for rubidium

The relative matrix elements $R_{rel}\left(E_nL \rightarrow E_{n'}L'\right)$, $R_{rel}\left(E_nL \rightarrow E'L'\right)$, $R_{rel}\left(EL \rightarrow E'L'\right)$ for transitions between S, P, D and F states of alkali-metal atoms, starting from the ground state, have been calculated using the following equations (Beterov *et al.*, 2012):

$$
\begin{aligned}
R\left(nL \rightarrow n'L'\right) &= \frac{0.4108 \times R_{rel}\left(E_nL \rightarrow E_{n'}L'\right)}{n_{eff}'^{3/2} \times n_{eff}^{3/2} \times \left|E_{n'} - E_n\right|^{5/3}} = \\
&= \frac{0.4108 \times R_{rel}\left(E_nL \rightarrow E_{n'}L'\right)}{\left(-2E_{n'}\right)^{-3/4} \times \left(-2E_n\right)^{-3/4} \times \left|E_{n'} - E_n\right|^{5/3}} \\
R\left(nL \rightarrow E'L'\right) &= \frac{0.4108 \times R_{rel}\left(E_nL \rightarrow E'L'\right)}{n_{eff}^{3/2} \times \left|E' - E_n\right|^{5/3}} = \\
&= \frac{0.4108 \times R_{rel}\left(E_nL \rightarrow E'L'\right)}{\left(-2E_n\right)^{-3/4} \times \left|E' - E_n\right|^{5/3}} \\
R\left(EL \rightarrow E'L'\right) &= \frac{0.4108 \times R_{rel}\left(EL \rightarrow E'L'\right)}{\left|E' - E\right|^{5/3}},
\end{aligned}
\tag{5.9}
$$

where n_{eff} is effective principal quantum number and E_n is the energy of the alkali-metal quantum state. The maps of Cooper minima for all alkali atoms can be found in Beterov *et al.* (2012), here only results obtained for rubidium atoms will be presented, as this element is commonly used in experiments with ultra-cold atoms including ours. The R_{rel} obtained numerically are presented as density plots. The plots are both E- and n-scaled. n-scaling is more suitable to the R_{rel} of bound-bound and bound-free transitions from states with large n. The plots present the absolute values of R_{rel} as the signs of the radial matrix elements are not relevant in the calculation of transition probabilities and photo-ionization cross-sections.

The relative matrix elements $R_{rel}\left(S_{1/2} \rightarrow P_{1/2}\right)$ obtained for rubidium are shown in Fig. 5.7. The horizontal axis indicates the principal quantum number of the nS states, while the vertical axis is the binding energy E' of the continuum P states (in atomic units). For example, from Fig. 5.7(a) one can read out the R_{rel} for a transition from $40S_{1/2}$ state to the continuum $E'P_{1/2}$ state with the $E' = 0.18$, $R_{rel}\left(nS_{1/2} \rightarrow E'P_{1/2}\right) = 0.02$. Using the expression for the binding energy and accounting for the quantum defect (values listed in Table 2.2), the energy of the $40S_{1/2}$ state can be found $E_{40S} = -3.68 \times 10^{-4}$, with given energy difference $\left|E' - E_{40S}\right| = 0.18$ the absolute radial matrix

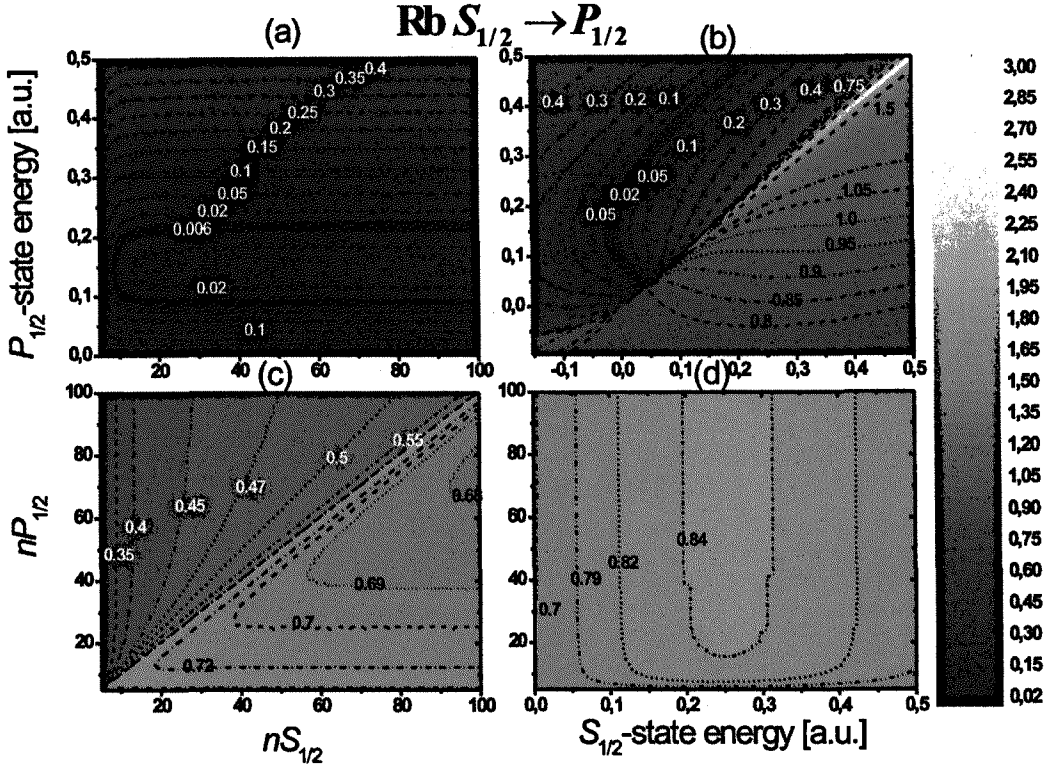

Figure 5.7: Density plots of the relative matrix elements for (a) Rb bound-free $nS_{1/2} \rightarrow E'P_{1/2}$ transitions; (b) arbitrary Rb free-free $ES_{1/2} \rightarrow E'P_{1/2}$ transitions including discrete and continuum spectra; (c) Rb bound-bound $nS_{1/2} \rightarrow n'P_{1/2}$ transitions; (d) Rb bound-free $nP_{1/2} \rightarrow E'S_{1/2}$ transitions.

element can be found from the equations given by Eq. (5.9): $R\left(40S_{1/2} \rightarrow E'P_{1/2}\right) = 6.1 \times 10^{-4}$. The same procedure is applied to the calculation of radial matrix elements for all bound-bound, bound-free and free-free transitions. Cooper minima are highlighted in black, they indicate the regions where $R_{rel}\left(nS_{1/2} \rightarrow E'P_{1/2}\right) < 0.2$. One can observe two sharp Cooper minima at $E' = 0.09$ and $E' = 0.21$ for $n > 10$.

The relative matrix elements for all possible bound-bound, bound-free and free-free $R_{rel}\left(S_{1/2} \rightarrow P_{1/2}\right)$ transitions in rubidium atoms, are plotted in energy scale in Fig. 5.7(b). The binding energy of the S states is given in the horizontal axis while the vertical axis shows the binding energy of P states. Clear sharp Cooper minima can be observed for the bound-free $nS_{1/2} \rightarrow E'P_{1/2}$ and free-free $ES_{1/2} \rightarrow E'P_{1/2}$ transitions in rubidium, especially for the $nS_{1/2}$ states with $E_n > -0.03$ (corresponding to $n > 7$), where the R_{rel} falls below 0.02. The minimum for the lower states is not so pronounced.

In Fig. 5.7(c) the relative matrix elements for bound-bound transitions in rubidium are presented, $R_{rel}\left(E_nP_{1/2} \rightarrow E_{n'}S_{1/2}\right)$. Accurate calculation of the radial matrix

elements from this plot is possible using the same procedure as shown earlier. As one can notice, there is no prominent Cooper minimum in this graph as the R_{rel} do not fall below 0.3. Similarly there is lack of minimum for for bound-free $nP_{1/2} \rightarrow E'S_{1/2}$ transitions in rubidium atoms. The relative matrix elements $R_{rel}\left(nP_{1/2} \rightarrow E'S_{1/2}\right)$ are of order 0.7 or higher and are plotted in Fig. 5.7(d).

Similarly the relative matrix elements for transitions $P_{3/2} \rightarrow D_{5/2}$ and $D_{3/2} \rightarrow F_{5/2}$ in rubidium are presented in Fig. 5.8. Cooper minima are observed for bound-free $nP_{3/2} \rightarrow E'D_{5/2}$ transitions with $E' \approx 0.37$ (Fig. 5.8(a)), free-free $EP_{3/2} \rightarrow E'D_{5/2}$ and $ED_{3/2} \rightarrow F_{5/2}$ transitions (Fig. 5.8(b)), and bound-free $nF_{5/2} \rightarrow E'D_{3/2}$ transitions with $E' \approx 0.17$ (Fig. 5.8(h)). Relative matrix elements for other fine-structure components of the rubidium P and D states are not included as the difference between them is too small to be distinguishable on our density plots.

5.3 Summary

To calculate different spectroscopic properties of Rydberg atoms, such as oscillator strengths, photo-ionisation cross-sections, polarizabilities and radiative lifetimes, the knowledge of radial matrix elements is required. Due to the non-hydrogenic character of alkali-metal atoms, there is no exact analytical solution for this problem. Although many theoretical models have been developed during the years, they require experimental verification, which is difficult to carry out due to the complexity of the required experiments.

In this chapter the first direct measurements of the electric dipole moments for the $5P_{3/2} \rightarrow nD_{5/2}$ transitions to the Rydberg states by investigation of the EIT and AT splitting in ultra-cold rubidium gas were presented. Analysis of the absorption profile of the weak probe beam allowed to extract the Rabi frequency of the probed transition and exploiting its dependence on the square root of the power of coupling laser we obtained the dipole moments. The experimental data have been compared to existing semi-classical theoretical models based on Coulomb approximation and D'yachkov-Pankratov model, and good agreement have been observed (Piotrowicz *et al.*, 2011).

The positively benchmarked DP model has also been used to study the structure of

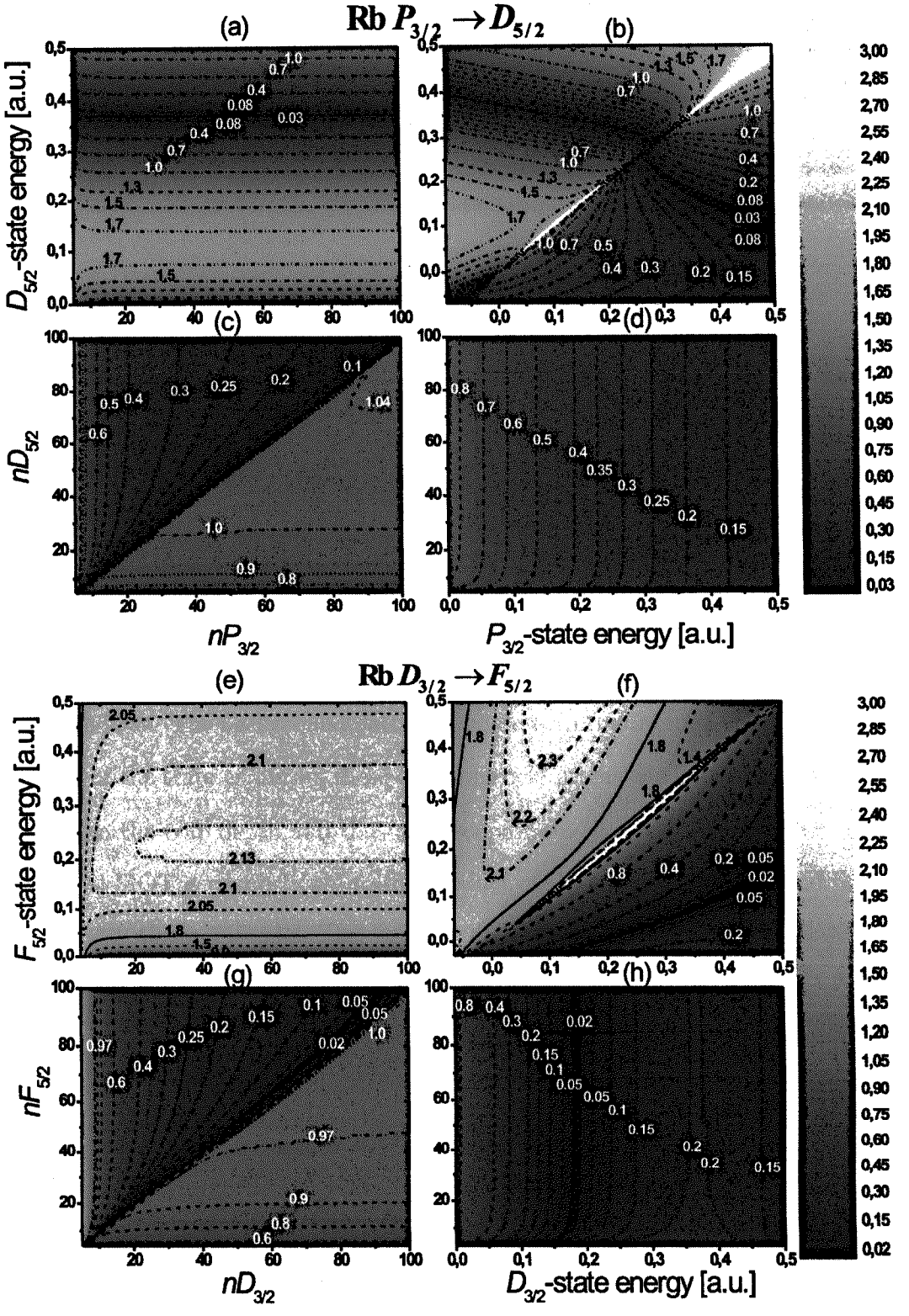

Figure 5.8: Density plots of the relative matrix elements in Rb atoms for (a) bound-free $nP_{3/2} \rightarrow E'D_{5/2}$ transitions; (b) all $EP_{3/2} \rightarrow E'D_{5/2}$ transitions; (c) bound-bound $nP_{3/2} \rightarrow n'D_{5/2}$ transitions; (d) bound-free $nD_{5/2} \rightarrow E'P_{3/2}$ transitions; (e) bound-free $nD_{3/2} \rightarrow E'F_{5/2}$ transitions; (f) all $ED_{3/2} \rightarrow E'F_{5/2}$ transitions; (g) bound-bound $nD_{3/2} \rightarrow n'F_{5/2}$ transitions; (h) bound-free $nF_{5/2} \rightarrow E'D_{3/2}$ transitions.

the Cooper minima in the transition probabilities for low excited nS, nP, nD and nF states of alkali atoms. This model provides reliable and fast calculations of the radial matrix elements for bound-bound, bound-free and free-fee transitions. The results obtained for rubidium atoms have been presented in this chapter. It would be interesting to confirmed calculated Cooper minima experimentally.

CHAPTER 6

NEW VACUUM SYSTEM

The loading dynamics of a MOT are strongly related to the physical conditions of the background gas. The background particles collide with the trapped atoms and can kick them out of the trap, as during these collisions cold atoms can gain energies which are higher than the trap depth and thus can escape from the trap. The number of atoms in a typical MOT is proportional to the product of the trap loading rate and the mean time between these collisions. The number of atoms follows the rate equation:

$$\frac{dN}{dt} = R - \frac{N}{\tau} - \beta_L \int n_{MOT}^2 d^3r, \tag{6.1}$$

where N is the number of atoms in the trap, n_{MOT} is the density inside the MOT, R is the loading rate from the background vapour, τ is the lifetime of atoms in the trap before collisions with the background gas knock them out of the MOT, β_L is the loss rate due to intra-trap two-body inelastic collisions. Therefore, the lifetime of the atoms in the trap depends strongly on the velocity of the background gas particles and thus its pressure. Ideally cold atoms experiments should be carried out in the absence of the background gas thus it is essential to keep the pressure as low as possible. To achieve a storage time of atoms in the trap of order of tens of seconds, the background pressure should be kept at a level of few 10^{-9} Torr or lower (Haubrich *et al.*, 1996). These conditions can be obtained in ultra-high vacuum (UHV) systems.

The experiments presented in Chapter 5 were carried out in an existing vacuum chamber. During the course of this PhD it was necessary to design a new apparatus, that would allow for optical and electrical components to be placed inside the vacuum chamber. This chapter describes the new vacuum system designed and developed at the Open University to investigate the interactions between Rydberg atoms. The observation of the Rydberg-Rydberg interactions requires ultra-cold and dense atomic samples where the dipole-blockade effect takes place (Section 2.4.2). Additionally the number of atoms in each sample should be controllable. One of the approaches is to trap the atoms in a micron size dipole traps (see Section 7.4), which can be implemented with high numerical aperture lenses. Another important component of the experiment is the detection system, based in our case on selective field ionisation (Section 2.4.3). These elements had to be included in the design of the new apparatus. Section 6.1 describes the stainless steel chamber with all its components. To achieve the pressure of few 10^{-10} Torr special care must be taken during the assembling, and the whole system has to be baked out. Sections 6.2 and 6.3 describe in details the process of obtaining of the ultra-high vacuum.

6.1 Design of the chamber

In this section all the components of the new vacuum system are described. Putting the UHV system in operation is challenging and a time consuming task. Careful planning at the early stage allows to avoid some problems which often come up along the way. Here are few precautions which one should take while designing the vacuum systems:

- to keep the volume of the chamber as small as possible
- there will always be some residual degassing from the surfaces, therefore, the number of components inside the chamber and thus the surface area should be kept as small as possible to minimize the internal source of contaminations
- all parts should be made out of low outgassing materials
- all materials used, devices and components inside the chamber should be bakeable at high temperatures
- to avoid trapped volumes inside the chamber which will lead to virtual leaks

- to provide sufficient optical access through viewports with anti-reflection coating if necessary
- to supply the chamber with atoms reservoir

Our choice of material is stainless steel, which can be baked even at the temperature 450 °. The design was made in collaboration with Chris Hall from S&T Workshop. The core chamber is based on commercially available parts, where the main component is the spherical octagon chamber (Kimball Tech.), and the added elements have been manufactured also in the S&T Workshop. The main challenge was to fit all the necessary bits inside the chamber and yet provide enough optical for the cooling and other laser beams. A simplified scheme of the apparatus is shown in Fig. 6.1 and the assembled chamber is presented in Fig. 6.3.

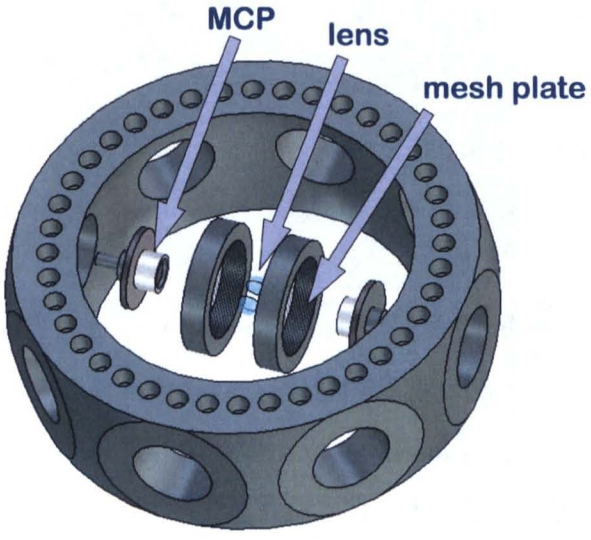

Figure 6.1: The interior of the vacuum chamber with aspheric lenses, MCP's and ionizing grids.

The chamber

The main chamber was ordered at Kimball (8" Multi-CF Spherical Octagon: MCF800-SphOct-G2C8). It is a 7 cm ring cut out of hollow sphere of the outer diameter 22.4 cm made of unitary stainless steel grade 316 L[1]. Its total volume is 1.75 l. There are eight

[1]Grade according to SAE (The Society of Automotive Engineers). The four digit numbers of the grade represent the chemical composition of the steel.

standard sealing surfaces of size $2^3/_4$ CF[2] equally spaced to form an octagon and one on each face in size 8" CF.

The aspheric lenses

The main feature of our apparatus is the lens employed to create the dipole trap, which will be described in Section 7.4. We use an aspheric lens from LightPath Technologies (product code 352240) with NA=0.5. The working distance of such a lens is 5.918 mm which requires it to be placed very close to the MOT. Therefore in our set-up it has to be mounted inside the chamber. As it was already mentioned the detection of Rydberg atoms relies on selective field ionisation, and fixing the lens inside the ionisation region may lead to charge induction and accumulation on the surface of the glass. One way to reduce this effect is to mount two lenses at equal distances from the symmetry axis of the electrodes used to generate the ionisation field (which will minimize the net charge accumulated at each lens due to Coulomb interactions).

Taking the cylindrical symmetry of the chamber into account, the lenses need to be mounted in the middle. We chose to use two 10 cm long metal tubes of inner diameter 9 mm to deliver each lens to the region of interest separately. This provides maximal access for the laser beams and using metal tubes additionally allows to partially shield the lenses and to ground them. Each tube is pushed into the 2 cm long ceramic ring, that in turn is enclosed into a metal mounting attached by 6 bolts to the zero length[3] reducer flange ($2^3/_4$CF $1^1/_3$CF)). The holding for the lenses is presented in Fig. 6.5 (a) and (b) and the lenses inside the chamber are shown in Fig. 6.2 (a).

Having two aspheric lenses perfectly on axis and at distance $2f$ which can be used simultaneously is an advantage of the set-up. To be of use the lenses had to be positioned exactly at $2f$ from each other (f is the focal length of the lens), which creates $1:1$ objective and the focal points of each lens overlap in space. Using the aligning tool (a metal tube of the outer and inner diameter 14 mm and 10 mm respectively, finished with thread matching to the mounting of the lens) the ceramic ring with the

[2]There are several types of vacuum flanges. CF (ConFlat) flange is a knife-edge flange which is used with a copper gasket to provide good sealing between two connected metal parts. Such a seal allows to achieve pressure of 10^{-13} Torr. It is measured in inches.

[3]Zero length means that the described element has a thickness smaller or of size of its mounting flange.

lens tube could be moved inside the mounting and thus the position of the lens could be adjusted. To accurately locate the lenses, a *shearing interferometry technique* was used[4]. The 830 nm beam was expanded on a telescope to 8 mm diameter and sent through both aspheric lenses, already mounted inside the chamber at approximate distance $2f$, creating a 1:1 telescope. The collimation of the output beam was tested using fused silica $\lambda/20$ wave optical flat by Edmund Optics (NT-43-408). The observed pattern for the converging (b), collimated (c) and diverging (d) beam respectively is shown on Fig. 6.2 (b-d) respectively. Due to the parameters of the employed optical flat, for the collimated beam only one big ring fringe is observed. Using this technique the separation between lenses was fixed to 10.5 mm, measured between the edges of the metal mountings. (Fig. 6.2 (a)).

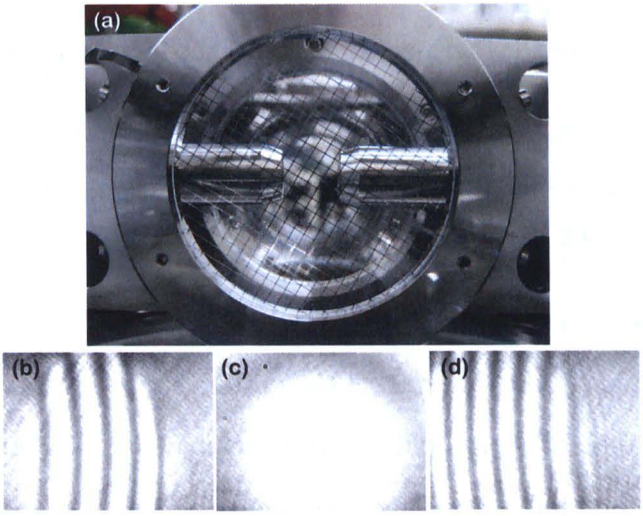

Figure 6.2: Positioning of the aspheric lenses inside the chamber: (a) side view of the lenses mounted in the metal tubes, (b-d) testing of the beam collimation using shearing interferometer: (b) converging beam (c) collimated beam, (d) diverging beam.

The method described above for the mounting of the lens is quite easy to build and inexpensive, however, it has a few disadvantages. Each lens is fixed separately at the end of relatively long tube, which is in turn fixed to the flange. As there is a copper gasket between the flange and the chamber, which has a thickness of about 2 mm, the tightening of bolts holding the flange changes the position of the lens inside

[4]This method is used to test the collimation of the beam by observation of the interference fringes created as a result of the optical path difference of the beam reflected on the front and back surfaces of the optical wedge shear plate. If the beam is close to collimation, a series of equally spaced straight fringes is observed. The direction of the fringes rotation and their spacing changes according to the degree of beam collimation.

the chamber. Thus positioning should be done with the flange already fixed as even tightening of one bolt can significantly tilt the lens. The aligning tool allowed to move the lens only in one direction, thus if the lens was moved to far, the whole part holding it had to be taken out, the ceramic tube pressed back inside, the gasket replaced and the procedure of adjusting had to be started from the beginning. Thus, after fixing the lenses, the bolts holding the flange should not be tighten any more, which is not convenient if there is a leak detected. Furthermore, after few adjusting procedures the friction between the metal and the ceramic crumbled tiny bits of ceramic which stacked between these two surfaces making it really difficult to move the ceramic again. The aspheric lens is only pressed in the metal tube, thus one needs to make sure that it is not tilted. It happened once, and not only made very difficult to position the lenses, but the lens broke during the baking (the thermal expansion of the glass was not evenly distributed in reference to the thermal expansion of the metal and the overstressed glass crushed).

Detection of Rydberg atoms

As mentioned in Section 2.2, Rydberg atoms can be easily ionised and the resultant ions can be registered by the detector. This state-selective field ionisation technique, not only provides a tool for counting Rydberg atoms, but it enables to resolve the distribution of population in different atomic states and, by combining it with time-of-flight technique, it is possible to obtain one-dimensional position sensitive detection. In experiments investigating the interactions between Rydberg atoms, when the interaction range is of order few μm, the detection system should be able to spatially resolve single Rydberg atoms separated by this distance. In addition it should be very sensitive as only one or very few Rydberg atoms will be ionised and registered. A detection system which meets this requirements has been designed and described in Piotrowicz (2010).

To detect such small charges micro-channel plates (MCP)[5] are used. We employ a F4655-13 MCP assembly from Hamamatsu, which is a two-stage MCP with $4\,\mu$m channel diameter giving a gain of 10^6 at 2 kV and provides for high resolution time-of-

[5]Micro-channel plate is an array of micron size electron multipliers which is used to detect electrons, ions, X and Γ and vacuum UV rays. The detected signal is significantly amplified in electron multiplier channels, in which the multiplication occurs if a strong electric field is applied.

flight mass spectroscopy. The electric field for ionisation of Rydberg atoms is generated by two electrodes fixed around the trapping region. The electrodes are made of mesh grid to enable optical access. In order to record the electron and ion simultaneously two MCP's are used.

Another advantage of our set-up is that as opposed to standard TOF position detection, it allows to detect atoms in a two-dimensional plane. This can be achieved using an electrostatic lensing. The simulations performed show (Piotrowicz, 2010), that two ions initially separated by 25 μm can be guided apart by the electrostatic lenses and arrive to the MCP separated by few hundreds μm, which allows to detect the ions position in 2-D. According to the simulations, even atoms trapped at a distance of only 2 μm should be resolved (Piotrowicz, 2010), provided a good control over stray fields is achieved.

Fig. 6.1 presents the arrangement of MCP's and ionizing electrodes in the chamber. The electrostatic lenses have not been implemented yet, however there is a space reserved for them. Fig. 6.5 (c) shows the disassembled mounting for the MCP and the 4-pin electrical feed-through (which can carry 5 kV DC) used to provide the electricity inside the chamber.

The rubidium source

The source of rubidium vapour is provided by the alkali metal dispensers from SAES Getters. The rubidium is generated from a mixture of rubidium chromate (Rb_2Cr0_4) and a reducing agent zirconium/aluminium (Zr-Al) alloy, which is the getter material. The mixture is held in a trapezoidal metal container. Heating of the getter electronically starts the reduction reaction and as a result free rubidium atoms are evaporated. The reducing agent also absorbs the products of the reaction thus the rubidium vapours are free of contaminations. Adjusting the current passing through the getter allows to control the amount of evaporated rubidium (SAES getters, 2000).

Two 12 mm long dispensers each containing 4.5 mg of Rb are connected in parallel to a 7-pin electrical feed-through (which can operate at 700 V DC max, and the current of 15-23 A per pin can be applied). The long pins of the feed-through deliver getters at the distance of 3 cm from the trap region (Fig. 6.3). During the experiment we use

one dispenser at a time, and typically a current of 3.3 A is continuously applied.

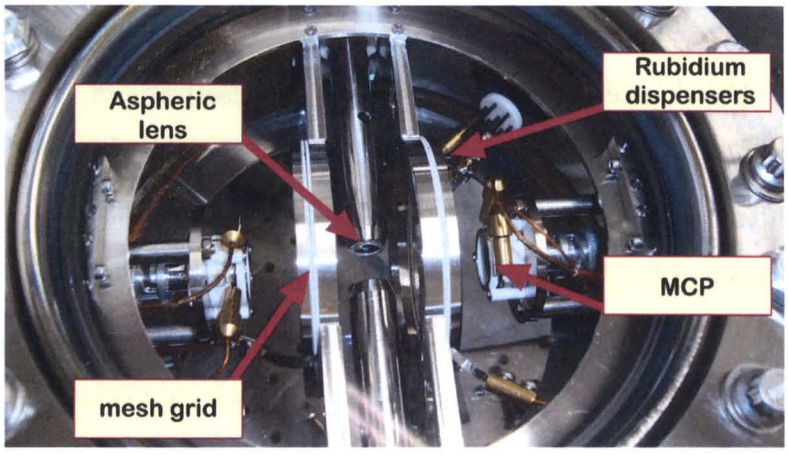

Figure 6.3: Photo of the assembled apparatus.

Optical access

The optical access is provided by two NW150CF[6] zero length ISO flange viewports manufactured by Torr Scientific. They are made of Kodial® [7] glass which is sealed to a Kovar®[8] weld ring - a transition piece which in turn is attached to 304 L steel 8" CF flange and the connection is sealed with fluorocarbon o-ring. Kodial glass offers a maximum transmission of order 94% at wavelengths in a range 0.4-2 μm (Scientific, 2011), however to reduce the reflectivity on both sides of the window four-layers of a broadband anti-reflective coating are added, optimised to 480-780 nm wavelength range, thus these viewports provide the optical access for the MOT beams, the excitation blue laser and the probe beam. This reduces the reflection to about 0.5% (Scientific, 2011). Two other Kodial viewports NW16CF are used to close the reducer flange of the lens mounting system. The anti-reflection coating is optimized to cover the range of 780-830 nm, as these viewports provide the input for the dipole trap laser and simultaneously allow to collect the fluorescence of the atoms. There are two more viewports (NW35CF) fitted to one of the 2 3/4CF outputs of the chamber and the end of a 5-way cross to provide extra view in a different plane, e.g. for the CCD camera

[6]NW-XX-CF the flange size expressed in ISO flange notation. The NW (acronym *Nennweiten* - nominal diameter) usually refers to internal diameter of the vacuum tubing or window diameter. NW and is given in mm and CF refers to the sealing type

[7]Kodial is alkali borosilicate glass.

[8]Kovar is a nickel-cobalt ferrous alloy, which was designed to match the thermal expansion characteristics of borosilicate glass. Thus, Kovar provides a mechanical connection of glass to other materials e.g. stainless steel over a wide range of temperatures.

to monitor the cloud. These are standard Kodial glass windows with a single QWOT (Quarter Wave Optical Thickness) layer of MgF_2 coating.

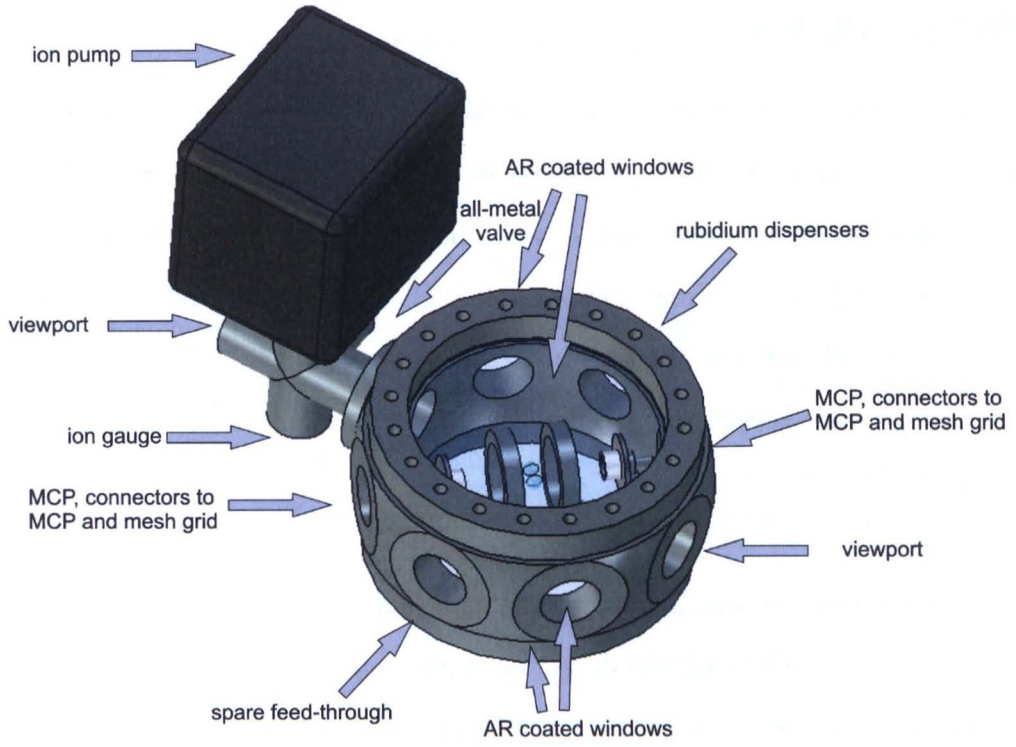

Figure 6.4: Scheme of the whole apparatus (drawn in T-Flex CAD software).

The pumping system

Fig. 6.4 presents the chamber with the rest attached components. To obtain UHV vacuum three different vacuum pumps are used (see Section 6.3). To maintain the low pressure the Varian Plus Star Cell ion pump is employed. It has a nominal pumping speed for nitrogen of $20\,l/s$ and it allows us to achieve a pressure down to 10^{-11} mBar. The other two pumps are needed only during the baking thus they are connected via an all-metal valve, attached to 5-way cross. Valve is used to control the flow of the gas into the vacuum chamber to provide good seal from the atmospheric pressure after detaching the turbo-pump. We use an all-metal angle valve, MAV-150-v, which can seal the chamber from the atmospheric pressure down to 10^{-11} mBar. One valve can be used up to 100 open/close cycles without changing the gasket. To monitor the pressure an 580 Nude Ionization Gauge Tube from Varian Vacuum Technologies is used. The pressure can be read out in a range $10^{-1} - 4 \times 10^{-10}$ Torr, and this is used together with

ion gauge controller from Edwards. The ion gauge was used only during the baking, on the day to day operation the pressure is determined from the current in the ion pump.

Mechanical supports

The chamber is designed in such a way that the laser beams can enter it either through the top or the bottom window, thus it has to be held at some level above the optical table, which is not easy as the chamber with the ion pump connected is heavy. In this case two steel pedestals of dimensions $8 \times 0.9 \times 23.5$ cm have been designed, which lift the center of the chamber at the level of 25 cm. To be very solid, they have to be very wide. They are also separated by only 23 cm. This makes it difficult to arrange the optics under the chamber.

Fig. 6.4 presents the chamber with the attached ion pump and some viewports. The arrows indicate where all the described components are fitted. The advantage of the set-up is its simplicity and its compact nature. MCP's, ionizing grids and aspheric lenses are fit into relatively small (1.75 l) chamber, and all the extra components are taken outside the chamber via 5-way cross.

6.2 Cleaning and Assembling

To obtain UHV special care must be taken during the assembling of the apparatus. Grease and oil contamination limit the ultimate pressure to about 10^{-6} Torr, thus all the parts have to be cleaned and handled with gloves.

The cleaning procedure

All the parts of the apparatus were cleaned separately, thus the chamber was completely disassembled. Fig. 6.5 (a-h) show all the components of the chamber taken into pieces ((a-c) show the mounting for the lens and MCP, (d-g) present all parts of the mounting of the mesh grids). The parts were handled only when necessary and always using powder-free nitrille gloves. Two types of surface active cleaning agent were used: Decon90 and Neutracon. Decon is a vacuum compatible detergent for the cleaning of

glass, ceramics, rubbers, plastics, stainless steel and ferrous metals. As it is alkaline it is not suitable for cleaning non-ferrous materials such aluminium and zinc. To clean anti-reflection coated windows which might be damaged by acidic or alkaline cleaning solutions, a neutral detergent Neutracon was used. The fragile parts like ceramic, grids and all the tiny element were washed separately.

The cleaning procedure was adapted from Arnold *et al.* (1998) and was as follows:

- soaking overnight in a solution of detergent
- ultrasonic cleaning for one hour in the same solution
- rinsing thoroughly first with tap water and then with distilled water
- soaking overnight in distilled water
- ultrasonic cleaning for one hour in distilled water and then for another hour in fresh distilled water
- left to dry
- soaking overnight in methanol
- ultrasonic cleaning for one hour in the same methanol and then then for another hour in fresh methanol
- left to dry in fume cupboard

After the cleaning each part was carefully wrapped in a clean thin foil. During the cleaning the 5-way cross (from MDC Vacuum Products) got corroded, which indicates the poor quality of the stainless steel used. Also pins of one of the electrical feed-through got tarnished when cleaned with Decon, but it was removed with sand paper and cleaned again only in methanol. In turn cleaning one of the windows in Neutracon damaged the coating, however we suspect that it was a result of the chemical reaction with some oil introduced accidentally in the mechanical workshop. Despite these problems the cleaning procedure is safe and allows to achieve very good vacuum.

The assembling

During the assembling special precautions need to be taken as well. It is very important to use powder free gloves, so in case of tear no powder or other contamination will be accidentally transferred to freshly cleaned apparatus. All ConFlat knife-edge seals

Figure 6.5: Cleaning of all components of the chamber: (a) mounting for the aspheric lens separated into pieces and (b) the lens mounting assembled, (c) the mounting for MCP taken into pieces, (d-g) mounting for the ionizing grid, (h) all components separated and prepared for cleaning.

between flanges are filled with copper gaskets. Additionally to seal viewports special annealed copper gaskets are used. They require lower pressure applied to make a tight seal, which is of great importance when fixing the windows, so that the glass will not get overstressed. When connecting the flanges, the gasket should be carefully placed between the knife edges in a way that the seal is even all the way around the flange. All bolts should be finger tighten first, and then each bolt should be screwed by a small amount and the tightening should be done in a "star-shaped" pattern Birnbaum (2005). All the bolts and threads used for fixing the flanges outside of the vacuum area should be protected with an anti-seize compound (Molybdenum Disulphide), which provides an insulating layer between metal parts and prevents them from sticking. As

it is dispersed in a grease, it should be used carefully so it will not accidentally get into the chamber. To stick insulating ceramics to the mesh grids a vacuum compatible epoxy is used (Varian Torr Seal).

Electrical wiring

The electricity inside the vacuum is provided by electrical feed-throughs, however the connections between their pins and devices cannot be made with ordinary wires. Thus a special Kapton®[9] insulated wiring is used. For the connection of MCP, a KAP50-5 UHV 50 Ohm coaxial cable is used, which is Kapton insulated with silver plated wire screen. To connect the mesh grids a KAP2 UHV wire is used. The wires are fixed with push-in connectors made of beryllium copper alloy, or in-vacuum ground shielded and BNC connectors (LewVac). It is important that all connectors have holes drilled in shields so the air will not be trapped inside.

6.3 Baking of the chamber

Achieving very good vacuum means having to remove all the molecules that are present in the air such as nitrogen, oxygen, hydrogen, carbon dioxide, water vapours and more. Some of them, like nitrogen, are easily removable but other can stick to the surfaces in the chamber and are difficult to remove, especially water vapours which are easily adsorbed by the glass and metal surfaces. Raising the temperature of the system increases the out-gassing rates and accelerates the removal of the molecules. To facilitate pumping out of the water the temperature should be raised at at least 100 °C, usually the heating is limited by the durability of the materials. The stainless steel parts can be baked at temperatures of order 400 °C, however the fluorocarbon seal used at the viewports limits it to 220 °C. The other limiting device in our set-up are MCP's, thus the ultimate baking temperature was set to be 150 °C for the chamber and 180 °C for the ion pump. The ferrite magnets of the pump have been taken off at the time of the baking.

[9]Kapton is an aromatic polyimide film, which retains its unique physical, chemical, and electrical properties balanced over a wide temperature range -273-400 °C

Monitoring of the temperature

Typically the vacuum apparatus is enclosed in an oven and baked at the desired temperature. We employed heating tapes for the baking and to make sure that the heat is distributed evenly around the chamber, the baking temperature has been controlled by 7 different thermocouples placed at different points around the chamber. The sensors were fixed in the most crucial places - one on each 8" CF viewport, around the MCP's mounting flanges, at the ion pump, and the most outer points. The chamber has been wrapped in few layers of a thin foil, to ensure good heat conductance, and heating tapes have been added. The inset in Fig. 6.6 shows the arrangement of the tapes. The temperature gained by the tapes is controlled by the variable voltage transformer (VARIAK). The heating tapes we have used have been different length and brand, thus each of them had to be controlled separately. The chamber had been wrapped again in lots of layers of aluminium foil on top of the heating tapes to achieve uniform temperature around the chamber.

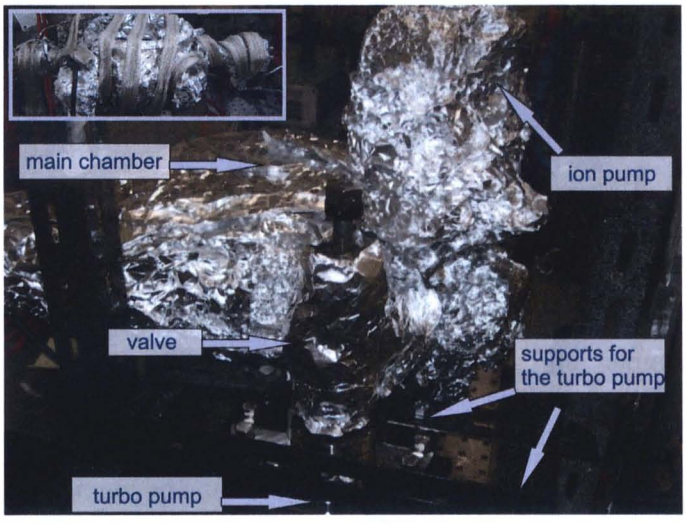

Figure 6.6: Baking of the chamber: the turbo pump is secured by the scaffold, the heating tapes (visible on the inset) are covered with loads of aluminium foil so the heat is evenly distributed, the magnets from the ion pump are removed for the baking.

Vacuum pumps

The pressure in the system is maintained by the ion pump, however this pump cannot operate at atmospheric pressure, thus it was turned on after the high vacuum was achieved. During the baking a turbo molecular vacuum pump was used which had

pumping speed 60 l/s. The turbo pump had to be backed up by the dry rotary pump. The rotors in the turbo pump rotate at high speed, thus it needs to be specially bolted to the table which will be able to absorb the energy of the rotors in case of emergency. Thus the top flange was fixed by 4 bolts to specially built scaffold. It also allowed to lift the pump and avoid a load directly on the chamber mountings. The pump was connected to the system by an all-metal valve. The valve and the top flange of the pump had been baked as well, but at the same time the rest of the turbo pump had been water cooled. Fig. 6.6 show the whole system ready to bake.

Baking

The procedure we followed to obtain UHV is as follows: first the rotary pump is turned on and when the pressure of order 10^{-3} mBar is achieved (after a couple of minutes) the turbo pump is also turned on. After an hour of turbo pump working, the pressure dropped down to about 2.7×10^{-7} mBar. At this point the temperature of the chamber was raised, taking some precautions. To increase the durability of the Kodial glass, the temperature should be increased at a maximum rate $3\,^{\circ}\mathrm{C/min}$. Fig. 6.7 presents

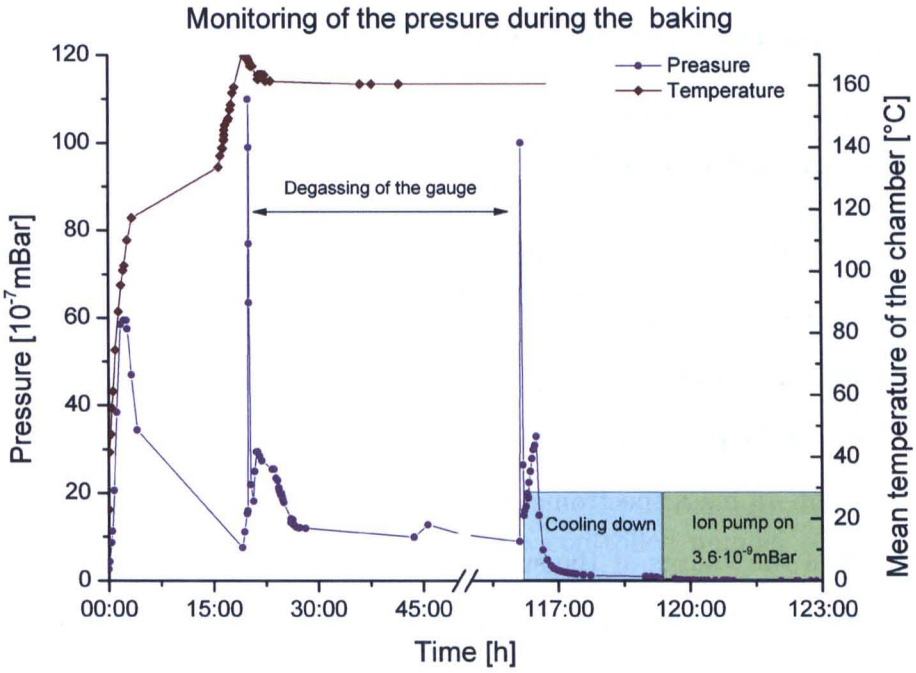

Figure 6.7: The graph presents the change of the pressure (purple trace) and the mean temperature (red trace) during the baking of the chamber.

the change of the pressure during the baking. The dark red trace indicates the mean temperature of the chamber (excluding the temperature of the ion pump as it was much higher). As can be seen, during the first 3 hours when the temperature was increased, the outgassing was dominating and the pressure rose rapidly, by almost 2 orders of magnitude. Then the pumping out dominated the outgassing and the pressure started to drop. The few hours gap in the increase of the temperature is due to the night break - during that time the temperature stabilised at 130 °C and the pressure dropped back to 7.6×10^{-7} mBar. After the raising of the temperature restarted, the pressure increased again. The rapid increase in the pressure at about 20 h, is due to the degassing of the ion gauge. The temperature of the gauge reaches at that point 400 °C and thus the mean temperature of the chamber raised as well. The baking continued for another 100 h. Near the end, the ion gauge had been degassed again, and after an hour we begun cooling the system down (similarly at a rate 3 °C/min to protect the glass). After cooling the system down the pressure dropped to 2.7×10^{-8} mBar, the valve had been closed and the turbo pump had been switched off. From that point the ion pump took over maintaining the pressure which reached 3.6×10^{-9} mBar. After days of working of the ion pump the pressure is of order few 10^{-10} Torr. It is now read out from the current of the ion pump directly, which is constantly at the base level (removing the magnets results in the same value of the ion pump current).

Leak detection and virtual leaks

Obtaining the UHV is a time consuming task, we baked our chamber a couple of times before we reached 10^{-10} Torr regime. Each time there was a small leak present in the system, preventing us from achieving a pressure lower than 10^{-8} mBar. The common source of leak is a flange tighten not fast enough. Typically the leaks are traced using the leak detector - a mass spectrometer which detects helium gas spread through the special groves in the flanges at the suspected leaking connection. Due to the lack of a mass spectrometer in our system, we traced leaks by observing the changes in the pressure while spreading the helium gas. This method was sensitive enough to discover two sources of leaks. One of the mistakes we have made was assembling two rotable flanges together and that connection was not tight enough. The other problem was

given by fixing a small turbo pump without any support straight to the valve. Although it was not heavy it overloaded the 5-way cross part of the chamber, and bent the gasket over creating the leak. This also suggests that the supports for the chamber we use are not placed properly and should be re-designed.

The second type of leaks are virtual leaks. This is a volume of gas physically trapped inside the chamber, which cannot be pumped out easily due to the small conductance of the path between the trapped gas and the rest of the chamber. The main problem with virtual leaks is that they cannot be traced with the leak detectors. One of the approaches is to observe the pressure: if there is a periodic increase, it probably means that a 'bulb' of the gas has found its way to the chamber and this caused the rapid change in the pressure. We had two sources of virtual leaks, one was a grounded connector for the wires which did not have an out-gassing hole manufactured in it. We cut out a bit of it and the whole system had to be baked again. The second virtual leak was created by the valve, which was fully open during the baking and it trapped some air inside. Thus it is recommended to keep the valve half open to make sure that the air is out-gassed from all of its surfaces.

Summary

Building up new apparatus is always a challenging task, especially when UHV system is required, where all the mistakes are found out at the last stage when the desired pressure has not been achieved. Therefore a thorough analysis of the design and devoting attention in choosing the parts helps to avoid lots of problems at the later stages, such as assembling and baking. To achieve UHV all the parts have to be cleaned and handled only when necessary. Care must be taken also during the assembling to avoid any contaminations of the apparatus. Diligent connection of the elements allows to avoid leaks and facilitates obtaining ultra low pressure. We have obtained a pressure of order 10^{-10} Torr, which is necessary to load a controlled number of atoms in the dipole trap.

BLANK PAGE IN ORIGINAL

CHAPTER 7

MOT IN THE 4-BEAM CONFIGURATION

As described in Section 3.2, magneto-optical traps are usually operated using six orthogonal counter-propagating laser beams, which provide the scattering force necessary to slow down the atoms in all three dimensions, and a quadrupole magnetic field which confines the atoms at the centre of the trap. In a typical laser cooling experiment this configuration is used, as glass cells or chambers with perpendicular view-ports provide easy optical access. However, in our new vacuum chamber, which is presented in details in Chapter 6, the optical access is very restricted. Therefore it is impossible to send six orthogonal laser beams and our set-up involves an unusual laser geometry of the MOT. A variety of works have been presented involving different configurations of magneto-optical traps. Shimizu *et al.* (1991) showed that 4 collimated beams of equal intensity arranged in a regular tetrahedron can also create a strong MOT. Chesman *et al.* (1994) have demonstrated that a three-dimensional MOT can be formed even by using only two focused Gaussian beams, however the cooling forces are quite weak in this case. Lee *et al.* (1996) used a single beam multiply reflected from the surface of pyramidal or conical mirrors to create a set of appropriately polarized beams for the creation of a MOT. Micro-fabrication of pyramidal mirrors by etching set the basis for integrating magneto-optical traps on atomic chips (Trupke *et al.*, 2006; Pollock *et al.*,

2009, 2011), however with this approach the MOT is formed inside the hollow pyramid and as a consequence the manipulation of atoms is rather limited because of restricted optical access. A 4-beam version of the pyramid MOT was proposed by the group in Glasgow (Vangeleyn *et al.*, 2009), where a single beam was reflected by a set of three mirrors adjusted at such angle that the MOT is formed above the surface of the pyramid. The works of Shimizu and Arnold were an inspiration to our project, which will be described in this chapter.

7.1 A tetrahedral MOT

The tetrahedral MOT "built" in our laboratory is schematically depicted in Fig. 7.1 (a) and the tetrahedron which constitutes the base of the configuration is shown in Fig. 7.1 (b). Three laser beams propagate upwards along the edges of a pyramid (b in pink) toward the vertex, and a fourth vertical beam is propagating along the axis of symmetry of the pyramid (h labelled in orange) to counter-balance their force, so the atoms are cooled at the location of vertex. To achieve trapping a quadrupole magnetic field, created by two coils in anti-Helmholtz configuration (see Section 7.1.1), is added and aligned in such way that the zero field overlaps with the vertex of the pyramid. The polarisation for each beam is chosen to be circular by employing quarter-wave plates. The angle between the edge and the height is denoted as α and will be referred to as beam incidence angle. The tetrahedral angle[1] of a regular tetrahedron corresponds to $\alpha = 70.53°$. In our experiment, we use instead a very acute angle of intersection for the beams, resulting in $\alpha = 13 \pm 1.5\,°$. To our knowledge, cooling and trapping at such a small angle have never been achieved before.

A MOT operating in similar configuration, have been studied by Arnold's group. In their set-up one laser beam was expanded to 2.5 cm diameter and split in 3 and back reflected by triplet of 8×10 mm mirrors fixed at an angle of $\theta = 45°$ with respect to the horizontal plane (Vangeleyn *et al.*, 2009). They have modelled the properties of a tetrahedral trap and they have compared it to the standard 6-beam MOT, described in Section 3.2. In the case of a standard MOT, the laser light has wavevector $\boldsymbol{k} =$

[1]The tetrahedral angle is an angle between the segments joining the center of the solid and the vertices, which equals 109.47°

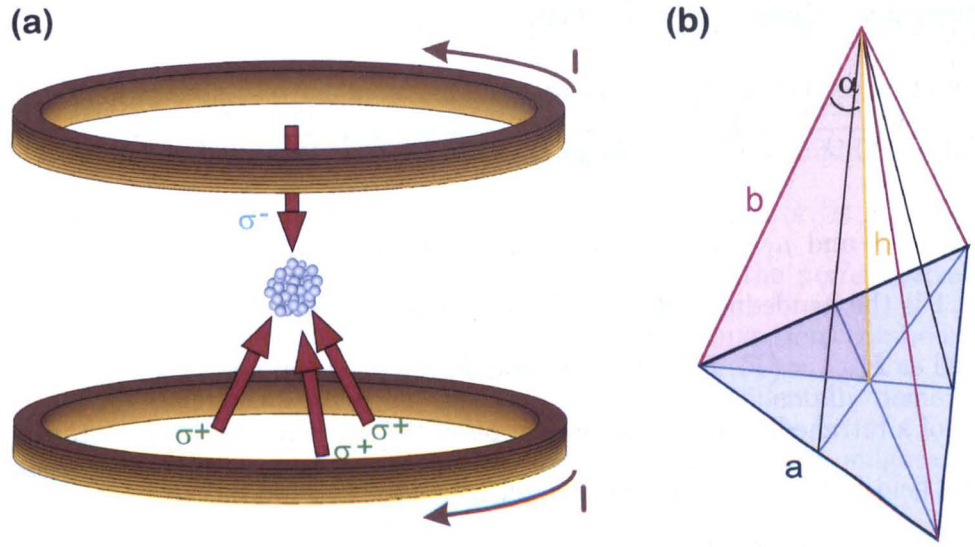

Figure 7.1: Configuration of a tetrahedral MOT: (a) beam arrangements in the experimental set-up, (b) scheme of a pyramid, a regular tetrahedron is formed when b=a. α is refereed to as a beam incidence angle.

$\frac{2\pi}{\lambda}\hat{\boldsymbol{k}}$, where $\hat{\boldsymbol{k}}$ is the unit vector which points out the beam propagation direction and propagates in the direction of the local magnetic field: $\hat{\boldsymbol{k}}$ is parallel or anti-parallel to $\boldsymbol{B}$. The light is circularly polarized, thus depending on the value of $\hat{\boldsymbol{k}} \cdot \boldsymbol{B}$ and the helicity of light only the transition to $m_F = +1$ or $m_F = -1$ state is excited.

However, if the two vectors are not parallel, which is the case of the tetrahedral configuration, all three transitions $m_F = 0, \pm 1$ will be excited. The dot product $\hat{\boldsymbol{k}} \cdot \boldsymbol{B} = \xi$, determines the projection of the laser propagation direction onto the local magnetic field and thus the decomposition of circularly polarized into its relative components, σ^+, π, σ^-. Thus the cooling forces strongly depend on ξ and on the beam incidence angle. Similarly to Eq. (3.26), the force experienced by an atom moving in $+x$ direction, in the low intensity limit $I \ll I_{sat}$ takes the form (Arnold, 1996):

$$\boldsymbol{F}_x = \hbar k \hat{\boldsymbol{x}} \frac{\Gamma}{2} \left(\frac{I_{\sigma^-}/I_{sat}}{1 + (\frac{2}{\Gamma})^2(\Delta - kv_x + \beta z)^2} + \frac{I_{\pi}/I_{sat}}{1 + (\frac{2}{\Gamma})^2(\Delta - kv_x)^2} + \frac{I_{\sigma^+}/I_{sat}}{1 + (\frac{2}{\Gamma})^2(\Delta - kv_x - \beta z)^2} \right). \tag{7.1}$$

Theoretical analysis of the cooling and trapping forces in the MOT in three dimensions is very complicated due to the interference of standing waves, thus only approximations based on a one-dimensional model are used. The total force exerted on the atoms can

be expressed as (Vangeleyn *et al.*, 2009):

$$\boldsymbol{F}_{total} = \sum_i \frac{h\pi\Gamma_\nu}{\lambda}\frac{I_i}{I_{sat}}\hat{\boldsymbol{k}}_i\left(\frac{1}{1+I_{total}/I_{sat}+4\Delta_\Gamma^2}+8\Delta_\Gamma\frac{k_\Gamma\hat{\boldsymbol{k}}_i\cdot\boldsymbol{v}-s\xi\mu_\Gamma|\boldsymbol{B}|}{1+I_{total}/I_{sat}+4\Delta_\Gamma^2}\right), \quad (7.2)$$

where k_Γ, Δ_Γ and μ_Γ are given in units Γ_ν ($k_\Gamma = 1/\lambda\Gamma_\nu$, and $\mu_\Gamma = \mu_B/(2\pi\Gamma_\nu)$), $s = 0, \pm 1$ is the handedness of light. This force is cylindrically symmetric and can be expressed as $\boldsymbol{F}_{total} = (\boldsymbol{F}_r, \boldsymbol{F}_z)$, where $\boldsymbol{F}_r$ and $\boldsymbol{F}_z$ are its radial and axial components. In the case of a tetrahedral MOT the projection of the beam propagation vector onto the magnetic field has to be taken into account, thus the total force can be approximated by (Vangeleyn *et al.*, 2009)

$$\boldsymbol{F}_{total} = 2\frac{h\pi\Gamma_\nu}{\lambda}\frac{I_{total}}{I_{sat}}8\Delta_\Gamma\frac{1}{1+I_{total}/I_{sat}+4\Delta_\Gamma^2}\left[k_\Gamma(\gamma_r v_r, \gamma_z v_z)+\mu_\Gamma B_0(\kappa_r r, \kappa_z 2z)\right], \quad (7.3)$$

where $\gamma_r = \kappa_r = \frac{1}{4}\sin 2\theta \tan 2\theta$, $\gamma_z = cos^2\theta$, $\kappa_z = 2sin^2\theta$ and the quadrupole magnetic field is given by $B = B_0(x, y, -2z)$.

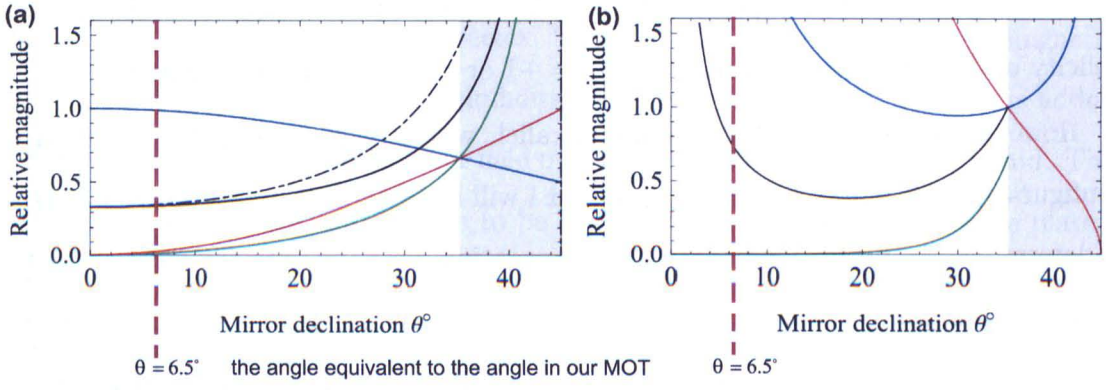

Figure 7.2: The influence of mirror declination angle on the efficiency of laser cooling and trapping, from Vangeleyn *et al.* (2009): (a) axial cooling (blue), axial trapping (red) and radial cooling and trapping forces (green), as a function of the mirror declination angle θ, shown relative to radial forces in a standard 6-beam MOT. The black curve represents ideal reflected (solid) and maximum reflected (dashed) beam power I_{up}/I_{down}, (b) the total (black) and sub-plane (green) MOT capture volume and the relative axial (blue) and radial (red) MOT sizes as a function of θ. The red dashed line indicates the equivalent angle achieved in our MOT.

In Vangeleyn *et al.* (2009) the influence of the beams intersection angle on the efficiency of laser cooling and trapping was investigated by analogous of Eq. (7.3). Fig. 7.2 (a) shows simulations of the cooling and trapping forces along different directions as a function of the mirrors declination angle θ (which corresponds to $\alpha/2$ in our settings)

and forces are shown relative to the radial forces in a standard MOT. The blue line represents axial cooling, the red line axial trapping and the green line radial cooling and trapping. The beam balancing ratio I_{up}/I_{down} is shown as a black solid line. The black dashed line, describing maximum reflected power from the mirror, is not important from our point of view, as we use 4 independent beams. At the perfect tetrahedron angle $\theta = 70.6°$, a strong cooling and confinement in three dimensions can be achieved by using only 4 laser beams of equal intensity, as was experimentally demonstrated by Shimizu *et al.* (1991). The forces (cooling and trapping) in this configuration correspond to 70 % of forces in a standard MOT. As $\theta \to 0$ the axial cooling begins to dominate in the system whilst the radial cooling rapidly decreases. This is because the upwards beams which are responsible for radial trapping become axially anti-trapping, and if their intensity is too high the force they impose on the atoms is not balanced by the downward beams making the formation of a MOT impossible. Therefore, to obtain a stable MOT and good optical molasses, the balancing of the intensity of upwards and downward beams is critical. The black solid line in Fig. 7.2 shows the dependence of the ratio I_{up}/I_{down} on the angle θ, where I_{up} is the intensity of a single beam propagating upwards along the edge of the pyramid. This ratio equals 1 for the perfect tetrahedron and decreases to about 30% as $\theta \to 0$, in turn the upwards beams should be more intense than the vertical beam for $\theta > 35.3°$. The general relation for a good balance is given by $I_{down} = 3I_{up}cos(\alpha)$ and it is extremely critical in our case for achieving good optical molasses. In our set-up the MOT beams have a power P_{down} =4.8±0.2 mW and P_{up} =1.5±0.2 mW, whilst the beam diameter is 6.0±0.1 mm. The re-pumping laser has a power of ∼4 mW and 8.0±0.1 mm beam diameter and it is overlapped with the vertical MOT beam to minimize the amount of light reflected on the metal parts inside the chamber. From Fig. 7.2 it can be seen that the axial trapping dominates over the radial trapping. This is due to the difference in the magnetic field gradients in the two directions due to the shape of the field generated by the anti-Helmholtz coils.

The capture volume, which is defined by the volume where the laser beams intersect (also called overlap volume), determines the number of atom captured by the trap and is proportional to $V_{total} \propto r^3/(sin2\alpha(1 + cos\alpha))$. Fig. 7.2 (b) presents the dependence of the capture volume on the angle θ. For a perfect tetrahedron (i.e. $\theta = 35°$) the

capture volume is the same as for the standard MOT. However as θ decreases, the capture volume decreases up to 40% of a 6-beam MOT at $\theta = 20°$ and then rapidly increases again for small angles. In our case the capture volume is $\sim$140 mm^3 (and for comparison it is about $\sim$125 mm^3 in a standard configuration). The overlap volume rapidly increases for small α (black line in Fig. 7.2 (b)) whilst the trapping and radial cooling minimize in this regime and the radial confinement is very weak. The large trapping volume region results in a quite big range of possible places where the MOT can be formed within the volume, i.e. we can displace it as far as $\pm$0.4 cm in the vertical direction using a controllable magnetic field.

A fluorescence image of the atoms in the tetrahedral MOT generated in our laboratory is shown in Fig. 7.3.

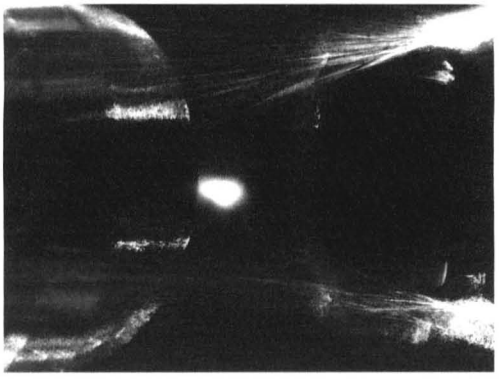

Figure 7.3: The photo of the MOT created in our laboratory. The trap is formed between two mountings (visible on the photo) for the aspheric lenses used for the diople trapping.

7.1.1 Magnetic fields

Experiments with laser cooling make use of two different kinds of the magnetic field. The restoring force necessary to confine the atoms in space exploits a field which is zero in the region of the beams intersection, where the atoms are being confined, whilst the magnitude of the magnetic field increases linearly in all directions as one moves away from the center of the intersection region (Foot, 2005).

Since the first development of a MOT, a lot of experimental and theoretical work has been focused on the optimisation of the number of trapped atoms and the density inside the MOT. The modelling of the capture range and the comparison to experimental

observations as a function of different parameters such as intensity and detuning of the laser beams and magnetic field gradient has been described in Monroe *et al.* (1990); Lindquist *et al.* (1992); Gibble *et al.* (1992). It was found that the number of atoms in the trap strongly depends on the quadrupole magnetic field. In turn the optimum magnetic field gradient is determined by the laser beam size and intensity as well as its detuning. It is desirable to have a high magnetic field gradient at the center of the trap, which results in a stronger trapping force, however, for very large beam size the Zeeman shift of the energy levels for atoms positioned at the edge of the trap is disrupting the slowing force, thus the gradient cannot be too high either (Lindquist *et al.*, 1992). For alkali atoms the optimal gradient lies in a range 5-20 $^{\mathrm{G}}/_{\mathrm{cm}}$.

The coils used in our experiment are made of 100 of turns each, their inner diameter of D_{coil} is 6 cm and they are separated by a distance of 12 cm. Although in the ideal anti-Helmholtz configuration they should be separated by a distance equal to the radius of the coil, the separation between the anti-Helmholtz coils is not that critical, as whilst the strength of the gradient decreases with increasing the separation, the linearity of the field is maintained. The typical value which we use in the experiment is B_z =6 $^{\mathrm{G}}/_{\mathrm{cm}}$ that is reached for a current of 4 A of current circulating in the coils. The power dissipated by the coils operating at this current is of the order of 6 W, thus no additional coil cooling mechanism is necessary.

The MOT operation also requires an offset B-field to compensate for any stray field present in the lab. This is done by a pair of coils in a Helmholtz configuration[2], which produce a homogeneous magnetic field in the mid-plane between these two coils. The strength of the magnetic field varies on the mid-plane as a function of distance from the axis of symmetry of coils and its uniformity depends on the separation between the coils. To achieve a uniform 'flat' field the coils should be separated by the radius or half of the square side. There are usually three pairs of square Helmholtz coils composing a cube, which are used to ensure zero magnetic field at the trap location in all directions, which is important for obtaining a good optical molasses. In the lab the are several sources of unwanted field: the Earth's magnetic field, magnetized

[2]A pair of identical coils connected in series and placed symmetrically along a common axis in such a way that the current is flowing through the two coils in the same direction, is called Helmholtz configuration and it produces a uniform magnetic field.

metal parts on the optical table all play a role, but the main source of stray magnetic field in our case is a large magnet attached to the ion pump. This magnet creates high gradients of magnetic field across the trap region, especially in the vertical (z) direction, and it prevents the formation of the MOT. In the vertical direction we compensate for this B-field by using circular coils consisting of 100 turns each, with a radius of 7 cm and separated by 13 cm. They generate a relatively strong magnetic field in the trap region, which is of order 2.5 G. Additionally, there are two sets of square coils, in the planes parallel and perpendicular to the facet of the magnet, which are made of 25 turns separated by distance which equals the length of the square side 22 cm. Due to the geometry of the chamber all the compensation coils are separated by the distance larger then the diameter of half side of the square of the coil, which has an influence on the uniformity of the generated field. The effect of such coils separation can be seen in Fig. 7.4. The value of the magnetic field changes rapidly as the distance from the coils symmetry axis increases. However as can be seen in the insets, the field is fairly uniform in the trapping region of atoms (over the distance ± 2 cm) and provides a good control over the MOT.

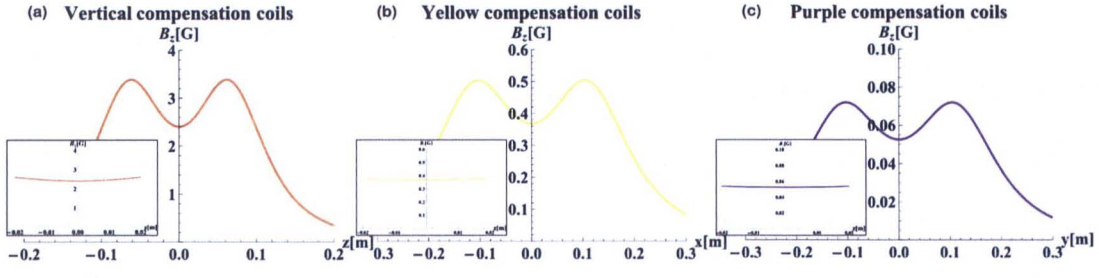

Figure 7.4: Magnetic field generated by the compensation coils in a Helmholtz configuration: (a) vertical (z - direction) coils nullifying the magnetic field of the ion pump, (b) and (c) generating magnetic field in the x and y direction.

All coils have their own inductance which limits how fast the current can be switched-off. This parameter is very important in experiments with optical molasses, thus special drivers for the coils have been design in the Electronic Workshop, which ensure a switch-off time of 75 μs and a current raising time is about 500 μs. For the compensation coils the switch-off time is set to $\sim$100 μs as well.

7.2 Characterisation of the MOT

In this section I describe a set of the measurements that were taken to characterize the MOT and derive important parameters, like the number of atoms in the trap, the number density and the temperature of the atoms inside the trap. To probe the atomic cloud two methods were used: fluorescence and absorption imaging. Both techniques will be briefly described in the following sections together with the methods used for the analysis of the number of atoms. To estimate the temperature of the cloud the time-of-flight technique was used, which is introduced in Section 7.2.3. The final results are presented in Section 7.3

7.2.1 Fluorescence imaging

When a nearly resonant laser beam propagates through a medium, atoms will absorb from the beam and re-emit photons in a random direction. The light scattered by the atoms in a MOT can be registered by a detector - either a photo-diode or a CCD (charge coupled device) camera. The advantage of this method is that the detector can be placed along any axis, as atoms scatter the light uniformly in all directions. However, this also results in a weak detection signal, as typically only a small portion of the light (determined by the solid angle of collection) reaches the detector. The signal strength can be improved by increasing the exposure time or the solid angle by employing a lens of a high numerical apreture.

Number of atoms

The total power of the light emitted by the atoms in the MOT, P_{MOT}, is proportional to the number of atoms N according to the relation: $P_{MOT} = NR_{sc}E$, where R_{sc} is the scattering rate (Section 3.1) and E is the energy per photon, $E = {}^{hc}/_{\lambda}$ which equates to 2.56×10^{-19} J for λ =780 nm. In our experiment we use a CCD camera with pixel size $(9.9 \times 9.9)\,\mu\text{m}^2$ to detect the fluorescence signal. The number of counts is determined by summing over all the registered pixel counts c_{pix}, $n_{counts} = \sum_{pix} c_{pix}$. The counts can be converted to the power of the emitted light using the quantum efficiency coefficient of the camera, η. This calibration coefficient can be estimated by determining the

count rate of a light source with known power, for example a laser beam. We also have to take into account the fact that only a fraction of light scattered by the atoms, given by the solid angle κ, is recorded by the camera. The solid angle equals $\kappa = {}^{\pi r^2}/_{4\pi d^2}$, where r is the radius of the imaging lens and d is the distance between the lens and the atoms. The number of atoms in the MOT can be derived from the number of counts using the relation:

$$N = \frac{n_{counts}\eta}{R_{sc}\kappa\tau}, \tag{7.4}$$

where τ is the imaging time. This technique also offers a useful tool for monitoring the trap performance in real-time as well as for the optimisation and alignment of the trap.

7.2.2 Absorption imaging

This technique relies on the resonant absorption of light by atoms. A cloud of atoms is illuminated by a weak probe beam (Fig. 7.5), which is delivered from a laser locked to an atomic transition. As the light of intensity I_0 is propagating through the atomic cloud, the atoms absorb and scatter photons. As a result, the CCD camera registering the image of the probe beam will record a weakened intensity of the beam in a form of a shadow cast by the cloud and caused by the absorption of the light by the atoms. The amount of absorbed light is connected to the *column density* of the atomic cloud.

If N atoms are confined in a volume element d^3x, then the number density n_{dens} is given by $n_{dens} = {}^{N}/_{d^3x}$ and the power scattered per unit volume is related to n_{dens} by $P_{MOT} = n_{dens}ER_{sc}$. The change in the beam intensity I along the propagation direction z equals:

$$dI/dz = -n_{dens}ER_{sc}. \tag{7.5}$$

Writing Eq. (7.5) in terms of resonant cross-section (Eq. (3.20)), $\sigma_0 = \frac{\Gamma}{2}\frac{E}{I_{sat}}$, leads to the expression:

$$\frac{dI}{dz} = -n_{dens}\sigma_0 \frac{I}{1 + I/I_{sat} + 4(\Delta/\Gamma)^2}. \tag{7.6}$$

According to the equipartition law, the mean energy of a particle moving in one dimension is given by $\frac{1}{2}k_BT = \frac{1}{2}m\langle v^2\rangle$, where the particles' velocity follows a Maxwell-

Boltzmann distribution. Furthermore, as already mentioned in Section 3.1.4 the atoms in the MOT undergo a 'random walk' characterized by a momentum diffusion coefficient D_0. Therefore, to describe the evolution of such a system, in other words to derive the equation of motion for a distribution function, a Fokker-Planck equation is used Risken (1996). The solution to this equation for a simple harmonic oscillator gives a Gaussian density distribution. Thus the cloud density distribution is given by normalized Gaussian $n_{dens}(x,y,z) = n_{dens}(x,y)\frac{1}{\sigma_z\sqrt{2\pi}}e^{-z^2/2\sigma_z^2}$, where σ_z is width of the cloud in z direction. Substituting it into Eq. (7.6) and integration along z leads to:

$$\int_{I_0}^{I} \frac{1 + I/I_{sat} + 4(\Delta/\Gamma)^2}{I} dI = -\sigma_0 \int_{-\infty}^{+\infty} n_{dens}(x,y) \frac{1}{\sigma_z\sqrt{2\pi}} e^{-z^2/2\sigma_z^2} dz, \tag{7.7}$$

which gives:

$$(1 + 4\Delta^2/\Gamma^2)\, ln\left(\frac{I}{I_0}\right) + \left(\frac{I - I_0}{I_{sat}}\right) = -\sigma_0 n_{dens}(x,y) = -OD(x,y). \tag{7.8}$$

OD(x,y) represents the integrated optical depth $OD(x,y)$:

$$OD(x,y) = \sigma_0 n_{dens}(x,y) = \sigma_0 \frac{Ne^{\left(\frac{-x^2}{2\sigma_x^2} - \frac{y^2}{2\sigma_y^2}\right)}}{2\pi\sigma_x\sigma_y}, \tag{7.9}$$

where $n(x,y)$ represents the column density at (x,y). In the limit of small intensities of the resonant probe beam, from Eq. (7.8) and Eq. (7.9) it follows:

$$I = I_0 e^{-OD(x,y)}, \tag{7.10}$$

which can be likened to a well known Beer-Lambert law $I = I_0 e^{(\alpha lc)}$, where α is the absorptivity coefficient, l is the length of the path of light propagation through the sample, and c is the concentration of atoms.

Fig. 7.5 depicts the experimental implementation of the absorption imaging. The probe beam is shifted to resonance frequency ($F = 3 \rightarrow F' = 4$ transition of ^{85}Rb) by an AOM, which also enables the changing of the intensity as well as fast switching on/off a beam. To ensure that the beam overlaps with the cloud and that its intensity profile is uniform over the cloud, it is expanded to a diameter of 1 cm by a telescope

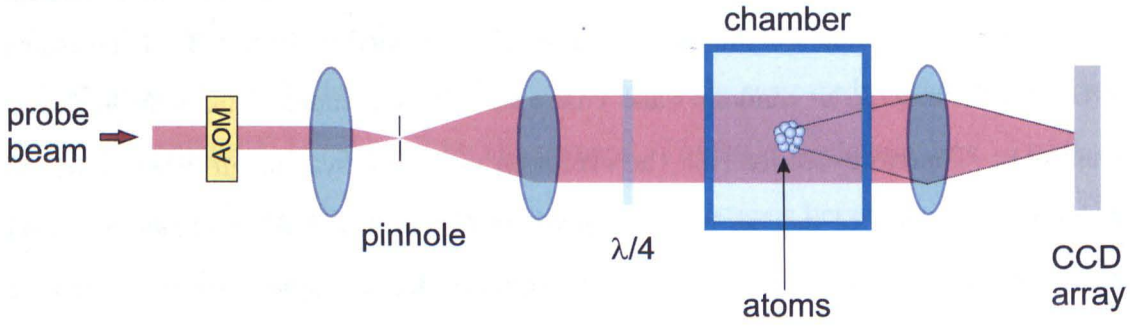

Figure 7.5: Scheme of the experimental set-up for the absorption imaging technique.

and spatially filtered on a 50 μm pinhole to provide a Gaussian profile of the beam. To image a focusing lens is used, placed at $2f$ distance to obtain the magnification close to 1. The quarter-wave plate in front of the chamber is used to adjust the polarisation of the laser beam so that more atoms interact with the beam, which improves the signal to noise ratio. If incorrectly polarized or off-resonant light interacts with the atoms, the measured optical depth will be much lower than the true value.

To experimentally measure the optical depth of the atomic cloud we take two separate images. First the probe beam is transmitted through the atomic cloud and the shadow cast by the atoms in the probe beam (I) is recorded. A second image is taken without the atoms present, but with the probe beam on (I_0). The optical density is given by: $OD(x,y) = -ln(I(x,y)/I_0(x,y))$ and to calculate the I/I_{sat} ratio, each pixel in the images is mathematically processed using MatLab.

Number of atoms

Having obtained the two-dimensional density distribution, parameters such as the widths of the cloud σ_x and σ_y, the coordinates of the center of cloud x_c and y_c, and the maximum optical density max_{OD} can be derived by fitting a 2-D Gaussian function to the data. Subsequently, the total number of atoms $N = 2\pi max_{OD}\sigma_x\sigma_y(1 + I/I_{sat} + 4\Delta^2/\Gamma^2)/\sigma_0$ or the number density of the cloud given by $n_0 = N/(2\pi)^{3/2}\sigma_x^2\sigma_z$ could be calculated. In the second expression it is assumed that the cloud has a cylindrical symmetry along the z axis. This is a justified assumption, given the symmetry of the MOT beams and the magnetic field spatial dependence, thus we can assume $\sigma_y = \sigma_x$.

Both methods of imaging presented are commonly used in experiments with cold atoms. Fig. 7.6 shows the comparison between the images recorded using fluorescence

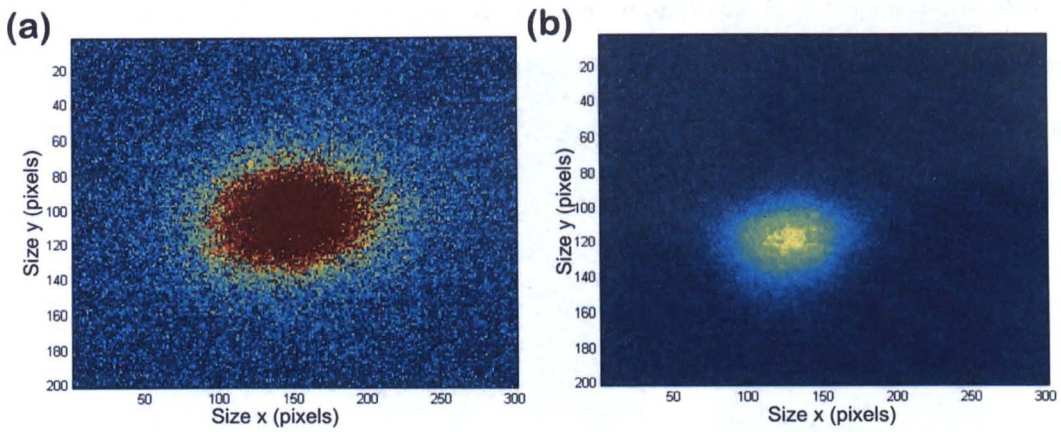

Figure 7.6: Comparison of images of the atoms in the MOT taken with fluorescence and absorption imaging techniques: (a) fluorescence imaging signal recorded with camera gain=200, imaging time=250 μs and Matlab gain=300, (b) absorption imaging signal with camera gain=0, imaging time=50 μs and Matlab gain=1000.

and absorption imaging techniques. The fluorescence imaging requires the cooling and re-pumping beams being on during the recording, thus there is an increased level of stray light as laser beams partially get scattered by parts of the chamber, which contributes to the registered noise. This can be improved by subtracting the background in each shot. The signal can be intensified by increasing the gain of the camera or by increasing the integration time. Instead, during the absorption imaging only the probing beam is on so the main source of noise is the shot noise. However, the fluctuations in the probe intensity are contributing to the uncertainty in the background. In this case taking many images averages the background to zero, but if the number of atoms is small this fluctuations can still dominate the absorption signal (Harsono, 2006). Fig. 7.6 shows typical images recorded with fluorescence (a) and absorption (b) imaging technique after processing the signal recorded on the CCD in MatLab. Although the images were taken with different settings, the signals were optimised to get the best signal to noise ratio. In general, when a small number of atoms is imaged, fluorescence imaging is a preferable method. However to characterize the tetrahedral MOT and to measure its temperature both techniques have been implemented.

7.2.3 Temperature

The temperature of an ultra-cold atomic sample is usually measured using the time of flight (TOF) technique, which relies on the analysis of the spatial distribution of atoms

after they are released from the trap and are let to expand freely. This method was first described by (Lett *et al.*, 1988; Ungar *et al.*, 1989). As the spatial distribution of atoms at any time is a Gaussian, $P(x_i) = \frac{1}{\sqrt{2\pi}\sigma_x} exp(-x_i/2\sigma_x^2)$, where σ_x is the width of the cloud, and the velocity distribution is Maxwellian, $f(v_x) = \left(\frac{m}{2\pi k_B T_x}\right)^{1/2} exp\left(\frac{-mv_x^2}{2k_B T_x}\right)$, thus the expansion of the cloud in one dimension is given by:

$$\sigma_x(t) = \sqrt{\sigma_0^2 + \frac{k_b T_x}{m} t^2}, \tag{7.11}$$

where m is the atomic mass of rubidium. The temperature of atoms can be extracted using the above equation from the gradient of the linear dependence of σ_x^2 against t^2.

7.3 Results and characterisation of the trap

The tetrahedral MOT was designed to operate in the new vacuum. As mentioned restrictions in the optical access made the proper characterisation of the trap difficult to carry out experimentally in those settings. In order to measure temperature of the MOT in the axial and radial directions, the 4-beam MOT was recreated in a different vacuum system (Fig. 7.7 (a)). In this section the results obtained for both set-ups are presented.

4-beam MOT in the old vacuum system

We reproduced our 4-beam MOT in a different vacuum chamber (old vacuum chamber) with easier optical access. The old vacuum chamber, showed in Fig. 7.7 (b), is described in details in (Piotrowicz, 2010). The atoms are confined in a cubical glass cell of side 6 cm. The pressure inside the chamber is maintained at the level of few 10^{-9} Torr by an ion pump. The tetrahedral MOT was recreated in the same configuration as in the new system with a beam incidence angle $\alpha = 13°$. The same coils were used to provide quadrupole magnetic field. In addition, compensation coils have been mounted in the axial direction of the trap. As previously, the coils were separated at distances 12 cm and 13 cm respectively. Due to the design of the old vacuum chamber, the beam path was rotated by 90° thus the axial direction of the trap was in the horizontal direction.

The measurements were carried out using fluorescence imaging technique. The

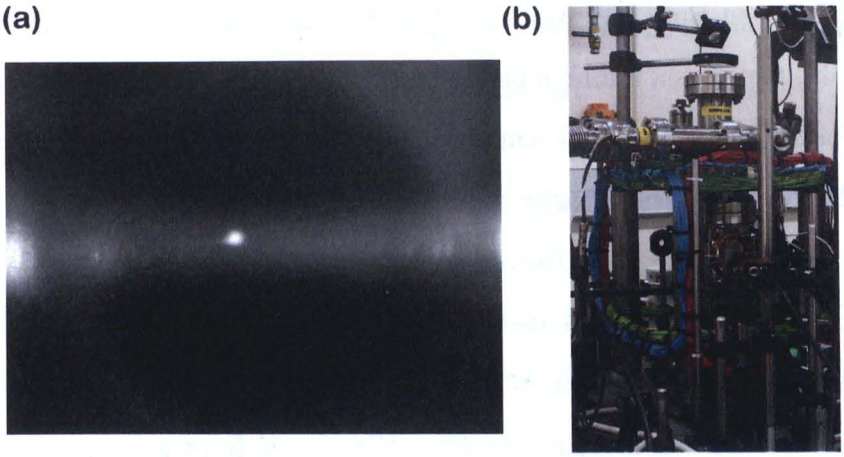

Figure 7.7: The tetrahedral MOT (a) recreated in the old-vacuum system (b).

imaging time was set to 250 μs. In this set-up an imaging lens of focal length 5 cm and diameter 5 cm was placed 10 cm from the trap to provide a magnification factor close to 1. This resulted in a solid angle $\kappa = 0.0156 \pm 0.0009$. To estimate the number of atoms, the quantum efficiency coefficient was measured to be η=250±22 $^{\text{photons}}/_{\text{counts}}$ for the given imaging time. Using Eq. (7.4) we have determined the number of atoms in our MOT to be $2.26 \pm 0.24 \times 10^6$ and the number density 6.33±0.69×10^8 $^{\text{atoms}}/_{\text{cm}^3}$.

To measure the temperature inside the MOT, the trap was loaded for 3.5 s, then the magnetic field and the lasers were switched off letting the atoms expand freely. Subsequently, after a variable delay time, the cooling and re-pumping lasers were switched on and the cloud was imaged for 250 μs. Fig. 7.8 shows the time dependence of the size of the cloud squared and the temperature of the could is derived from the gradient of the linear fit. As it can be noticed, the gradients of the axial and radial directions are clearly different, and the temperatures in these directions are 437 μK± 38 μK and 722 μK± 37 μK respectively. As it was shown in the simulations carried out in Vangeleyn *et al.* (2009), for the angle θ =6.5 °, the relative cooling rate in the axial direction is almost 100% of the rate in a standard MOT configuration, while cooling in the radial direction is only of order of few %. Similarly at that angle the trapping forces are very small in both directions. Thus the difference seen in the temperatures obtained for the axial and radial direction is compatible with the results of the modelling published in (Vangeleyn *et al.*, 2009), as the cooling is more efficient in the axial direction and the atoms display a lower temperature along this axis. The ratio of the damping coeffi-

cients introduced in Eq. (7.3), $\gamma_z/\gamma_r \sim 25$ at $\theta = 6.5°$, suggests that the temperature in the radial direction should be much higher, of the order mK which would probably make the formation of the MOT impossible. It also suggests that the polarization of the upwards beams and its intensity provide for compensation of the cooling force. The spring constant ratio κ_z/κ_r is of the order of 2, thus the trapping force is not influenced that strongly by the beam incidence angle. The interesting observation is that cooling atoms further by adding 10 ms of optical molasses stage, lowers down the temperature of the cloud to 54.4 μK± 11.4 μK and 49.2 μK± 5.5 μK in axial and radial directions and makes them the same within the uncertainties. A reduction in temperature is expected, as the molasses is obtained with much higher detuning, thus its temperature is reduced. However we have not explained how the running of a molasses in this configuration allows for 3-D "thermalization" of the cloud (axial and radial temperatures are the same within uncertainties).

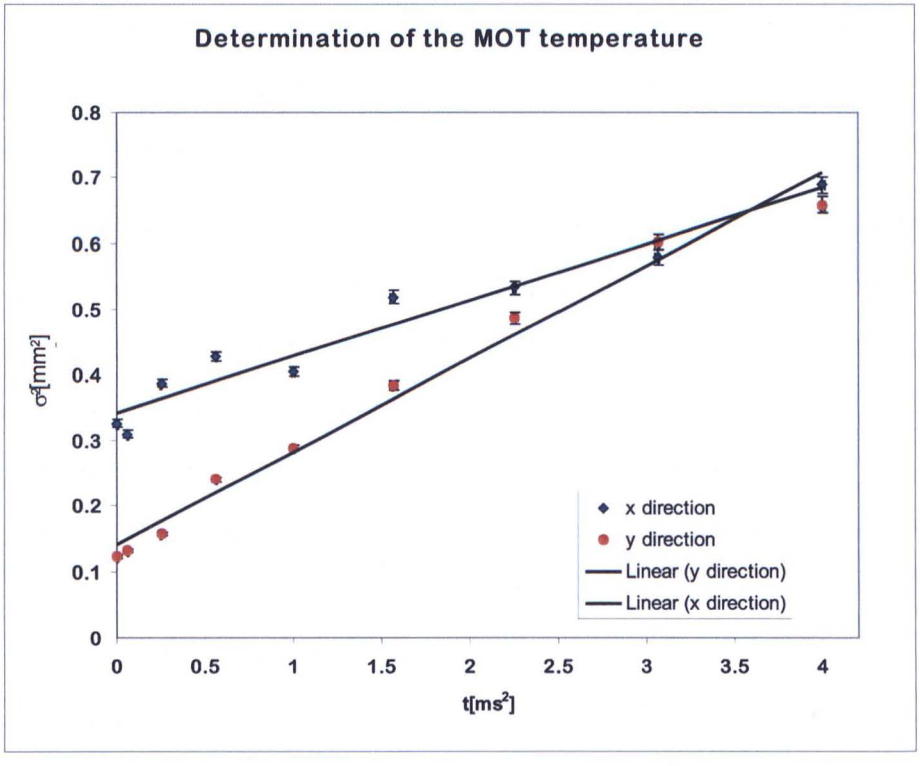

Figure 7.8: The determination of the temperature of atoms in the MOT. The dependence of the size of the cloud on the time of the expansion both squared is presented. The temperature is extract from the fitted gradient.

We have also recorded a trace of the fluorescence of the cloud while loading the MOT. The fluorescence from the MOT is recorded by the photo-diode as a function of

time, and it gives information about the rate at which atoms are loaded into the trap. The dynamics of the loading are described by the equation:

$$\frac{dN}{dt} = R - \frac{N}{\tau} - \beta_L \int n_{MOT}^2 d^3r, \tag{7.12}$$

where N is the number of atoms in the trap, n_{MOT} is its density, R is the loading rate from the background vapour, τ is the lifetime of atoms in the trap limited by collisions with the background gas, β_L is the loss rate due to intra-trap two-body inelastic collisions. Intra-trap collisions include fine and hyper-fine state changing collisions and radiative redistribution collisions. The first and the last occur between excited atoms thus their rate increases with laser intensity. The hyperfine state changing collisions involve ground state atoms thus they dominate at low laser intensities. At low densities, when the trap is loaded, the intra-trap collisions can be neglected, as $\beta_L N^2/V \ll N/\tau$. The solution to the above equation is the exponential function and is thus given by:

$$N(t) = R\tau(1 - e^{-t/\tau}) + R\tau N(0), \tag{7.13}$$

representing the loading rate with the steady state atom number given by $R\tau$ and N(0) is the initial number of atoms in the MOT, and for the trap loaded from the background vapour the initial condition is $N(0) \approx 0$. Fig. 7.9 presents the loading curve of the tetrahedral MOT fitted using the function given by Eq. (7.13). The loading characteristic time is roughly 1 s. In general, the loss rate of trapped cold particles due to collisions with hot atoms of the background gas depends on its density and pressure (Steane *et al.*, 1992):

$$\frac{1}{\tau} = n_b \sigma v_p, \tag{7.14}$$

where n_b is the density of the background gas, σ is the collisional cross-section and v_p is the mean velocity of the background atoms. In the case of the old chamber the density of rubidium vapours is high as the chamber was in use for about 10 years and the ion pump cannot pump out rubidium efficiently. Thus the rapid increase in the number of the trapped atoms in the initial stage of loading. From the fitting, the loading rate is

$1.5 \times 10^6 s^{-1}$.

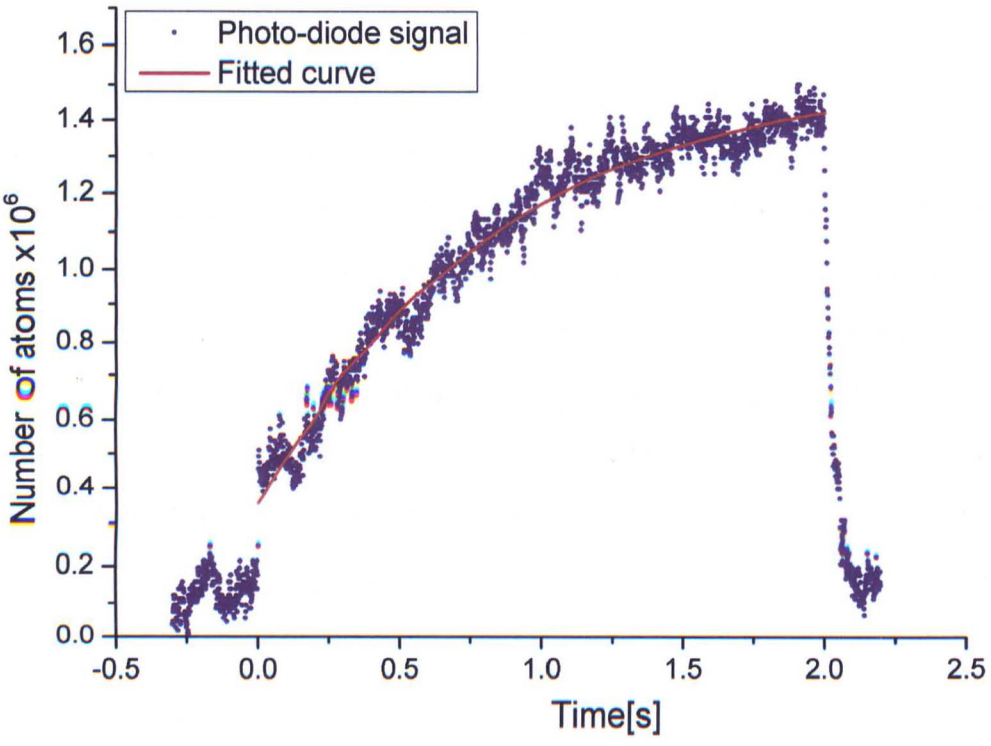

Figure 7.9: The ^{85}Rb MOT loading curve from a background pressure.

4-beam MOT in the new vacuum system

The new vacuum system, presented in Chapter 6 gives limited optical access and there are other experimental restrictions, so it is difficult to fully characterize the trap. The number of atoms inside the MOT was again estimated using fluorescence imaging technique. Typically we trap 1-3 $\times 10^5$atoms. This is significantly lower than in the reference trap presented in the previous section, however there are few discrepancies between the set-ups. The new chamber is supplied with rubidium atoms by a different type of dispensers, which are usually driven at low current so the background pressure of the vapour is not that high as in the old vacuum system. Also there is a metal mesh mounted between the trap and the window which is blocking part of the light collected by the CCD camera. Furthermore, when the measurements were carried out, the cooling laser beam diameter was narrower. The atoms capture rate is proportional

to the surface area of the trapping region and thus is proportional to the square root of to the radius of the laser beam. Additionally the total power of the cooling beams was 30% lower. That explains why the number of confined atoms is clearly lower in the new set-up. The number density is of the order of 2.5×10^8 $^{\text{atoms}}/_{\text{cm}^3}$

Due to the mesh blocking the optical access the measurement of the cloud expansion in the axial direction was impossible. As shown in the previous section, we expect the temperature in the radial direction to be $\sim$ 1 mK. Taking into consideration the small number of atoms in the trap and that the hot cloud expands fast, it was difficult to measure accurately the temperature of the MOT. However, the temperature of the atoms cooled in the optical molasses stage has been determined using absorption imaging technique.

In these settings, the MOT loading time is now roughly 4 s. Thus in a typical experiment the MOT is loaded for 5s, then the atoms are cooled down further in the optical molasses for 10 ms. Fig. 7.10 shows the time dependence of the size of the cloud squared, measured in the radial direction. Similarly, the temperature is extracted from the gradients. We take two measurements of the "radial" temperature along two orthogonal axis of x and y. The temperature has been estimated to be T_x =43.8±4.8 μK and T_y =34.8±2.8 μK. The difference in the temperature can be explained either by the fact that the camera is mounted at the angle of about 25° to the vertical axis and there is a component of a cooling in the axial direction measured too, or that the power is not perfectly balanced by the upwards beams. Having demonstrated the 3-D thermalization in the molasses phase (see Section 7.3) we do expect the temperature in the axial direction to be the same.

The temperature achieved is low enough to allow loading of the dipole trap, as demonstrated in Section 7.4.

The temperatures obtained in the optical molasses in the radial direction in both set-up are similar. The main difference is in the number of the trapped atoms, however as mentioned a fraction of the collected light was blocked and the background pressure of the rubidium atoms is significantly lower in the new set-up. In addition the power and the diameter of the cooling beam was increased when the trap have been recreated in the old system. For comparison a standard MOT operated in the old

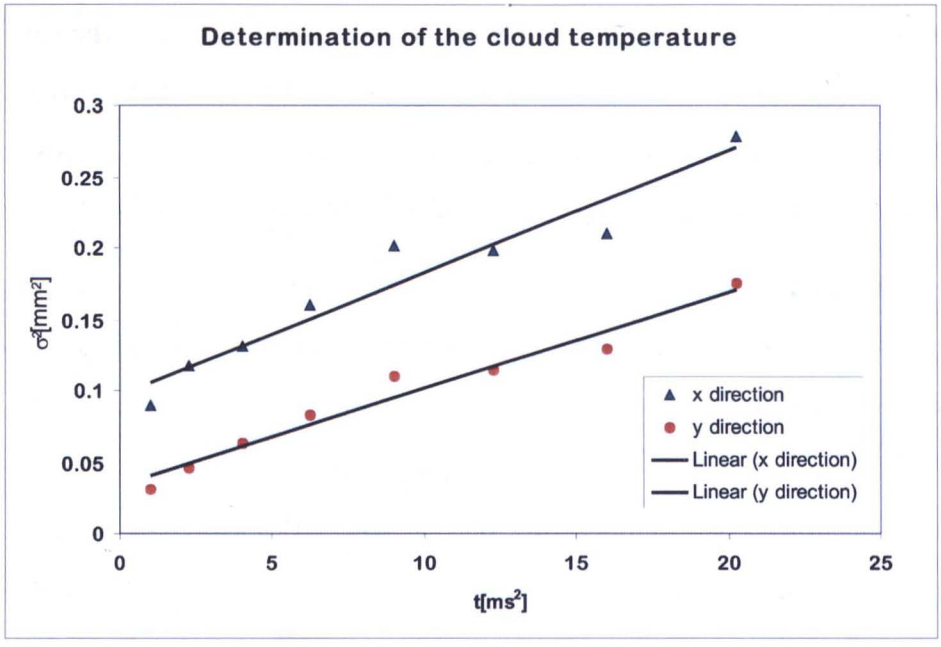

Figure 7.10: The determination of the temperature of atoms confined in the tetrahedral MOT created in the new vacuum system after 10 ms of optical molasses stage. The dependence of the size of the cloud on the time of the expansion both squared is presented. The error bars are not included due to the original data loss.

chamber in standard six-beam configuration, allows us to confine around 3×10^6 atoms, achieving densities of order $10^9\,{}^{\text{atoms}}/_{\text{cm}^3}$ and the temperatures obtained after 10 ms of the optical molasses stage is of order $8\,\mu$K (Piotrowicz, 2010). The cooling and trapping mechanisms in the standard configuration are obviously more effective, however the tetrahedral configuration seems to be a good solution if one needs to gain on the optical access while still using low power coils for the magnetic field.

The tetrahedral MOT operating at such an acute angle is not an easy tool to work with. There were some problems associated with the general performance of the tetrahedral trap, which we have investigated. The most critical factor is to perfectly balance the upward and downwards beams in order to obtain good optical molasses. The beam balancing is slightly different for the MOT and the molasses. Usually during the molasses stage, the detuning of the cooling beam is increased. We have noticed, that this procedure leads to slight changes in the relative powers of the cooling beams as well as in small changes in the beam deflection by the AOM. While the six beam MOT was pretty robust to all that kinds of imperfections in the performance of the laser system, the new set-up is extremely sensitive. In a standard configuration, power

fluctuations in two counter-propagating laser beams cancel each other. In the 4-beam MOT, the fluctuations in the number of atoms and also in the relative position of the trap inside the chamber amplify. This is probably due to the large beam overlapping region, so the MOT has more space where it can form, and any imbalance in the laser power makes it shift mainly in the vertical direction. We have noticed, that even a change in the deflection of the beam coming out of the AOM as low as 1° makes a noticeable change in the position of the MOT beams, as the length of optical path of the laser beam is of order of 3 meters before it reaches the chamber. This again, results in a change of the relative positions of all four beams leading to an imbalance in the cooling forces.

We have also decreased the diameter of the cooling beams to $6mm$, as it makes easier the proper alignment of the beams. However, the total number of trapped atoms went down, as a result one has to choose a good compromise between stable set-up and smaller recapture volume.

7.4 Dipole trapping

In the previous chapters the radiation force which relies on scattering of resonant photons was introduced. Another type of radiation force arises from the interaction of induced electric dipoles with far-detuned light. In such a regime the scattering of atoms is negligible compared to the optical dipole force. It was first observed by Askaryan (1991) that light intensity gradients can exert substantial forces on atoms and few years later Letokhov (1968) suggested to exploit this dipole force to trap the atoms at the nodes (or anti-nodes) of a standing-wave light field detuned far from the atomic resonance. The experimental breakthrough in trapping of neutral atoms was achieved by Chu *et al.* (1985). Sodium atoms cooled in optical molasses have been trapped in the potential created by a strongly focused laser beam detuned by hundred GHz below resonance. Since then the optical dipole traps became a widely used tool for manipulation of atoms as variety of trap shapes and configurations can be created using interference patterns of laser beams (Bergamini *et al.*, 2004).

In this section the physical concept of the dipole trapping will be introduced. The

optical dipole trap implemented in our lab by use of high numerical aperture lens will be described and the initial results of loading of the dipole trap will be presented.

7.4.1 Classical model of the optical dipole force

The electric field $\boldsymbol{E}(\boldsymbol{r},t) = \hat{\boldsymbol{e}}E_0e^{-i\omega_l t} + c.c$ of the laser light oscillating at ω_l induces an atomic dipole moment $\boldsymbol{d}$ oscillating at the same driving frequency ω_l. The amplitude of the dipole moment is given by $\boldsymbol{d} = \alpha\boldsymbol{E}$, where α is the *complex polarizability*, which depends on ω_l as well. In order to calculate the polarizability the atoms are considered in a classical oscillator model (Lorentz model), where an electron (of mass m_e and charge e) is assumed to be elastically bound to the atomic core by a damping harmonic potential. The electron oscillation frequency corresponds to the atomic transition frequency ω_0 and the damping Γ_{ω_l} is due to the radiative energy loss. The classical damping rate is given by $\Gamma_{\omega_l} = \frac{e^2\omega_l^2}{6\pi\epsilon_0 m_e c^3}$. By solving the equation of motion of the electron driven by the laser field, the polarizability can be calculated as (Grimm *et al.*, 1999):

$$\alpha = 6\pi\epsilon_0 c^3 \frac{\Gamma/\omega_0^3}{\omega_0^2 - \omega_l^2 - i(\omega^3/\omega_0^2)\Gamma}, \tag{7.15}$$

where $\Gamma = (\omega_0/\omega_l)^2\Gamma_{\omega_l}$ is the on resonance damping rate. With the above expression for the polarizability two fundamental quantities characterizing a dipole trap, the dipole potential and scattering rate can be derived.

The interaction potential of the induced atomic electric dipole moment $\boldsymbol{d}$ in the laser field is:

$$U_{dip} = -\frac{1}{2}\langle \boldsymbol{d}\cdot\boldsymbol{E}\rangle = -\frac{1}{2\epsilon_0 c} Re(\alpha) I, \tag{7.16}$$

where the brackets denote that the potential is time averaged over the oscillation period and I is the intensity of light given by $I = 2\epsilon_0 c|E_0|^2$ (Grimm *et al.*, 1999). The factor 1/2 points out to the fact that the dipole moment is an induced one. The optical potential is thus proportional to the intensity of the light and to the real part of the polarizability $Re(\alpha)$, describing the in-phase components of the driving field. The dipole force acting on atoms results from the gradient of the interaction potential, $\boldsymbol{F}_{dip}(\boldsymbol{r}) = -\nabla U_{dip}(\boldsymbol{r})$ and thus gradient of the intensity of the light field.

The imaginary part of the polarizability, $Im(\alpha)$ causes the absorption of the radia-

tion of the trapping light. The averaged absorbed power is $P_{abs} = \langle \dot{\boldsymbol{d}} \cdot \boldsymbol{E} \rangle = \frac{\omega_L}{\epsilon_0 c} Im(\alpha) I$. Contrary to classical assumption that the power is emitted continuously, here the absorption and re-emission is interpreted as photons are being scattered in cycles at a rate given by (Grimm *et al.*, 1999):

$$\Gamma_{sc}(\boldsymbol{r}) = \frac{P_{abs}}{\hbar\omega_l} = \frac{1}{\hbar\epsilon_0 c} Im(\alpha) I(\boldsymbol{r}). \tag{7.17}$$

The scattering of photons leads to heating of atoms and their loss from the trap, thus in general a far-detuned regime with $\Gamma_{sc} \ll \Gamma$ is desired. However, if the laser detuning $\Delta = \omega_l - \omega$ is still kept relatively close to atomic resonance, $|\Delta| \ll \omega_0$, the expression for the dipole potential and the scattering take the form (Grimm *et al.*, 1999)

$$U_{dip}(\boldsymbol{r}) = \frac{3\pi c^2}{2\omega_0^3} \frac{\Gamma}{\Delta} I(\boldsymbol{r}) \tag{7.18}$$

$$\Gamma_{sc}(\boldsymbol{r}) = \frac{3\pi c^2}{2\hbar\omega_0^3} \left(\frac{\Gamma}{\Delta}\right)^2 I(\boldsymbol{r}). \tag{7.19}$$

The above equations describe the fundamental physics of dipole trapping. The atoms are attracted into the red-detuned light field ($\Delta < 0$), as the potential is negative, and can be trapped in the potential minimum created at the position of maximum intensity which typically correspond to the focus of laser beam. The blue-detuned light ($\Delta > 0$) repels the atoms as the potential is positive and its minima correspond to points of minimum intensity of light.

The second conclusion resulting from the above equations is the scaling with intensity and detuning law: the dipole potential is proportional to I/Δ whilst the scattering scales as I/Δ^2. Therefore, to minimize the scattering large detuning is required and to maintain the depth of the potential the intensity has to be increased.

The depth of the optical potential is typically of the order of a few mK. Therefore to efficiently load the trap the atoms are first pre-cooled in magneto-optical trap.

7.4.2 Experimental set-up

In our experiment to create the dipole trap we use high numerical aperture lens and the trapping light is detuned by 50 nm from the resonance. The light is provided by a

diode laser operating at 830 nm (DL7032-001) which has the maximum output power of 150 mW. First the laser beam is sent through a single pass AOM operating at about 80 MHz. This provides the remote control over the dipole trap and allows its fast switching. However only about 60% of the initial power comes out in a deflected first order beam. After passing the AOM the beam is coupled to the optical fibre (with efficiency of 60%) the output of which is lifted at the level of the chamber and mounted in a optical bench. Due to the loss of the power on different components of the set-up, we are able to send up to 50 mW of the trapping light to the chamber.

Our goal is to trap small number of atoms, between 1-100. To achieve that two major requirements have to be fulfilled. First, to load the dipole trap with a single atom, the trapping beam should be focused to a waist smaller than 1 μm. In such small trap the collisions between the atoms inside the trap will cause the atoms to be ejected from the trap leaving there 0 or 1 atom (Schlosser *et al.*, 2001). By manipulating the size of the trap, the number of atoms remaining in the trap can be controlled. The fluorescence of such small ensemble will be very small e.g. for 10 μs of imaging time one atom will scatter only about 400 photons during imaging and only a fraction of these photons, determined by the solid angle, will reach the detector. Employing a high numerical aperture lens with small working distance allows to increase the amount of the light reaching the detector. In our set-up we use a lens number 352240 from Geltech (NA=0.5) which has a working distance 6 mm and a diameter of 8 mm. As a result we can collect about 13% of the scattered photons. To record such a small number of photons an intensified CCD camera (ICCD) is used. For even shorter integration time an avalanche photo-diode operating in a single photon count mode can be used.

The aspheric lens we use for imaging is diffraction limited at 780 nm. However, it can be also employed for the creation of the dipole trap using 830 nm laser light. To focus the light to a 1 μm spot using this lens, the incident beam needs to be expanded to 8 mm diameter, which is done by a telescope. The focal points for the two different wavelengths differ by a fraction of mm, therefore by converging or diverging the laser beam for the dipole trap using this telescope, the position of the dipole trap can be manipulated and superimposed with the imaging point.

Fig. 7.11 shows the arrangement of the optics for the dipole trapping and imaging

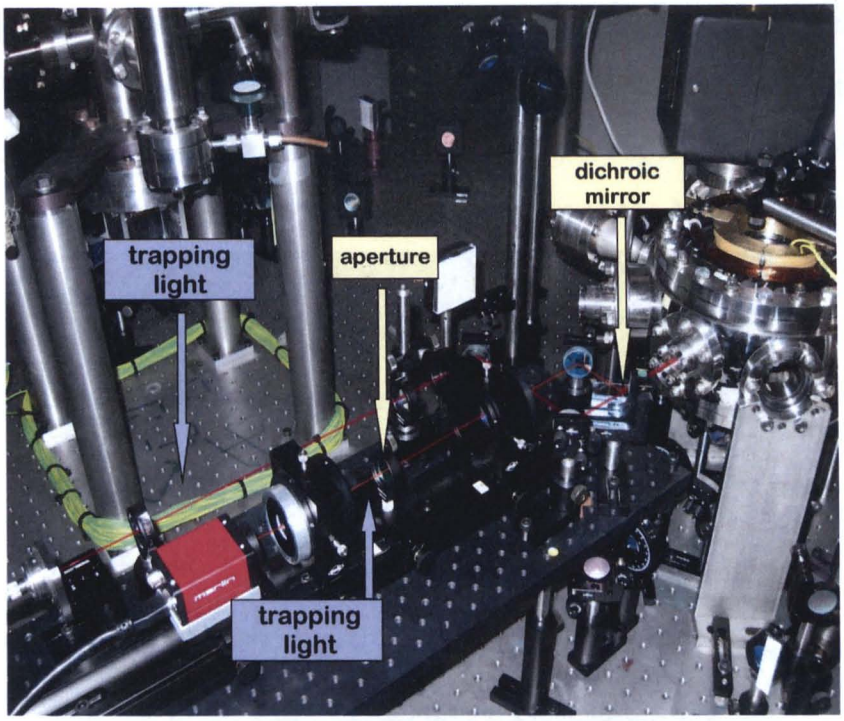

Figure 7.11: The imaging system implemented in our lab. The same aspheric lens is used to create the dipole trap and collect the fluorescence light of trapped atoms.

system. The imaging and trapping optical paths are separated by a dichroic mirror which reflects the 780 nm light and lets the trapping light at 830 nm pass through.

7.4.3 Loading the dipole trap

To load the dipole trap, the magneto-optical trap has to be aligned with the focal point of the trapping beam. In order to do that, a resonant 780 nm light is sent through the chamber using the second aspheric lens whilst the MOT is operating in a continuous mode. The resonant light depletes the number of atoms in the MOT and if a weak laser beam is used, the resonant beam can be observed as the cloud is being split in two parts.

After ensuring that the MOT and the dipole trap are overlapping properly the dipole trap is loaded. The experimental sequence is as follows: the MOT is loaded for 3 ms, the magnetic field is switched off letting the atoms cool in the optical molasses for 5 ms. Then the atoms which are not captured by the dipole trap are let to fall away from the trapping region for about 2.5 ms. During all this time the dipole trap is switched on. Subsequently the cloud was imaged for 25 μs using the absorption

imaging technique described earlier in this chapter. Fig. 7.12 presents the first dipole trap obtained in our lab. A careful analysis of the images gave us the average number of trapped atoms to be 65.

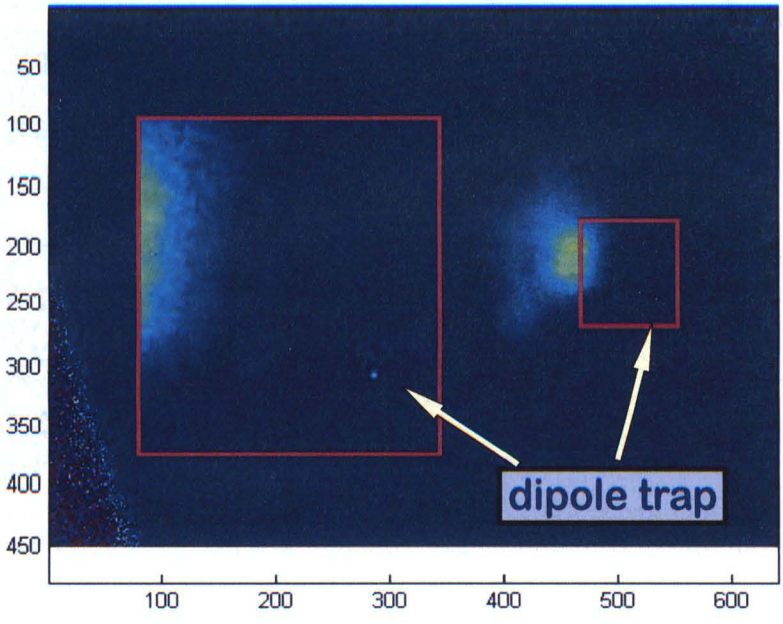

Figure 7.12: Absorption image of the dipole trap, atoms released from the MOT are also visible.

Summary

In this chapter a unique configuration of the magneto-optical trap has been presented. The tetrahedral MOT with a very acute beam intersection angle is extremely difficult to operate and characterized. However, the measurements of the basic parameters of the trap such as number of atoms, density and temperature has been performed using absorption and fluorescence imaging techniques. In a tetrahedral trap the strength of the cooling and trapping forces depends on the beam intersection angle. It has been confirmed experimentally, that the cooling mechanism is more efficient in the axial than in the radial direction. The temperature in the MOT has been measured to be $437\,\mu\text{K}\pm\ 38\,\mu\text{K}$ in the axial and $722\,\mu\text{K}\pm\ 37\,\mu\text{K}$ in the radial direction. Cooling the atoms further in the optical molasses lowers the temperature to about $50\,\mu\text{K}$ in both directions. These measurements of the MOT temperature seem to agree with

the model developed in (Vangeleyn *et al.*, 2009). However the predicted ratio between cooling in axial and radial direction is much higher then the recorded temperatures ratio. It would be interesting to investigate this further. The future work will focus on the investigation of the dependence of the temperature of the MOT in both directions on the laser detuning. Modelling of the cooling in the optical molasses could be carried out to see why the temperature is in this case the same.

The proposed tetrahedral configuration of the MOT is very useful tool in experimental set-ups were the optical access is considerably restrained. In particular we use it as a pre-cooling mechanism for loading the dipole trap created by a high numerical aperture lens which has a working distance $\sim 6\,\mathrm{mm}$ and hinders implementation of a regular 6-beam MOT.

The last section of this chapter introduced far-off resonance dipole traps. In contrast to radiation pressure traps, in dipole traps the atoms can be stored for a long time without changing their internal state and continuous excitation. In addition, such traps allow to achieve the density regime where the Rydberg-Rydberg interactions take place. These make them a useful tool for experiments exploiting neutral atoms for quantum information processing. At this purpose a micron-sized dipole trap has been created in our lab, which has proved to efficiently load an average of 60 atoms.

Their laser frequency can be detuned very far from all atomic resonances, so that it is possible to store atoms without continuous excitation, in contrast to radiation pressure traps such as the MOT. Long-lived internal states can thus be preserved and used for spectroscopic experiments or as quantum memories.

BLANK PAGE IN ORIGINAL

CHAPTER 8

SUMMARY AND FUTURE PLANS

We have developed and built an experimental set-up which enables laser cooling of rubidium atoms and the loading into tightly focused dipole traps. with exception of the laser system for cooling the atoms, the entire set-up was assembled during the course of my PhD. There were few milestones on our path:

- implementation of a two-photon laser scheme for excitation to Rydberg states
- measurements of electric dipole moments and investigation of Cooper minima
- achieving UHV in the new chamber
- the first MOT in the new system
- the loading of the dipole-trap

which have been described in this thesis.

In Chapter 2 a review of the unique properties of Rydberg atoms has been given, placing emphasis on their interactions. The Rydberg blockade effect which is a fundamental component of quantum gates operation, has been elucidated. It has been concluded that Rydberg atoms fulfil all required criteria for successful quantum computation and the progress in this field has been presented. Recent achievements such as the demonstration of the CNOT gate with Rydberg atoms (Isenhower *et al.*, 2010) or the demonstration of full Rydberg blockade in meso-scopic sample (Dudin and Kuzmich, 2012) are very encouraging for our future plans.

The creation of qubits requires the atoms to be cooled and trapped. Chapter 3 introduces atom-light interaction, necessary to explain the laser cooling and the operation of the MOT. The requirements for the experimental realisation of a MOT for rubidium atoms have been introduced in this chapter as well as the laser system used for the cooling of atoms and its stabilisation method.

Chapter 4 gives the insight of the two-photon excitation scheme based on work of McCarron *et al.* (2008) and Abel *et al.* (2009). To provide light for the first transition at 780 nm an extended cavity diode laser has been built. This laser has been stabilised by means of a frequency modulation technique where the error signal is obtained using modulation transfer spectroscopy. The commercial 480 nm laser system for the second transition has been stabilized using FM technique as well. To obtain the error signal the electromagnetically induced transparency spectroscopy is employed. The laser frequency stabilisation system was successfully implemented to provide us with two narrow laser sources, frequency stabilized and locked to each other. As a result the reference frequencies for excitation of rubidium atoms to n states as high as 90 are achievable.

Setting the excitation lasers for a two-photon excitation scheme opens up the possibilities of EIT spectroscopy. We employed EIT to measure the electric dipole moments for the $5p_{3/2} \rightarrow nD_{5/2}$ transitions to the Rydberg states in rubidium (Piotrowicz *et al.*, 2011), which was described in Chapter 5. Investigation of the electromagnetically induced transparency and Autler-Townes splitting in ultra-cold sample allowed to extract the Rabi frequency of the probed transition. The dipole moments have been extracted from the dependence of the Rabi frequency on the square root of the power of the coupling laser. The data have been compared to semi-classical models based on Coulomb approximation. Particularly good agreement with the D'yachkov-Pankratov model has been observed. This model has been later used to investigate the structure of the Cooper minima in the transition probabilities for low excited nS, nP, nD and nF states of alkali atoms (Beterov *et al.*, 2012). As a result so far unknown Cooper minima have been identified for rubidium, which are presented in the form of density plots. We concluded that DP model provides reliable and fast method of calculations of the radial matrix elements for bound-bound, bound-free and free-free transitions.

The above results help us to understand the spectroscopic properties of Rydberg atoms, which is essential in our experiment. Furthermore, the method developed for fitting absorption profiles of electromagnetically induced transparency spectra can be used for recently proposed method of optical imaging of individual Rydberg atoms (Günter *et al.*, 2012). This method exploits the interaction induced shifts on energy levels of Rydberg atoms, which can be spatially resolved using electromagnetically induced transparency, to optically detect the Rydberg excitation without destroying the sample.

The setting up of a new apparatus and the detailed description of all its components have been presented in Chapter 6. The biggest advantage of our new vacuum chamber is that a high numerical aperture aspheric lens can be placed inside the chamber, close to the atoms reservoir. Adding a programmable spatial light modulator will allow us to create arrays of micron-sized dipole traps for registers of meso-qubits. The lens also enables detection of weak fluorescence even coming from single atoms. An alternative method of detection of Rydberg atoms is also possible in our set-up, exploiting selective field ionisation. Obtaining UHV was challenging and time consuming. All the parts have been cleaned, and the system was baked for couple of days at 150 °C. We have obtained a pressure of order 10^{-10} Torr, which is low enough to load a controlled number of atoms in the dipole trap.

The design of the new chamber and in particular the small working distance of the imaging lens, restricts the optical access. Therefore, a unique configuration of the magneto-optical trap has been implemented in our experiment. The tetrahedral MOT with very acute beam intersection angle has been presented in Chapter 7. A characterisation of the MOT has been performed using absorption and fluorescence imaging techniques. In the tetrahedral configuration the beam intersection angle influences the efficiency of the cooling and trapping forces in the radial and axial direction, as was shown in Vangeleyn *et al.* (2009). We have measured the temperature in the MOT and yield 437 μK$\pm$ 38 μK and 722 μK$\pm$ 37 μK in the axial and radial direction respectively. We have confirmed that the cooling mechanism is much more efficient in the axial direction. Cooling the atoms further in the optical molasses lower the temperature to about 50 μK in both directions. This result is rather surprising, as we plan to investi-

gate further how this configuration allows for 3-D thermalization in the molasses stage. The densities achievable in our MOT are of order 10^8 atoms/cm^3, which is not enough to investigate Rydberg-Rydberg interactions. Therefore a far-detuned optical dipole trap is added to the set-up. Focusing the beam to a waist size of 1 μm allows to achieve a trap depth of the order few mK. Using our tetrahedral MOT, and cooling the atoms for 10 ms in optical molasses we managed to load the dipole trap with about 60 atoms. The MOT provides a cold diluted cloud of atoms that efficiently loads the microscopic dipole trap.

Future work of course will focus on creation of meso-qubit. The first task will be to improve the loading of atoms into the dipole trap and the optimisation of the detection system. A spatial light modulator will also be included in the set-up which will allow to create arrays of dipole traps and design patterns for their geometrical distribution.

In parallel we want to investigate further the cooling mechanism of our tetrahedral trap. The MOT temperature measured in axial and radial direction seem to agree with the theoretical model developed in (Vangeleyn *et al.*, 2009). However, the predicted ratio between cooling in axial and radial direction is much higher then the ratio measured. A dedicated modelling of the cooling and trapping for our particular case could be done and more systematic measurements at different angles should be taken for a thorough comparison of the results to the theory.

BIBLIOGRAPHY

Abel, R. P.; Mohapatra, A. K.; Bason, M. G.; Pritchard, J. D.; Weatherill, K. J.; Raitzsch, U. and Adams, C. S.: *Laser frequency stabilization to excited state transitions using electromagnetically induced transparency in a cascade system*; Applied Physics Letters (2009): **94**; 071107

Amthor, T.: *Interaction-Induced Dynamics in Ultracold Rydberg Gases âĂŞ Mechanical Effects and Coherent Processes*; Ph.D. thesis; Mathematik und Physik, Albert-Ludwigs-Universität Freiburg (2008)

Amthor, T.; Denskat, J.; Giese, C.; Bezuglov, N. N.; Ekers, A.; Cederbaum, L. S. and Weidemuller, M.: *Autoionization of an ultracold Rydberg gas through resonant dipole coupling*; Eur. Phys. J. (2009): **53**; pp. 329

Arnold, A.: *Cool things you can do with lasers*; Ph.D. thesis; University of Otago (1996)

Arnold, A. S.; Wilson, J. S. and Boshier, M. G.: *A simple extended-cavity diode laser*; Review of Scientific Instruments (1998): **69**; pp. 1236

Askaryan, G. A.: *Effect of the field gradient of an intense electromagnetic beam on electrons and atoms* (1991): ; pp. 1567

Atkins, P. and Friedman, R.: *Molecular Quantum Mechanics*; Oxford Univeristy Press, Oxford; 4th edition (2005)

Autler, S. H. and Townes, C. H.: *Stark Effect in Rapidly Varying Fields*; Phys. Rev. (1955): **100**; pp. 703

Aymar, M.: *Theoretical investigation on photoionization from Rydberg states of lithium, sodium and potassium*; J. Phys .B (1978): **1413**; p. 11

Baig, M. A.; Mahmood, S.; Kalyar, M. A.; Rafiq, M.; Amin, N. and Haq, S. U.: *Oscillator strength measurements of the 3p → nd Rydberg transitions of sodium*; The European Physical Journal D - Atomic, Molecular, Optical and Plasma Physics (2007): **44**; pp. 9

Balmer, J.: *Notiz über die Spektrallinien des Wasserstoffs (A note on the spectral lines of hydrogen)*; Annual Review of Physical Chemistry (1885): **25**; p. 80

Bason, M. G.; Mohapatra, A. K.; Weatherill, K. J. and Adams, C. S.: *Electro-optic control of atom-light interactions using Rydberg dark-state polaritons*; Phys. Rev. A (2008): **77**; p. 032305

Bates, D. R.: *The Quantal Calculation of the Photo-Ionization Cross-Section of Atomic Potassium*; Proc. R. Soc. Lond. A (1947): **188**; pp. 350

Bates, D. R. and Damgaard, A.: *The Calculation of the Absolute Strengths of Spectral Lines*; Philosophical Transactions of the Royal Society of London. Series A, Mathematical and Physical Sciences (1949): **242**; pp. 101

Bergamini, S.; Darquié, B.; Jones, M.; Jacubowiez, L.; Browaeys, A. and Grangier, P.: *Holographic generation of microtrap arrays for single atoms by use of a programmable phase modulator*; J. Opt. Soc. Am. B (2004): **21**; pp. 1889

Bersuker, I. B.: *Effect of the core on transitions of optical electrons*; Opt. Spektrosk (1957): **3**; pp. 97

Beterov, I. I.; Mansell, C. W.; Yakshina, E. A.; Ryabtsev, I. I.; Tretyakov, D. B.; Entin, V. M.; MacCormick, C.; Piotrowicz, M. J.; Kowalczyk, A. and Bergamini, S.: *Cooper minima in the transitions from low-excited and Rydberg states of alkali-metal atoms*; ArXiv e-prints (2012):

Beterov, I. I.; Ryabtsev, I. I.; Tretyakov, D. B. and Entin, V. M.: *Quasiclassical calculations of blackbody-radiation-induced depopulation rates and effective lifetimes of Rydberg nS, nP, and nD alkali-metal atoms with* $n \leq 80$; Phys. Rev. A (2009): **79**; p. 052504

Beterov, I. I.; Tretyakov, D. B.; Entin, V. M.; Yakshina, E. A.; Ryabtsev, I. I.; MacCormick, C. and Bergamini, S.: *Deterministic single-atom excitation via adiabatic passage and Rydberg blockade*; Phys. Rev. A (2011): **84**; p. 023413

Bethe, H. A. and E., S. E.: *Quantum Mechanics of One- and Two-Electron Atoms*; Springer (1957)

Birnbaum, K. M.: *Ultra-High Vacuum Chambers* (2005):

Bjorklund, G. C.: *Frequency-modulation spectroscopy: a new method for measuring weak absorptions and dispersions*; Opt. Lett. (1980): **5**; pp. 15; iBM Invention Disclosure SA 8790135 (March 1979); U.S. Patent 4, 297, 035 (November 1981)

Bjorklund, G. C.; Levenson, M. D.; Lenth, W. and Ortiz, C.: *Frequency modulation (FM) spectroscopy*; Applied Physics B: Lasers and Optics (1983): **32**; pp. 145

Blatt, R. and Wineland, D.: *Entangled states of trapped atomic ions*; Nature (London) (2008): **453**; pp. 1008

Bohr, N.: *On the Constitution of Atoms and Molecules*; Philosophical Magazine (1913): **26**; pp. 1

Boller, K.-J.; Imamolu, A. and Harris, S. E.: *Observation of electromagnetically induced transparency*; Phys. Rev. Lett. (1991): **66**; pp. 2593

Branden, D. B.; Juhasz, T.; Mahlokozera, T.; Vesa, C.; Wilson, R. O.; Zheng, M.; Kortyna, A. and Tate, D. A.: *Radiative lifetime measurements of rubidium Rydberg states*; J. Phys. B (2010): **43**; p. 015002

Bransden, B. and Joachain, C.: *Physics of atoms and molecules*; Pearson Education; Prentice Hall (2003)

Brink, D. and Satchler, G.: *Angular Momentum*; Oxford Science Publications; Oxford University Press, USA (1994)

Camy, G.; BordÃľ, C. and Ducloy, M.: *Heterodyne saturation spectroscopy through frequency modulation of the saturating beam*; Optics Communications (1982): **41**; pp. 325

Chaves, R. and Davidovich, L.: *Robustness of entanglement as a resource*; Phys. Rev. A (2010): **82**; p. 052308

Chéron, B.; Gilles, H.; Hamel, J.; Moreau, O.; and Sorel, H.: *Laser frequency stabilization using Zeeman effect*; J. Phys. III France (1994): **4**; pp. 401

Chesman, C.; Lima, E. G.; de Oliveira, F. A. M.; Vianna, S. S. and Tabosa, J. W. R.: *Two- and four-beam magneto-optical trapping of neutral atoms*; Optics Letters (1994): **19**; pp. 1237

Chu, S.; Bjorkholm, J. E.; Ashkin, A. and Cable, A.: *Experimental Observation of Optically Trapped Atoms*; Phys. Rev. Lett. (1986): **57**; pp. 314

Chu, S.; Hollberg, L.; Bjorkholm, J. E.; Cable, A. and Ashkin, A.: *Three-dimensional viscous confinement and cooling of atoms by resonance radiation pressure*; Phys. Rev. Lett. (1985): **55**; pp. 48

Clarke, J. and Wilhelm, F. K.: *Superconducting quantum bits*; Nature (2008): **453**; pp. 1031

Cooper, J. W.: *Photoionization from outer atomic subshells. A model study*; Phys .Rev. (1962): **128**; p. 681

Crowe, J. W. and R. M. Craig, J.: *Small-signal amplification in GaAs laserS*; Applied Physics Letters (1964): **4**; pp. 57

Dalibard, J. and Cohen-Tannoudji, C.: *Laser cooling below the Doppler limit by polarization gradients: simple theoretical models*; J. Opt. Soc. Am. B (1989): **6**; pp. 2023

Davydkin, V. A. and Zon, B. A.: *Radiation and polarization characteristics of Rydberg atomic states*; Optics and Spectroscopy (1981): **51**; pp. 13

DiVincenzo, D. P.: *The Physical Implementation of Quantum Computation*; Fortschritte der Physik (2000): **48**; pp. 771

Drever, R. W. P.; Hall, J. L.; Kowalski, F. V.; Hough, J.; Ford, G. M.; Munley, A. J. and Ward, H.: *Laser phase and frequency stabilization using an optical resonator*; Applied Physics B: Lasers and Optics (1983): **31**; pp. 97; r. W. P. Drever, J. L. Hall, F. V. Kowalski, J. Hough, G. M. Ford, and A. J. Munley, Joint Institute for Laboratory Astrophysics, University of Colorado and National Bureau of Standards, Boulder, Colo. 80309 (personal communication, 1979)

Dudin, Y. O. and Kuzmich, A.: *Strongly Interacting Rydberg Excitations of a Cold Atomic Gas*; Science (2012): **336**; pp. 887

Dumke, R.; Volk, M.; Müther, T.; Buchkremer, F. B. J.; Birkl, G. and Ertmer, W.: *Micro-optical Realization of Arrays of Selectively Addressable Dipole Traps: A Scalable Configuration for Quantum Computation with Atomic Qubits*; Phys. Rev. Lett. (2002): **89**; p. 097903

Dür, W.; Vidal, G. and Cirac, J. I.: *Three qubits can be entangled in two inequivalent ways*; Phys. Rev. A (2000): **62**; p. 062314

D'yachkov, L. G. and Pankratov, P. M.: *On the use of the semiclassical approximation for the calculation of oscillator strengths and photoionization cross sections*; Journal of Physics B: Atomic, Molecular and Optical Physics (1994): **27**; p. 461

Fabry, M. and Cussenot, J. R.: *Photoionization from the $6p^2P_{3/2}$ state of neutral cesium*; Can. J. Phys. (1976): **54**; p. 836

Fano, U. and Cooper, J. W.: *Spectral distribution of atomic oscillator strengths*; Rev. Mod. Phys. (1968): **40**; p. 441

Feng, Z. G.; Zhang, L. J.; Zhao, J. M.; Li, C. Y. and Jia, S. T.: *Lifetime measurement of ultracold caesium Rydberg states*; J. Phys. B (2009): **42**; p. 145303

Fleischhauer, M.; Imamoglu, A. and Marangos, J. P.: *Electromagnetically induced transparency: Optics in coherent media*; Reviews of Modern Physics (2005): **77**; pp. 633

Foot, C. J.: *Atomic Physics*; Oxford University Press (2005)

Frese, D.; Ueberholz, B.; Kuhr, S.; Alt, W.; Schrader, D.; Gomer, V. and Meschede, D.: *Single Atoms in an Optical Dipole Trap: Towards a Deterministic Source of Cold Atoms*; Phys. Rev. Lett. (2000): **85**; pp. 3777

Frisch, R.: *Experimenteller Nachweis des Einsteinschen Strahlungsrückstoßes*; Zeitschrift für Physik A Hadrons and Nuclei (1933): **86**; pp. 42

Gaëtan, A.; Miroshnychenko, Y.; Wilk, T.; Chotia, A.; Viteau, M.; Comparat, D.; Pillet, P.; Browaeys, A. and Grangier, P.: *Observation of collective excitation of two individual atoms in the Rydberg blockade regime*; Nature Physics (2009): **5**; pp. 115

Gallagher, T. F.: *Rydberg atoms*; Cambridge University Press (1994)

Gallagher, T. F. and Cooke, W. E.: *Interactions of Blackbody Radiation with Atoms*; Phys. Rev. Lett. (1979): **42**; pp. 835

Gea-Banacloche, J.; Li, Y.-q.; Jin, S.-z. and Xiao, M.: *Electromagnetically induced transparency in ladder-type inhomogeneously broadened media: Theory and experiment*; Phys. Rev. A (1995): **51**; pp. 576

Gibble, K. E.; Kasapi, S. and Chu, S.: *Improved magneto-optic trapping in a vapor cell*; Opt. Lett. (1992): **17**; pp. 526

Grimm, R.; Weidemüller, M. and Ovchinnikov, Y. B.: *Optical dipole traps for neutral atoms*; ArXiv Physics e-prints (1999):

Günter, G.; Robert-de Saint-Vincent, M.; Schempp, H.; Hofmann, C. S.; Whitlock, S. and Weidemüller, M.: *Interaction Enhanced Imaging of Individual Rydberg Atoms in Dense Gases*; Phys. Rev. Lett. (2012): **108**; p. 013002

Hall, R. N.; Fenner, G. E.; Kingsley, J. D.; Soltys, T. J. and Carlson, R. O.: *Coherent Light Emission From GaAs Junctions*; Phys. Rev. Lett. (1962): **9**; pp. 366

Hänsch, T. W. and B., C.: *Laser frequency stabilization by polarization spectroscopy of a reflecting reference cavity*; Optics Communications (1980): **35**; pp. 441

Hänsch, T. W. and Schawlow, A. L.: *Cooling of gases by laser radiation*; Optics Communications (1975): **13**; pp. 68

Haroche, S.; Goy, P.; Raimond, J. M.; Fabre, C. and Gross, M.: *Exploration of Radiative Properties of Very Excited Atoms*; Royal Society of London Philosophical Transactions Series A (1982): **307**; pp. 659

Harris, S. E.: *Lasers without inversion: Interference of lifetime-broadened resonances*; Phys. Rev. Lett. (1989): **62**; pp. 1033

Harsono, A.: *Dipole trapping and manipulation of ultra-cold atoms*; Ph.D. thesis; University of Oxford (2006)

Haubrich, D.; Schadwinkel, H.; Strauch, F.; Ueberholz, B.; Wynands, R. and Meschede, D.: *Observation of individual neutral atoms in magnetic and magneto-optical traps*; Europhysics Letters (1996): **34**; p. 663

Hawthorn, C. J.; Weber, K. P. and Scholten, R. E.: *Littrow configuration tunable external cavity diode laser with fixed direction output beam*; Review of Scientific Instruments (2001): **72**; pp. 4477

Henry, C.: *Theory of the linewidth of semiconductor lasers*; IEEE Journal of Quantum Electronics (1982): **18**; pp. 259

Hoogenraad, J. H. and Noordam, L. D.: *Rydberg atoms in far-infrared radiation fields. I. Dipole matrix elements of H, Li, and Rb*; Phys. Rev. A (1998): **57**; pp. 4533

Hopper, D. J.: *Investigation of laser frequency stabilisation using modulation transfer spectroscopy*; Ph.D. thesis; Queensland University of Technology (2008)

Hudson, R. D. and Carter, V. L.: *Atomic absorption cross-sections of lithium and sodium between 600 and 1000 Å**; Journ. Opt. Soc. Am. (1967): **651**; p. 57

Hussain, S.; Saleem, M. and Baig, M. A.: *Measurement of oscillator strength distribution in the discrete and continuous spectrum of lithium*; Phys. Rev. A (2007): **75**; p. 022710

Isenhower, L.; Urban, E.; Zhang, X. L.; Gill, A. T.; Henage, T.; Johnson, T. A.; Walker, T. G. and Saffman, M.: *DemoIsenhower2010nstration of a Neutral Atom Controlled-NOT Quantum Gate*; Phys. Rev. Lett. (2010): **104**; p. 010503

Jaatinen, E.: *Theoretical determination of maximum signal levels obtainable with modulation transfer spectroscopy*; Optics Communications (1995): **120**; pp. 91

Jaksch, D.; Cirac, J. I.; Zoller, P.; Rolston, S. L.; Côté, R. and Lukin, M. D.: *Fast Quantum Gates for Neutral Atoms*; Phys. Rev. Lett. (2000): **85**; pp. 2208

Kaulakys, B.: *Consistent analytical approach for the quasi-classical radial dipole matrix elements*; J. Phys. B (1995): **28**; p. 4963

Klarsfeld, S.: *Alternative forms of the Coulomb approximation for bound-bound multipole transitions*; Phys. Rev. A (1989): **39**; pp. 2324

Kocharovskaya, O. A. and Khanin, Y. I.: *Coherent amplification of an ultrashort pulse in a three-level medium without a population inversion*; Pis'ma v Zhurnal Eksperimental'noi i Teoreticheskoi Fiziki (1988): **48**; pp. 581

Kok, P.; Munro, W. J.; Nemoto, K.; Ralph, T. C.; Dowling, J. P. and Milburn, G. J.: *Linear optical quantum computing with photonic qubits*; Rev. Mod. Phys. (2007): **79**; pp. 135

Lee, K. I.; Kim, J. A.; Noh, H. R. and Jhe, W.: *Single-beam atom trap in a pyramidal and conical hollow mirror*; Opt. Lett. (1996): **21**; pp. 1177

Letokhov, V. S.: *Doppler line narrowing in a standing light wave*; JETP Lett. (1968): **7**; p. 272; original Pis'ma Zh. Eksp. Teor. Fiz. 7, 348 (1968)

Lett, P. D.; Watts, R. N.; Westbrook, C. I.; Phillips, W. D.; Gould, P. L. and Metcalf, H. J.: *Observation of Atoms Laser Cooled below the Doppler Limit*; Phys. Rev. Lett. (1988): **61**; pp. 169

Li, W.; Mourachko, I.; Noel, M. W. and Gallagher, T. F.: *Millimeter-wave spectroscopy of cold Rb Rydberg atoms in a magneto-optical trap: Quantum defects of the ns, np, and nd series*; Phys. Rev. A (2003*a*): **67**; p. 052502

Li, X.; Wu, Y.; Steel, D.; Gammon, D.; Stievater, T. H.; Katzer, D. S.; Park, D.; Piermarocchi, C. and Sham, L. J.: *An All-Optical Quantum Gate in a Semiconductor Quantum Dot*; Science (2003*b*): **301**; pp. 809

Lindquist, K.; Stephens, M. and Wieman, C.: *Experimental and theoretical study of the vapor-cell Zeeman optical trap*; Phys. Rev. A (1992): **46**; pp. 4082

Liveing, G. D. and Dewar, J.: *On the Spectra of Sodium and Potassium*; Proceedings of the Royal Society of London (1879): **29**; pp. 398

Lorenzen, C.-J. and Niemax, K.: *Quantum Defects of the n^2 $P_{1/2,3/2}$ Levels in ^{39}K I and ^{85}Rb I*; Physica Scripta (1983): **27**; p. 300

Loudon, R.: *The quantum theory of light.*; Oxford Science Publications (1973)

Lukin, M. D.; Fleischhauer, M.; Cote, R.; Duan, L. M.; Jaksch, D.; Cirac, J. I. and Zoller, P.: *Dipole Blockade and Quantum Information Processing in Mesoscopic Atomic Ensembles*; Phys. Rev. Lett. (2001): **87**; p. 037901

Ma, L.-S. and Hall, J.: *Optical heterodyne spectroscopy enhanced by an external optical cavity: toward improved working standards*; Quantum Electronics, IEEE Journal of (1990): **26**; pp. 2006

Marcassa, L. G.: *Measurement of Rydberg state lifetimes using cold trapped neutral atoms*; Physica Scripta (2009): **2009**; p. 014011

Marinescu, M.; Sadeghpour, H. R. and Dalgarno, A.: *Dispersion coefficients for alkali-metal dimers*; Phys. Rev. A (1994): **49**; pp. 982

McCarron, D. J.; King, S. A. and Cornish, S. L.: *Modulation transfer spectroscopy in atomic rubidium*; Measurement Science and Technology (2008): **19**; pp. 105601

Metcalf, H. J. and van der Straten, P.: *The Quest for BEC*; Wiley-VCH (2003)

Mohapatra, A. K.; Jackson, T. R. and Adams, C. S.: *Coherent Optical Detection of Highly Excited Rydberg States Using Electromagnetically Induced Transparency*; Phys. Rev. Lett. (2007): **98**; p. 113003

Monroe, C.; Swann, W.; Robinson, H. and Wieman, C.: *Very cold trapped atoms in a vapor cell*; Phys. Rev. Lett. (1990): **65**; pp. 1571

Moore, G. E.: *Cramming more components onto integrated circuits*; Electronics Magazine (1965): **38**; p. 4

Msezane, A. Z. and Manson, S. T.: *Generality and systematics of multiple mininma in photoionization cross-sections of excited atoms*; Phys. Rev. Lett (1982): **473**; p. 48

Nadeem, A. and Haq, S. U.: *Photoionization from the $6p^2P_{3/2}$ state of neutral cesium*; Phys. Rev. A (2010): **81**; p. 063432

Nadeem, A. and Haq, S. U.: *Photoionization from the $5p^2P_{3/2}$ state of rubidium*; Phys. Rev. A (2011): **83**; p. 063404

Nawaz, M.; Farooq, W. A. and Connerade, J. P.: *The influence on the Paschen-Back effect on magneto-optical rotation spectra*; Journal of Physics B: Atomic, Molecular and Optical Physics (1992*a*): **25**; p. 3283

Nawaz, M.; Farooq, W. A. and Connerade, J. P.: *Magneto-optical spectra of lithium and sodium*; Journal of Physics B: Atomic, Molecular and Optical Physics (1992*b*): **25**; p. 5327

Nielsen, M. and Chuang, I.: *Quantum computation and quantum information*; Cambridge Series on Information and the Natural Sciences; Cambridge University Press (2000)

Osterwalder, A. and Merkt, F.: *Using High Rydberg States as Electric Field Sensors*; Phys. Rev. Lett. (1999): **82**; pp. 1831

Ovsiannikov, V. D.; Derevianko, A. and Gibble, K.: *Rydberg Spectroscopy in an Optical Lattice: Blackbody Thermometry for Atomic Clocks*; Phys. Rev. Lett. (2011): **107**; p. 093003

Pearman, C. P.; Adams, C. S.; Cox, S. G.; Griffin, P. F.; Smith, D. A. and Hughes, I. G.: *Polarization spectroscopy of a closed atomic transition: applications to laser frequency locking*; Journal of Physics B Atomic Molecular Physics (2002): **35**; pp. 5141

Photonics, T.: *Sys DC 110, Diode Laser Supply Electronics* (2007):

Piotrowicz, M. J.: *Ultra-cold rydberg atoms*; Ph.D. thesis; The Open University (2010)

Piotrowicz, M. J.; MacCormick, C.; Kowalczyk, A.; Bergamini, S.; Beterov, I. I. and Yakshina, E. A.: *Measurement of the electric dipole moments for transitions to rubidium Rydberg states via Autler-Townes splitting*; New Journal of Physics (2011): **13**; p. 093012

Pollock, S.; Cotter, J. P.; Laliotis, A. and Hinds, E. A.: *Integrated magneto-optical traps on a chip using silicon pyramid structures*; Opt. Express (2009): **17**; pp. 14109

Pollock, S.; Cotter, J. P.; Laliotis, A.; Ramirez-Martinez, F. and Hinds, E. A.: *Characteristics of integrated magneto-optical traps for atom chips*; New Journal of Physics (2011): **13**; p. 043029

Potvliege, R. M. and Adams, C. S.: *Photoionization in far-off-resonance optical lattices*; New Journal of Physics (2006): **8**; p. 163

Prentiss, M. G.; Peuse, B. W.; Sanders, G. A. and Ezekiel, S.: *Quantum Electronics, Progress Report 123*; Technical report; Research Laboratory of Electronics at the Massachusetts Institute of Technology (1981)

Raab, E. L.; Prentiss, M.; Cable, A.; Chu, S. and Pritchard, D. E.: *Trapping of Neutral Sodium Atoms with Radiation Pressure*; Phys. Rev. Lett. (1987): **59**; pp. 2631

Rabi, I. I.: *Space Quantization in a Gyrating Magnetic Field*; Physical Review (1937): **51**; pp. 652

Riehle, F.: *Frequency Standards: Basics and Applications*; Wiley-VCH (2004)

Risken, H.: *The Fokker-Planck Equation: Methods of Solution and Applications*; Springer Series in Synergetics; Springer (1996)

Robins, N. P.; Slagmolen, B. J. J.; Shaddock, D. A.; Close, J. D. and Gray, M. B.: *Interferometric, modulation-free laser stabilization*; Optics Letters (2002): **27**; pp. 1905

Rydberg, J.: *Recherches sur la constitution des spectres d'émission des éléments chimiques*; Kungliga Svenska Vetenskaps Akademiens Handlingar (1889): **23**

SAES getters: *Alkali metal dispensers* (2000):

Saffman, M.; Walker, T. G. and Mølmer, K.: *Quantum information with Rydberg atoms*; Rev. Mod. Phys. (2010): **82**; pp. 2313

Safronova, M. S.; Williams, C. J. and Clark, C. W.: *Relativistic many-body calculations of electric-dipole matrix elements, lifetimes, and polarizabilities in rubidium*; Phys. Rev. A (2004): **69**; p. 022509

Salvat, F.; Fernández-Varea, J. and Jr., W. W.: *Accurate numerical solution of the radial Schrödinger and Dirac wave equations*; Computer Physics Communications (1995): **90**; pp. 151

Sansonetti, J. E.: *Wavelengths, Transition Probabilities, and Energy Levels for the Spectra of Rubidium (Rb I through Rb XXXVII)*; Journal of Physical and Chemical Reference Data (2006): **35**; pp. 301

Schlosser, N.; Reymond, G.; Protsenko, I. and Grangier, P.: *Sub-poissonian loading of single atoms in a microscopic dipole trap*; Nature (2001): **411**; pp. 1024

Schwindt, P. D. D.; Knappe, S.; Shah, V.; Hollberg, L.; Kitching, J.; Liew, L.-A. and Moreland, J.: *Chip-scale atomic magnetometer*; Applied Physics Letters (2004): **85**; pp. 6409

Scientific, T.: *Kodial Zero Length Viewports With Anti-Reflective Coatings* (2011):

Shabanova, L. N. and Khlyustalov, A. N.: *Oscillator strengths of lines of the principal series of rubidium*; Opt. Spectrosc. (1984): **56**; p. 128

Shaddock, D. A.; Gray, M. B. and McClelland, D. E.: *Frequency locking a laser to an optical cavity by use of spatial mode interference*; Opt. Lett. (1999): **24**; pp. 1499

Shimizu, F.; Shimizu, K. and Takuma, H.: *Four-beam laser trap of neutral atoms*; Opt. Lett. (1991): **16**; pp. 339

Shirley, J. H.: *Modulation transfer processes in optical heterodyne saturation spectroscopy*; Optics Letters (1982): **7**; pp. 537

Shor, P.: *Algorithms for Quantum Computation*; Proceedings of the 35th Annual Symposium on Foundations of Computer Science (1994): **124**

Snyder, J. J.; Raj, R. K.; Bloch, D. and Ducloy, M.: *High-sensitivity nonlinear spectroscopy using a frequency-offset pump*; Opt. Lett. (1980): **5**; pp. 163

Stanojevic, J. and Côté, R.: *Many-body Rabi oscillations of Rydberg excitation in small mesoscopic samples*; Phys. Rev. A (2009): **80**; p. 033418

Steane, A. M.; Chowdhury, M. and Foot, C. J.: *Radiation force in the magneto-optical trap*; J. Opt. Soc. Am. B (1992): **9**; pp. 2142

Steck, D. A.: *Quantum and Atom Optics*; Technical report; Oregon Center for Optics and Department of Physics, University of Oregon (2007)

Tada, M.; Kishimoto, Y.; Kominato, K.; Shibata, M.; Yamada, S.; Haseyama, T.; Ogawa, I.; Funahashi, H.; Yamamoto, K. and Matsuki, S.: *Single-photon detection of microwave blackbody radiations in a low-temperature resonant-cavity with high Rydberg atoms*; Physics Letters A (2006): **349**; pp. 488

Teo, B. K.; Feldbaum, D.; Cubel, T.; Guest, J. R.; Berman, P. R. and Raithel, G.: *Autler-Townes spectroscopy of the* $5S_{1/2}$–$5P_{3/2} - 44D$ *cascade of cold* ^{85}Rb *atoms*; Phys. Rev. A (2003): **68**; p. 053407

Theodosiou, C. E.: *Minima in the emission oscillator strengths of alkali Rydberg states*; J. Phys. B (1980): **L1**; p. 13

Trupke, M.; Ramirez-Martinez, F.; Curtis, E. A.; Ashmore, J. P.; Eriksson, S.; Hinds, E. A.; Moktadir, Z.; Gollasch, C.; Kraft, M.; Prakash, G. V. and Baumberg, J. J.: *Pyramidal micromirrors for microsystems and atom chips*; Applied Physics Letters (2006): **88**; 071116

Ungar, P. J.; Weiss, D. S.; Riis, E. and Chu, S.: *Optical molasses and multilevel atoms: theory*; J. Opt. Soc. Am. B (1989): **6**; pp. 2058

Urban, E.; Johnson, T. A.; Henage, T.; Isenhower, L.; Yavuz, D. D.; Walker, T. G. and Saffman, M.: *Observation of Rydberg blockade between two atoms*; Nature Physics (2009): **5**; pp. 110

Vangeleyn, M.; Griffin, P. F.; Riis, E. and Arnold, A. S.: *Single-laser, one beam, tetrahedral magneto-optical trap*; Optics Express (2009): **17**; pp. 13601

Walker, T. G. and Saffman, M.: *Zeros of Rydberg Rydberg Föster interactions*; Journal of Physics B Atomic Molecular Physics (2005): **38**; p. 309

Walker, T. G. and Saffman, M.: *Consequences of Zeeman degeneracy for the van der Waals blockade between Rydberg atoms*; Phys. Rev. A (2008): **77**; p. 032723

Wasik, G.; Gawlik, W.; Zachorowski, J. and Zawadzki, W.: *Laser frequency stabilization by Doppler-free magnetic dichroism*; Applied Physics B: Lasers and Optics (2002): **75**; pp. 613; 10.1007/s00340-002-1041-2

Weatherill, K. J.; Pritchard, J. D.; Abel, R. P.; Bason, M. G.; Mohapatra, A. K. and Adams, C. S.: *Electromagnetically induced transparency of an interacting cold Rydberg ensemble*; Journal of Physics B Atomic Molecular Physics (2008): **41**; pp. 201002

Weiner, J. and Ho, P. T.: *Light-matter interaction*; Wiley-Interscience (2003)

Weitenberg, C.; Endres, M.; Sherson, J. F.; Cheneau, M.; Schausz, P.; Fukuhara, T.; Bloch, I. and Kuhr, S.: *Single-spin addressing in an atomic Mott insulator*; Nature (2011): **471**; pp. 319

Wilk, T.; Gaëtan, A.; Evellin, C.; Wolters, J.; Miroshnychenko, Y.; Grangier, P. and Browaeys, A.: *Entanglement of Two Individual Neutral Atoms Using Rydberg Blockade*; Phys. Rev. Lett. (2010): **104**; p. 010502

Wineland, D. J. and Dehmelt, H.: *Proposed* $10^{14}\Delta\nu < \nu$ *Laser Fluorescence Spectroscopy on* Ti^{+} *Mono-Ion Oscillator III (side band cooling)*; Bulletin of the American Physical Society (1975): **20**; p. 637

Ye, C.: *Tunable external cavity diode lasers*; World Scientific (2004)

Zhang, S.; Robicheaux, F. and Saffman, M.: *Magic-wavelength optical traps for Rydberg atoms*; Phys. Rev. A (2011): **84**; p. 043408

Zhang, X. L.; Isenhower, L.; Gill, A. T.; Walker, T. G. and Saffman, M.: *Deterministic entanglement of two neutral atoms via Rydberg blockade*; Phys. Rev. A (2010): **82**; p. 030306

Zimmerman, M. L.; Littman, M. G.; Kash, M. M. and Kleppner, D.: *Stark structure of the Rydberg states of alkali-metal atoms*; Phys. Rev. A (1979): **20**; pp. 2251